Design and Development of Efficient Electrodes for Rigid and Flexible Solar Cells

A dissertation submitted in partial fulfilment of requirements for the degree of

Doctor of Philosophy

by

Chandan Dawo

Roll No. 176151001

School of Energy Science and Engineering

Indian Institute of Technology Guwahati

Guwahati-781039, Assam, India

January 2024

Abstract

Photovoltaic technology has been regarded as a renewable power source which converts sunlight directly into electricity with least impact on the environment. Dye sensitized solar cells (DSSCs) is one such 3rd generation photovoltaic technology which drawn a significant attention due to its low manufacturing cost, simple preparation methodology compared to other technologies. It is an electrochemical cell consist of working electrode/photoanode, dye, electrolytes and counter electrodes. The electrodes in DSSCs play a significant role in charge transport and collection during operation. Dye (N719) in DSSCs harvests solar energy and transfer electrons to a semiconductor material (TiO_2) for the generation of electricity. DSSCs assembled with abundant and cheap materials seems to be a substantial contributor for commercial development in the near future. The thesis focuses on the development of economically competitive rigid and flexible electrodes with the motivation to further enhance energy conversion efficiency of DSSCs.

The experimental works in this thesis has been broadly divided into three parts. The first part focus on development of efficient working electrodes for conventional DSSCs. Basically, the working electrode made of a Titanium dioxide (TiO_2), treated with UVO_3 system and doped with Cesium Bromide (CsBr) to further enhance the performance of DSSCs. The study revealed that UVO_3 treatment increases oxygen vacancies, conductivity, and surface energy that leads in enhancing dyes absorption. As a result, the UVO_3 exposure working electrode outperformed with a power conversion efficiency (PCE) of 8.31%. With an aim to design an efficient electrode for DSSC, the bandgap of TiO_2 ETL is tune through doping with different concentration of cesium bromide (CsBr). An attractive PCE of 9% was achieved for TiO_2-CsBr doped photoanode based device. The results demonstrated that bandgap engineering of TiO_2 ETL provide an efficient electron extraction and improves charge transfer properties. The second part deal with an inexpensive polyaniline (PANI), carbon nanotubes (CNTs) and their composite as a counter electrodes material to replace traditionally used Platinum (Pt). The PANI-PSSNa and CNTs-PANI CEs enhanced effective surface area of the catalytic film that improved electrocatalytic activity, faster electron transfers and suppressed charge recombination. As a result, the PCE of 7.15%, and

6.67% are achieved for the fabricated devices based on PANI-PSSNa and CNTs-PANI CEs respectively.

The third part deals with the fabrication and characterization of flexible DSSCs. The objective of fabricating DSSCs on polymer substrates enables cost-effective and speedy roll-to-roll (R2R) processing systems along with making the device light-weight and flexible. However, flexible plastic substrates set restrictions to their materials and annealing processes. So, extensively studied have been carried out concentrating on the factors related to colloid binder free paste preparation, deposition and processing of ETL to improve the photovoltaic properties of FDSSC. The ETL processed with UVO_3 system improved inter-particle connectivity and hence better solar cell performance was found with maximum PCE of 2.5%.

The efforts made in this thesis highlights an efficient development of electrodes for rigid and flexible DSSCs.

Dedicated to my parents and family

Statement

I do hereby declare that the work incorporated in this thesis entitled, "**Design and Development of Efficient Electrodes for Rigid and Flexible Solar Cells**" is the result of investigations carried out by me under the guidance of Dr. Harsh Chaturvedi at the School of Energy Science and Engineering, Indian Institute of Technology Guwahati, Guwahati, Assam, India.

In keeping with the general practice of reporting scientific observations, due acknowledgements have been made wherever the work described is based on the findings of other investigators. I further declare that this work has not been submitted in part or full to any other university or institute for award of any degree or diploma.

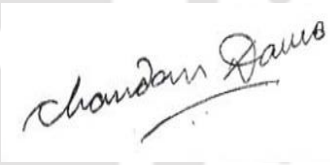

IIT Guwahati **Chandan Dawo**

January 2024

भारतीय प्रौद्योगिकी संस्थान गुवाहाटी
Indian Institute of Technology Guwahati
North Guwahati, Guwahati
PIN- 781039, Assam State, INDIA
Phone: +91 361 2583000 Extn 2702, 2582702
Fax: +91 361 2690 762 (Institute), 2582749 (Department)

Certificate

This is to certify that the work included in this thesis entitled "**Design and Development of Efficient Electrodes for Rigid and Flexible Solar Cells**" by Chandan Dawo, School of Energy Science and Engineering, Indian Institute of Technology Guwahati has been carried out under my supervision. I further certify that this work has not been submitted to any other University or Institution in part or full for the award of any degree or diploma.

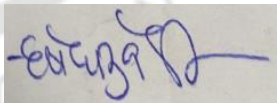

Late Harsh Chaturvedi

Thesis supervisor

School of Energy Science and Engineering

Indian Institute of Technology Guwahati

Guwahati- 781039, Assam, India

Secretary, SPPC

School of Energy Science and Engineering.

Indian Institute of Technology Guwahati.

Acknowledgements

I feel delighted to express my deep gratitude and sincere appreciation to those who have contributed to this thesis and help me during this truly memorable and overwhelming journey. I would like to acknowledgement all of them who have made this thesis possible.

At the outset, I am very grateful to my supervisor Dr. Harsh Chaturvedi for giving me an opportunity to work in his research group. His diligent, deep insights, scientific guidance, critical thinking, patience, motivate and well-balanced style influences my research tremendously. I thank him for giving freedom in my research, believing in me and pushing me further than I thought I could go. I feel lucky enough to have him as my advisor who always encouragement and support me with his hard work, breadth of knowledge, strong logic, dedication, creativity and optimism.

Besides my mentor, I am extremely grateful to my doctoral committee members, Prof. Harshal B. Nemade, Dr. Arun Tej Mallajosyula, and Dr. Pankaj Kalita for assessing my research work regularly. Their suggestions, insightful advices, crucial comments and helpful discussion helped me to improve my research and professional development from various perspectives.

My deepest appreciation also goes to my collaborator, Prof. Parameswar Krishnan Iyer department of chemistry and center for Nano technology, IIT Guwahati for his continuous help and support. He is always very generous and allowing me to access valuable equipment (such as solar simulator, EQE, impedance spectroscopy CH instrument etc.) for my research. The thesis could not have been complete without the help of my collaborators, who had provided lab facilities along with strong support and guidance.

I am grateful to all the staff and researchers of school of energy science and engineering, department of chemistry, physic, center for nanotechnology, and central instrument facility, IIT Guwahati for their support and cooperation. I am also obliged to the staff of academic affairs, student affairs, and finance sections of IIT Guwahati for being kind enough to help and advice in their respective roles.

Undoubtedly, my research team Dr. Adil and Dr. Maimur deserves the greatest respect for their diligence, hard work, and key input into the overall research work. Thanks to Adil for his brotherly caring nature, sharing knowledge of basics techniques that were needed in performing experiments. He shows endless patience in helping me and to improve my thinking approach.

It is great pleasure to thank my senior lab mates Dr. Rabindra, Dr. Ritesh, Dr. Deepika, Dr. Raman, Dr. Shaad, Dr. Ashish, Dr. Rahul, and Dr. Anamika and present lab mates, Priyalakshmi, Brijesh, Debika, Jyotishman, Jeet, Ramesh for their timely support and help. I also want to thank them for creating a vibrant and pleasant atmosphere in the lab and making my days memorable.

I also extend my sincere thanks to my friends Jaishree, Abhishek, Juhi, Pilik, Samar, Hemanto, Durlov, Bhupen, Bhaskar, Basanta, Saptarshi and other friends for their encouragement, support and all the help they extended whenever required. I greatly value their friendship and will miss the memorable moments shared with them during my stay at IIT Guwahati.

I sincerely express my deep gratitude towards entire fraternity from my school, college and university especially Mrs. Baruah Ma'am, Mrs. Amilita Ma'am, Mrs. Anju Ma'am, Mr. Pratap Sir, Sandip Sir, Dr. Jupitora, Dr. R. Arun Prasath, Dr. A. Sreekumar, Dr. P. Elumalai, and Dr. P. Thilakan for imbibing good values and knowledge in me.

My Ph. D. journey could not have been completed without the endless support, love, tolerance and blessings from my family. I am privilege and blessed enough to have such a supportive and caring parents. It is because of their sacrifice, prayers, and struggle, I am able to live my dream to complete Ph.D. from a prestigious institute. I am also grateful to my brothers, sisters, uncle and aunt for their cooperation, love, and emotional support. Special thanks should goes to my wife Preety, who has done so much for my study which had immensely needed to complete this work. No words can express my heartfelt appreciation for her.

I am grateful to the Ministry of Education (MoE), Govt. of India, for the financial assistance in the form of a scholarship.

Finally, I thank almighty God for giving me a strength to chase my dreams, and being with me in all my failure and success.

Chandan Dawo

Abbreviations

2D	Two-dimensional
3D	Three-dimensional
AFM	Atomic force microscopy
AM	Air mass
CB	Conduction band
CdS	Cadmium sulfide
CdSe	Cadmium selenide
CdTe	Cadmium telluride
CE	Counter electrode
CIGS	Cadmium Indium Gallium Sulfide
CsBr	Cesium bromide
CNT	Carbon nanotube
CPE	Constant phase element
CV	Cyclic voltammetry
DC	Direct current
DSSC	Dye sensitizes solar cell
EDX	Energy dispersive X-ray spectroscopy
E_G	Bandgap
EIS	Electrochemical impedance spectroscopy
ETL	Electron transporting layer
Eq.	Equation
EQE	External quantum efficiency
eV	Electrovolt
FESEM	Field Emission Scanning Electron Microscope
Fig.	Figure
FF	Fill factor
FTIR	Fourier-transform infrared spectroscopy
FTO	Fluorine-doped tin oxide
G	Global
HOMO	Highest occupied molecular orbital
Hz	Hertz
IPCE	Incident Photon to Current Efficiency
I_{SC}	Short circuit current
ITO	Tin-doped indium oxide
IV	Current-voltage
J_o	Current density
JV	Current density-voltage
Lab	Laboratory
LUMO	Lowest unoccupied molecular orbital
M	Molar
mA	milliampere
mg	milligram
mV	millivolt
mW	milliwatt
nm	nanometer
NREL	National renewable energy laboratory
ns	nanosecond
N719	cis-diisothiocyanato-bis(2,2′-bipyridyl-4,4′-dicarboxylato)

	ruthenium(II) bis(tetrabutylammonium)
OCVD	Open circuit voltage decay
PANI	Polyaniline
PCE	Power conversion efficiency
PEN	Polyethylene naphthalate
PET	Polyethylene terephthalate
PL	Photoluminescence
PSSNa	Poly (sodium 4-styrenesulphonate)
Pt	Platinum
P25	Titanium dioxide powder
R	Reistance
RMS	Root mean square
Ru	Ruthenium
s	second
Si	Silicon
SI	Supplementary Information
TCO	Transparent conducting oxide
TiO_2	Titanium dioxide
TTIP	Titanium tetra-isopropoxide
UV-O_3	Ultraviolet ozone
UV-Vis	Ultraviolet visible
V	Volt
V/V	Volume/volume
Wt.%	Weight percent
XPS	X-ray photoelectron spectroscopy
XRD	X-ray diffraction
ZnO	Zinc oxide
µm	micrometer
Ω	Ohm

Table of Contents

List of Figures

List of Tables

CHAPTER 1 Introduction

Photovoltaic technology as a solution to global warming

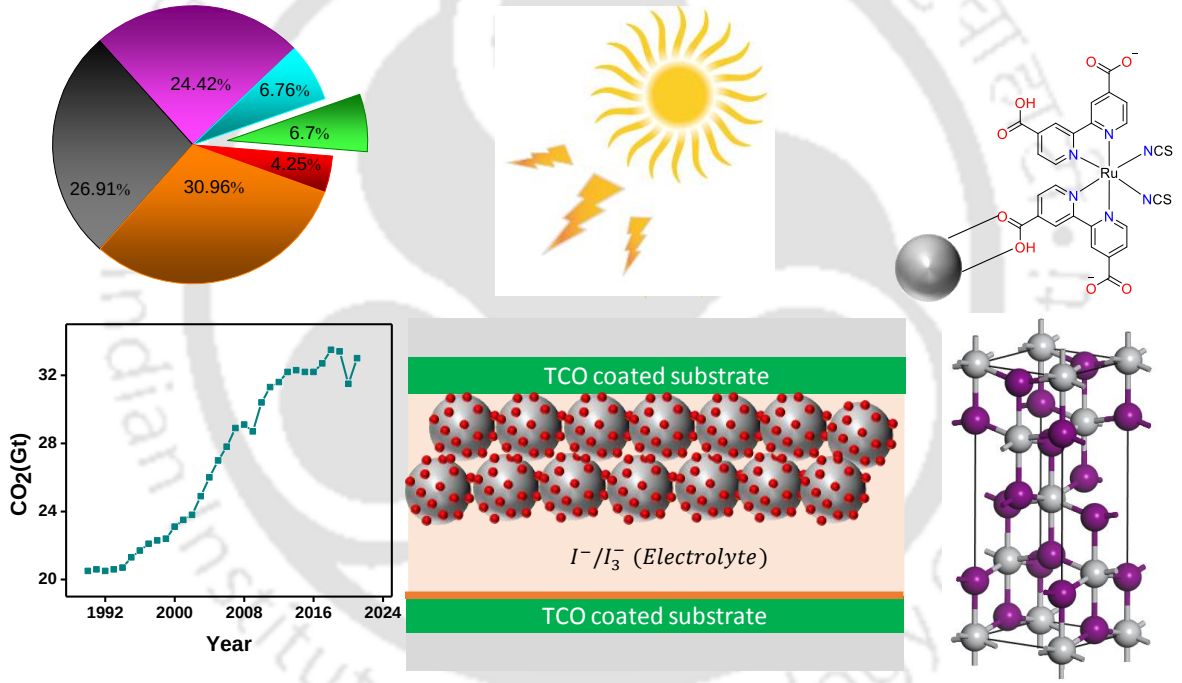

1.1 Photovoltaic

Energy plays an essential role in our modern lifestyle such as transportation, cooking, lighting, cooling, heating, operating computers, and machinery etc. Therefore, the global energy demand is growing continuously due to increasing population and industrialization. The major source of energy consuming today for the generation of electricity depend on fossil fuels. The combustion of fossil fuels has polluted the environment by the emission of carbon dioxide (CO_2), methane and other greenhouse gases. Fortunately, a large number of renewable energy resources are available in nature such as hydropower, biomass, wind, tidal, geothermal and solar energy. Renewable energy is sustainable, and seems to play a major role in the near future to overcome the energy crisis and climate changes. Among the renewable energy sources available solar energy is considered as a champion, owing huge amount of energy on the earth from the sun which is inexhaustible, free and non-polluting. The quantity of solar energy that radiates on Earth's surface in 60 minutes is approximately equivalent to the annual energy required for humans. According to statistics, energy needs worldwide can be fulfilled by just covering 0.1% of Earth's crust with a solar cell having a power conversion efficiency of 10% [1]. Photovoltaic (PV) technology is particularly very attractive, which directly converts solar energy into high quality electrical energy. It has been considered as an appropriate renewable power source for the fulfillment of demanding world energy consumption with least impact on the environment [2]. So far, various types of PV technologies have been developed and name as first (1^{st}), second (2^{nd}) and third (3^{rd}) generation solar cells. The fabrication process of 1^{st} generation solar cell such as monocrystalline, multi-crystalline, microcrystalline, nano crystalline, and amorphous silicon (Si) based solar cells involves high vacuum systems, which are costly, complicated, and energy consuming [3-4]. 2^{nd} generation are often called thin film technologies such as cadmium telluride (CdTe) [5-6], copper indium gallium selenide (CIGS) [7-8], gallium arsenide (GaAs) [9-10], and CZTSSe [11] cells etc., [12]. 3^{rd} generation are described as an emerging PV technology, as it is still in the development or research phase. The motivation for developing 3^{rd} generation solar cell is to replace the conventional expensive silicon based photovoltaics with simple production method. These technologies are cost effective, ease manufacturing, energy efficiency, and also compatible on flexible substrates. With the abundance of PV technology potential yet to be harnessed, the percentage of CO_2 emission can be dramatically reduced in near future. A PV based energy transition is the most realistic avenue to avoid the worst effects of climate change [13]. Recently, PV technology has

been turned out to be a multi-billion and fast-growing renewable technology industry. Currently, the 1st generation solar cells have dominated the PV market worldwide [14-16].

1.2 Dye Sensitized Solar Cell (DSSC)

The dye sensitized solar cell (DSSC) is a photoelectron chemical device directly converts solar radiation into electrical energy. The development of DSSCs initiated with the pioneering work of O'Regan and Grätzel in 1991. A thin layer of TiO_2 nanoparticles film approximately 8-12 µm is successfully coated on the surface of FTO glass substrate and sensitized with dye for absorbing light. The photoelectric conversion efficiency (PCE) of the first Grätzel's cell exceeding 7% under the condition of AM 1.5G. This solar cell is popularly known as Grätzel cell after his invention [17-18]. Among various PV technologies, DSSCs is very attractive due to their potential advantages like easy fabrication, low production cost, transparency, compatible with flexibility substrates, light weight, and multi-color options. Flexibility and multi-color design offer huge potential as a part of the building architecture and portable electronics applications. DSSCs performance better than other PV technologies under different solar incident angles and low light environments. And also almost all the components of DSSCs are "tunable" such as semiconducting electron transport layers (ETLs), photoactive layer (dye),

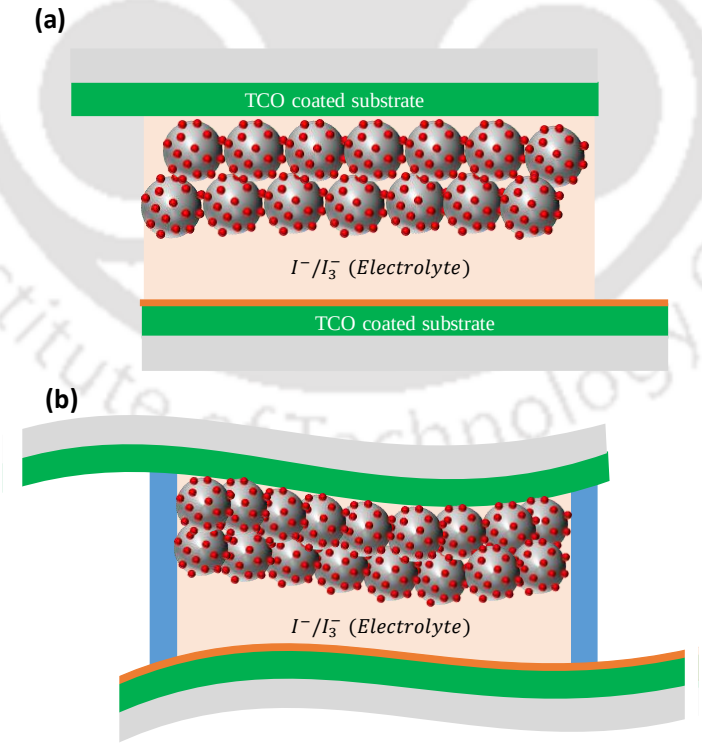

Figure 1. 1: Structure of (a) Rigid and (b) Flexible DSSCs

electrolytes and the counter electrodes [19]. So many features of DSSCs are unique and advantageous over the 1st generation silicon (Si) based solar cells. Si solar cell fabrication process need high vacuum systems, which are complicated, costly, and energy consuming [20]. Therefore, an alternative to Si solar cells is DSSC. The structure of DSSC typically consist of three major components, namely (i) working electrode or photoanode, (ii) an electrolyte (I^-/I_3^- couple), and (iii) counter electrode. It has a sandwich structure of dye loaded TiO_2 photoanode/electrolyte/counter electrode. Fig. 1.1(a and b) illustrates the structure of rigid and flexible DSSCs.

1.2.1 **Rigid and Flexible Substrates**

DSSCs are usually fabricated over transparent conducting oxide (TCO) substrates. The functions of TCO substrate in DSSC is to support the electron transport layer (ETL) and catalyst of CE to transport and collect the electrons. Therefore, TCOs with high conductivity and optical transmittance are the basic requirement for higher performance of devices. The electrical conductivity helps in charge transport while transparency allows the sunlight to pass through it to the photoactive layer i.e., dye anchored on TiO_2 film. Among the TCOs, the most popular indium doped tin oxide (ITO) and florine doped tin oxide (FTO) are widely and commercially demonstrated in optoelectronics and photovoltaic devices. For rigid glass substrate, TCOs is dc-magnetron at high temperature approximately 300 °C to 400 °C or sputtered is done on the cold substrate and then sintering at high temperatures would form high degree of crystallinity structure that are very effective in enhancing its conductivity. In the first and second part of the thesis that is based on rigid substrate we used FTO coated substrate. Under atmospheric conditions the FTO coated glass substrate is known to have chemically inert, mechanically robust, resistance to high temperature and relatively better stability. Moreover, it has high abrasion, low absorption, reflection and cost effective.

The electrical conductivity of TCOs in polymer based substrate is lower than rigid glass, due to relatively poorer carrier concentration of TCOs film on polymer substrate. The microstructure of TCO film at low temperatures is generally amorphous in nature, that create defect sites for charge traps leading to poor electrical properties. Therefore, the overall performance of FDSSCs would be lower than that of conventional DSSCs due to inferior optical transmittance and conductivity of plastic substrates [21-24]. Due to the lower sheet resistance and better transmittance, ITO is one of the most extensively used TCO in polymer substrates. Deposition of TCOs on plastic substrates such as Polyethylene naphthalate (PEN)

and Polyethylene terephthalate (PET) is carried out in low temperature or power due to their limitation in thermal sensitivities. The optical and electrical conductivity properties of FTO and ITO mainly depend on film composition and deposition parameters like film thickness, oxygen pressure, substrate deposition temperature and sputtering power. The sheet resistance of ITO PET increased at 180 °C and ITO PEN at 135 °C, respectively. Polymer substrate also absorbed visible and ultraviolet light to some extent and relatively showed lower transmittance.

The selection of a suitable substrate is crucial for the device's performance and stability. Substrate can be divided into two part rigid and flexible. Several desired characteristics of substrates are listed as follows (i) optical properties: high transparency of light, more than 90 % in the visible region as solar cells are light absorbing devices. (ii) conductivity properties: transparent conducting electrodes (TCEs) substrates are usually coated with TCO as a charge collecting layer. The sheet resistance of substrate is directly related to photovoltaic parameters, exclusively the photocurrent and fill factor (FF) of the solar cells. (iii) chemical properties: the substrates must have good resistance toward various solvents exposed during the fabrication process. (iv) barrier properties: some flexible substrates are vulnerable to moisture or oxygen, severely affecting the device's performance. (v) mechanical properties: under stress and strain, the flexible substrate must comply with deformation transformation and effectively release stress to maintain its original dimensions without losing functionality. (vi) thermal properties: softening temperature of the substrates must be compatible with the maximum processing temperature that the film can be subjected to. The substrates can be contracted or expand during temperature change resulting in additional stress on the lattice and creating a crack [21][25].

Glass substrates

Conventional DSSCs used FTO or ITO coated rigid glass as a substrate, and an efficiency of over 14.30% has been fairly achieved in a lab so far [26]. The glass substrate possesses excellent conductivity, transmittance, thermally stable properties which withstand high temperature above 450°C, and good stability against water permeability and oxygen. However, it cost around 20-30% of the device value, in addition, its rigidity, brittleness, heavyweight, and shape limitation affect the potential integration in wearable and portable electronic device and cannot be used for roll to roll (R2R) production. Therefore, the scientific community has shifted their research toward flexible substrates regarding these restriction [27-28]. There is an ultrathin flexible glass substrate with a thickness of around several hundred μm called willow glass. Flexible glass substrates fulfil most of the desired properties of substrates. It possesses attractive properties such as high-temperature resistance up to 600 °C, good mechanical

stability, and excellent barrier for oxygen and moisture. Sheehan et al. demonstrated an ITO coated flexible glass as a substrate and achieved a PCE of 4.53% [29]. However, heavyweight, fragility, and expensive would be a big concern compared to other flexible substrates.

Plastic substrate

Flexible substrates are the major components needed to fabricate FDSSCs. Conducting plastic substrates like indium doped tin oxide polyethylenenaphtalate (ITO PEN) and indium doped tin oxide polyethyleneterephtalate (ITO PET) are the most commonly used substrate in FDSSCs. These materials offer some advantages like flexibility, lightweight, good transparency, chemically stable against electrolytes, and compatibility for R2R production, which enables high throughout production. Plastic substrates are used for both working and counter electrodes. An efficiency of 7.6% has been reported for FDSSC based on plastic substrate [30]. However, plastic substrate's drawback is that they cannot be used above 150 °C as they tend to deform and start melting at 235 °C. Mainly because of low glass transition temperature and a high coefficient of thermal expansion, shrinkage or expansion occurred at elevated temperature changes that causing sheet resistance of the plastic substrates increased. They are also brittle due to excessive UV irradiation, water vapour, and other contaminants may diffuse into FDSSCs [22][25][27].

1.2.2 Electron Transporting Material TiO_2

The main function of electron transport layer (ETL) is preferentially collects and inject the photogenerated electrons from the dyes to TCO. The matching energy level between the ETL and dye prevents recombination of photo-excited electrons in the device. The electron transport materials used in DSSCs and FDSSCs are TiO_2 [31], SnO_2 [32], ZnO [33-34], and Zn_2SnO_4 [35] etc. Among them, TiO_2 is the most widely used electron transport material in DSSCs due to its superior characteristics such as nontoxicity, high refractive index, strong oxidizing power, cost-effectiveness, mesoporous nature, long term chemical stability, large band gap and ideal Fermi level. TiO_2 has three primary crystalline forms, brookite phase (orthorhombic, bandgap (E_G) 3.26 eV), anatase phase (tetragonal, E_G 3.23 eV), and rutile phase (tetragonal, E_G 3.05 eV). The photocatalytic activity of TiO_2 dependent strongly on its specific surface areas, phase structure, crystallite size, and pore structure. Compared to anatase phase, rutile has lower specific surface area, larger grain size, and weak surface adsorption capacity. The photocatalytic activity of the TiO_2 materials can be balanced through calcination. Thermodynamically, Rutile is the most stable form of TiO_2, whereas anatase is a metastable

phase and its shows better efficiency in solar energy conversion due to less recombination and fast carrier transport. The crystal structure of anatase TiO_2 is shown in Fig. 1.2. Anatase phase of TiO_2 has indirect band gap, while brookite and rutile has direct bandgap. Due to indirect bandgap, the effective life time of photoexcited electrons is longer for anatase compared to brookite and rutile. Among the three polymorphs, the average effective mass of photoexcited electrons of anatase is also the lightest that facilitate faster movement of photoexcited electrons with lower recombination. Anatase also exits higher conduction band edge that leads to higher open circuit voltage (V_{oc}) in DSSCs [36-38].

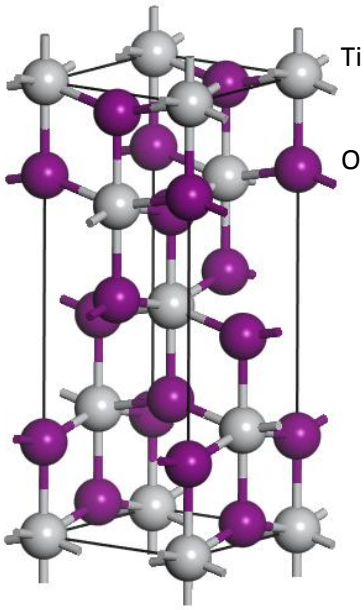

Figure 1. 2: Crystal structure of anatase TiO_2

1.2.3 **Dye**

Another key component in DSSCs is Dye, as it harvests sunlight and generates photo-excited electrons at the semiconductor. It is basically anchored on the surface of photoanode and for efficient performance, it must possess several desired properties as follows: (i) The absorption properties of the dye must have high molar absorption coefficient i.e., sufficiently wide to cover the entire visible and part of the near-infrared region (NIR). (ii) it should have good photostable and thermal stability along with chemically adsorbed functional group is essential (-COOH, -SO_3H, -H_2PO_3, etc.) to load strongly on semiconductor materials. (iii) Suitable highest occupied molecular orbital (HOMO) and lowest unoccupied molecular orbital (LUMO) energy levels of the sensitizer is necessary for efficient charge transfer into the conduction band of semiconductor materials and dye regeneration from the electrolyte [39]. As far literature most

of the DSSCs used di-tetrabutylammonium cis-bis(isothiocyanato)bis(2,20-bipyridyl-4,40-dicarboxylato) ruthenium (II) (N719) as the photosensitizer. The most efficient and commonly used dye in rigid and flexible DSSCs is N719 [40-41]. The molecular structure and absorbance spectrum of N719 is show in Fig. 1.3. The experimental works carried out in thesis used N719 dye as a sensitizer.

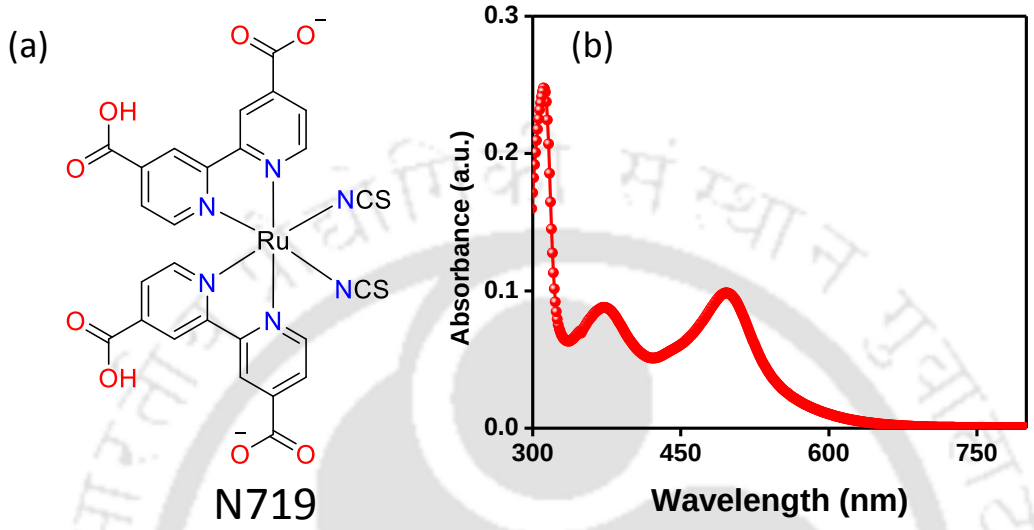

Figure 1. 3: (a) Molecular structure of N719 Dye and (b) its absorbance spectrum [39].

1.2.4 **Electrolyte**

The electrolyte in DSSCs works as a medium to transfer charge carrier from counter electrode to oxidised dye. Its major function is to regenerate the dye continuously during operation and also greatly influences the light to electrical energy conversion efficiency and long term stability of the devices [15]. Electrolytes in DSSCs can be categorized into three types: liquid, quasi solid, and solid electrolytes. Solid electrolytes are hardly employed in FDSSCs since they have a very high resistance, low charge carrier mobility, and weak interfacial connection resulting in lower PCE. Quasi-solid and liquid electrolytes are usually employed in FDSSCs due to their high mobility of ion and good interfacial connection with dye that provides high power conversion efficiency [42-43]. Liquid electrolyte is the most commonly used electrolyte in FDSSC. It possesses some important features like easy preparation, low viscosity to minimize charge transfer resistance, high conductivity, a good interfacial connection between electrodes, and thus produced high PCE [15][44]. The Liquid electrolyte (I^-/I_3^-) used in this thesis work composed of 0.05M I_2, 0.5M LiI, 0.1M guanidium thiocyanate, 0.5M 4-tert-

butylpyridine and 0.5M 1-Butyl-3-methylimidazolium iodide dissolved in acetonitrile/valeronitrile (Volume ratio of 85:15) solvent.

The above listed components are basic constituents of a dye sensitized solar cells that is commonly used.

1.3 Working Principle of DSSCs

The structure and operating principle of the DSSCs are shown in Fig. 1.4.

Step 1: Photoexcitation (D*).

When dye molecules absorb light (D), it changes an electronic state from the highest occupied molecular orbital (HOMO) to the lowest unoccupied molecular orbital (LUMO), the excited state (D^*).

$$D/TiO_2 + h\vartheta \rightarrow D^* /TiO_2(photoexcitation)$$

Step 2 and 3: Electron injection and transport

The excited electrons from dye molecules inject into the conduction band of TiO_2 and leave holes (D^+) in the dye. The injected electron travels toward the transparent conductive oxide surface.

$$D^*/TiO_2 \rightarrow D^+ /TiO_2 + e^-/TiO_2$$

Step 4: Regeneration of dye (D)

The oxidised dye (D^+), due to loss of an electron, accepts electrons from the reduced iodide ion(I^-)and refills the HOMO of the dye i. e., regenerating its original form (D) and making it ready for electron generation again.

$$2D^+/TiO_2 + (RE)3I^- \rightarrow 2D/TiO_2 + I_3^-(\text{OX})$$

Step 5: Regeneration of I^-.

The photoexcited electrons travel through an external load, reach the counter electrode, and reduce the iodine in the electrolyte. The Pt coated on the counter electrode acts as a catalyst for the reduction.

$$(OX)I_3^- + (CE)2e^- \rightarrow (RE)3I^- (regenerationofI^-)$$

Step 6: Emission

The excited photoelectrons from LUMO can go back to the HOMO without injecting electrons into the conduction band of the electron transport layer.

$$D^* \rightarrow D^+ + h\vartheta \ (Emission)$$

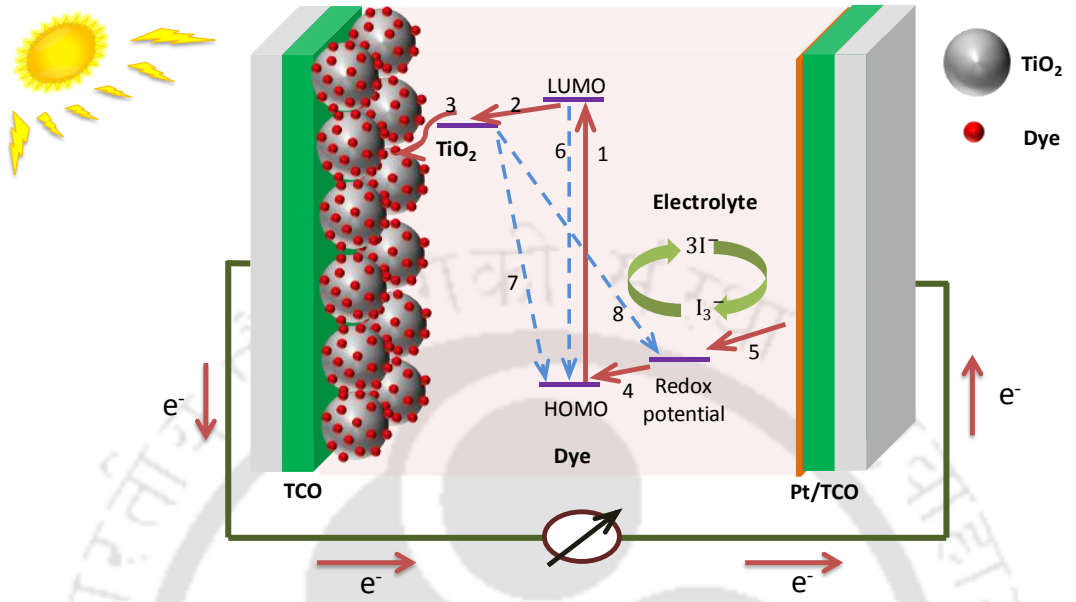

Figure 1. 4: Schematic diagram showing different processes involved during the operation of a DSSC [15].

Step 7: Recombination by donating electrons to D^+.

Injected electrons in the conduction band of ETL recombine rapidly with the reduced oxidized dye (D^+) in the absence of a redox mediator without any measurable photocurrent.

$$D^+/TiO_2 + e^-/TiO_2 \rightarrow D/TiO_2 \ (Recombination)$$

Step 8: Recombination by donating electrons to OX.

$$(OX)I_3^- + e^-/TiO_2 \rightarrow (RE)3I^-$$

Steps 1−5 are desirable reactions for complete conversion of light-to-high quality electric energy whereas, steps 6-8 are undesired reactions mainly responsible for the charge carrier recombination process, which are limitations for the efficiency of FDSSCs [15][39][45-48].

1.3.1 Parameters of DSSCs

Short circuit current density (J_{SC})

The short circuit current density (Jsc) is the maximum current generated in a solar cell when load resistance is zero (Fig. 1.5 (a)). The Jsc value depends on the optical properties and bandgap of dye, charge transportation and collection probability of the device.

$$J_{SC} = \frac{I_{SC}}{A} \ (mA/cm^2)$$

Where, A is the effective area of the solar cell.

Open circuit voltage (V_{OC})

The open circuit voltage (V_{OC}) is the maximum voltage determined from a solar cell when no current flows in the circuit i.e., load with infinite resistance. It mainly depends on fermi level of semiconductor and redox potential of electrolytes in DSSCs. The V_{OC} of DSSC is given by (Fig. 1.5).

$$V_{OC} = \frac{E_{CB}}{q} + \frac{KT}{q} ln\left(\frac{n}{N_{CB}}\right) - \frac{E_{redox}}{q} \ (volts)$$

where, the first two terms define the quasi-fermi level of TiO_2 and E_{redox} is the Nernst potential of the redox mediator, N_{CB} is the effective density of states and n is the number of electron in TiO_2 conduction band [49].

Power conversion efficiency (PCE, η)

The PCE is defined as the fraction of power (P_{in}) from the incident light is directly converted to maximum electrical power by solar cell and it can be calculated using equation

$$PCE \ (\eta) = \frac{P_{max}}{P_{in}} = J_{sc}V_{oc}\text{FF}/P_{in}$$

Where, P_{max} is the maximum power and is illustrated in Fig. 1.5(b). The internationally recognized standard condition for the efficiency measurement of solar cells is under 'AM 1.5 Global [NREL].

Fill factor (FF)

FF is the ratio of maximum power ($P_{max} = J_{mp}V_{mp}$) generated by a solar cell to the product of V_{OC} and J_{SC}. It represents the squareness of J-V curve. Higher the FF is better the good quality of solar cells. Ideally it should be 1. Using following equation, the FF of a solar cell can be determined

$$FF = \frac{J_m V_m}{J_{sc} V_{oc}}$$

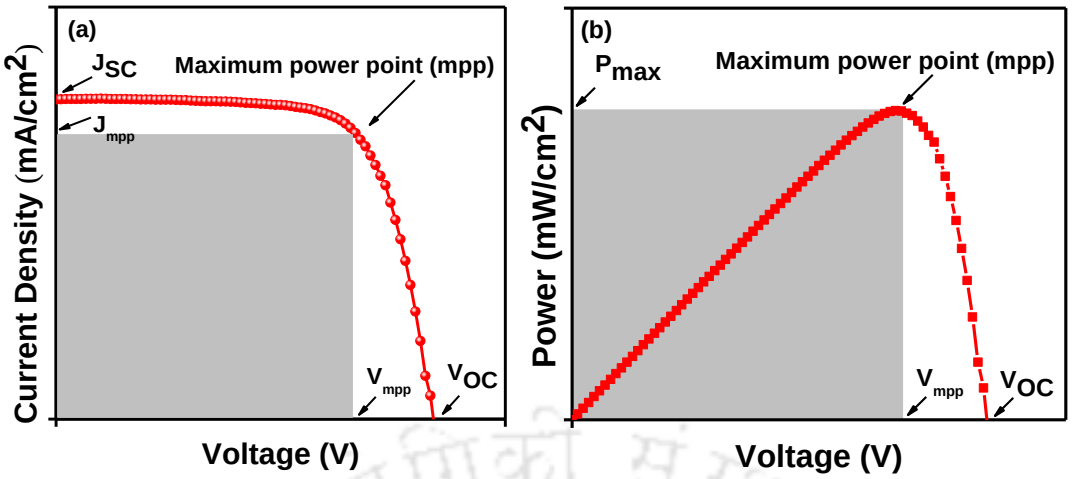

Figure 1. 5: A typical example of (a) *J-V* curve and (b) power output versus voltage curve recorded under light illumination.

1.4 Engineering efficient electrodes for rigid and flexible DSSCs

1.4.1 Photoanode/working electrode

The photoanode or working electrode mainly consist of transparent conducting oxide (TCO) coated substrates, a mesoporous semiconductor metal oxide (TiO_2) film known as electron transport layer (ETL) and a dye anchored on the surface of ETL. In order to achieve higher PCE, a photoanode should possess several desired characteristics as identified from literature: (ii) High transparency to reduce the loss of incident photon. (ii) High surface area for maximum dye loading and hence effective light absorption. (iii) Conduction band of ETL should be sufficiently below 0.3eV from the LUMO of the dye to allow adequate injection of photo generated electrons. (iii) High electron mobility to facilitate electron transport. (iv) Does not react with redox electrolyte to minimize recombination rate [38]. The ETL i.e., TiO_2 paste was prepared by sol-gel technique with solvents and organic binders. The binders in TiO_2 slurry reduce stress of the film while drying, and help in creation of well adhered TiO_2 layer on FTO glass substrates. The paste is deposited on a FTO-coated glass substrate using doctor blade. The electrodes are then annealed at~450 °C to remove binders from the film, to form chemical bonding among TiO_2 nanoparticles and contact between TiO_2 particles with FTO coated glass. Besides, the feasibility of fabricating DSSC with the employment of flexible ITO PET substrate has also been explored. Due to thermal instability of ITO PET substrate they cannot be heated above 150 °C. The surface morphology and composition of ETLs have remarkable impact on the photovoltaic performance of DSSCs. Therefore, extensive research has been carried out to

explore the influences of photoanode modifications on DSSCs performance. The modifications can be based on nano archictures, interfacial engineering, post treatment or surface treatment and band gap engineering through doping (Fig. 1.6).

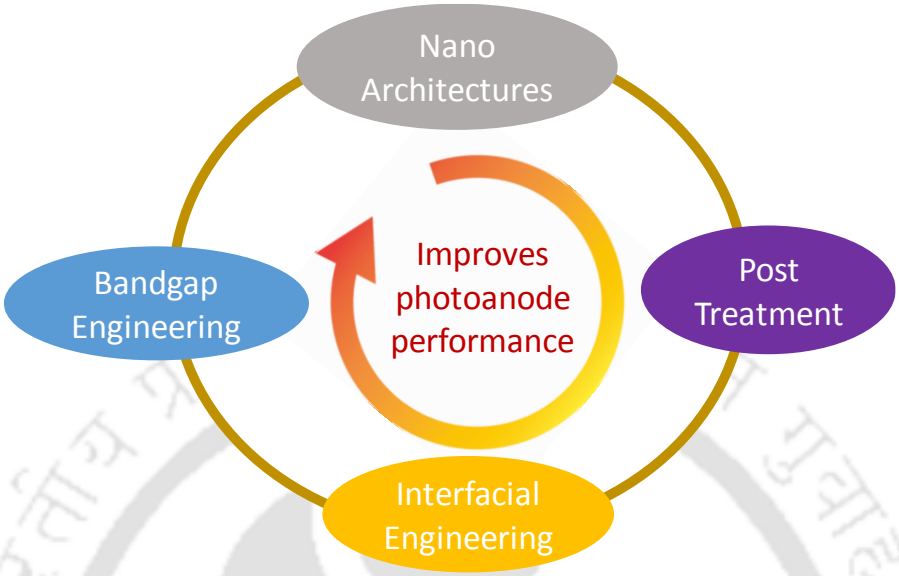

Figure 1. 6: Strategies for improving the photoanodes of DSSCs [38].

To obtain effective photoanodes various structure such as zero dimension (0D) nanoparticles [17], one dimension (1D) nanostructures (nanotube [50-51], nanorod [52-54], nanosheet [55]), 3D hierarchical architectures [56-57] and mesoporous structures [58] are employed in DSSCs. Compared to nanoparticles most of these structures offer considerable improvements in PCE. For example, 1D nanostructures reduce grain boundaries and exhibit excellent charge transport properties but lower effective surface area which led to insufficient dye absorption [59]. Additionally, in 3D and mesoporous structure by virtue of their larger surface area improve dye absorption, possess better light harvesting properties and enhance device performance [57]. Although high surface area of mesoporous TiO_2 active layer is good for efficient dye loading and light absorption in DSSCs performance. However, due to its mesoporous nature it also provides so many opening site for electrolytes to the bare TCO substrate. So, the triiodide ions diffused in to the mesoporous layer and direct contact with the TCO substrate or recombine with the photo injected electrons i.e., $2e^- + I_3^- \rightarrow 3I^-$ and reduced the photocurrent. So, to enhance the photovoltaic performance of DSSCs, recombinations in the two interfaces namely TCO substrate/electrolyte and TiO_2 photoanode/electrolyte should be minimum. Therefore, a thin layer of approximately 50 nm is introduced between TCO and mesoporous TiO_2 film which is called blocking or compact layer. Materials such as Nb_2O_5,

TiO_2, ZnO, V_2O_5, Al_2O_3 and MgO etc. have been effectively used as blocking layer in DSSC. Light scattering is employed in DSSCs to enhance the optical absorption of incident photons for higher energy conversion. However, due to small size of TiO_2 nanoparticles most of the incident solar radiation are transmitted from the ETL without scattering. Therefore, it is essential to increase the light scattering capability of ETL so that the sensitizer could absorbed the incident photon efficiently. In order to achieve this property an additional over layer of ~3 μm nanoparticles relatively larger particles with diameters comparable to the wavelength of the incident light is introduced or mixed with smaller TiO_2 nanoparticles [1][60]. Doping is a process used to adjust the position of either the valence band (VB) or conduction band (CB) of TiO_2 for DSSCs applications. For DSSCs, some non-metals [61-62], alkali metals Ca [63], Li [64] , metalloids [65-66],transition metals [67-68], post-transition metals [69-70],etc., are used as dopants in TiO_2 to modify the charge transport properties, band structure, and surface area etc. Tuning the band structure of TiO_2 is a promising method for improving the driving force of injected electrons from the lowest unoccupied molecular orbital (LUMO) of dye to TiO_2 ETL [71-73]. The surface post treatment of TiO_2 electron transport layer (ETL) has become an important step for improving the performance of DSSCs. Surface treatment such as TiCl4 [74], urea [75], oxygen plasma [76],electron beam [77], oxygen plasma and oxygen ion beam treatment [78] has been successfully employed in improving the performance of conventional DSSCs. The drawback of oxygen plasma treatment, however, is its cost, which requires considerable capital investment. For FDSSCs, low-temperature annealing does not provide adequate necking between nanoparticles, resulting in the lower performance of DSSCs. So, to improve the inter-nanoparticles connection, mechanical stability, and high-quality film-substrate adhesion, the TiO_2 coated film needs additional processing techniques. Several techniques has been used to obtain high efficiency of the flexible DSSCs such as hydrothermal crystallization or chemical sintering [79-81], blocking layer [82-83], UV-Ozone treatment [84-86], UV radiation exposed [87-88], microwave heating [89], mechanical compression [90-91], cold isostatic pressing (CIP) [92-93], lift-off [94] and building block [95] etc.

1.4.2 **Counter Electrode (CE)**

Counter electrode (CE) is an essential component and its main role to reduce the redox species I_3^- to I^- in DSSCs. The characteristics of high-performance CEs are as follows: (i) low resistance to minimize loss of open-circuit voltage (ii) high conductivity and electrocatalytic activity for the reduction of tri-iodide ion (I_3^-). (iii) robust electrochemical and mechanical stability to improve lifetime. (iv) high reflecting of light is desirable in CE. However, due to

the high cost and rare earth metal significant efforts are directed towards the replacement of Pt. Therefore, a large number of alternative materials have been explored as catalyst for CEs such transition metal cobalt sulphides (CoS) [96], nitrides [97], carbides [98] ,oxides [99-100], conductive polymers [101-104], carbon-based materials like carbon black [105], carbon bead [106], graphite [107], activated carbon [108], mesoporous carbon [109], carbon nanofibers [110], graphene [111], and carbon nanotubes [112-113]. In this thesis work Platinum (Pt), conducting polymer polyaniline (PANI) and carbon nanotubes (CNTs) are used as counter electrode catalyst and are deposited by spin coating and doctor blade techniques. The Counter electrode materials should have a work function equal to the redox potential of the electrolytes. The materials for the CE should be, easily available, low cost, and good catalytic activity.

1.4.3 Cost effective production of electrodes

The DSSCs fabrication process and materials used plays an important role in the development of high performance and toward commercialization route. The selection of materials and manufacturing technique is the trade-off between the efficiency performance and cost of production. The electrodes development techniques depend on various parameters such as substrate used, deposition rate, temperature, and surface morphology etc. which dictate the properties and performance of deposited electrodes. Most importantly the other concerns are issues related to water contamination and environmental pollutions. Some fabrication processes employed toxic materials which cannot be discharged into environment directly without proper treatment. Therefore, it is necessary to select easily available materials, low cost, good catalytic activity and environmental friendly fabrication route [60].

My research articles will focus on the surface treatment, bandgap engineering of TiO_2 ETL and cost effective materials for CEs such as PANI, and CNTs. Effect of surface morphology, composition, band structure and charge transport properties were systematically studied. Modified electrodes could be utilized more efficiently in rigid and flexible DSSCs.

1.5 Thesis Synopsis

This thesis comprises of 8 chapters.

Chapter 1 provide the basic introduction of the thesis, especially deal with Photovoltaic technology followed by literature review of dye sensitized solar cells (DSSCs) technology to generate clean energy from sun, a brief explanation on device materials, architectures, working principle along with its different parameters. Further, a brief description about the engineering

of electrodes materials is presented. The motivation of this thesis is to develop sustainable energy production by further progressing of dye sensitized solar cells (DSSCs) in terms of improve performance.

Chapter 2 gives a brief description of electrodes preparation method and different characterization techniques used for analysing the morphological, structural, optical and electrical properties of ETL, photoanodes, counter electrodes and performance of solar cells.

Chapter 3 deal with the surface states of active electron transport layer (TiO_2) which is crucial while fabricating an efficient solar cell. This work experimentally analyses the effect of exposing TiO_2 based electron transport layer (ETL) to the ultraviolet-ozone (UV-O_3) and optimizes the exposure time for improving power conversion efficiency (PCE) of fabricated dye-sensitized solar cells (DSSCs). These results demonstrate that the performance of DSSCs can be improved significantly by UV-O_3 exposure of sintered TiO_2 surface, the duration of exposure being a critical parameter. Fabricated devices show 33.01 % increase in PCE for the optimum exposure. Nevertheless, overexposure of the sample beyond the optimum time decreases the efficiency of the fabricated solar cells. The device with optimum exposure exhibits the highest PCE of 8.34% with short circuit current density (Jsc) of 15.15 mA/cm^2, open circuit voltage (Voc) of 756 mV and Fill factor (FF) of 71.10%. This increase in efficiency is attributed to the enhanced crystallization and reduction in the organic contaminants C-C/C-H from 57.90 to 52.40% as shown by the X-ray diffraction (XRD) and X-ray photoelectron spectroscopy (XPS), respectively. The XPS result further indicates an increase in oxygen vacancy from 12.40 to 23.40% for O 1s state and from 9.30 to 14.30% for Ti 2p state of Ti^{3+}. Results from the Atomic force microscope (AFM) also confirms the minimized surface roughness of 16.36 nm for the optimally exposed TiO_2 film, and increase in hydrophilicity leading to improve efficiency of the solar cells which were optimally exposed to UV-O_3.

Chapter 4 described TiO_2 is one of the most widely explored materials as an electron transport layer (ETL) in dye sensitized solar cells (DSSCs) owing to its excellent physical and chemical properties. However, recombination at the device's interface slackens the charge carrier movement, adversely affecting their device performance. Rapid extraction of photogenerated charge carriers plays a vital role in developing high efficiency DSSCs. The conduction band offset between TiO_2 ETL and N719 dye light absorber plays a crucial role in charge carrier dynamics of DSSCs. Herein, the band structure of TiO_2 ETL is finely tuned by the incorporation of cesium bromide (CsBr). At the optimal concentration of doping (0.4 Wt. %), DSSCs achieved the best power conversion efficiency (PCE) of 9.28% compared to 7.61% for

pristine TiO_2. CsBr doping in TiO_2 ETL induced a negative shift in flat band potential (V_{fb}) from -0.46 to -0.50 V, which improved the open circuit voltage (V_{OC}), modified its work function (ϕ) from -4.51 to -4.21 eV and increased conduction band minimum (CBM) from -3.7 to -3.55 eV. We also demonstrated that CsBr incorporation increased electron density in TiO_2 matrix, indicating the suppression of trap state and significantly improved the overall photovoltaic performance of DSSCs.

Chapter 5 illustrated a promising yet straightforward approach has been demonstrated to prepare efficient and inexpensive counter electrodes (CEs) for dye-sensitized solar cells (DSSCs) based on Polyaniline (PANI) doped with Poly (sodium 4-styrenesulphonate) (PSSNa). The optimized concentration of the PANI in m-cresol is doped with PSSNa at different percent (5, 10, and 15 %) and compared the device performance with standard Pt electrode. The effects of doping are examined by cyclic voltammetry (CV), Tafel plot, impedance spectroscopy, and FESEM. The PANI-PSSNa CEs improved electrocatalytic activity that facilitated higher electron transfer, suppressed charge recombination, and enhanced effective surface area. As a result, at the optimal condition, the fabricated device shows an overall energy conversion efficiency of 7.15% ± 0.17. It is worth noting that the performance of DSSCs with PANI-PSSNa CEs demonstrates a 25.21% higher efficiency than PANI based counter electrodes.

Chapter 6 focused on the development of counter electrode materials for DSSCs. Platinum (Pt) is generally employed as a catalyst due to their high catalytic activity toward triiodide reduction. Yet the use of Pt in DSSCs highly increases the cost, which became a challenge for practical and industrial applications from their economic feasibility point of view. Therefore, in this work, we have developed a cost-effective material for counter electrodes (CEs) to replace expensive Pt. We prepared Carbon nanotubes (CNTs)/Polyaniline (PANI) composite as a CE material for DSSCs by doctor blade technique. The DSSCs fabricated with CNTs-PANI composite CE show the best power conversion efficiency (PCE) of 6.67%, which is comparable to 7.70% of Pt CE. The electrocatalytic properties of the CNTs, CNTs-PANI, and Pt CEs were confirmed by impedance spectroscopy, Cyclic voltammetry (CV), and Tafel analysis. A comparative study of these electrodes by surface morphology characterization technique, i.e., FESEM and AFM reveal that effective surface roughness plays an essential role in improving the electrochemical properties of the devices.

Chapter 7 discussed the development of a multilayer TiO_2 film thickness of around 4 µm at lower temperature (120 °C) by spin coating and doctor blade technique on polyethylene

terephthalate (ITO PET) substrate. Further, the additional processing step Ultraviolet-Ozone (UVO_3) treatment was performed on TiO_2 electron transport layer (ETL) to enhance the performance of FDSSCs. UVO_3 treatment significantly improved the crystallinity and charge transport characteristic of ETL by removing the organic impurities. The photovoltaic devices based on 4 hours of UVO_3 treated TiO_2 film exhibited superior device performance with an overall power conversion efficiency (PCE) of 2.53% compared to 1.43% (without UVO_3 treatment). Electrochemical impedance measurement indicated that TiO_2 layer treated with UVO_3 decreased series resistance, electron recombination and improved electron life substantially. The improved device properties, simple preparation procedure and low processing cost, enable this FDSSCs fabrication method to be a credible alternative of conventional techniques.

Chapter 8 discusses conclusions of the thesis and future prospects. A brief summary of research work carried out and possibilities of investigations required towards commercialization the rigid and flexible dye sensitized solar cells in indoor application, and flexible electronics near future is presented.

1.6 References

[1] K. Fan, W. Ho, K. Fan, Improving photoanodes to obtain highly efficient dye-sensitized solar cells : a brief review, (2017) 319–344. doi:10.1039/c6mh00511j.

[2] N.S. Lewis, Solar energy use, Sol. Energy. 315 (2007) 798–801. doi:10.1126/science.1137014.

[3] S. Bhattacharya, S. John, Beyond 30% Conversion Efficiency in Silicon Solar Cells: A Numerical Demonstration, Sci. Rep. 9 (2019) 1–15. doi:10.1038/s41598-019-48981-w.

[4] C. Battaglia, A. Cuevas, S. De Wolf, High-efficiency crystalline silicon solar cells: Status and perspectives, Energy Environ. Sci. 9 (2016) 1552–1576. doi:10.1039/c5ee03380b.

[5] J. Britt, C. Ferekides, Thin-film CdS/CdTe solar cell with 15.8% efficiency, Appl. Phys. Lett. 62 (1993) 2851–2852. doi:10.1063/1.109629.

[6] M. Nardone, D.S. Albin, Degradation of CdTe Solar Cells: Simulation and Experiment, IEEE J. Photovoltaics. 5 (2015) 962–967. doi:10.1109/JPHOTOV.2015.2405763.

[7] M. Powalla, S. Paetel, D. Hariskos, R. Wuerz, F. Kessler, P. Lechner, W. Wischmann, T.M. Friedlmeier, Advances in Cost-Efficient Thin-Film Photovoltaics Based on Cu(In,Ga)Se_2, Engineering. 3 (2017) 445–451. doi:10.1016/J.ENG.2017.04.015.

[8] H. Heriche, Z. Rouabah, N. Bouarissa, High-efficiency CIGS solar cells with optimization of layers thickness and doping, Optik (Stuttg). 127 (2016) 11751–11757. doi:10.1016/j.ijleo.2016.09.071.

[9] S. Moon, K. Kim, Y. Kim, J. Heo, J. Lee, Highly efficient single-junction GaAs thin-film solar cell on flexible substrate, Sci. Rep. 6 (2016) 1–6. doi:10.1038/srep30107.

[10] K. Attari, L. Amhaimar, A. El Yaakoubi, A. Asselman, M. Bassou, The Design and Optimization of GaAs Single Solar Cells Using the Genetic Algorithm and Silvaco ATLAS, Int. J. Photoenergy. 2017 (2017). doi:10.1155/2017/8269358.

[11] W. Wang, M.T. Winkler, O. Gunawan, T. Gokmen, T.K. Todorov, Y. Zhu, D.B. Mitzi, Device characteristics of CZTSSe thin-film solar cells with 12.6% efficiency, Adv. Energy Mater. 4 (2014). doi:10.1002/aenm.201301465.

[12] L. El Chaar, L.A. Lamont, N. El Zein, Review of photovoltaic technologies, Renew. Sustain. Energy Rev. 15 (2011) 2165–2175. doi:10.1016/j.rser.2011.01.004.

[13] IRENA, World energy transitions outlook 2022, (2022) 1–54. doi:WWW.irena.org.

[14] M. Kokkonen, P. Talebi, J. Zhou, S. Asgari, S.A. Soomro, F. Elsehrawy, J. Halme, S. Ahmad, A. Hagfeldt, S.G. Hashmi, Advanced research trends in dye-sensitized solar cells, J. Mater. Chem. A. 9 (2021) 10527–10545. doi:10.1039/d1ta00690h.

[15] J. Wu, Z. Lan, J. Lin, M. Huang, Y. Huang, L. Fan, G. Luo, Electrolytes in dye-sensitized solar cells, Chem. Rev. 115 (2015) 2136–2173. doi:10.1021/cr400675m.

[16] R. Eisenberg, D. Nocera, Overview of the forum on solar and renewable energy, Inorg. Chem. 44 (2005) 6799–6801. doi:10.1021/ic058009v.

[17] Brain O'Regan & Michael Grätzel, A low-cost, high-efficiency solar cell based on dye-sensitized colloidal TiO_2 films, Nature. 353 (1991) 737–740. doi:10.1038/353737a0.

[18] M. Grätzel, Photoelectrochemical Cells, Nature. 414 (2001). doi:10.1002/9781118003350.ch15.

[19] L.M. Goncalves, V. De Zea Bermudez, H.A. Ribeiro, A.M. Mendes, Dye-sensitized solar cells: A safe bet for the future, Energy Environ. Sci. 1 (2008) 655–667. doi:10.1039/b807236a.

[20] J. Gong, J. Liang, K. Sumathy, Review on dye - sensitized solar cells (DSSCs) : Fundamental concepts and novel materials, Renew. Sustain. Energy Rev. 16 (2012) 5848–5860. doi:10.1016/j.rser.2012.04.044.

[21] and M.J.K. Hyun Suk Jung, Gill sang Han, Nam-Gyu Park, Flexible Perovskite Solar Cells, Joule. 3 (2019) 1850–1880.

[22] V. Zardetto, T.M. Brown, A. Reale, A. Di Carlo, Substrates for flexible electronics: A practical investigation on the electrical, film flexibility, optical, temperature, and solvent resistance properties, J. Polym. Sci. Part B Polym. Phys. 49 (2011) 638–648. doi:10.1002/polb.22227.

[23] H. Kim, C.M. Gilmore, A. Piqué, J.S. Horwitz, H. Mattoussi, H. Murata, Z.H. Kafafi, D.B. Chrisey, Electrical, optical, and structural properties of indium-tin-oxide thin films for organic light-emitting devices, J. Appl. Phys. 86 (1999) 6451–6461. doi:10.1063/1.371708.

[24] B. Zhao, Z. He, X. Cheng, D. Qin, M. Yun, M. Wang, X. Huang, J. Wu, H. Wu, Y. Cao, Flexible polymer solar cells with power conversion efficiency of 8.7%, J. Mater. Chem.

C. 2 (2014) 5077–5082. doi:10.1039/c3tc32520b.

[25] K.A. and P.D.L. Minna Toivola, Janne Halme, Kati Miettunen, Nanostructured dye solar cells on flexible substrates—Review, Int. J. Energy Res. 33 (2009) 1145–1160. doi:10.1002/er.

[26] K. Kakiage, Y. Aoyama, T. Yano, K. Oya, J.I. Fujisawa, M. Hanaya, Highly-efficient dye-sensitized solar cells with collaborative sensitization by silyl-anchor and carboxy-anchor dyes, Chem. Commun. 51 (2015) 15894–15897. doi:10.1039/c5cc06759f.

[27] G. Hashmi, K. Miettunen, T. Peltola, J. Halme, I. Asghar, K. Aitola, M. Toivola, P. Lund, Review of materials and manufacturing options for large area flexible dye solar cells, Renew. Sustain. Energy Rev. 15 (2011) 3717–3732. doi:10.1016/j.rser.2011.06.004.

[28] S.Y. kinji Onoda, Supachai Ngamsinlapasathian, Takuya Fujieda, The superiority of Ti plate as the sunstrate of dye-sensitized solar cells, Sol. Energy Mater. Sol. Cells. 91 (2007) 1176–1181.

[29] S. Sheehan, P.K. Surolia, O. Byrne, S. Garner, P. Cimo, X. Li, D.P. Dowling, K.R. Thampi, Flexible glass substrate based dye sensitized solar cells, Sol. Energy Mater. Sol. Cells. 132 (2015) 237–244. doi:10.1016/j.solmat.2014.09.001.

[30] T. Yamaguchi, N. Tobe, D. Matsumoto, T. Nagai, H. Arakawa, Highly efficient plastic-substrate dye-sensitized solar cells with validated conversion efficiency of 7.6%, Sol. Energy Mater. Sol. Cells. 94 (2010) 812–816. doi:10.1016/j.solmat.2009.12.029.

[31] H.C. Weerasinghe, P.M. Sirimanne, G. V. Franks, G.P. Simon, Y.B. Cheng, Low temperature chemically sintered nano-crystalline TiO_2 electrodes for flexible dye-sensitized solar cells, J. Photochem. Photobiol. A Chem. 213 (2010) 30–36. doi:10.1016/j.jphotochem.2010.04.016.

[32] S. Li, Y. Li, Z. Chen, J. Liu, W. Zhang, Electrodeposition and low-temperature post-treatment of nanocrystalline SnO_2 films for flexible dye-sensitized solar cells, J. Nanomater. 2012 (2012). doi:10.1155/2012/536810.

[33] S. Chu, D. Li, P.C. Chang, J.G. Lu, Flexible Dye-Sensitized Solar Cell Based on Vertical ZnO Nanowire Arrays, Nanoscale Res. Lett. 6 (2011) 1–4. doi:10.1007/s11671-010-9804-x.

[34] W. Chen, Y. Qiu, S. Yang, A new ZnO nanotetrapods/SnO_2 nanoparticles composite

photoanode for high efficiency flexible dye-sensitized solar cells, Phys. Chem. Chem. Phys. 12 (2010) 9494–9501. doi:10.1039/c000584c.

[35] Z. Li, Y. Zhou, C. Bao, G. Xue, J. Zhang, J. Liu, T. Yu, Z. Zou, Vertically building Zn_2SnO_4 nanowire arrays on stainless steel mesh toward fabrication of large-area, flexible dye-sensitized solar cells, Nanoscale. 4 (2012) 3490–3494. doi:10.1039/c2nr30279a.

[36] Mian-En Yeoh and Kah-Yoong, Recent advances in photo-anode for dye-sensitized solar cell, Int. J. Energy Res. 31 (2017) 2446–2467. doi:10.1002/er.

[37] J. Zhang, P. Zhou, J. Liu, J. Yu, New understanding of the difference of photocatalytic activity among anatase, rutile and brookite TiO_2, Phys. Chem. Chem. Phys. 16 (2014) 20382–20386. doi:10.1039/c4cp02201g.

[38] D. Sengupta, P. Das, B. Mondal, K. Mukherjee, Effects of doping , morphology and fi lm-thickness of photo-anode materials for dye sensitized solar cell application – A review, Renew. Sustain. Energy Rev. 60 (2016) 356–376. doi:10.1016/j.rser.2016.01.104.

[39] H.P. Anders Hagfeldt, Gerrit Boschloo, Licheng Sun, Lars Kloo, Dye-Sensitized Solar Cells, Chem. Rev. 110 (2010) 6595–6663.

[40] H.G. Yun, B.S. Bae, M.G. Kang, A simple and highly efficient method for surface treatment of Ti substrates for use in dye-sensitized solar cells, Adv. Energy Mater. 1 (2011) 337–342. doi:10.1002/aenm.201000044.

[41] A.H. Gerrit Boschloo, Henrik Lindström, Eva Magnusson, Anna Holmberg, Optimization of dye-sensitized solar cells prepared by compression method, J. Photochem. Photobiol. A Chem. 148 (2002) 11–15. doi:10.15541/jim20150576.

[42] P.Y. Hsu, H.F. Lee, S.M. Yang, Y.T. Chua, Y.L. Tung, J.J. Kai, Highly efficient quasi-solid state flexible dye-sensitized solar cells using a compression method and light-confined effect for preparation of TiO_2 photoelectrodes, Procedia Eng. 36 (2012) 439–445. doi:10.1016/j.proeng.2012.03.064.

[43] S. Denizalti, A.K. Ali, Ç. Ela, M. Ekmekci, S. Erten-Ela, Dye-sensitized solar cells using ionic liquids as redox mediator, Chem. Phys. Lett. 691 (2018) 373–378. doi:10.1016/j.cplett.2017.11.035.

[44] G. Boschloo, A. Hagfeldt, Characteristics of the iodide/triiodide redox mediator in dye-sensitized solar cells, Acc. Chem. Res. 42 (2009) 1819–1826. doi:10.1021/ar900138m.

[45] J. Wu, Z. Lan, J. Lin, M. Huang, Y. Huang, L. Fan, G. Luo, Y. Lin, Y. Xie, Y. Wei, Counter electrodes in dye-sensitized solar cells, Chem. Soc. Rev. 46 (2017) 5975–6023. doi:10.1039/c6cs00752j.

[46] M. Grätzel, Highly Efficient Nanocrystalline Photovoltaic Devices, Platin. Met. Rev. 38 (1994) 151–159.

[47] M. Gra¨tzel, The Advent of Mesoscopic Injection Solar Cells, Prog. Photovoltaics Res. Appl. 14 (2006) 429–442. doi:10.1002/pip.

[48] M. Gratzel, Dye-sensitized solar cells, J. Photochem. Photobiol. C Photochem. Rev. 4 (2003) 145–153. doi:10.1016/s1389-5567(03)00026-1.

[49] T. Marinado, K. Nonomura, J. Nissfolk, M.K. Karlsson, D.P. Hagberg, L. Sun, S. Mori, A. Hagfeldt, How the nature of triphenylamine-polyene dyes in dye-sensitized solar cells affects the open-circuit voltage and electron lifetimes, Langmuir. 26 (2010) 2592–2598. doi:10.1021/la902897z.

[50] X. Yu, Z. Sun, J. Lian, Y. Li, X. Wang, M. Zhao, High efficiency dye-sensitized solar cells based on natural dyes, J. Comput. Theor. Nanosci. 12 (2015) 1936–1939. doi:10.1166/jctn.2015.4212.

[51] M. Ye, D. Zheng, M. Lv, C. Chen, C. Lin, Z. Lin, Hierarchically structured nanotubes for highly efficient dye-sensitized solar cells, Adv. Mater. 25 (2013) 3039–3044. doi:10.1002/adma.201205274.

[52] M. Lv, D. Zheng, M. Ye, J. Xiao, W. Guo, Y. Lai, L. Sun, C. Lin, J. Zuo, Optimized porous rutile TiO_2 nanorod arrays for enhancing the efficiency of dye-sensitized solar cells, Energy Environ. Sci. 6 (2013) 1615–1622. doi:10.1039/c3ee24125d.

[53] H. Zhang, Y. Wang, D. Yang, Y. Li, H. Liu, P. Liu, B.J. Wood, H. Zhao, Directly hydrothermal growth of single crystal $Nb_3O_7(OH)$ nanorod film for high performance dye-sensitized solar cells, Adv. Mater. 24 (2012) 1598–1603. doi:10.1002/adma.201104650.

[54] H. Hafez, Z. Lan, Q. Li, J. Wu, High efficiency dye-sensitized solar cell based on novel TiO_2 nanorod/nanoparticle bilayer electrode, Nanotechnol. Sci. Appl. 3 (2010) 45–51. doi:10.2147/NSA.S11350.

[55] Y. Shi, C. Zhu, L. Wang, W. Li, K.K. Fung, N. Wang, Asymmetric ZnO panel-like hierarchical architectures with highly interconnected pathways for free-electron

transport and photovoltaic improvements, Chem. - A Eur. J. 19 (2013) 282–287. doi:10.1002/chem.201202527.

[56] M. Ye, C. Chen, M. Lv, D. Zheng, W. Guo, C. Lin, Facile and effective synthesis of hierarchical TiO_2 spheres for efficient dye-sensitized solar cells, Nanoscale. 5 (2013) 6577–6583. doi:10.1039/c3nr01604h.

[57] M. Ye, H.Y. Liu, C. Lin, Z. Lin, Hierarchical rutile TiO_2 flower cluster-based high efficiency dye-sensitized solar cells via direct hydrothermal growth on conducting substrates, Small. 9 (2013) 312–321. doi:10.1002/smll.201201590.

[58] K. Li, Y. Wang, Y. Xu, H. Chen, C. Su, D. Kuang, Macroporous SnO_2 Synthesized via a Template-Assisted Re fl ux Process for E ffi cient Dye-Sensitized Solar Cells, (2013).

[59] X. Liu, J. Fang, Y. Liu, T. Lin, Progress in nanostructured photoanodes for dye-sensitized solar cells, Front. Mater. Sci. 10 (2016) 225–237. doi:10.1007/s11706-016-0341-0.

[60] M. Shakeel Ahmad, A.K. Pandey, N. Abd Rahim, Advancements in the development of TiO_2 photoanodes and its fabrication methods for dye sensitized solar cell (DSSC) applications. A review, Renew. Sustain. Energy Rev. 77 (2017) 89–108. doi:10.1016/j.rser.2017.03.129.

[61] M.A.K.L. Dissanayake, J.M.K.W. Kumari, G.K.R. Senadeera, C.A. Thotawatthage, B.E. Mellander, I. Albinsson, A novel multilayered photoelectrode with nitrogen doped TiO_2 for efficiency enhancement in dye sensitized solar cells, J. Photochem. Photobiol. A Chem. 349 (2017) 63–72. doi:10.1016/j.jphotochem.2017.08.067.

[62] J.C. Zhang, Z.Y. Han, Q.Y. Li, X.Y. Yang, Y. Yu, W.L. Cao, N, S-doped TiO_2 anode effect on performance of dye-sensitized solar cells, J. Phys. Chem. Solids. 72 (2011) 1239–1244. doi:10.1016/j.jpcs.2011.07.014.

[63] W. Li, J. Yang, J. Zhang, S. Gao, Y. Luo, M. Liu, Improve photovoltaic performance of titanium dioxide nanorods based dye-sensitized solar cells by Ca-doping, Mater. Res. Bull. 57 (2014) 177–183. doi:10.1016/j.materresbull.2014.05.034.

[64] M. Nada, T. Gonda, Q. Shen, H. Shimada, T. Toyoda, N. Kobayashi, Electric characteristics of Li_2O-doped TiO_2 nanocrystalline film and its application to dye-sensitized solar cells, Jpn. J. Appl. Phys. 48 (2009) 2–6. doi:10.1143/JJAP.48.025505.

[65] A. Subramanian, H.W. Wang, Effects of boron doping in TiO_2 nanotubes and the

performance of dye-sensitized solar cells, Appl. Surf. Sci. 258 (2012) 6479–6484. doi:10.1016/j.apsusc.2012.03.064.

[66] H. Imahori, S. Hayashi, T. Umeyama, S. Eu, A. Oguro, S. Kang, Y. Matano, T. Shishido, S. Ngamsinlapasathian, S. Yoshikawa, Comparison of electrode structures and photovoltaic properties of porphyrin-sensitized solar cells with TiO_2 and Nb, Ge, Zr-added TiO_2 composite electrodes, Langmuir. 22 (2006) 11405–11411. doi:10.1021/la061527d.

[67] A. Latini, C. Cavallo, F.K. Aldibaja, D. Gozzi, D. Carta, A. Corrias, L. Lazzarini, G. Salviati, Efficiency improvement of DSSC photoanode by scandium doping of mesoporous titania beads, J. Phys. Chem. C. 117 (2013) 25276–25289. doi:10.1021/jp409813c.

[68] Z. Liu, Y. Li, C. Liu, J. Ya, E. Lei, W. Zhao, D. Zhao, L. An, TiO_2 photoanode structure with gradations in V concentration for dye-sensitized solar cells, ACS Appl. Mater. Interfaces. 3 (2011) 1721–1725. doi:10.1021/am200232g.

[69] S.K. Pathak, A. Abate, P. Ruckdeschel, B. Roose, K.C. Gödel, Y. Vaynzof, A. Santhala, S.I. Watanabe, D.J. Hollman, N. Noel, A. Sepe, U. Wiesner, R. Friend, H.J. Snaith, U. Steiner, Performance and Stability Enhancement of Dye-Sensitized and Perovskite Solar Cells by Al Doping of TiO_2, Adv. Funct. Mater. 24 (2014) 6046–6055. doi:10.1002/adfm.201401658.

[70] S.P. Berglund, S. Hoang, R.L. Minter, R.R. Fullon, C.B. Mullins, Investigation of 35 elements as single metal oxides, mixed metal oxides, or dopants for titanium dioxide for dye-sensitized solar cells, J. Phys. Chem. C. 117 (2013) 25248–25258. doi:10.1021/jp4073747.

[71] R.T. Ako, P. Ekanayake, D.J. Young, J. Hobley, V. Chellappan, A.L. Tan, S. Gorelik, G.S. Subramanian, C.M. Lim, Evaluation of surface energy state distribution and bulk defect concentration in DSSC photoanodes based on Sn, Fe, and Cu doped TiO_2, Appl. Surf. Sci. 351 (2015) 950–961. doi:10.1016/j.apsusc.2015.06.015.

[72] D. Cahen, G. Hodes, M. Grätzel, J.F. Guillemoles, I. Riess, Nature of Photovoltaic Action in Dye-Sensitized Solar Cells, J. Phys. Chem. B. 104 (2000) 2053–2059. doi:10.1021/jp993187t.

[73] J. Zhang, W. Peng, Z. Chen, H. Chen, L. Han, Effect of cerium doping in the TiO_2

photoanode on the electron transport of dye-sensitized solar cells, J. Phys. Chem. C. 116 (2012) 19182–19190. doi:10.1021/jp3060735.

[74] P.M. Sommeling, B.C. O'Regan, R.R. Haswell, H.J.P. Smit, N.J. Bakker, J.J.T. Smits, J.M. Kroon, J.A.M. van Roosmalen, Influence of a $TiCl_4$ Post-Treatment on Nanocrystalline TiO_2 Films in Dye-Sensitized Solar Cells, J. Phys. Chem. B. 110 (2006) 19191–19197. doi:10.1021/jp061346k.

[75] G.-D.L. Kezhen Qi, Shu-yuan Liu, Yuan Chen, Boshu Xia, A simple post-treatment with urea solution to enhance the photoelectric conversion efficiency for TiO_2 dye-sensitized solar cells, Sol. Energy Mater. Sol. Cells. 183 (2018) 193–199. doi:10.1016/j.solmat.2018.03.038.

[76] J. Tak Kim, S. Ho Kim, Surface modification of TiO_2 electrode by various over-layer coatings and O_2 plasma treatment for dye sensitized solar cells, in: Sol. Energy Mater. Sol. Cells, Elsevier, 2011: pp. 336–339. doi:10.1016/j.solmat.2010.04.045.

[77] J. Jun, M. Dhayal, J.H. Shin, J.C. Kim, N. Getoff, Surface properties and photoactivity of TiO_2 treated with electron beam, Radiat. Phys. Chem. 75 (2006) 583–589. doi:10.1016/j.radphyschem.2005.10.015.

[78] M.K. Parvez, G.M. Yoo, J.H. Kim, M.J. Ko, S.R. Kim, Comparative study of plasma and ion-beam treatment to reduce the oxygen vacancies in TiO_2 and recombination reactions in dye-sensitized solar cells, Chem. Phys. Lett. 495 (2010) 69–72. doi:10.1016/j.cplett.2010.06.038.

[79] L.Z. Xin Li, Hong Lin, Jianbao Li, Ning Wang, Chunfu Lin, Chemical sintering of graded TiO_2 film at low temperature for flexible dye-sensitized solar cells., J. Photochem. Photobiol. A Chem. 195 (2008) 247–253.

[80] Y. Kijitori, M. Ikegami, T. Miyasaka, Highly efficient plastic dye-sensitized photoelectrodes prepared by low-temperature binder-free coating of mesoscopic titania pastes, Chem. Lett. 36 (2007) 190–191. doi:10.1246/cl.2007.190.

[81] and B.A.G. Franc¸ois Pichot, J. Roland Pitts, Low-Temperature Sintering of TiO_2 Colloids: Application to Flexible Dye-Sensitized Solar Cells, Langmuir. 16 (2000) 5626–5630.

[82] B.A.L. Curtiss S. Kovash Jr., James D. Hoefelmeyer, TiO_2 compact layers prepared by low temperature colloidal synthesis and deposition for high performance dye-sensitized

solar cells., Electrochim. Acta. 67 (2012) 18–23.

[83] A. Sangiorgi, R. Bendoni, N. Sangiorgi, A. Sanson, B. Ballarin, Optimized TiO_2 blocking layer for dye-sensitized solar cells, Ceram. Int. 40 (2014) 10727–10735. doi:10.1016/j.ceramint.2014.03.060.

[84] D. Zhang, T. Yoshida, T. Oekermann, K. Furuta, H. Minoura, Room-temperature synthesis of porous nanoparticulate TiO_2 films for flexible dye-sensitized solar cells, Adv. Funct. Mater. 16 (2006) 1228–1234. doi:10.1002/adfm.200500700.

[85] X. Zhang, J. Yao, M. Ali, J. Wei, H. Wang, L.Y. Yeo, J.R. Friend, D.R. MacFarlane, UV/ozone-assisted low temperature preparation of mesoporous TiO_2 with tunable phase composition and enhanced solar light photocatalytic activity, J. Mater. Chem. A. 2 (2014) 18791–18795. doi:10.1039/c4ta04020a.

[86] N.-G.P. Taek-Yong Lee, Hui-Seon Kim, Evaluation of Limiting Factors Affecting Photovoltaic Performance of Low-Temperature-Processed TiO_2 Films in Dye-Sensitized Solar Cells, Chemphyschem. 15 (2014) 1098–1105. doi:DOI: 10.1002/cphc.201301043.

[87] J.A.A. David Gutiérrez -Tauste, Inti Zumeta, Elena Vigil, Maria Angeles Hernández-Fenollosa, Xavier Domènech, New low temperature preparation method of the TiO_2 porous photoelectrode for dye-sensitized solar cell using UV irradiation, J. Photochem. Photobiol. A Chem. 175 (2005) 165–171.

[88] M.K. Junichi Nemoto, Mami Sakata, Takayuki Hoshi, Hirohita Ueno, All-plastic dye-sensitized solar cell using a polysaccharide film containing excess redox electrolyte solution, Jour Electroanal. Chem. 599 (2007) 23–30.

[89] M.K. Satoshi Uchida, Miho Tomiha, Hirotsugu Takizawa, Flexible dye-sensitized solar cells by 28 GHz microwave irradiation, Chem. J. Photochem. Photobiol. A Chem. 164 (2004) 93–96.

[90] H. Lindström, A. Holmberg, E. Magnusson, L. Malmqvist, A. Hagfeldt, A new method to make dye-sensitized nanocrystalline solar cells at room temperature, J. Photochem. Photobiol. A Chem. 145 (2001) 107–112. doi:10.1016/S1010-6030(01)00564-0.

[91] J.K.-T. henrietti Santa- Nokki, Jani Kallioinen, Terho Kololuoma, Vladimir Tuboltsev, Dynamic preparation of TiO_2 film for fabrication of dye-sensitized solar cells, J. Photochem. Photobiol. A Chem. 182 (2006) 187–191.

[92] Y.B. Cheng, Y. Peng, J.Z. Liu, K. Wang, Influence of parameters of cold isostatic pressing on TiO_2 films for flexible dye-sensitized solar cells, Int. J. Photoenergy. 2011 (2011). doi:10.1155/2011/410352.

[93] G.P.S. and Y.C. Hasitha C. Weerasinghe, Prasad M. Sirimanne, Cold isostatic pressing technique for producing highly efficient flexible dye-sensitised solar cells on plastic substrates, Prog. PHOTOVOLTAICS Res. Appl. 20 (2011) 231–332. doi:10.1002/pip.

[94] M. Dürr, A. Schmid, M. Obermaier, S. Rosselli, A. Yasuda, G. Nelles, Low-temperature fabrication of dye-sensitized solar cells by transfer of composite porous layers, Nat. Mater. 4 (2005) 607–611. doi:10.1038/nmat1433.

[95] F. Huang, D. Chen, Q. Li, R.A. Caruso, Y.B. Cheng, Construction of nanostructured electrodes on flexible substrates using pre-treated building blocks, Appl. Phys. Lett. 100 (2012). doi:10.1063/1.3695080.

[96] M. Wang, A.M. Anghel, N.C. Ha, N. Pootrakulchote, CoS Supersedes Pt as Efficient Electrocatalyst for Triiodide Reduction in Dye-Sensitized Solar Cells, J. AM. CHEM. SOC. 131 (2009) 15976–15977.

[97] M. Wu, Q. Zhang, J. Xiao, C. Ma, X. Lin, C. Miao, Y. He, Y. Gao, A. Hagfeldt, T. Ma, Two flexible counter electrodes based on molybdenum and tungsten nitrides for dye-sensitized solar cells, J. Mater. Chem. 21 (2011) 10761–10766. doi:10.1039/c1jm11422k.

[98] H. Zhou, Y. Shi, D. Qin, J. An, L. Chu, C. Wang, Y. Wang, W. Guo, L. Wang, T. Ma, Printable fabrication of Pt-and-ITO free counter electrodes for completely flexible quasi-solid dye-sensitized solar cells, J. Mater. Chem. A. 1 (2013) 3932–3937. doi:10.1039/c3ta00960b.

[99] M.S. Wu, J.F. Wu, Pulse-reverse electrodeposition of transparent nickel phosphide film with porous nanospheres as a cost-effective counter electrode for dye-sensitized solar cells, Chem. Commun. 49 (2013) 10971–10973. doi:10.1039/c3cc45670f.

[100] Y. Wang, M. Wu, X. Lin, Z. Shi, A. Hagfeldt, T. Ma, Several highly efficient catalysts for Pt-free and FTO-free counter electrodes of dye-sensitized solar cells, J. Mater. Chem. 22 (2012) 4009–4014. doi:10.1039/c2jm15182k.

[101] K.M. Lee, C.Y. Hsu, P.Y. Chen, M. Ikegami, T. Miyasaka, K.C. Ho, Highly porous PProDOT-Et2 film as counter electrode for plastic dye-sensitized solar cells, Phys.

Chem. Chem. Phys. 11 (2009) 3375–3379. doi:10.1039/b823011k.

[102] Q. Qin, J. Tao, Y. Yang, Preparation and characterization of polyaniline film on stainless steel by electrochemical polymerization as a counter electrode of DSSC, Synth. Met. 160 (2010) 1167–1172. doi:10.1016/j.synthmet.2010.03.003.

[103] X. Yin, F. Wu, N. Fu, J. Han, D. Chen, P. Xu, M. He, Y. Lin, Facile synthesis of poly(3,4-ethylenedioxythiophene) film via solid-state polymerization as high-performance Pt-free counter electrodes for plastic dye-sensitized solar cells, ACS Appl. Mater. Interfaces. 5 (2013) 8423–8429. doi:10.1021/am401719e.

[104] J.M. Pringle, V. Armel, D.R. MacFarlane, Electrodeposited PEDOT-on-plastic cathodes for dye-sensitized solar cells, Chem. Commun. 46 (2010) 5367–5369. doi:10.1039/c0cc01400a.

[105] M.G. Andreas Kay, Low cost photovoltaic modules based on dye sensitized nanocrystalline titanium dioxide and carbon powder, Sol. Energy Mater. Sol. Cells. 44 (1996) 99–117.

[106] C. Gao, H. Wang, Z. Hu, M. Wu, A novel carbon bead string cathode for dye-sensitized solar cells, Electrochim. Acta. 255 (2017) 9–14. doi:10.1016/j.electacta.2017.09.132.

[107] Y.Y. Li, C.T. Li, M.H. Yeh, K.C. Huang, P.W. Chen, R. Vittal, K.C. Ho, Graphite with Different Structures as Catalysts for Counter Electrodes in Dye-sensitized Solar Cells, Electrochim. Acta. 179 (2015) 211–219. doi:10.1016/j.electacta.2015.06.007.

[108] K.M. Kiyoaki Imoto, Kohshin Takahashi, Takahiro Yamaguchi, Teruhisa Komura, Jun-ichi Nakamura, High-performance carbon counter for dye-sensitized solar cells, Sol. Energy Mater. Sol. Cells. 79 (2003) 459–469.

[109] S.Z. Guiqiang Wang, Wei Xing, Application of mesoporous carbon to counter electrode for dye-sensitized solar cells, J. Power Sources. 194 (2009) 568–573.

[110] M.W. Hongyue Guo, Yajing Zhu, Wenyan Li, Haikuo Zheng, Kezhong Wu, Keqiang Ding, Bei Ruan, Anders Hagfeldt, Tingli Ma, Synthesis of highly effective Pt/carbon fiber composite counter electrode catalyst for dye-sensitized solar cells, Electrochim. Acta. 176 (2015) 997–1000.

[111] K. Lukaszkowicz, M. Szindler, A. Drygała, L.A. Dobrzański, M. Prokopiuk vel Prokopowicz, I. Pasternak, A. Przewloka, M.M. Szindler, M. Domański, Graphene-based layers deposited onto flexible substrates: Used in dye-sensitized solar cells as

counter electrodes, Appl. Surf. Sci. 424 (2017) 157–163. doi:10.1016/j.apsusc.2017.02.040.

[112] K. Suzuki, M. Yamaguchi, M. Kumagai, S. Yanagida, Application of carbon nanotubes to counter electrodes of dye-sensitized solar cells, Chem. Lett. 32 (2003) 28–29. doi:10.1246/cl.2003.28.

[113] S.R. Shengjie Peng, Yongzhi wu, Peining Zhu, Velmurugan Thavasi, Subodh G. Mhaisalkar, Facile fabrication of polypyrrole/functionalized multiwalled carbon nanotubes composite as counter electrodes in low-cost dye-sensitized solar cells, J. Photochem. Photobiol. A Chem. 223 (2011) 97–102.

CHAPTER 2 Electrodes preparation and characterisation techniques

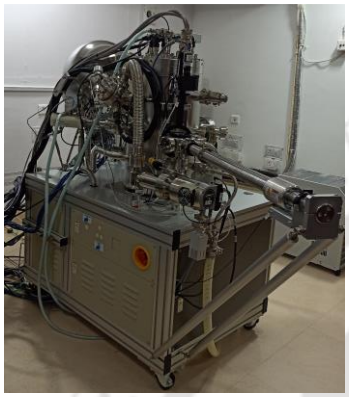

PES

Solar simulator

FESEM

Spin coating

CV

XRD

RAMAN

Doctor blade

2.1 Electrode preparation

The electrode preparation method on device start from the selection of substrate. Two main deposition techniques; chemical and physical methods available for the preparation of electrodes. The chemical methods include chemical vapour deposition (CVD), electrochemical deposition (ECD), and atomic layer deposition (ALD) etc., whereas the physical method such as casting, spin coating, deep coating, electrospray deposition (ESD), doctor blade, and spray deposition etc. In this thesis works doctor blade and spin coating techniques has been utilized to prepared the electrodes.

2.1.1 Doctor blade coating

Doctor blade technique is one of the most popularly used methods for preparing thin films and this technique is generally used to make working electrode in DSSCs [1]. Fig. 2.1(a) show the doctor blade coating machine of our device lab and Fig. 2.1(b) show the schematic illustration of Doctor blade technique. It is a sheet-to-sheet coating approach, where the blade is moving over the stationary substrate. Typically, a well-mixed TiO_2 or ZnO paste with non-toxic solvent is placed above the substrate. The blade is positioned above the substrate at a specific height and spreads uniformly to form a thin layer. This technique can operate at different speeds, and it is suitable to coat a wide range of film thicknesses by adjusting the blade position and repeating it several times. The film growth is faster than any other deposition method, such as

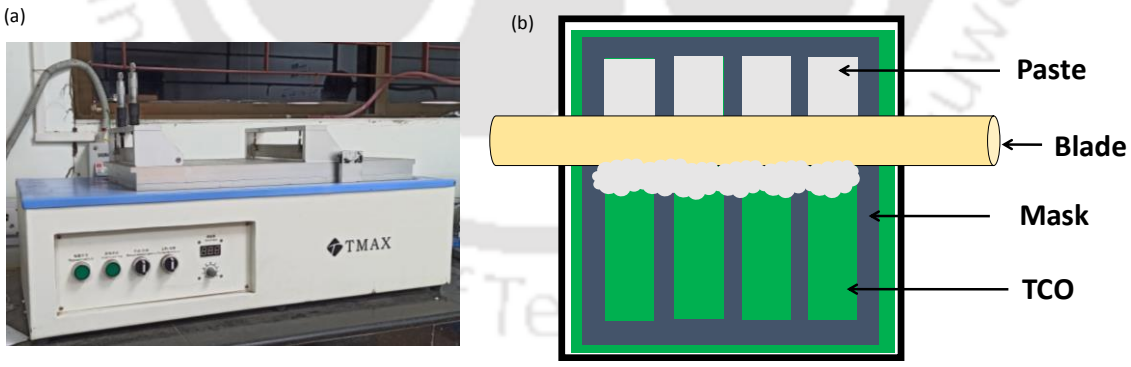

Figure 2. 1: (a) A picture of the TMAX doctor blade system (b) along with a schematic illustration of the doctor blade process.

chemical vapor, spray coating, etc. We can also conduct this coating process manually (Fig. 2.1(b)); first the substrate is masked with two scotch tapes to control the film width and thickness. Then, a fixed amount of paste is placed on one edge over the substrate to be deposited and moved on the spacer on both sides to the other end using a glass rod. The coated film

thickness (d) can be calculated from the empirical relationship

$$d = \frac{1}{2}(g\frac{c}{\rho}) \qquad 2.1$$

Where g is the gap between the substrate and blade, c is the concentration (conc.) of materials in the paste (g/cm^3), and ρ is the density of materials in the coated film (g/cm^3). Doctor blade is truly an efficient technique of film forming due to its simple, straightforward, economical, and less materials waste [1-2]. For efficient and small-scale preparation of working electrodes in DSSCs, doctor blading is widely used [3-5]. However, only uniform films across a substrate can be created, but patterning with this technique is not possible. This can be a serious downfall in its large-scale commercial module manufacturing technique. A commercial module comprises a number of cells interconnected in series and parallel to achieve the required power.

2.1.2 Spin coating

Practically, spin coating is a widely spreading method for deposition of thin film from solution in photovoltaic technology. The merit of using spin coating technique is that it can easily and quickly form uniform film with thickness ranging from few nanometers to microns. Initially, the deposition should be done either the disc is rotating at low velocity or static, after that it is

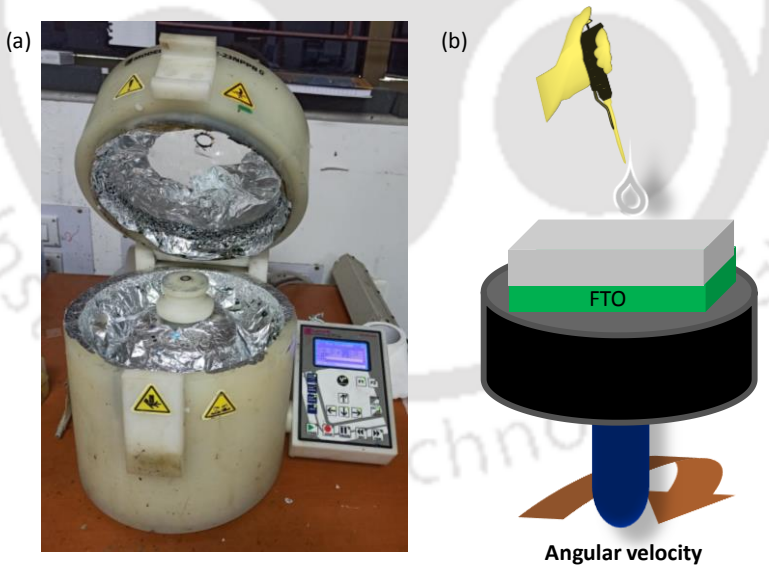

Figure 2. 2: (a) A photograph of a typical spin coating process in device lab (b) along with a schematic illustration of spin coating.

quickly accelerated to high angular velocity to form uniform film. A substrate with an overlying solution is eject out due to the high angular velocity and is left with only a thin film on the substrate. The film thickness (d) and surface morphology mainly depends on the viscoelastic

properties of the ink, rotational speed etc., but are not dependent on the spinning time or amount of materials. The thickness form in the spin coating can be estimated by the following empirical relationship

$$d = k\omega^{\alpha} \qquad 2.2$$

Where ω is the angular velocity, k and α are empirical constants related to the physical properties of the solvent, solute and substrate[6-7]. Fig. 2.2(a) show the spin coating machine of our device lab and Fig. 2.2(b) show the schematic illustration of this technique.

2.2 Characterization techniques

J-V characteristics

A solar simulator is a device for characterization of photonic properties. It includes lenses, reflectors, shutters, control electronics, power supplies, and a high intensity light source that closely resemble natural sunlight. Therefore, it is also known as artificial sun used to characterized the electrical parameters of the solar cell. The solar simulator model (Newport, Oriel Sol 3A) consists of xenon arc lamp with 450 Watt output powers is used for testing DSSCs in our experimental works. Current density-voltage (J-V) characteristic curves is one of the most essential method to determine the photo conversion efficiency of solar cell. The J-V measurements are executed on a Keithley 2400 source meter by illuminating the DSSCs under standard air mass 1.5 global (AM 1.5G) illumination. The spectrum of sunlight has traveled 1.5 times the thickness of atmosphere in AM1.5G. The light intensity of the solar simulator is calibrated with a standard silicon solar cell of the National Renewable energy laboratory (NREL) to 100 mW/cm^2, equal to 1 sun. The J-V curve is monitor by linearly sweeping the voltage across the photoanode and counter electrodes meter from -1 to 1V in a step of 10 mV.

External quantum efficiency (EQE)

EQE is the ratio between the number of charge carriers collected from a solar cell to the number of photons incident on the solar cell. EQE is also commonly known as Incident Photon to Current Efficiency (IPCE). It governs how efficiently the incoming photons are converted into electrons by the DSSCs and is estimated using equation 2.3.

$$EQE(\lambda) = \frac{n_{electrons}(\lambda)}{n_{photons}(\lambda)} = \frac{J_{sc}(\lambda)/q}{P_{in}/hf} = \frac{h\nu}{q\lambda} \times \frac{J_{sc}(\lambda)}{P_{in}} = \frac{1240}{\lambda} \times \frac{J_{sc}(\lambda)}{P_{in}} \qquad 2.3$$

Where, $n_{photons}$ and $n_{electrons}$ are number of photons and electrons respectively. q stands for an elementary charge, Jsc is photocurrent density in mA cm^{-2}, P_{in} is the power of incident light (mW cm^{-2}), f is the frequency of light in vacuum (Hz), h is the Planck's constant, λ is the wavelength of incident light (nm) and υ is the speed of light in vacuum (nm s^{-1}) [8]. The EQE spectrum of DSSC is obtained by applying monochromatic light with continuously varying the wavelength of the excitation light. EQE measurements were done by Newport monochromator (Model 74125) and the Xenon lamp (Newport, Model 67005).

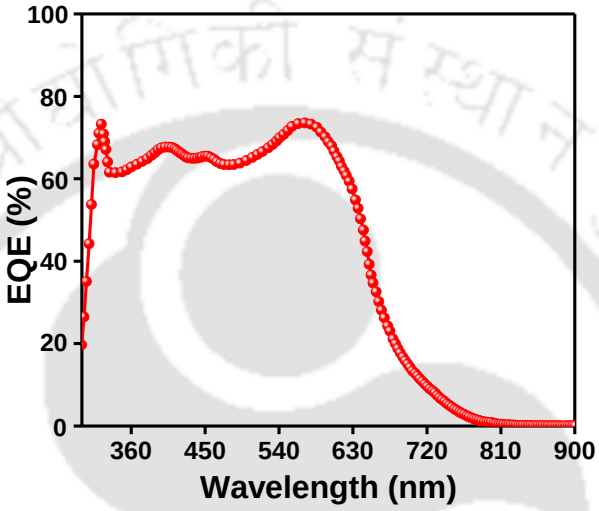

Figure 2. 3: A typical EQE spectrum of a dye sensitized solar cell [8].

Electrochemical impedance spectroscopy (EIS)

EIS is a powerful technique to investigate the kinetics of different process and charge transport properties involved in a DSSC [9]. The EIS measurement of DSSC is performed on CH instrument (CH 680) in the frequency range from 0.1 Hz–1 MHz with small sinusoidal voltage of 10 mV under room temperature. Usually, the impedance spectra of DSSC can be presented in the form of Nyquist plot or Bode plot. By using EC-Lab software the impedance spectrum is fitted to its equivalent circuit and determined many parameters such as total ohmic resistance, shunt resistance, constant phase elements, and time constant. Mott-Schottky measurement is also performed for the DSSCs at 977 Hz of frequency under ambient conditions to determine the free charge carrier density and shift in the flat band potential. Using the same workstation Tafel polarization curves of DSSCs are measured with a scanning rate of 100 mV/sec.

Characterization of components

X-ray diffraction (XRD)

XRD is a very powerful tool for analysing the crystalline structures, crystal orientation, crystal defect, phase, lattice strain of materials [10-11]. It is based on constructive interference of monochromatic X-rays and a crystalline sample. When a high energy X-ray incident on a sample, it interacts with the atomic electrons and accelerated with the same frequency of the incident X-ray in all direction. These scattered X-ray have no phase change and energy loss thus interference would occur known as Bragg's condition. The Bragg's condition is given by a simple equation:

$$2dsin\theta = n\lambda \qquad 2.4$$

Where, d is the interplanar distance of a specific plane, θ is the Bragg angle, λ is the X-ray wavelength and n is the diffraction order. In this thesis, XRD is performed using Rigaku, Smart Lab equipped with CuKα radiation of 1.54 Å, for the phase and crystal structural study of TiO_2, TiO_2-CsBr doped films deposited on FTO glass substrates. The measurements are performed at a grazing angle of incidence 1° with a scan rate of 5 degrees/min in 2θ range from 20-70°.

Photoelectron spectroscopy (PES)

PES is an important surface characterization technique that allows to analysis the electronic structure and chemical environment of different materials with high precision. The basic working principle behind PES is photoelectric effect [11-12]. The sample under measurement is irradiated by photons ($h\vartheta$) with energy higher than the ionization energy, so that the electrons in atoms would be emitted from sample. The kinetic energy (E_{kin}) of the ejected electron can be determined through an electron energy analyser, and the binding energy (BE) can be estimated using the following equation

$$BE = h\vartheta - E_{kin} - \emptyset \qquad 2.5$$

Where ∅ is the work function.

In this thesis PES of both X-ray photoelectron spectroscopy (XPS) and ultraviolet photoelectron spectroscopy (UPS) were used to study the chemical and structural changes of TiO_2 film exposed to the UV-O_3 system for a different duration and TiO_2 doped with CsBr.

Atomic force microscopy (AFM)

AFM is a nondestructive technique to investigate the surface morphology of sample [13-14]. It consists of a sharp tip use for imaging attached to a flexible cantilever placed above the sample surface. When the tip deflects on the sample surface, the interactions between the them cause a positive or negative bending of the cantilever depending upon the surface properties of the sample. This bending is detected by a focused laser beam reflected from the top surface of the cantilever to the photodiode. The displacement of the tip is recorded and finally convert into topographical image. Two basic modes of operating AFM are tapping and contact mode. The tip is vibrated at a certain amplitude in tapping mode, while in contact mode the tip is in contact with the sample surface. The AFM used in this characterization is a Cypher, Oxford instrument (Agilent 5500-STM) in tapping mode. The root mean square (RMS) roughness of the sample were analysed using WSxM software.

Field emission scanning electron microscopy (FESEM)

FESEM is a technique where a high energy electron beam is used to create an image of the sample. It uses a field emission gun as the electron source. As the electron beam exits from the electron gun, they are confined and focused on a small spot using metal apertures and magnetic lenses. To obtain information about surface topography high energy electron beam interacts with the atoms on the surface of the sample. Finally, detectors in the microscope collect electron signals emitted from the specimen to produce an image. Secondary electrons emitted by atoms due to electron beam is the most common mode of detection [14]. In order to performed FESEM measurement the sample surface should be electrically conductive, and electrically grounded to prevent accumulation of electrostatic charge at the surface. In this thesis FESEM (ZEISS, SIGMA 300) is used for studying the surface morphology of photoanode and counter electrodes. FESEM was operated with an accelerating voltage of 2 to 4 KeV and the samples were coated with a very thin gold layer by sputtering to avoid the surface charging effect during measurement.

RAMAN

Raman Spectroscopy is a versatile non-destructive tool where scattered light is utilized to assess the vibrations energy mode of a sample. It works on the principle of inelastic scattering. The sample is excited with a laser source, which is essentially an oscillating electromagnetic wave. It can provide both chemical and structural information, as well as the identification of substances through their characteristic Raman ‘fingerprint’[11][15]. In this study, the Raman

spectra were recorded using Horiba Jobin Vyon, Model LabRam HR spectrometer. Before measuring the sample, all Raman spectra were calibrated with respect to the standard Si spectrum at room temperature.

Fourier transform infrared spectroscopy (FTIR)

FTIR is an analytical technique used to obtain infrared spectrum of absorption and emission of the sample. It is a powerful tool to detect the different functional groups present in the nanomaterials from the spectral band recorded between 5000 and 400 cm^{-1}. The spectrum consists of absorption or transmission peaks corresponding to the frequencies of vibration between the bonds of atoms in the nanoparticle [11][16]. In this thesis, FTIR analysis was performed for both photoanode and counter electrodes. FTIR spectra of TiO_2, TiO_2-UVO_3 treated film at low temperature, PSSNa, PANI, and PANI-PSSNa coated films are recorded on Perkin Elmer (Spectrum 100) spectrometer.

UV-vis Spectroscopy

UV-vis spectroscopy is an analytical tool for measuring absorbance or transmittance as a function of wavelength. It is based on the interaction between light and matter. When the matter absorbs the light, it undergoes excitation and de-excitation, resulting in the production of a spectrum [11]. As we know that in photovoltaic photons are converted to electrons. So, it is desired that as many photons as possible are absorbed. In this thesis UV-vis analysis was performed to estimate the possibility of photons absorption at different wavelengths and the quantity of dyes anchored on photoanode. Therefore, the absorbance of dye loaded on TiO_2 films or desorb the dye in base solution is recorded. Also, the UV-vis transmittance spectra of bare ITO PET, TiO_2/ITO PET, and UVO_3 treated TiO_2/ ITO PET were recorded. The measurements are performed using Perkin-Elmer Lambda 950 and Carry 100 spectrometer.

Photoluminescence (PL) spectroscopy

PL spectroscopy is a nondestructive method to probe the electronic structure of materials. In PL, the material absorbs the incident light and then photoexcitation occurs. The photoexcitation causes the material to jump to a higher electronic state, releasing energy as it relaxes and returns to a lower energy level. The emission of light through this process is photoluminescence. The intensity and wavelength of the emitted photoluminescence directly measure important material properties such as bandgap, defects and recombination mechanisms [17]. In the present thesis, PL spectroscopy is used to characterize the optoelectronic properties of

semiconductors materials TiO_2 with and without UVO_3 treatment. The measurements of the samples are carried out using Horiba Jobin-Yvon, Flouromax-4 at room temperature.

Cyclic voltammetry (CV)

CV is a versatile electrochemical technique commonly used to investigate the oxidation and reduction processes of molecular species. It is also important to investigate electron transfer-initiated chemical reactions, which include catalysis [18-19]. The Cyclic voltammetry (CV) measurement was performed on Autolab (Metrohm) electrochemical work station in a three-electrode system, where the FTO coated with carbon nanotubes PANI (polyaniline), (CNTs), PANI-PSSNa, CNTs-PANI, and Pt as a working electrode, an Ag/AgCl as a reference electrode, and a standard Pt counter electrode immersed in an acetonitrile solution mixed with 10 mMLiI, 0.1 M $LiClO_4$, and 1 mM I_2 and scan rate of 100 mV/s.

Energy dispersive x-ray spectroscopy (EDX)

EDX is an analytical technique used for the elemental characterization of a sample. EDX is actually inbuilt within the scanning electron microscope (SEM) setup. When the sample is bombarded by high energy electron beam, electrons in the specimen are ejected creating vacancies. X-rays are thus emitted when such vacancies are filled with electrons in the higher states. The EDX detector detects the x-ray radiation and creates a voltage signal, which is proportional to the energy of the emitted radiation [14]. Thus, the elemental composition of the specimen is determined by measuring the intensity and the energy of the x-rays emitted from a specimen. Zeiss, Model: Gemini scanning electron microscope was used for examining the elemental composition of TiO_2 and TiO_2-CsBr doped electrodes prepared during this work.

2.3 References

[1] H.C. Weerasinghe, P.M. Sirimanne, G.P. Simon, Y.B. Cheng, Journal of Photochemistry and Photobiology A : Chemistry Fabrication of efficient solar cells on plastic substrates using binder-free ball milled titania slurries, 206 (2009) 64–70. doi:10.1016/j.jphotochem.2009.05.013.

[2] H.C. Weerasinghe, G. V. Franks, J.D. Plessis, G.P. Simon, Y.B. Cheng, Anomalous rheological behavior in chemically modified TiO_2 colloidal pastes prepared for flexible dye-sensitized solar cells, J. Mater. Chem. 20 (2010) 9954–9961. doi:10.1039/c0jm02063j.

[3] M.C. Aurelien Du Pasquier, Mattwe Stewart, Timothy Spitler, Aqueous coating of fefficient flexible TiO_2 dye solar cell, Sol. Energy Mater. Sol. Cells. 93 (2009) 528–535.

[4] Y.B. Cheng, Y. Peng, J.Z. Liu, K. Wang, Influence of parameters of cold isostatic pressing on TiO_2 films for flexible dye-sensitized solar cells, Int. J. Photoenergy. 2011 (2011). doi:10.1155/2011/410352.

[5] T. Yamaguchi, N. Tobe, D. Matsumoto, T. Nagai, H. Arakawa, Highly efficient plastic-substrate dye-sensitized solar cells with validated conversion efficiency of 7.6%, Sol. Energy Mater. Sol. Cells. 94 (2010) 812–816. doi:10.1016/j.solmat.2009.12.029.

[6] F.C. Krebs, Fabrication and processing of polymer solar cells: A review of printinf and coating techniques, Sol. Energy Mater. Sol. Cells. 93 (2009) 394–412.

[7] A.G.-S. and N.B.L. K. Norrman, 6 Studies of spin-coated polymer films, R. Soc. Chem. 101 (2005) 174–201. doi:10.1039/b408857n.

[8] M. Grätzel, Recent Advances ins sensitized Mesoscopic Solar Cells, Acc. Chem. Res. 42 (2009) 1788–1798. doi:10.1021/ar900141y.

[9] M. Mahbuburrahman, N. Chandradebnath, J.J. Lee, Electrochemical Impedance Spectroscopic Analysis of Sensitization-Based Solar Cells, Isr. J. Chem. 55 (2015) 990–1001. doi:10.1002/ijch.201500007.

[10] M. Lee, X-Ray diffraction for materials research, 2016.

[11] J. Campbell, S. Burkitt, N. Dong, C. Zavaleta, Nanoparticle characterization techniques, Nanoparticles Biomed. Appl. Fundam. Concepts, Biol. Interact. Clin. Appl. (2019) 129–144. doi:10.1016/B978-0-12-816662-8.00009-6.

[12] J.W. John F. Watts, An introduction to Surface Analysis by XPS and AES, in: WILEY, 2003.

[13] N.H. W.Richard Bowen, An introduction to AFM for improved processes and products, 2009.

[14] A.K.N. and N. kalarikkal Anshida Mayeen, Leyana K. Shji, Morphological Characterization of Nanomaterials | Enhanced Reader, in: 2018.

[15] E. Smith, G. Dent, Modern raman spectroscopy: A practical approach, 2019. doi:10.1002/0470011831.

[16] K. Torres-Rivero, J. Bastos-Arrieta, N. Fiol, A. Florido, Metal and metal oxide nanoparticles: An integrated perspective of the green synthesis methods by natural products and waste valorization: applications and challenges, Compr. Anal. Chem. 94 (2021) 433–469. doi:10.1016/bs.coac.2020.12.001.

[17] D.R. Baer, S. Thevuthasan, Characterization of Thin Films and Coatings, in: Handb. Depos. Technol. Film. Coatings Sci. Appl. Technol., 2009: pp. 749–864. doi:10.1016/B978-0-8155-2031-3.00016-8.

[18] M. Pazoki, U.B. Cappel, E.M.J. Johansson, Energy & Environmental Science Characterization techniques for dye-sensitized solar cells, Energy Environ. Sci. 10 (2017) 672–709. doi:10.1039/C6EE02732F.

[19] P.T. Kissinger, W.R. Heineman, Cyclic voltammetry, J. Chem. Educ. 60 (1983) 702–706. doi:10.1021/ed060p702.

Effect of UV-Ozone exposure on the dye-sensitized solar cells performance

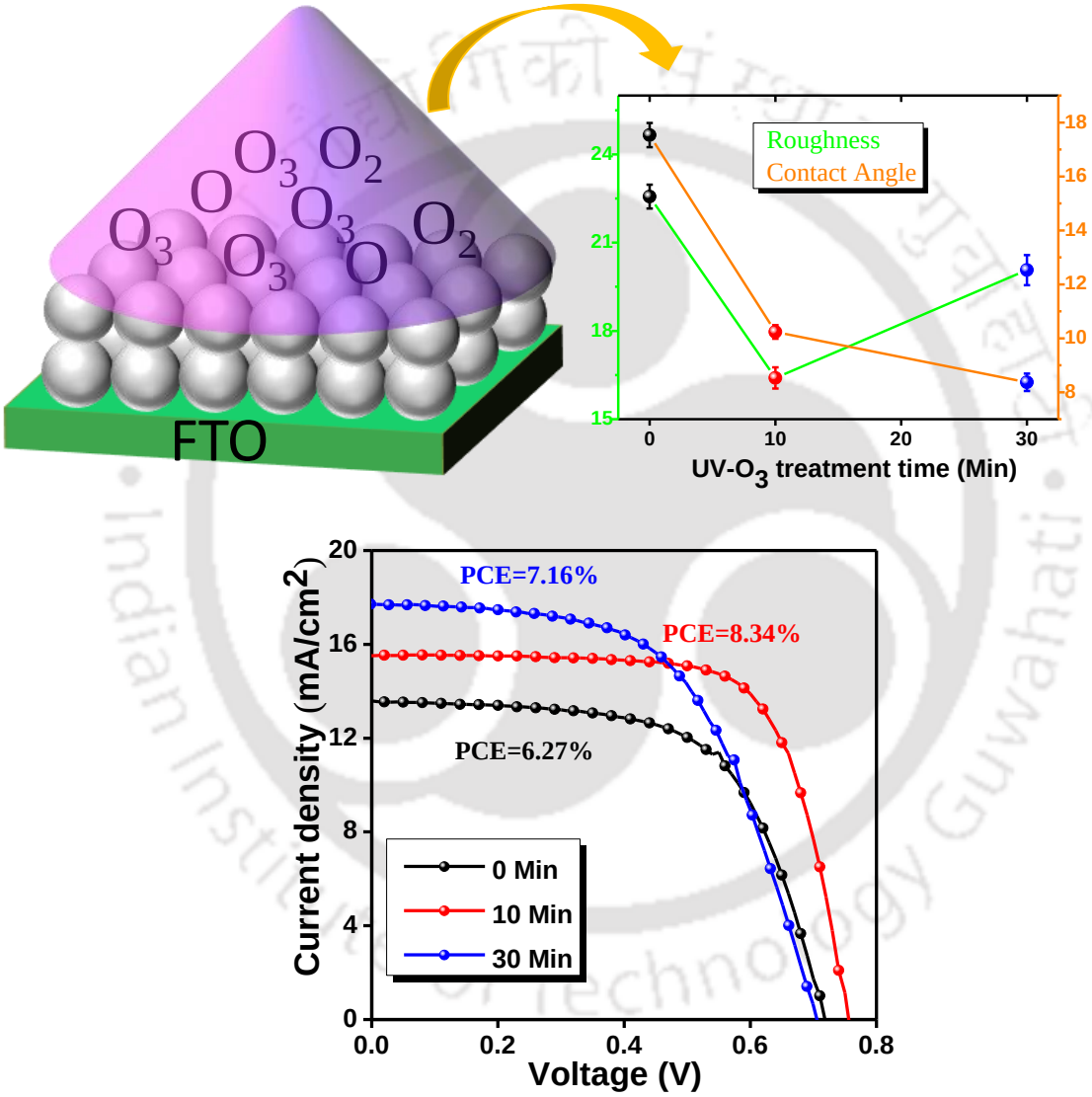

Chandan Dawo, Mohammad Adil Afroz, Parameswar Krishnan Iyer, and Harsh Chaturvedi, Solar Energy, Volume 208, 2020, Pages 212-219, https://doi.org/10.1016/j.solener.2020.07.064.

3.1 Introduction

The most preferred photoanode material for DSSC is nanocrystalline TiO_2 due to its electro-optical characteristics i.e., favorable valence band and conduction band position for dye and FTO, chemical stability, high refractive index (2.45), cost-effectiveness, strong oxidizing power, mesoporous nature and low toxicity [1-6]. TiO_2 based photoanode plays multiple roles for efficient charge generation, charge separation, and charge transfer from dye molecule to transparent conducting oxide (TCO) substrate. The conversion of light to electricity consists of multiple dynamic processes in DSSCs. Several undesired recombination processes are also known to occur at the photoanode, significantly reducing the PCE. Minimizing such unwanted processes at the active layer of TiO_2 is required for efficient performance of DSSCs. Hence, the surface states and structural parameters of TiO_2 plays an important role in the fabrication of an efficient DSSCs [7-11]. Several modifications of the TiO_2 photoanode have been reported to increase the efficiency of DSSCs, such as compact or blocking layer [12-14], scattering layer [15], atomic doping [16-17], surface treatment [18], etc. The surface treatment of TiO_2 electron transport layer (ETL) has become an essential step for improving the performance of DSSCs. Surface treatment of the photoanode affects dye loading capacity, electron transport, and electron recombination processes. $TiCl_4$ treatment on the TiO_2 ETL has been the most commonly applied method to increase efficiency of DSSCs [19-21]. However, $TiCl_4$ is not stable at room temperature as it reacts with moisture present in the air to produce the harmful hydrochloric acid [22]. A simple post-treatment of TiO_2 photoanode by urea solution with a concentration of 1 g/mol showed improvement in the efficiency of solar cells [23]. A comparative study of oxygen plasma treatment and oxygen ion beam treatment has reported that Oxygen ion beam treatment of DSSCs shows higher efficiency than plasma treatment. As it is much more efficient in removing the number of oxygen vacancies from a TiO_2 active film [24]. Deposition of various other layers of $Ba(NO_3)_2$, N_2O_6Sr, and $Mg(NO_3)_2$, on TiO_2 electrode followed by an O_2 plasma treatment, also shows significant improvement in the photo-conversion efficiency of the DSSCs [25]. Oxygen (O_2) plasma treatment of TiO_2 ETL, remarkably increase in the performance of DSSCs [26]. The drawback of oxygen plasma treatment, however, is its cost, which requires considerable capital investment. Therefore, UV-O_3 treatment provides an effective and economical alternative method [27].

In this study, an attempt has been made to study and optimize the effect of UV-O_3 exposure on a uniform TiO_2 ETL leading to DSSCs with higher efficiency. The samples were exposed to UV-O_3 for different duration of times (0, 5, 10, 15, and 30 min), under ambient

conditions, and keeping other parameters constant. The results demonstrate that by optimizing the exposure time, we can effectively control the stoichiometry of these samples. This results in an optimized condition affecting optical absorption, wettability, crystallinity, surface morphology, electrical conductivity etc., thereby improving the overall carrier dynamics of the prepared TiO_2 film. Consequently, at the optimum condition of 10 min exposure, the PCE of DSSCs shows significant improvement to 8.34% as compared to the untreated device with a PCE of 6.27%.

3.2 Experimental section

Chemicals and Materials

All chemicals and reagents purchased for the experiments were used as received and obtained from different commercial sources: FTO (Fluorine doped tin oxide) glass- 7 Ω/square sheet resistance (Sigma- Aldrich), TiO_2 nanoparticles (Degussa P25, Sigma-Aldrich, 21 nm), TiO_2 Paste (Sigma-Aldrich, 22 nm), terpineol (Sigma- Aldrich), tert-butanol (Sigma- Aldrich), acetonitrile (fisher scientific), absolute ethanol (Changshu yangyuan chemical, China) , acetic acid (Merck), ethyl cellulose (Himedia), iodine (Himedia), lithium iodide (Sigma-Aldrich), valeronitrile (sigma-Aldrich), 4-tert butylpyridine (Sigma-Aldrich), 1-butyl-3-methylimidazolium iodide (Sigma-Aldrich), NaOH (Merck), Chloroplatinic acid hexahydrate ($H_2PtCl_6.6H_2O$, Sigma-Aldrich), Anhydrous isopropanol (Sigma-Aldrich).

Preparation of working and counter electrode

FTO substrates were cleaned using 15 min ultrasonication in Mili-Q water, acetone, and 2-propanol, respectively. Cleaned and hot air dried FTO coated substrate was then exposed to UV-O_3 treatment for 15 min to remove any organic contaminants. The mesoporous layer of TiO_2 consists of two layers. The TiO_2 paste consists of 600 mg P25 powder, 5 mL ethanol, 100 µL acetic acid, 500 µL milli-Q water, 3 gm tarpineol, and 3 gm ethyl cellulose (15 Wt.% in ethanol). The mixture was stirred overnight and spin-coated at 5000 rpm for 45 secs on the clean substrate. After drying the first layer of TiO_2 at 100 $^{\circ}$C for 10 min, the second layer of TiO_2 Sigma paste was applied by the doctor blade technique and baked at 100 ºC for 20 min. Samples were then sintered at 500 $^{\circ}$C for 30 min to improve the interfacial contact between the deposited TiO_2 layer and the FTO substrate. TiO_2, which acts as a layer for electronic transport, was exposed to UV-O_3 for different time durations (0, 5, 10, 20, and 30 min). The Pt counter electrode was fabricated on another pre-cleaned FTO substrate by spin coating chloroplatinic acid hexahydrate solution (5 mg $H_2PtCl_6.6H_2O$ in 1 ml of anhydrous 2-propanol) at 5000 rpm

for 45 secs followed by annealing at 500 °C for 30 min. A set of 10 samples were prepared for each time interval to confirm the reproducibility of the experiment.

UV-O_3 exposure on TiO_2 ETL

UV-O_3 exposure was performed using NOVASCAN PSD Pro UV system. The UV-O_3 system produces ultraviolent light of two wavelengths, 254 and 185 nm simultaneously with very high photon energy of 470 and 647 kJ/mol, respectively. The bond energy of the organic contaminants C-C, C-H, C-O and O-H are 346, 411, 358 and 459 kJ/mol, respectively. The photon energies irradiated from the UV-O_3 system are much higher than the bond energies of contaminants. Therefore, the organic contaminant molecules are dissociated or excited by the irradiation of UV light. The atmospheric oxygen (O_2) is irradiated with ultraviolet rays at 185 nm; after absorption, it converts to atomic oxygen (O^*) and ozone (O_3) (equation 3. 1), whereas O_3 decomposes after irradiation with 254 nm UV light (equation 3. 2). Strong oxidizing atomic oxygen (O^*) is generated during the process of decomposition or formation of O_3. Atomic oxygen and O_3 strongly react with organic materials to produce volatile molecules such as CO_2, H_2O, N_2 etc. The samples treatment was performed at normal atmospheric pressure and room temperature [28-29].

$$h\vartheta(185\,nm) + 2O_2 \rightarrow O_3 + O^* \qquad 3.1$$

$$h\vartheta(254\,nm) + O_3 \rightarrow O_2 + O^* \qquad 3.2$$

Device fabrication and testing

The working TiO_2 films with and without UV-O_3 treatment were dipped into N719 dye solution (0.3 mM N719 in tert-butyl alcohol and acetonitrile, volume ratio 1:1) and kept for 24 hours to sensitize it at ambient condition. The solution of I^-/I_3^- electrolyte was made with 0.5 M LiI, 0.05 M I2, 0.5 M 1- Butyl-3-methylimidazolium iodide, 0.1 M guanidium thiocyanate, and 0.5 M 4-tert-butylpyridine dissolved in the mixture of acetonitrile/ valeronitrile (V/V = 85:15) solvent. DSSCs were assembled between dyed TiO_2 photoanode and Pt counter electrode using a hot melt spacer (Surlyn film, 60 μm, purchased from Ossila). The interspace available between the TiO_2 photoanode and the counter electrode was then filled with a liquid electrolyte to complete the fabrication of DSSCs. The electrical characteristics of DSSCs were measured with a Keithley 2400 source meter from -1 to 1 V in a step of 10 mV, under AM 1.5 G (100 mW/cm^2) illumination, which was provided by a solar light simulator (Newport, Oriel Sol 3A). The light intensity of the solar simulator was calibrated with a standard silicon solar cell of the National Renewable energy laboratory (NREL). The active area of DSSCs was 0.09 cm^2.

3.3 Results and discussion

XPS analysis

The structural and chemical changes on the TiO_2 ETL were studied by XPS upon UV-O_3 exposure. Fig. 3.1(a, b) demonstrates the XP spectra of carbon contaminants present in TiO_2 film for 0 and 10-min UV-O_3 treatment. The C 1s peak intensity found at 284.8 eV decreased significantly after UV-O_3 exposure. This suggests that UV-O_3 treatment burns out organic contaminants from the precursor of TiO_2 film [30-31]. The quantitative analysis of carbon atom percent, C-C/C-H peak area decreased from 57.90% to 52.40% after UV-O_3 treatment (Table 3.1). The relative changes in the peak area reveals that chemical environment of TiO_2 film changes with UV-O_3 exposure. Carbon contamination acts as interfacial trap sites and decreases cell performance. It affects the anchoring of dye molecules on TiO_2 film, which results in less quantity of dye adsorbed and therefore produces less photocurrent, fill factor, and efficiency. The O1s peak of TiO_2 film without and with UV-O_3 treatment was fitted with two Gaussian peaks (Fig. 3.1(c and d)). The central O1s peak found at 529.99 eV corresponds to the lattice oxygen of TiO_2 (Ti^{4+}). The higher binding energy on shoulder peak at 531.3 eV±0.2 eV is attributed to the formation of Ti^{3+} surface state through the creation of oxygen vacancies, commonly written as Ti_2O_3. The change of oxidation state from Ti^{4+} to Ti^{3+} occurred due to O^- and O_2^- species introduced on the surface of TiO_2 by UV-O_3 exposure [32-35]. The ratio of the atom percent calculated from the Ti_2O_3 peak area increases from 12.40% (0 min) to 23.4% (10 min) after the UV-O_3 treatment (Table 3.1). Oxygen vacancies generated from the reduction of Ti^{4+} to Ti^{3+} produces electrons, thereby affecting the surface functionality and charge state of the TiO_2 ETL. The excess number of electrons generated by UV-O_3 treatment helps in efficient charge transport and substantial reduction in electron-hole recombination rate as inferred through impedance measurements. Fig. 3.1(e and f) illustrates the XP spectra of Ti 2p for TiO_2 samples. For 0 and 10 min UV-O_3 exposure, the TiO_2 sample shows peaks at 457.5±0.1 eV, and 463±0.2 eV corresponding to the binding energy level of Ti^{4+} $2p_{3/2}$ and Ti^{4+} $2p_{1/2}$, along with the peaks at 456.4 eV±0.1 eV and 458.5 eV±0.2 eV imputed to $Ti^{3+}2p_{3/2}$ and

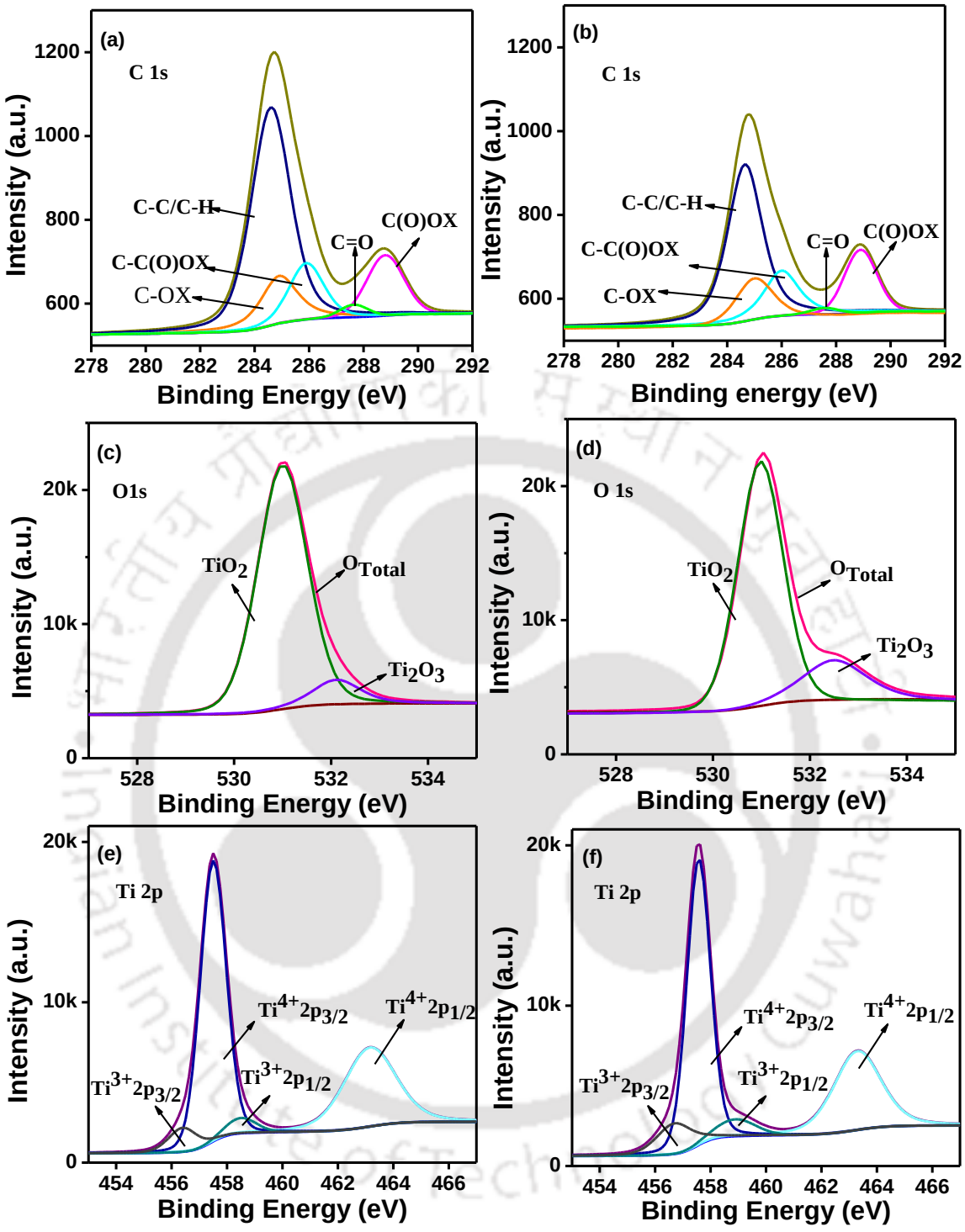

Figure 3. 1: XP spectra of TiO_2 films coated on FTO glass substrates with 0 min (a, c, and e), and 10 min (b, d, and f) UV-O_3 treatment.

$Ti^{3+}2p_{1/2}$ energy level of Ti^{3+} state respectively [18, 31, 36-37]. Peak areas of $Ti^{3+}2p_{3/2}$ state increases by 59.60% and $Ti^{3+}2p_{1/2}$ by 44.44% respectively after UV-O_3 treatment (Table 3.1).

The difference in these peak areas is attributed to the change in the stoichiometry of the TiO_2 film; due to increase in the number of oxygen vacancies by UV-O_3 exposure.

Table 3. 1: Summary of relative peak area with respect to total area of C 1s, O 1s, and Ti 2p for 0 min and 10 min UV-O_3 exposure TiO_2 ETL.

Samples	**C-C/C-CH**	**TiO_2**	**Ti_2O_3**	**Ti^{3+}(2p3/2)**	**Ti^{3+}(2p1/2)**
0 Min (%)	57.90	87.60	12.40	5.70	3.60
10 Min (%)	52.40	76.20	23.40	9.10	5.20

Contact angle and surface energy analysis of TiO_2 film with and without VU-O_3 treatment.

The contact angle of TiO_2 active layer films were measured using KRÜSS drop shape analyser instrument at ambient conditions. Deionized (DI) water (H_2O) and Diiodo-methane (CH_2I_2) were used as the test liquids. The test liquid was placed at different locations on TiO_2 active surface. Once the drop achieved metastable equilibrium, the measurement was carried out. Three measurements were taken from each sample, and the mean contact angle value is used to calculate the Surface free energy (SFE). The dispersive and polar components of the surface free energy were computed from the measured contact angles of DI water and Diiodo-methane using KRÜSS advance software (Table 3.2). The following equation was used to calculate the total SFE (equation 3.1) [38].

$$\gamma_S = \gamma_S^d + \gamma_S^p \qquad (3.1)$$

Where γ_S is the SFE, γ_S^d, and γ_S^p are the dispersive and polar component of the SFE of the examined TiO_2 films. Fig. 3.2(a, b and c) demonstrates the contact angle analysis of TiO_2 films after sintering without and with UV-O_3 irradiation. The contact angle reduces from 17.5±0.5° to 8.2±1° after 30 min of UV-O_3 exposure as shown in Fig. 3.2(d). Decrease in the contact angle (Fig. 3.2(a, b, and c)) indicates increase in hydrophilicity and corresponding increase in surface free energy (Fig. 3.2(e)). This increase in surface energy is attributed to the removal of unwanted hydrophobic organic components and the increase of hydrophilic oxygen vacancies in TiO_2 film [34, 39-41].

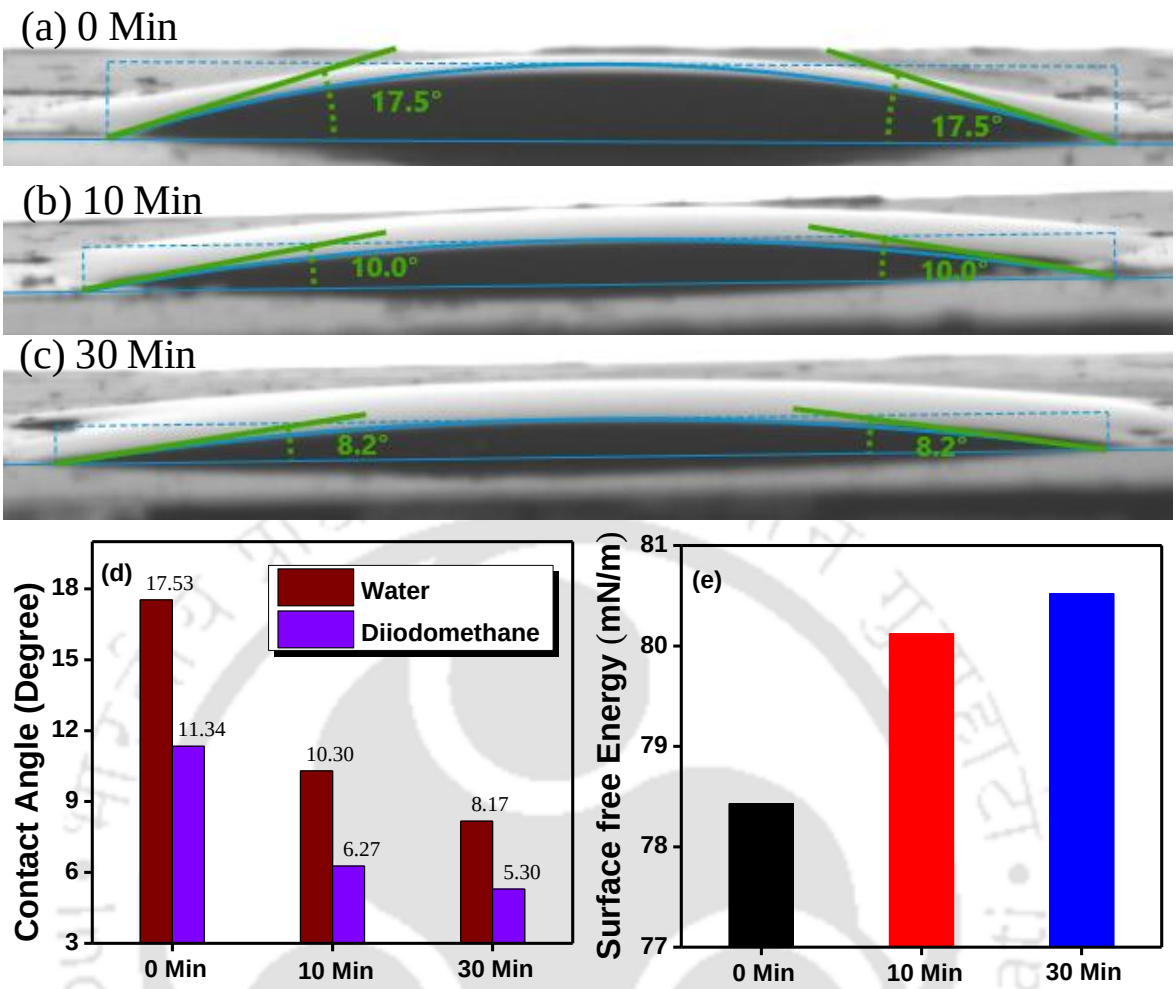

Figure 3. 2: Contact angle analysis pattern of water on TiO_2 films with (a) 0 min (b)10 min and (c) 30 min UV-O_3 exposure. Variation of (d) contact angle and (e) Surface free energy by UV-O_3 treatment time.

Table 3. 2: Variation of contact angle and surface free energy due to UV-O_3 exposure.

UV-O_3 treatment time (Min)	**Contact Angle (Degree)**		**Component of Surface free energy for examined material (mN/m)**		**Surface free Energy (mN/m). $\gamma_S = \gamma_S^d + \gamma_S^p$**
	Deionized water (H_2O)	**Diiodo-methane (CH_2I_2)**	**Disperse γ_S^d**	**Polar γ_S^p**	
0	17.5±0.5	11.32	49.82	28.62	78.43
10	10±1	6.25	50.50	29.68	80.12
30	8.2±1	5.21	50.59	29.93	80.52

Atomic force microscopy (AFM) analysis

AFM was utilized to analyse the surface topography and roughness/sectional profile of TiO_2 ETL film exposed to UV-O_3 system for different durations (Fig. 3.3(a, b, and c)). The root mean square (RMS) roughness decreases by 27.22% for 10 min exposure as compared to unexposed sample. However, roughness further increases by 19.52% for 30 min exposure. High roughness factor and irregular pores affect crystallization properties, increase the grain size of the TiO_2 film [39, 42]. 10 min UV-O_3 exposure has the lowest surface roughness indicating smooth, uniform pores and compact surface films, leading to efficient harvesting of light, better accessibility of dye adsorption, and prevents direct contact between TiO_2 and dye molecules thereby resulting in high conversion efficiency. Similarly, the highest conversion efficiency in perovskite solar cells was also achieved for the sample with lowest RMS value [33].

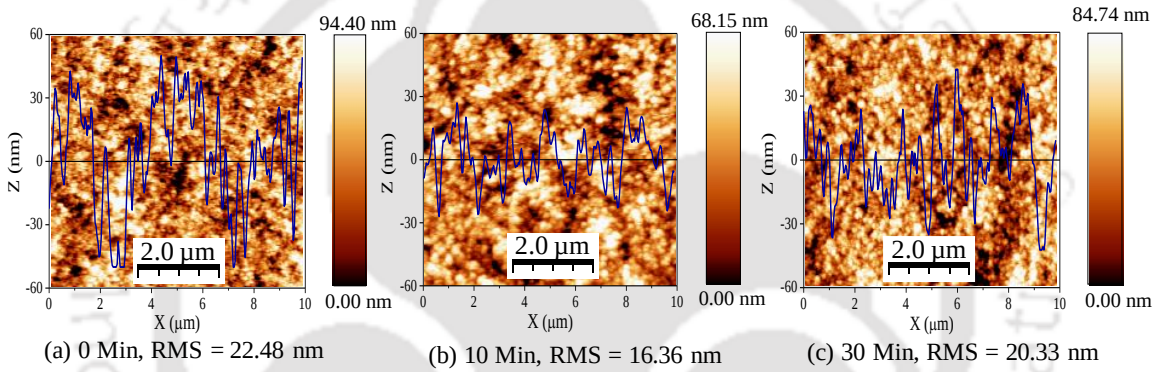

Figure 3. 3: Two-dimensional AFM images and sectional profile of TiO_2 film with (a) 0 min, (b) 10 min, and (c) 30 min UV-O_3 exposure.

X-ray diffraction (XRD) analysis

Fig. 3.4(a) displays the XRD pattern of TiO_2 film with different UV-O_3 treatment time. All samples show diffraction peaks of (101), (200), and (211) planes at corresponding Bragg angles of 25.35°, 48.06°, and 55.00° respectively, and are of anatase phase. The diffraction pattern of TiO_2 ETL photoanode with different UV-O_3 treatment times remains almost the same, with slight difference in intensity and relative peak area. The highest intensity and relative peak area are observed for 10 min UV-O_3 treatment. Changes in the relative peak area are presented in Table 3.3. Relative area of (211) plane decreased from 10.16% to 6.20% after UV-O_3 treatment for 10 min. The highest ratio of 4.09 for (200)/ (211) plane peak area is shown in Fig. 3.4(b). From the relative peak area analysis, it can be concluded that UV-O_3 treatment affects the

orientation of mesoporous TiO_2 ETLs. Favorable atomic arrangement of (101) and (200) orientation leads to better interconnection between the TiO_2 nanoparticle and FTO [43].

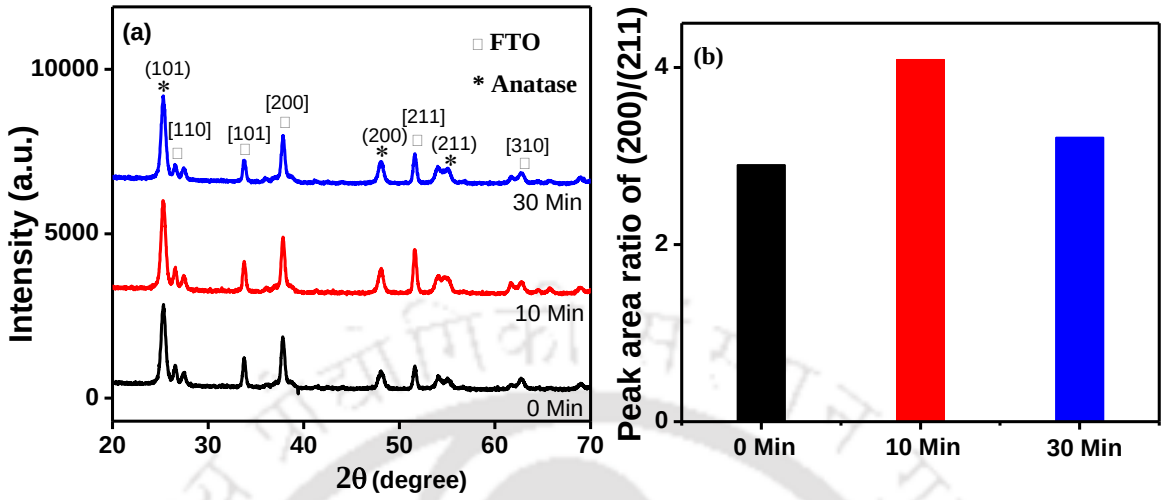

Figure 3. 4: X-ray diffraction pattern of TiO_2 film with (a) 0, 10, and 30 min UV-O_3 exposure. (b) Corresponding peak area ratio of (200)/ (211) plane.

Table 3. 3: Peak area analysis of XRD

hkl	Relative peak area			Remark
	0 Min	10 Min	30 Min	
(101)	100	100	100	Maximum peak area
(200)	29.56±0.5	25.37±1	29.30±1	Preferred (200) plane area.
(211)	10.16±0.5	6.20±1	9.106±1	TiO_2 peak area of (211) plane reduced after UV-O_3 treatment.
(200)/(211)	2.90±0.5	4.09±1	3.21±1	Ratio of (200)/(211) plane increased after UV-O_3 at optimum condition.

UV-visible analysis

The changes in the photocatalytic activity were examined using the UV-visible spectrometer. Fig. 3.5(a) shows the diffused reflectance UV-Vis absorption spectra of N719 sensitizer anchored on TiO_2 film. The photoanode absorption spectra shows two metal-to-ligand charge-transfer (MLCT) peak at 534 nm and 400 nm. Fig. 3.5(b) illustrates the absorption spectra of dye desorbing from the TiO_2 photoanode. The TiO_2 films with dimensions of 0.5 cm × 1.0 cm and a thickness of 8.5 µm are soaked in 3 mL of 0.1 M NaOH solution in ethanol and DI water

(volume ratio of 1:1) to desorbed the dye from the film and absorption spectra is taken by means of UV–vis spectrometer. Characteristic changes and blue shifts are observed in absorption pattern for TiO_2 loaded with dye. This blue shift is attributed to better deprotonation and less aggregation of the dye on TiO_2 surface [3, 9, 44-45]. Increase in absorption intensity is observed for corresponding exposure to UV-O_3 treatment (0 min <10 min< 30 min). This increase in absorption intensity of the photoanode sample exposed to UV- O_3 indicates efficient adsorption of the dye molecules on the TiO_2 surface due to removal of organic contamination there by providing better surface contact. Based on the quantitative estimation of the chemisorbed dye molecules on the TiO_2 surface, it was found that the 10 and 30 min UV-O_3 exposure exhibited the higher dye loading, viz. 2.20 x 10^{-7} mol.cm^{-2}, and 2.27 x 10^{-7} mol.cm^{-2} compared to 0 min (1.83 x 10^{-7} mol.cm^{-2}). This increase in dye loading capacity due to UV-O_3 exposure, leads to significant improvement in the current density of the fabricated DSSCs.

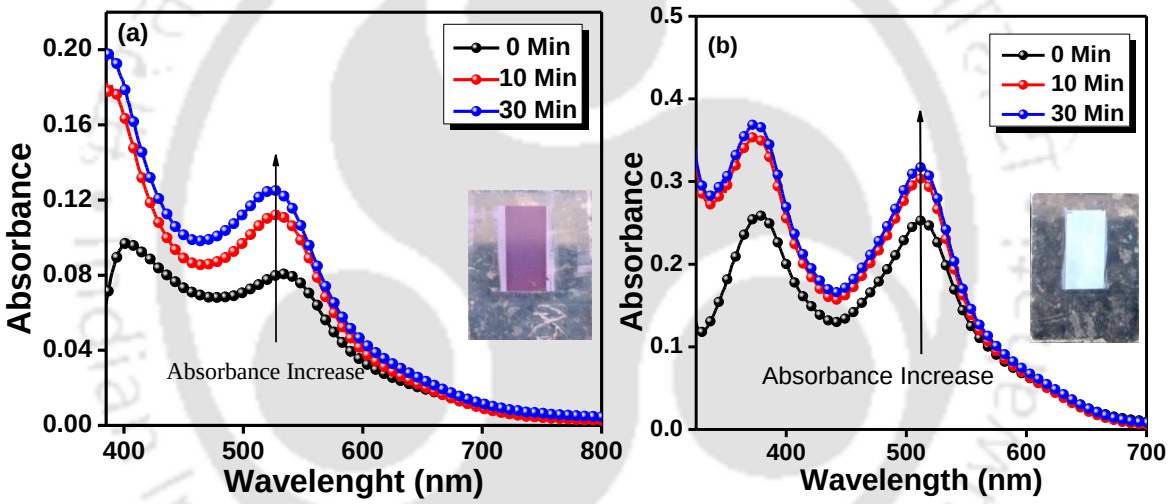

Figure 3. 5: UV-Visible absorption spectra of N719 dye (a) loaded on TiO_2 film, inset shows sensitized film and (b) dye solution desorbed from TiO_2 film in 0.1 M NaOH solution in ethanol and DI water (V:V=1:1), inset shows desorbed film.

Impedance analysis

Fig. 3.6 shows the Nyquist plots of electrochemical impedance spectra (EIS) for DSSCs along with the equivalent circuit (inset of Fig. 3.6). EIS measurement of DSSCs is a powerful technique to study the charge transfer resistance and recombination reactions taking place at different interfaces in the solar cell i.e., first semicircle in the high-frequency region (from 1-100 kHz) explains the charge transfer resistance and capacitance of counter electrode/electrolyte interface, second semicircle in the mid-frequency region (from 0.1 Hz-1 kHz) corresponds to the charge transfer resistance at photoanode/electrolyte interface with

chemical capacitance of the TiO_2 working electrode, and in the low frequency region (from 0.1 Hz- 0.01 Hz) provides information about impedance of diffusion of the liquid electrolytes [44, 46-47]. The parameters of equivalent circuit as obtained by fitting the data are presented in Table 3. 4. In the high frequency region, the onset point on the real axis of first semicircle corresponds to total ohmic series resistance (R_s) due to sheet resistance of electrode substrate and the resistance of electrolyte solution. The value of R_s decreases from 30.49 Ω (0 min) to

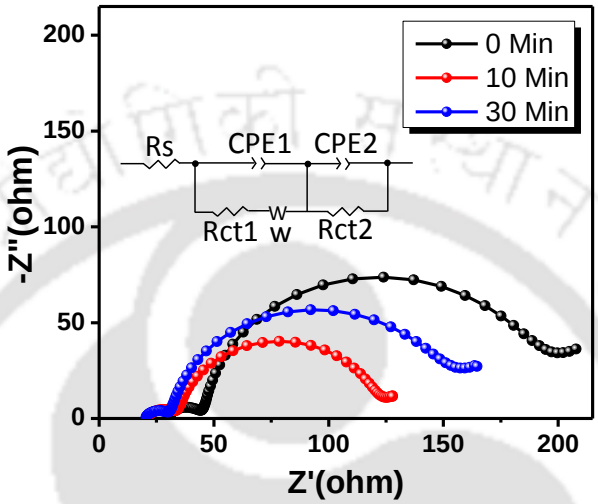

Figure 3. 6: Nyquist plot of DSSCs under ambient condition for different UV-O_3 treatment time.

20.62 Ω (30 min) after UV-O_3 exposure. This decrease in R_s indicates better interfacial contact of the TiO_2 film on FTO leading to increase conductivity. The parallel combination of electron transfer resistance 'Rct1 and capacitance CPE1' represented the impedance due to counter electrode/ electrolyte interaction at high frequency region. The Warburg diffusion impedance of the redox species in the electrolytes is represented with a finite length Warburg element (W). Rct2/CPE2 is basically due to electrochemical reaction taking place at working electrode/electrolyte interface. From Table 3.4 it can be observed that DSSC with 10 min UV-O_3 exposure show lowest values of Rct2 and Warburg diffusion impedance (W). Lowest Rct2 and W values for optimize photovoltaic device validates the minimal recombination with improved charge transport kinetics and faster diffusion of electrolytes. The smallest semicircle (red colour) in the mid-frequency region for optimum 10 min treatment indicates substantial decrease in the charge transfer resistance, indicating minimum trap state, lower recombination rate, higher electro-catalytic activity, and effective electrons life time (τ_{rec}). Large semi-circle (black colour) for untreated device shows considerable charge transfer resistance leading to

slower electronic transport, and increase in recombination reaction at the interface. This, results in overall lower performance of the untreated DSSCs.

Table 3. 4: DSSCs parameter obtained from EIS analysed.

Samples	**Rs (Ω)**	**Rct1 (Ω)**	**CPE1 10^{-6}(F)**	**W (Ω)**	**Rct2 (Ω)**	**CPE2 10^{-3}(F)**	τ_{rec} (ms)
0	30.49	11.75	7.09	20.47	125.00	0.40	50
10	21.2	11.42	15.75	6.70	90.00	0.80	72
30	20.62	10.09	10.83	15	100	0.60	60.4

Electrical parameters of DSSCs

The electrical conductivity of TiO_2 ETL significantly influences the performance of DSSCs. With different UV-O_3 irradiation time, the linear scan of dark current (I) vs. voltage (V) curves of TiO_2 samples are shown in Fig. 3.7(a). The slope of the I-V curves provides the electrical conductivity of the TiO_2 photoanode. This significant increase in I-V slope with increasing UV-O_3 exposure time is observed due to improved interfacial contact. UV-O_3 exposure of TiO_2 films may lead to enhanced conductivity due to the generation of oxygen vacancies [48-49]. In order to understand the influence of UV-O_3 exposure, the performance of DSSCs J-V curve is displayed in Fig 3.7(b). The PCE of DSSCs with different UV-O_3 exposure time are shown in Table 3.5. At 0 min, the photoelectric conversion efficiency (η) of DSSCs is 6.27% (V_{OC}=718.40 mV, J_{SC} = 13.02 mA/cm^2 and FF = 64.20%). The presence of residual organic contaminants on the TiO_2 film acts as recombination center at the interface of TiO_2 / N719 dye/electrolytes thereby critically influencing the collection and transport of electrons, thus, affecting the overall efficiency of the DSSCs [33]. Compared to unexposed TiO_2 ETL, UV-O_3 exposure shows remarkable improvement in photoelectric conversion efficiency (Fig. 3.7(c). By optimizing the duration of exposure, the best PCE of 8.34% achieved for 10 min with an increase of 33.01% efficiency (η= 6.27 to 8.34%), 16.27% photocurrent density (J_{SC}= 13.02 to 15.15 mA/cm^2), 5.20% open circuit voltage (V_{OC}= 718.40 to 756 mV) and 10.74% fill factor (FF= 64.20 to 71.10%). The enhancement of PCE with UV-O_3 exposure may be attributed to

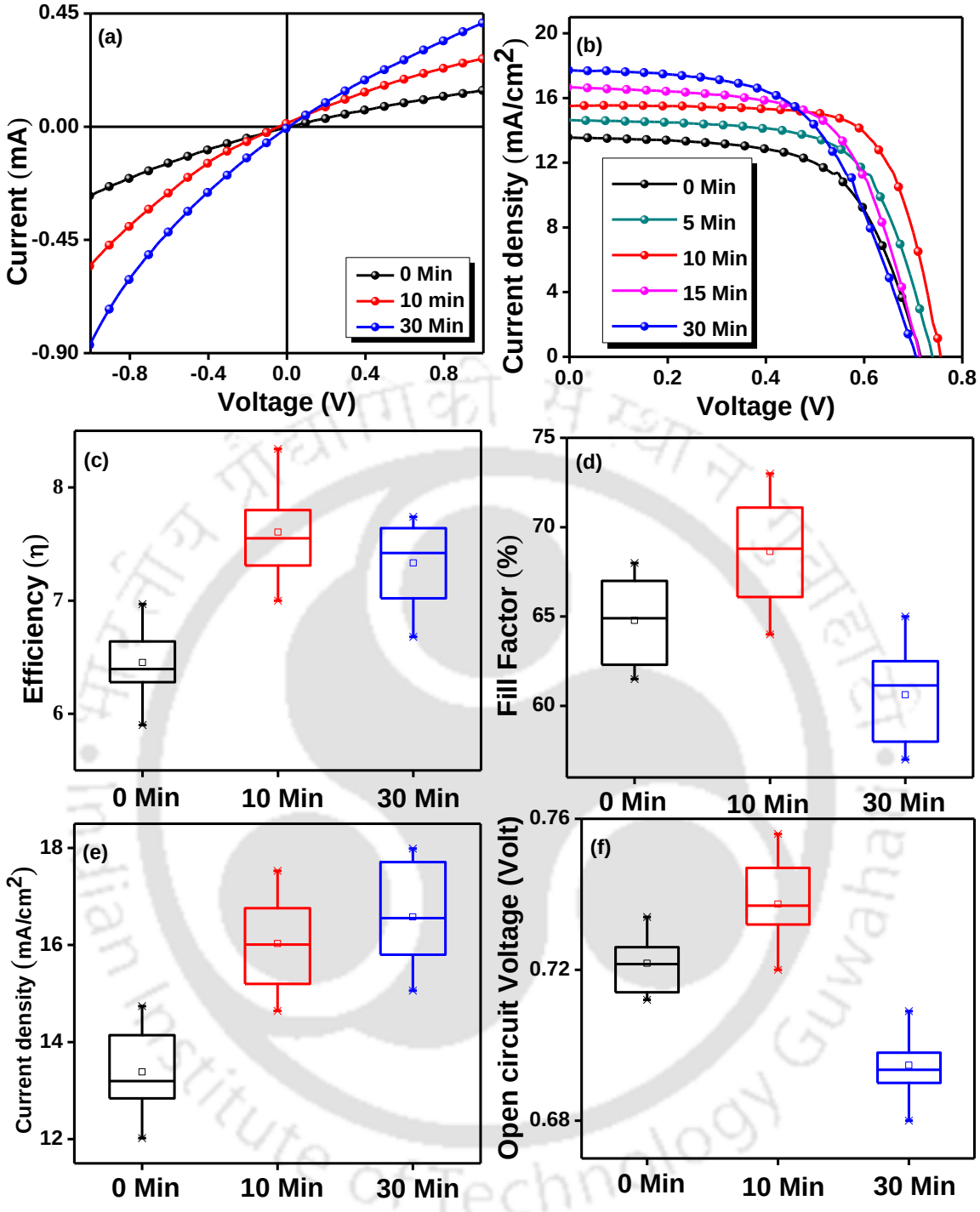

Figure 3. 7: (a) Dark linear I-V characteristics (b) Light J-V curves, Box charts of (c) efficiency (d) FF (e) J_{SC} and (f) V_{OC} of DSSCs as a function of UV-O_3 treatment performed on TiO_2 electron transport layer film.

fast electron transfer, increase in dye absorption, minimization of surface roughness and removal of organic binders [33-34]. However, the longer duration of UV-O_3 exposure time for 30 min gives no further enhancement in the performance of DSSCs. Although the Jsc was improved for 30 min exposed device (Fig. 3.7(e)), the efficiency decreases by 14.14% (η= 8.34

to 7.16%). This decrease in efficiency is attribute to lower FF (Fig. 3.7(d)) and $V_{OC,}$ (Fig. 3.7(f)) in overexposed surface which might be due to the role of oxygen vacancies in facilitating carrier recombination at the TiO_2/dye interface [33-35, 48].

Table 3. 5: Photovoltaic parameters of DSSCs fabricated using UV-O_3 treated TiO_2 layer.[3]

UV-O_3 exposure time (min)	**Voc (mV)**	**Jsc (mA/cm^2)**	**FF (%)**	**Efficiency (Average)[a] (η, %)**
0	718.40	13.02	64.20	6.27±0.31
5	741.90	14.64	65.50	7.06±0.33
10	756.00	15.15	71.10	8.34±0.38
15	707.20	16.66	63.40	7.47±0.37
30	705.60	17.71	57.20	7.16±0.37

[a]Average of 10 devices

[3]Performances of DSSCs were measured with 0.16 cm^2 working area under AM 1.5, 100 mW/cm^2 irradiation. Liquid electrolytes (0.05M I_2, 0.5M LiI, 0.1M guanidium thiocyanate, 0.5M 4-tert-butylpyridine and 0.5M 1-Butyl-3-methylimidazolium iodide dissolved in acetonitrile/valeronitrile (V: V= 85:15) solvent. Dye solution (0.3 mM N719) and Platinized counter electrodes.

3.4 Conclusions

Herein, the effect of UV-O_3 exposure on the efficiency of the DSSCs has been carefully analysed and optimized. The fabricated device with optimized time for 10 min UV-O_3 exposure shows the best PCE of 8.34% (J_{SC}=15.15 mA/cm^2, V_{OC}=756.00 mV, FF=71.10%) with good reproducibility. However, any further increase in exposure time leads to decrease in the photo conversion efficiency of the solar cells. XRD and impedance curve measurement denotes enhanced crystallinity and decrease in the ohmic resistance of the electron transport layer. Thus higher efficiency for the optimally exposed solar cells may be due to removal of the organic contaminants as indicated by the increase in the oxygen vacancies (XPS results) or due to lowering of surface roughness as confirmed by the AFM results, leading to improved wettability and increase in the adsorption of dye to the TiO_2 surface. However, further research is required to clearly identify the inherent mechanism. Moreover, additional experiments can be performed to explore the effect of UV-O_3 exposure on the photocatalytic activity, electrical conductivity and the recombination reaction at the dye/TiO_2 interface; leading to better optimized parameters for the development of efficient solar cells.

3.5 References

[1] B. O'Regan, M. Grätzel, A Low-Cost, High-Efficiency Solar-Cell Based on Dye-Sensitized Colloidal TiO_2 Films, Nature, 353 (1991) 737-740.

[2] K. Kakiage, Y. Aoyama, T. Yano, K. Oya, J. Fujisawab, M. Hanaya, Highly-efficient dye-sensitized solar cells with collaborative sensitization by silyl-anchor and carboxy-anchor dyes, Chem. Commun., 51 (2015) 15894.

[3] L. Kavan, Electrochemistry and dye-sensitized solar cells, Curr Opin Electrochem, 2 (2017) 88-96.

[4] A. Hadi, Q. Chen, M. Curioni, R. Xiao, T. Huang, Z. Liu, One-Step Fiber Laser Fabrication of Mesoporous and Compact TiO_2 Layers for Enhanced Performance of Dye-Sensitized Solar Cells, ACS Sustainable Chem. Eng., 6 (2018) 12299-12308.

[5] G.K. Mor, K. Shankar, M. Paulose, O.K. Varghese, C.A. Grimes, Use of Highly-Ordered TiO_2 Nanotube Arrays in Dye-Sensitized Solar Cells, Nano Lett., 6 (2006) 215-218.

[6] Y. Castro, N. Arconada, A. Durán, Synthesis and photocatalytic characterisation of mesoporous TiO_2 films doped with Ca, W and N, Boletín de la Sociedad Española de Cerámica y Vidrio, 54 (2015) 11-20.

[7] T.B. Raju, J.V. Vaghasiya, M.A. Afroz, S.S. Soni, P.K. Iyer, Twisted donor substituted simple thiophene dyes retard the dye aggregation and charge recombination in dye-sensitized solar cells, Org. Electron., 50 (2017) 25-32.

[8] W.-Q. Wu, Y.-F. Xu, H.-S. Rao, C.-Y. Su, D.-B. Kuang, A double layered TiO_2 photoanode consisting of hierarchical flowers and nanoparticles for high-efficiency dye-sensitized solar cells, Nanoscale, 5 (2013) 4362-4369.

[8] M. Zukalová, J. Procházka, A. Zukal, J. H. Yum, L. Kavan, Structural parameters controlling the performance of organized mesoporous TiO_2 films in dye sensitized solar cells, Inorg. Chim. Acta, 361 (2008) 656-662.

[9] M. A. Afroz, K. K. Sonigara, T. B. Raju, S. S. Soni, P. K. Iyer, Effect of fluorine substitution and position on phenylene spacer in carbazole based organic sensitizers for dye sensitized solar cells, Phys. Chem. Chem. Phys., 19 (2017) 28579-28587.

[10] A. Hagfeldt, G. Boschloo, L. Sun, L. Kloo, H. Pettersson, Dye-Sensitized Solar Cells, Chem. Rev., 110 (2010) 6595-6663.

[11] M. Grätzel, Dye-sensitized solar cells, J. Photochem. Photobiol. C, 4 (2003) 145-153.

[12] A. Sangiorgi, R. Bendoni, N. Sangiorgi, A. Sanson, B. Ballarin, Optimized TiO_2 blocking layer for dye-sensitized solar cells, Ceram. Int., 40 (2014) 10727-10735.

[13] M. S. Góes, E. Joanni, E. C. Muniz, R. Savu, T. R. Habeck, P. R. Bueno, F. Fabregat-Santiago, Impedance Spectroscopy Analysis of the Effect of TiO_2 Blocking Layers on the Efficiency of Dye Sensitized Solar Cells, J. Phys. Chem. C, 116 (2012) 12415-12421.

[14] Tanvi, V. Saxena, A. Singh, O. Prakash, A. Mahajan, A. K. Debnath, K. P. Muthe, S.C. Gadkari, Improved performance of dye sensitized solar cell via fine tuning of ultra-thin compact TiO_2 layer, Sol. Energy Mater. Sol. Cells, 170 (2017) 127-136.

[15] Z. A. Garmaroudi, M. Abdi-Jalebi, M. R. Mohammadi, R. H. Friend, A facile low temperature route to deposit a TiO_2 scattering layer for efficient dye-sensitized solar cells, RSC Advances, 6 (2016) 70895-70901.

[16] J. Huo, Y. Tu, M. Zheng, J. Wu, Fabrication a thin nickel oxide layer on photoanodes for control of charge recombination in dye-sensitized solar cells, J. Solid State Electrochem., 21 (2017) 1523-1531.

[17] S. Thogiti, J.Y. Park, C.T. Thanh Thuy, D. K. Lee, B.-K. Min, H. J. Yun, J. H. Kim, High-Performance Dye-Sensitized Solar Cells through Graded Electron Transport in Band-Engineered W-TiO_2 Cascade Layer, ACS Sustainable Chem. Eng., 6 (2018) 13025-13034.

[18] J. Jun, M. Dhayal, J.-H. Shin, J.-C. Kim, N. Getoff, Surface properties and photoactivity of TiO_2 treated with electron beam, Radiat. Phys. Chem., 75 (2006) 583-589.

[19] P. M. Sommeling, B. C. O'Regan, R. R. Haswell, H. J. P. Smit, N. J. Bakker, J. J. T. Smits, J. M. Kroon, J. A. M. van Roosmalen, Influence of a $TiCl_4$ Post-Treatment on Nanocrystalline TiO_2 Films in Dye-Sensitized Solar Cells, J. Phys. Chem. B, 110 (2006) 19191-19197.

[20] B. C. O'Regan, J. R. Durrant, P. M. Sommeling, N. J. Bakker, Influence of the $TiCl_4$ Treatment on Nanocrystalline TiO_2 Films in Dye-Sensitized Solar Cells. 2. Charge Density, Band Edge Shifts, and Quantification of Recombination Losses at Short Circuit, J. Phys. Chem. C, 111 (2007) 14001-14010.

[21] H. Park, W.-R. Kim, H.-T. Jeong, J.-J. Lee, H.-G. Kim, W.-Y. Choi, Fabrication of dye-sensitized solar cells by transplanting highly ordered TiO_2 nanotube arrays, Sol. Energy Mater. Sol. Cells, 95 (2011) 184-189.

[22] Q. Yi, S. Cong, H. Wang, Y. Wang, X. Dai, J. Zhao, Y. Sun, Y. Lou, G. Zou, High-stability Ti^{4+} precursor for the TiO_2 compact layer of dye-sensitized solar cells, Appl. Surf. Sci., 356 (2015) 587-592.

[23] K. Qi, S.-y. Liu, Y. Chen, B. Xia, G.-D. Li, A simple post-treatment with urea solution to enhance the photoelectric conversion efficiency for TiO_2 dye-sensitized solar cells, Sol. Energy Mater. Sol. Cells, 183 (2018) 193-199.

[24] M. K. Parvez, G. M. Yoo, J. H. Kim, M. J. Ko, S. R. Kim, Comparative study of plasma and ion-beam treatment to reduce the oxygen vacancies in TiO_2 and recombination reactions in dye-sensitized solar cells, Chem. Phys. Lett., 495 (2010) 69-72.

[25] J. Tak Kim, S. Ho Kim, Surface modification of TiO_2 electrode by various over-layer coatings and O_2 plasma treatment for dye sensitized solar cells, Sol. Energy Mater. Sol. Cells, 95 (2011) 336-339.

[26] J. Wang, Z. Lin, Dye-Sensitized TiO_2 Nanotube Solar Cells with Markedly Enhanced Performance via Rational Surface Engineering, Chem. Mater., 22 (2010) 579-584.

[27] F. D. Egitto, L. J. Matienzo, Transformation of Poly(dimethylsiloxane) into thin surface films of SiO_x by UV/Ozone treatment. Part I: Factors affecting modification, J. Mater. Sci., 41 (2006) 6362-6373.

[28] J. R. Vig, UV/ozone cleaning of surfaces, J. Vac. Sci. Technol., A 3 (1985) 1027-1034.

[29] L. Huang, X. Sun, C. Li, J. Xu, R. Xu, Y. Du, J. Ni, H. Cai, J. Li, Z. Hu, J. Zhang, UV-Sintered Low-Temperature Solution-Processed SnO_2 as Robust Electron Transport Layer for Efficient Planar Heterojunction Perovskite Solar Cells, ACS Appl. Mater. Interfaces, 9 (2017) 21909-21920.

[30] B.-K. Lee, J.-J. Kim, Enhanced efficiency of dye-sensitized solar cells by UV–O_3 treatment of TiO_2 layer, Curr. Appl. Phys., 9 (2009) 404-408.

[31] K.-H. Park, M. Dhayal, High efficiency solar cell based on dye sensitized plasma treated nano-structured TiO_2 films, Electrochem. Commun., 11 (2009) 75-79.

[32] H. Liu, W. Yang, Y. Ma, Y. Cao, J. Yao, J. Zhang, T. Hu, Synthesis and Characterization of Titania Prepared by Using a Photoassisted Sol−Gel Method, Langmuir, 19 (2003) 3001-3005.

[33] Y. Chu, H. Cai, L. Huang, Z. Xing, Y. Du, J. Ni, J. Li, J. Zhang, High-Efficient Flexible Perovskite Solar Cells with Low Temperature TiO_2 Layer via UV/Ozone Photo-Annealing Treatment, Phys. Status Solidi A, 216 (2019) 1800669.

[34] Z. Wang, J. Fang, Y. Mi, X. Zhu, H. Ren, X. Liu, Y. Yan, Enhanced performance of perovskite solar cells by ultraviolet-ozone treatment of mesoporous TiO_2, Appl. Surf. Sci., 436 (2018) 596-602.

[35] X. Zhang, H. Tian, X. Wang, G. Xue, Z. Tian, J. Zhang, S. Yuan, T. Yu, Z. Zou, The role of oxygen vacancy-Ti^{3+} states on TiO_2 nanotubes' surface in dye-sensitized solar cells, Mater. Lett., 100 (2013) 51-53.

[36] H. Liu, W. Yang, Y. Ma, J. Yao, Extended visible light response of binary TiO_2-Ti_2O_3 photocatalyst prepared by a photo-assisted sol–gel method, Applied Catalysis A, 299 (2006) 218-223.

[37] R. Liu, W.-D. Yang, L.-S. Qiang, Enhanced efficiency for dye-sensitized solar cells using a surface-treated photo-anode, J. Power Sources, 199 (2012) 418-425.

[38] A. Rudawska, E. Jacniacka, Analysis for determining surface free energy uncertainty by the Owen–Wendt method, Int. J. Adhes. Adhes., 29 (2009) 451-457.

[39] J. Wu, H. Lin, P. Kuo, B. Su, S. Chu, Y. Chen, S. Liu, C. Chang, C. Wu, Effect of UV-Ozone Treatment on the Performance of ZnO TFTs Fabricated by RF Sputtering Deposition Technique, IEEE Trans. Electron Devices, 61 (2014) 1403-1409.

[40] R. Wang, K. Hashimoto, A. Fujishima, M. Chikuni, E. Kojima, A. Kitamura, M. Shimohigoshi, T. Watanabe, Photogeneration of Highly Amphiphilic TiO_2 Surfaces, Adv. Mater., 10 (1998) 135-138.

[41] N. Sakai, R. Wang, A. Fujishima, T. Watanabe, K. Hashimoto, Effect of Ultrasonic Treatment on Highly Hydrophilic TiO_2 Surfaces, Langmuir, 14 (1998) 5918-5920.

[42] B.-G. Kim, J.-Y. Kim, S.-J. Lee, J.-H. Park, D.-G. Lim, M.-G. Park, Structural, electrical and optical properties of Ga-doped ZnO films on PET substrate, Appl. Surf. Sci., 257 (2010) 1063-1067.

[43] S. Saekow, W. Maiakgree, W. Jarernboon, S. Pimanpang, V. Amornkitbamrung, High intensity UV radiation ozone treatment of nanocrystalline TiO_2 layers for high efficiency of dye-sensitized solar cells, J. Non-Cryst. Solids, 358 (2012) 2496-2500.

[44] E. Dell'Orto, L. Raimondo, A. Sassella, A. Abbotto, Dye-sensitized solar cells: spectroscopic evaluation of dye loading on TiO_2, J. Mater. Chem., 22 (2012) 11364-11369.

[45] D. Chandra, T. Ohji, K. Kato, T. Kimura, Ligand-Assisted Fabrication of Small Mesopores in Semi-Crystalline Titanium Oxide Films for High Loading of Ru(II) Dyes, Langmuir, 27 (2011) 11436-11443.

[46] M.S. Ansari, R. Maragani, A. Banik, R. Misra, M. Qureshi, Enhanced photovoltaic performance using biomass derived nano 3D ZnO hierarchical superstructures and a D−A type CS-Symmetric triphenylamine linked bisthiazole, Electrochim. Acta, 259 (2018) 262-275.

[47] F. Fabregat-Santiago, G. Garcia-Belmonte, I. Mora-Seró, J. Bisquert, Characterization of nanostructured hybrid and organic solar cells by impedance spectroscopy, Phys. Chem. Chem. Phys., 13 (2011) 9083-9118.

[48] T. Wang, D. Ding, H. Zheng, X. Wang, J. Wang, H. Liu, W. Shen, Efficient Inverted Planar Perovskite Solar Cells Using Ultraviolet/Ozone-Treated NiOx as the Hole Transport Layer, Sol. RRL., 3 (2019) 1900045.

[49] R. Islam, G. Chen, P. Ramesh, J. Suh, N. Fuchigami, D. Lee, K. A. Littau, K. Weiner, R.T. Collins, K. C. Saraswat, Investigation of the Changes in Electronic Properties of Nickel Oxide (NiOx) Due to UV/Ozone Treatment, ACS Appl. Mater. Interfaces, 9 (2017) 17201-17207

Enhanced photovoltaic performance of dye sensitized solar cells using cesium bromide modified electron transport layer

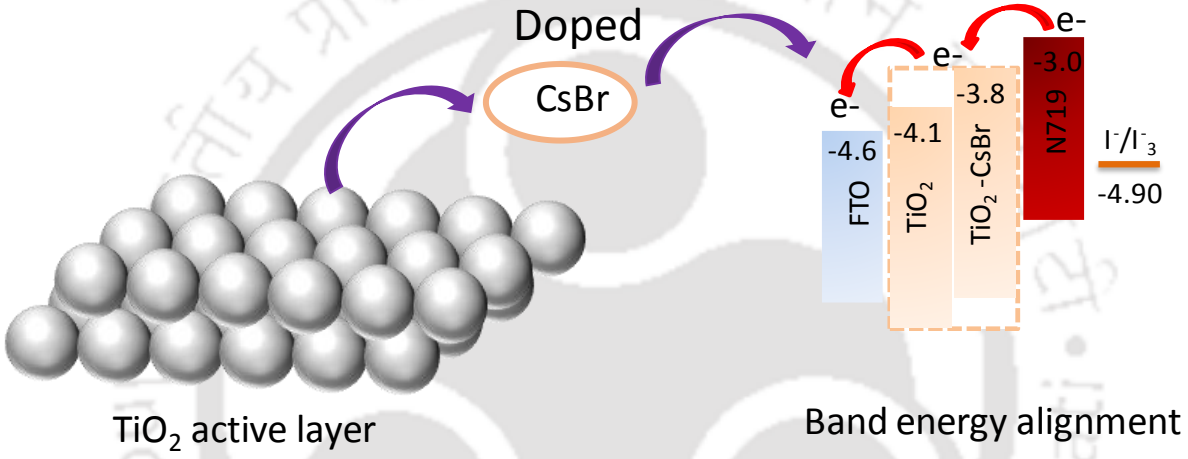

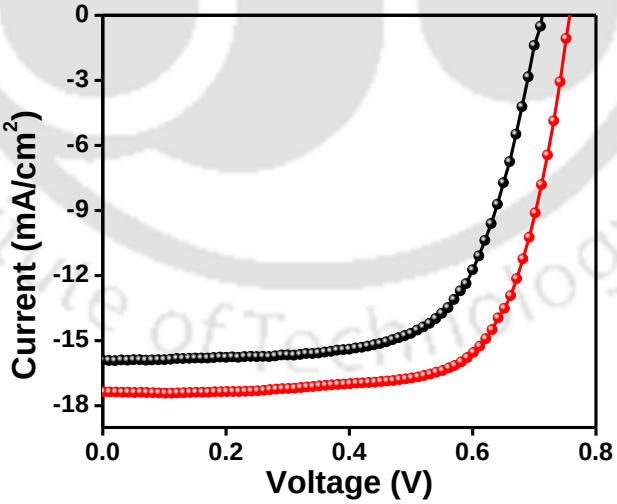

Chandan Dawo, Maimur Hossain, Parameswar Krishnan Iyer, and Harsh Chaturvedi

4.1 Introduction

Photoanode is one of the device's most crucial component, consisting of a few microns (~7-12 µm) thick porous semiconductor film on FTO/ITO coated glass substrate. The multifunction of photoanode includes dye absorption, injected excited electrons generated by the light absorbed dye molecules into the conduction band of electron transport layer. The power conversion efficiency (PCE) mainly depends on many factors like (i) suitable energy level between the dye and the redox couple of electrolytes, (ii) electron transfer from sensitizing dye (N719) to ETLs. To ensure efficient and fast electron injection into the conduction band, well matched energy level between the excited state of dye molecules and the conduction band of ETLs is desirable. (iii) charge separation and recombination; the charge transfer process is susceptible to recombination at the TiO_2/N719 interface since the large conduction band offset states can operate as recombination centers for excited electron and (iv) molar extinction coefficient of dye [1-6]. Various semiconductor materials such as TiO_2 [7], ZnO [8-9] and SnO_2 [10] etc. have been utilized as an electron transport layer (ETL) in DSSCs. TiO_2 (Anatase) has been proven to be one of the best among explored ETLs due to its high stability, suitable band position, lesser toxicity, wide commercial availability, and ease of tuning bandgap [11]. But the major problem associated with TiO_2 based ETL and N719 dye is the large conduction band energy gap between them. The random charge transfer occurred within the band structure of TiO_2 generating recombination [12-13]. Therefore, the doping technique can be utilized to improve the photo physical and transport properties of conventional TiO_2 ETL. Suitable doping can effectively minimize the trap states in mesoporous TiO_2 in DSSCs. Some alkali metals Ca [14], Li [15], non-metals [16-17], metalloids [18-19], post-transition metals [20-21], transition metals [22-23] etc., are used as dopants in TiO_2 to modify the band structure, charge transport properties, and surface area etc. Tuning the band structure of TiO_2 is a promising method for improving the driving force of injected electrons from the lowest unoccupied molecular orbital (LUMO) of dye to TiO_2 ETL [24-26]. The incorporation of dopants can also induce multiple salient properties in TiO_2, such as negative shifting in flat band potential (V_{fb}), resulting in a higher V_{OC} [19, 27-28], reduced recombination rate and enhanced charge transport rate by decreasing oxygen defect in the TiO_2 lattice [29-31], tuning bandgap for absorption in the visible region [32]. Therefore, significantly improved photovoltaic performance is expected to achieve by the optimum incorporation of strategically chosen dopants.

Here, the relative performance of DSSCs based on conventional TiO_2 and cesium bromide (CsBr) doped TiO_2 (TiO_2-CsBr) photoanodes are analysed. We varied the concentrations of

CsBr incorporated in TiO_2 to optimize the device performance. Consequently, 22% enhancement in PCE is observed with an optimum concentration of 0.4 weight percent (Wt. %) doping. Generally, doping tailor the energy level of the materials, so Mott-Schottky analysis is performed to calculate the flat band potential of TiO_2 and TiO_2-CsBr doped electrodes. The facilitating charge transfer and recombination kinetics of the modified ETLs are fully evaluated by impedance spectroscopy and open circuit voltage decay. The improvement in device performance after CsBr doping are also investigated by various characterisation techniques such as X-ray photoelectron spectroscopy (XPS), ultraviolet photoelectron spectroscopy (UPS), field-emission scanning electron microscopy (FESEM), atomic force microscopy (AFM), UV-vis absorption, energy dispersive X-Ray spectrometer (EDX), and X-ray diffraction (XRD) to examine the opto-electronic and morphological features of ETLs.

4.2 Experimental section

Chemicals and Materials

Fluorine doped tin oxide (FTO) coated glass- sheet resistance of 7 Ω/square, Titanium dioxide powder (Degussa P25, 21 nm), Terpineol, Diisopropoxide bis (acetylacetonate), Tert-butanol, Valeronitrile, Lithium iodide, 4-tert butylpyridine, 1-butyl-3-methylimidazolium iodide, Anhydrous isopropanol, Ruthenium dye (N719), Acetonitrile, and Chloroplatinic acid hexahydrate ($H_2PtCl_6.6H_2O$) are purchased from Sigma-Aldrich. Other chemicals for the experiments are obtained from different sources such as Absolute ethanol from Fisher scientific, Ethylcellulose and Iodine from Himedia, Acetic acid and Sodium hydroxide (NaOH) from Merck, and Cesium bromide (CsBr) from Alfa Aesar.

Preparation of TiO_2 and TiO_2-CsBr doped electron transport layer

The mesoporous TiO_2 paste with and without cesium bromide (CsBr) are prepared as follows: 600 mg TiO_2 nanoparticle (P25) is mixed with acetic acid (100 µL), ethanol (5 mL), milli-Q water (450 µL), terpineol (1.5 gm), and 2.5 gm ethyl cellulose which is dissolved in ethanol with 13 weight percent (Wt.%), followed by sonicating and stirring for overnight. Then mixed with different concentrations (0, 0.2, 0.4, and 0.6 Wt.%) of CsBr. The TiO_2-CsBr mixer is grinded for a few hours in mortle pestle. In this way, the TiO_2 and TiO_2-CsBr doped colloid paste are prepared. We obtained a well-dispersing paste without agglomerates and appreciated viscosity to produce a mechanically stable film. FTO coated transparent glass substrates are cleaned in a detergent solution for 15 minutes in sonicator bath and sequentially washed in tap water, deionised water, acetone, and propanol. Then, the substrates are dried using a hot air

dryer and then UV-Ozone exposure for 10 min to completely remove the last traces of organic contaminants. A thin TiO_2 compact layer ~ 50 nm is deposited on the clean FTO surface using a spin coating technique. An ethanol solution containing diisopropoxide bis (acetylacetonate) of 0.15 M is spin coated at 5000 rpm for 60 secs and consequently calcined at 450 °C for 30 min. After cooling down to room temperature, the mesoporous TiO_2 and TiO_2-CsBr doped paste are applied above the compact layer by doctor blade technique and subsequently heated in a muffle furnace at 450 °C for 40 min, to burn out the residual organic components and improve the interfacial contact.

Device fabrication and testing

The TiO_2 and TiO_2-CsBr deposited films are immersed into 3×10^{-4}M N719 dye solution and finally kept in the dark for 24 hours. Liquid electrolyte (0.05M I_2, 0.5M LiI, 0.1M guanidium thiocyanate, 0.5M 4-tert-butylpyridine and 0.5M 1-Butyl-3-methylimidazolium iodide) dissolved in acetonitrile/valeronitrile (Volume ratio of 85:15) solvent. The Platinized (Pt) counter electrodes (CEs) are prepared by spin coating (4000 rpm, 60 secs) $H_2PtCl_6.6H_2O$ solution in anhydrous 2-propanol, then sintering for 40 min at 450 °C. The photoanodes and counter electrodes are separated by hot-melt sealing foil (60 µm, Surlyn film, Ossila), and the space between the electrodes is filled with liquid electrolyte. The current density and voltage (J-V) analysis of DSSCs are performed using a 2400 source meter (Keithley, USA) from -1 to 1V in a step of 10 mV, under one-sun AM-1.5G 100 mW/cm^2 intensity (Sol3A Oriel, Newport, USA). The J-V measurements are defined with a specific active area of 0.16 cm^2.

4.3 Results and discussion

Current density-voltage (J-V) characteristic of DSSCs

The photovoltaic performance of DSSCs fabricated with conventional TiO_2 and TiO_2-CsBr based ETLs are analysed in AM 1.5G under the illumination of 100 mW/cm^2. The parameters of the DSSCs are summarised in Table 4. 1. The control device based on TiO_2 ETL produced a PCE of 7.61% with an open circuit voltage (V_{OC}) of 711.80 mV, short-circuit current density (J_{SC}) of 15.92 mA/cm^2, and a fill factor (FF) of 67.30%. The modified device based on TiO_2-CsBr ETL exhibited an enhanced PCE of 9.28% with a higher V_{OC} of 759.30 mV, J_{SC} of 17.36 mA/cm^2, and FF of 70.50%. In comparison 0.4% CsBr doped TiO_2 ETL yielded ~22% PCE enhancement. The V_{OC} increased up to 6.6% when TiO_2 was doped with CsBr. The V_{OC} enhancement can be attributed to the negative shifting of flat band potential (V_{fb}) after modifying with CsBr cluster. However, the excessive increase in CsBr incorporation beyond

0.4 Wt.% resulted in decline overall PCE. This decline of PCE can be caused by multiple reasons, such as hindered electron transfer and diffusion due to high CsBr content, or probably an undesirable recombination reaction taking place during the operating condition within the cell. The impacts caused by CsBr doping on flat band potential, donor density, charge transfer, recombination process, electron life, and band alignment of the DSSCs are discussed below with the aid of Mott-Schottky, OCVD studies, electrochemical impedance spectra, XPS, and UPS. A V_{OC} box chart of 10 devices are presented in Fig. 4.1(b), to highlight the reproducibility of devices.

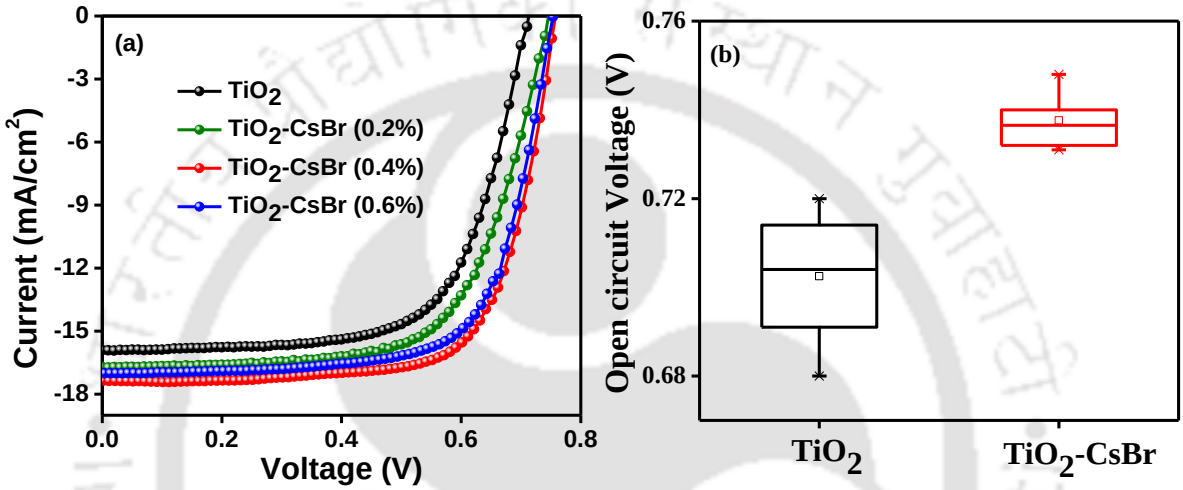

Figure 4. 1: (a) J-V characteristics curves and (b) V_{OC} box chart of DSSCs with TiO_2 and TiO_2-CsBr ETL.

Table 4. 1: Parameters of DSSCs.[4]

Electrodes	Wt.% of CsBr	J_{SC} (mA/cm^2)	V_{OC} (mV)	FF (%)	η (Average)[a] (%)
TiO_2	0	15.92	711.30	67.30	7.61±0.23
TiO_2-CsBr	0.2	16.59	746.10	65.90	8.15±0.25
	0.4	17.36	759.30	70.50	9.28±0.24
	0.6	16.94	751.55	69.40	8.82±0.26

[a]Average of 10 devices

[4]Performances of DSSCs were measured with 0.25 cm^2 working area under AM 1.5, 100 mW/cm^2 irradiation. Liquid electrolytes (0.05M I_2, 0.5M LiI, 0.1M guanidium thiocyanate, 0.5M 4-tert-butylpyridine and 0.5M 1-Butyl-3-methylimidazolium iodide dissolved in acetonitrile/valeronitrile (V: V= 85:15) solvent. Dye solution (0.3 mM N719) and Platinized counter electrodes.

Mott-Schottky (M-S) plot

Mott-Schottky (M-S) plot is an effective method to determine the free charge carrier density (N_C) and flat band potential (V_{fb}) in a semiconductor and electrolyte system. Fig. 4.2 shows the M-S plot of DSSCs based on TiO_2 and TiO_2-CsBr doped ETLs. The M-S plots of $\frac{1}{C^2}$ vs V shows a non-linearity curve with a positive slope, implying an N-type semiconductor behavior. The non-linearities in the M-S plots are generally associated with the presence of surface states or rough mesoporous nature of the electrodes. The N_C and V_{fb} could be calculated using the following equation [33-35].

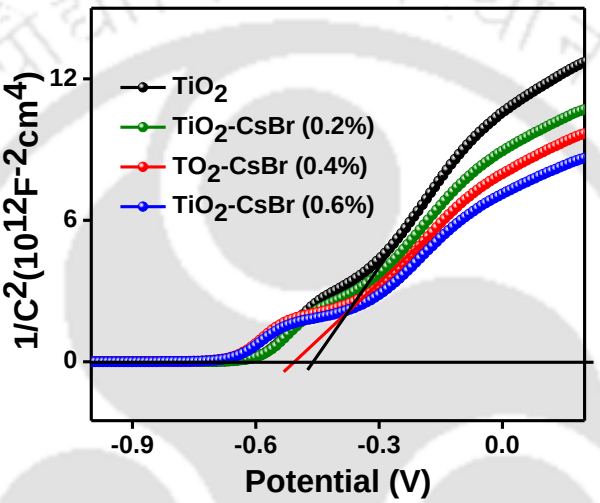

Figure 4. 2: Mott-Schottky plot of DSSCs with different conc. of CsBr in TiO_2 ETLs

$$\frac{1}{C_{sc}^2} = \frac{2}{\varepsilon\varepsilon_0 q A^2 N_C}\left(V - V_{fb} - \frac{Tk_B}{q}\right) \quad 4.1$$

$$slope = \frac{2}{\varepsilon\varepsilon_0 q A^2 N_C} \quad 4.2$$

Here, C_{sc} is the space charge capacitance, ε is the dielectric constant of TiO_2 =50, ε_0 is the permittivity of vacuum $= 8.85 \times 10^{-12}\ F/m$, A is the area= 0.16 cm^2, T is the absolute temperature=30 K, k_B is the Boltzmann's V is the applied voltage, V_{fb} is the flat-band potential, q is the electron charge $1.6 \times 10^{-19} C$, and N_C is the free carrier density=?.

For TiO_2 electrode, $slope = 11.2 \times 10^{12} F^{-2} V^{-1}$

$$N_C = \frac{2}{\varepsilon\varepsilon_0 q A^2 slope} = 0.98 \times 10^{17}/cm^3$$

For TiO_2-CsBr electrode with 0.4%, $slope = 7.26 \times 10^{12} F^{-2} V^{-1}$

$$N_C = \frac{2}{\varepsilon\varepsilon_0 q A^2 slope} = 1.56 \times 10^{17}/cm^3$$

The slope of the M-S plot yields the donor density ($N_{C)}$ and based on the above equation, the slope of the tangent line is inversely proportional to N_C. From Fig. 4.2 we observed that the slope of DSSCs based on TiO_2-CsBr ETL decreased, which indicates that CsBr incorporation improved N_C of the TiO_2 film. The calculated N_C from the slope is found to be $1.17 \times 10^{22}/cm^3$ and $1.76 \times 10^{22}/cm^3$ for TiO_2 and TiO_2-CsBr (0.4%) ETLs, respectively. In a semiconductor, fermi level (E_F) is closely related to N_C. As the donor concentration increases, E_F leads in the direction of the conduction band and correspondingly delivers higher V_{OC}. In DSSC, V_{OC} is directly correlated to the energy difference between the electrolytes' redox potential, i.e.,I^-/I_3^- and the quasi-fermi level, i.e., V_{fb} within TiO_2. The V_{fb} is another important parameter that can be determined from the intercept on the V axis i.e., $\frac{1}{C^2} = 0$. Comparing the V_{fb} of TiO_2 and CsBr-TiO_2 doped photoanodes, a negative shift is observed from -0.46 to -0.50 V. Thus, the increased in V_{OC} is attributed to a negative shift in V_{fb} due to TiO_2-CsBr doping [22][27][36]. The result obtained in the M-S plot agrees with J-V curve of the DSSCs.

Open circuit voltage decay (OCVD)

Further, in order to investigate the electron recombination in DSSCs, OCVD measurement is performed. The measurement is done by illuminating the DSSCs under a 100 mW/cm^2 light source for 20 seconds to attain a quasi-equilibrium state, and then the light is abruptly turned off with the help of a shutter to monitor the transient decay of V_{OC}(t) during the relaxation from quasi-equilibrium state to dark equilibrium. The decay curves of DSSCs are due to charge recombination, which decreases electron concentration as a function of time. Fig. 4.3(a) depicts the OCVD decay curves of DSSCs devices based on TiO_2 and TiO_2-CsBr doped photoanode. From Fig 4.3(a), the V_{OC}(t) responded of DSSC with TiO_2 photoanode is much faster than that of CsBr-TiO_2 photoanode, especially within 40 s time domain. The rate of V_{OC}(t) decay is directly proportional to the recombination rate. This result described that the TiO_2-CsBr doped photoanode reduced charge recombination considerably. The relation between transient decay of Voc(t) and electron lifetime (τ_e) can be expressed by the following equation (4.3) [37-41].

$$\tau_n = -\frac{k_B T}{q}\left(\frac{dV_{oc}}{dt}\right)^{-1} \qquad 4.3$$

where, k_B is the Boltzmann constant, q is the electron charge, and T is the absolute temperature in Kelvin. The electron lifetimes (τ_n) estimated from OCVD curve of DSSCs with conventional

TiO_2 and TiO_2-CsBr photoanode is presented in Fig 4.3(b). DSSCs with TiO_2-CsBr photoanodes significantly reduced photoelectron recombination rate and enhanced the photoelectrons' lifetime compared to device based on TiO_2 photoanode. This proved that electrons in TiO_2-CsBr photoanode survive longer in an excited state and facilitate electron transport resulting in enhanced performance of the DSSCs.

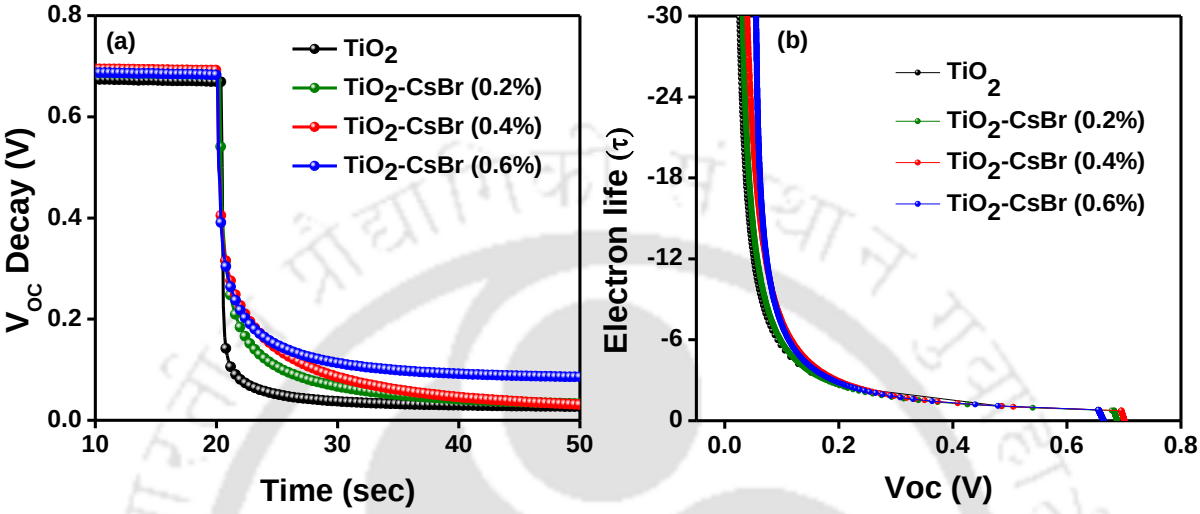

Figure 4. 3: (a) Open circuit voltage decay curves and (b) corresponding electron life of DSSCs based on TiO_2 and TiO_2-CsBr doped ETL.

Impedance analysis

To evaluate the charge transfer characteristic of DSSCs at three spatially separated interfaces i.e., FTO/TiO_2, TiO_2/dye/electrolyte, and electrolyte/Pt coated-FTO, electrochemical impedance spectroscopy (EIS) analysis is executed. Both the ionic and electronic processes govern the charge transfer in the DSSCs system. The high-frequency region reflects the impedance of Pt coated-FTO/electrolytes interface. The intermediate frequency range features the impedance of TiO_2/dye/electrolyte interface, and the diffusion of electrolytes in low frequency region [42-44]. To explore the effect of CsBr doping on the charge transfer process, we prepared DSSCs using TiO_2 and TiO_2-CsBr doped ETLs. Fig. 4.4(a) illustrates the result as a Nyquist plot. The spectra are fitted in EC Lab software using an appropriate equivalent circuit, and the corresponding circuit elements value is noted in Table 4.2. The equivalent circuit with series resistance (R_S), constant phase element (CPE), and charge-transfer resistance (R_{CT}) are shown in Fig. 4.4(a, inset). The DSSCs based on TiO_2-CsBr photoanodes exhibited lower R_S of 28 Ω compared to 30.04 Ω of pristine TiO_2 based device respectively. The decreasing value of Rs in modified devices assisted higher electron transfer rate that improved the J_{SC} and FF. The first semicircle in the EIS due to R_{PT1} and CPE1 over the high-frequency

region represents the impedance of Pt-coated FTO/ electrolyte interface. The small semicircle indicates a fast charge transfer process at the Pt coated-FTO/electrolytes interface. The second

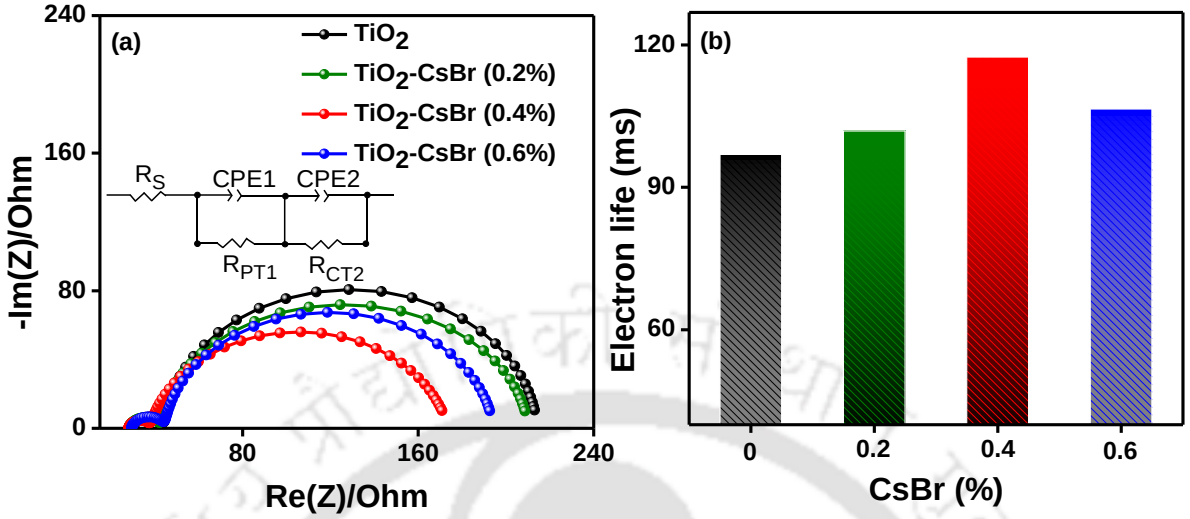

Figure 4. 4: (a) Typical Nyquist plots and (b) corresponding electron life of DSSCs based on TiO_2 and TiO_2-CsBr doped ETL.

Table 4. 2: Values of circuit elements.

CsBr Wt.% in TiO_2	R_S (Ω)	CPE1 (10^{-6}F)	R_{PT1} (Ω)	CPE2 (10^{-3} F)	R_{CT2} (Ω)	Life time (ms)
0	30.04	12.45	14.92	0.57	170	96.90
0.2	29.40	14.65	13.27	0.66	167	101.87
0.4	28.01	18.23	11.20	0.87	135	117.45
0.6	28.20	17.72	12	0.71	150	106.50

semicircle given by the parallel combination of R_{CT2} and CPE2 represents impedance at TiO_2/dye/electrolyte interface. The EIS results highlighted that the interference charge transfers resistance R_{CT1} and RCT2 significantly reduced for TiO_2-CsBr based devices, indicating substantial electron recombination suppression. This is attributed to the collective effect of CsBr in TiO_2 matrix which produces favorable energy level alignment and enhanced electron life (Fig. 4.4b) that accelerate electron transferred more easily with lower resistance compared to conventional TiO_2. The electron transport properties of the EIS spectra are in agreement with the values derived from transient photovoltage and photocurrent measurements.

XPS analysis

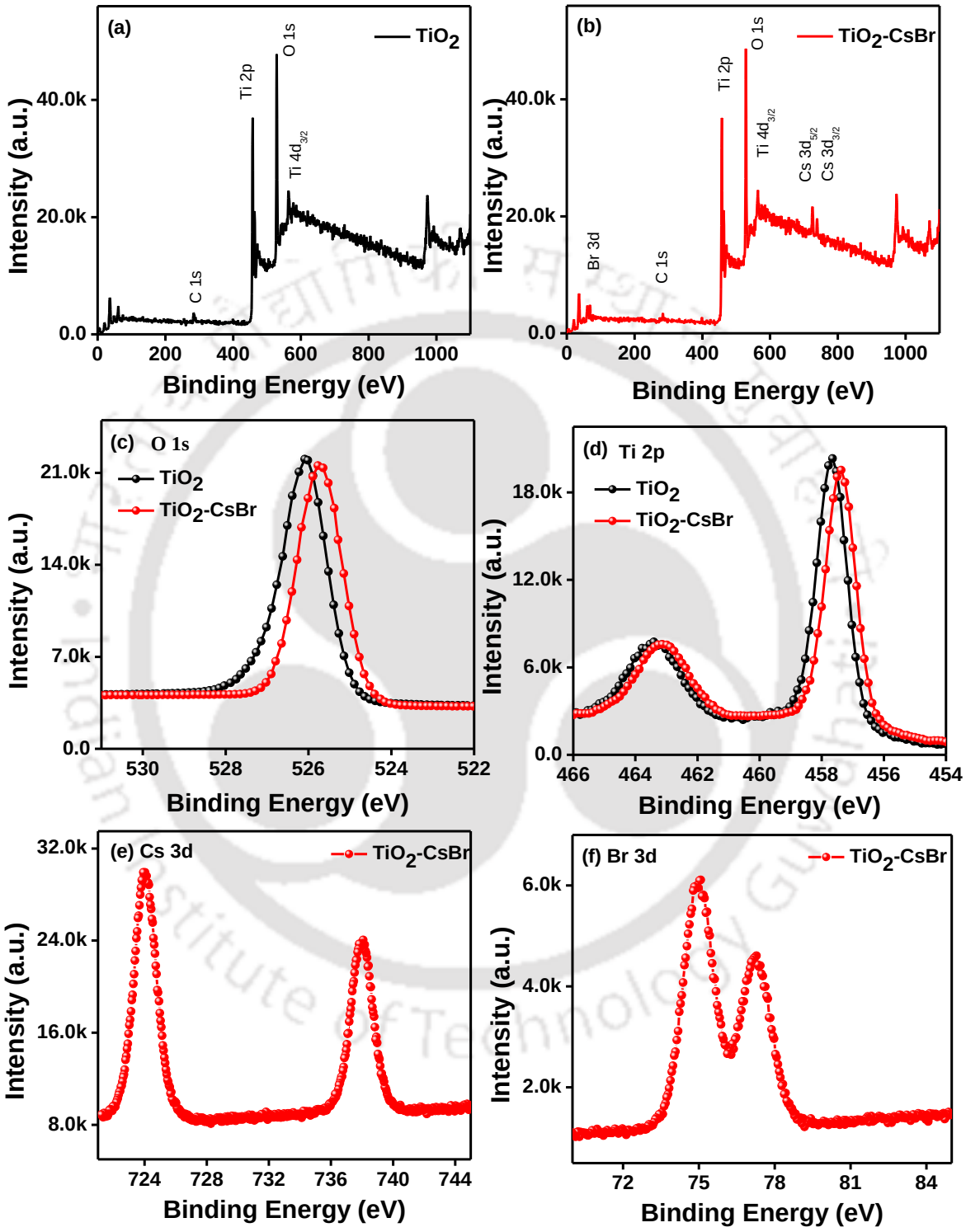

Figure 4. 5: Full range XP spectrum of (a) TiO_2 (b) TiO_2-CsBr doped films, and high resolution spectra of (c) O 1s (d) Ti 2p, (e) Cs 3d, and (f) Br 3d peaks. (TiO_2= Black, TiO_2-CsBr = Red).

XPS analysis is performed to identify the elemental composition of the TiO_2 and doped TiO_2-CsBr ETLs. The full range of XP spectra of the corresponding ETLs are presented in Fig. 4.5(a and b). The deposited TiO_2 film mainly consisted of oxygen (O), Titanium (Ti), and a small quantity of carbon (C). After CsBr incorporation in TiO_2, Cs and Br elemental peak is also observed in contrast to TiO_2. The XP spectra of Fig. 4.5(c, d, e and f) indicated the high-resolution O 1s, Ti 2p, Cs 3d and Br 3d for pristine and TiO_2-CsBr films. The binding energy (BE) O 1s peak at 529.43 eV is ascribed to the O^{2-} in the TiO_2 lattice and Ti-O band [45]. From Fig. 4.5(c), it is witnessed that the peak of O 1s slightly shifted toward a lower BE, 529.21 eV after doping with CsBr. The BE of Ti $2p_{3/2}$ and Ti $2p_{1/2}$ peaks presented at 456.35eV and 462.58 eV respectively, is assigned to Ti^{+4} state in TiO_2 [46]. Similarly, the Ti 2p peak slightly moved to lower BE from 456.35 to 456.14 eV and 462.58 to 462.24 eV after incorporating CsBr [47]. The shift of BE peaks implies the impact of CsBr in TiO_2 matrix. The lower valence state Cs cation might introduce electrons into neighbouring oxygen vacancies and finally partial conversion of Ti^{4+} to Ti^{3+} may take place within TiO_2. CsBr doping induced the shifting of 1s and 2p orbital levels of O and Ti peaks to lower BE, which implies the enhancement of free charge carrier density by generating oxygen vacancies.

UPS analysis

In order to describe the electronic band structure of TiO_2 and TiO_2-CsBr doped ELTs, UPS analysis is also performed. UPS study provides detailed insight of the band structure properties

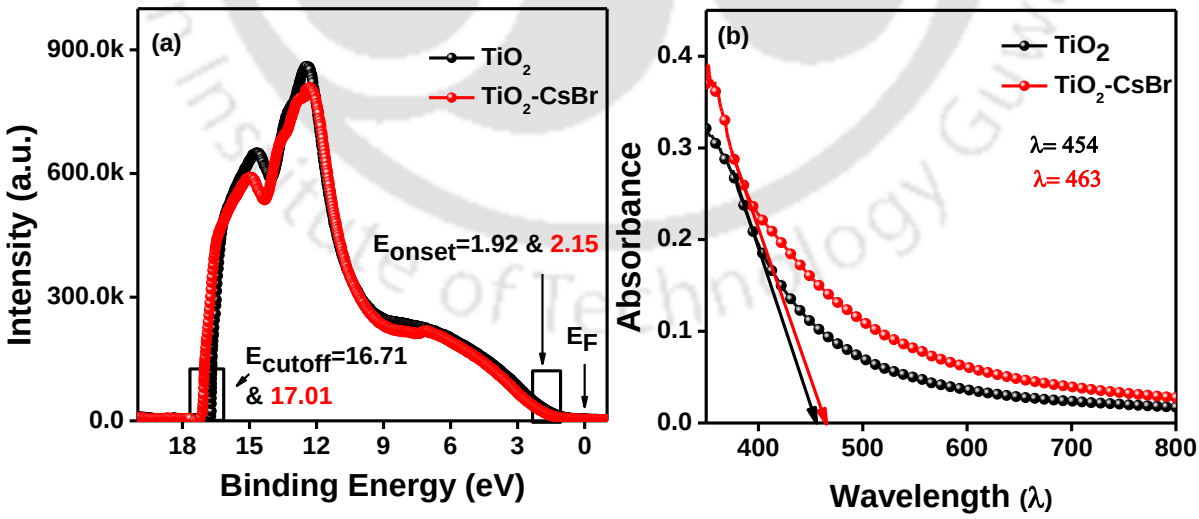

Figure 4. 6: (a) UP spectra and (b) absorption spectra of TiO_2 and TiO_2-CsBr doped films.

and directly measures work function. UPS analysis is conducted in an integrated ultrahigh vacuum system, and spectra were obtained with helium (He) I (hν = 21.2 eV) radiation. The

full scan of the UP spectra is depicted in Fig. 4.6(a). The position of the secondary electron onset (E_{onset}) is 1.92 eV, and 2.01 eV below the Fermi level and the cutoff (E_{cutoff}) point is fitted linearly to 16.71 eV, and 17.01 eV for TiO_2 and TiO_2-CsBr ETLs, respectively. The ETLs work functions (ϕ) are determined from the UPS secondary electron cut off (E_{cutoff}) by subtracting 21.22 eV i.e., $\phi = E_{cutoff} - 21.22$ versus (Vs) vacuum [48-50].

For TiO_2

$$E_{cutoff} = 16.71\ eV,\ E_{onset} = 1.92\ eV$$

$$\phi\ or\ E_{fermi} = E_{cutoff} - 21.22 = 16.71 - 21.22 = -4.51\ eV$$

$$E_{AV} = \phi - E_{Onset} = -4.51 - 1.92 = -6.43\ eV$$

$$E_g = 1240/\lambda = 1240/454 = 2.73\ eV$$

$$CBM = E_{AV} + E_G = -6.43 + 2.73 = -3.7\ eV$$

From UP spectrum, the position of the secondary electron onset is 1.92 eV below the Fermi level, and therefore the E_{VB} was calculated to be -6.43 eV versus vacuum. Considering the calculated optical bandgap of TiO_2~2.73 eV (Fig. 4.6(b)), the conduction band minimum (CBM) was calculated to be -3.7 eV versus vacuum.

Similarly, for TiO_2-CsBr (0.4 Wt.%) ETL

$$E_{cutoff} = 17.01\ eV,\ E_{onset} = 2.01\ eV$$

$$\phi\ or\ E_{fermi} = E_{cutoff} - 21.22 = 17.01 - 21.22 = -4.21\ eV$$

$$E_{AV} = \phi - E_{Onset} = -4.21 - 2.01 = -6.22\ eV$$

$$E_g = 1240/\lambda = 1240/463 = 2.67\ eV$$

$$CBM = E_{AV} + E_G = -6.22 + 2.67 = -3.55\ eV$$

$$E_g = 1240/\lambda = 1240/463 = 2.67\ eV$$

The results indicated the variation of work function (ϕ) and valence band maximum (E_{VB}) of TiO_2 ETL after doping with CsBr. In DSSCs, the work function (ϕ) of ETLs is particularly related to the band alignment of photoanode and redox potential of liquid electrolytes. The work function of TiO_2 drops from -4.51 to –4.21 eV after the addition of CsBr in TiO_2 matrix and the valence band maximum (E_{VB}) changed from -6.43 eV and -6.22 eV. The conduction band minimum (CBM) for TiO_2 and TiO_2-CsBr are calculated to be -3.7 eV and -3.55 eV

versus vacuum. The smaller (ϕ) and narrower CBM for TiO_2-CsBr ETL, gives better interfacial band alignment and higher built-in electric field. It provides an enhanced driving force for photogenerated charge and substantially reduced interface recombination, which are essential for producing improved V_{OC} and overall efficiency [36].

Surface morphology of mesoporous TiO_2 and TiO_2-CsBr ETLs

The photocatalytic properties of TiO_2 is closely related to their morphological characteristics such as particle size, pore structure and, specific surface area [51-52]. To evaluate the impact of CsBr doping on the mesoporous TiO_2 matrix, FESEM and AFM analysis is conducted. Fig. 4.7(a and b) presents the top view images of TiO_2 and TiO_2-CsBr ETLs that

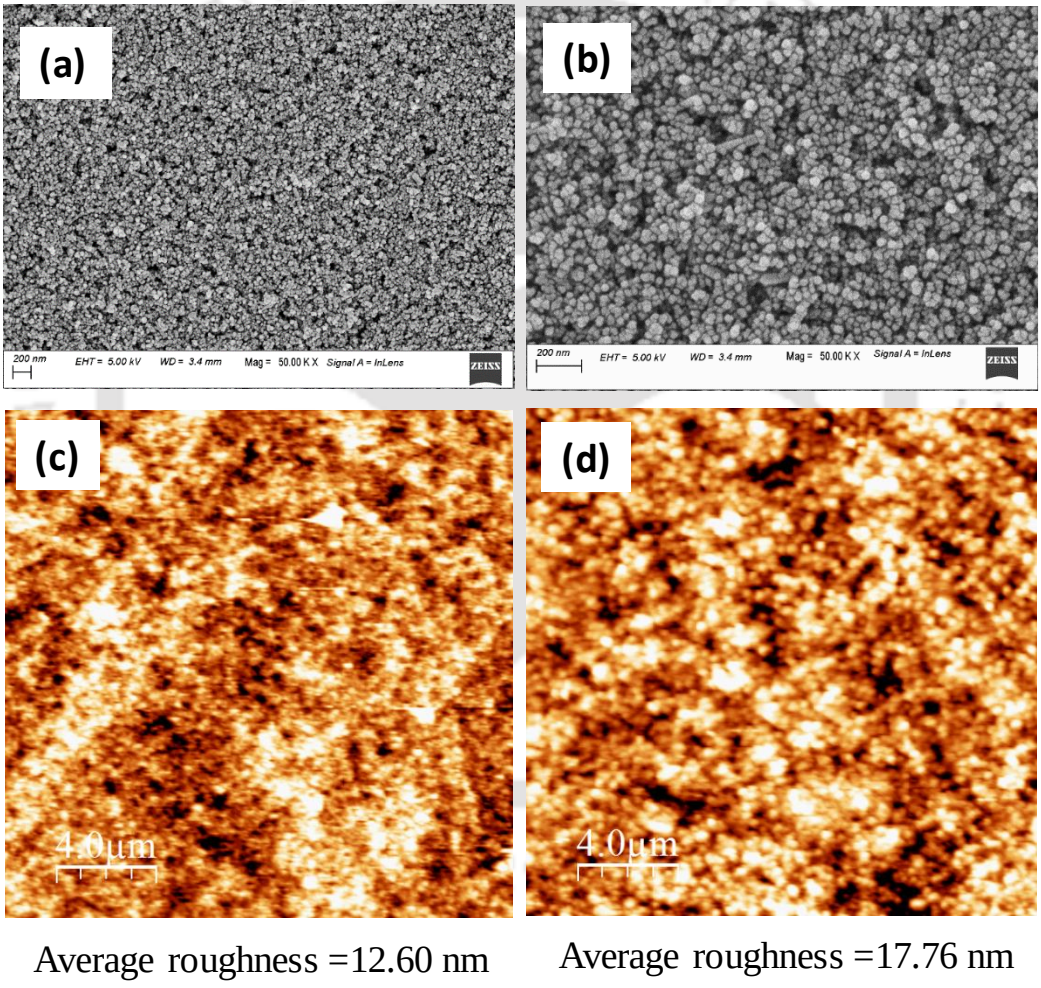

Figure 4. 7: FESEM image of (a) TiO_2 and (b) TiO_2-CsBr film, and corresponding 2D AFM image (c) TiO_2, (d) TiO_2-CsBr film.

described that the surface area of the coated films exhibited a porous structure with uniform grain-size distribution. A lower surface area is observed in the TiO_2 film comparing to TiO_2-

CsBr. The corresponding 2D AFM images are illustrated in Fig. 4.7(c and d). The average roughness factor for the TiO_2 and TiO_2-CsBr are found to be 12.60 and 17 nm, respectively, which confirmed that after doping, the surface roughness enhanced. The surface roughness of ETLs plays key role in charge carrier transport by increasing the contact area between ETL and dye molecules [51-54]. Here, FESEM and AFM results indicated that TiO_2-CsBr has a more surface area or surface roughness factor in comparison with the pristine TiO_2 film, which is essential for maximum loading of dye molecules, leading to an improvement in photocurrent of DSSCs [55-56].

Optical properties of TiO_2 and TiO_2-CsBr ETL

The changes in the absorption spectra before and after doping are also investigated using a UV–visible spectrometer. Fig. 4.8(a) illustrated the dye loaded absorption spectra of TiO_2 and TiO_2-CsBr doped photoanodes and their corresponding spectra depicted two metal to ligand charge transfer (MLCT) peaks at 530 nm and 391 nm [57]. According to the UV-visible absorption spectra of conventional TiO_2 and CsBr doped TiO_2 films, the spectral response from CsBr doped TiO_2 film had higher absorption intensity. To quantitatively determine the amount of adsorbed dye before and after doping, the dye loaded photoanode are desorbed using 0.1 M solution of NaOH in ethanol and H_2O (V: V= 1: 1) [58]. Photoanodes with an area of 0.5 x 1 cm^2 and thickness 9 µm films are soaked in 4 ml of solution to desorb the anchoring dye from

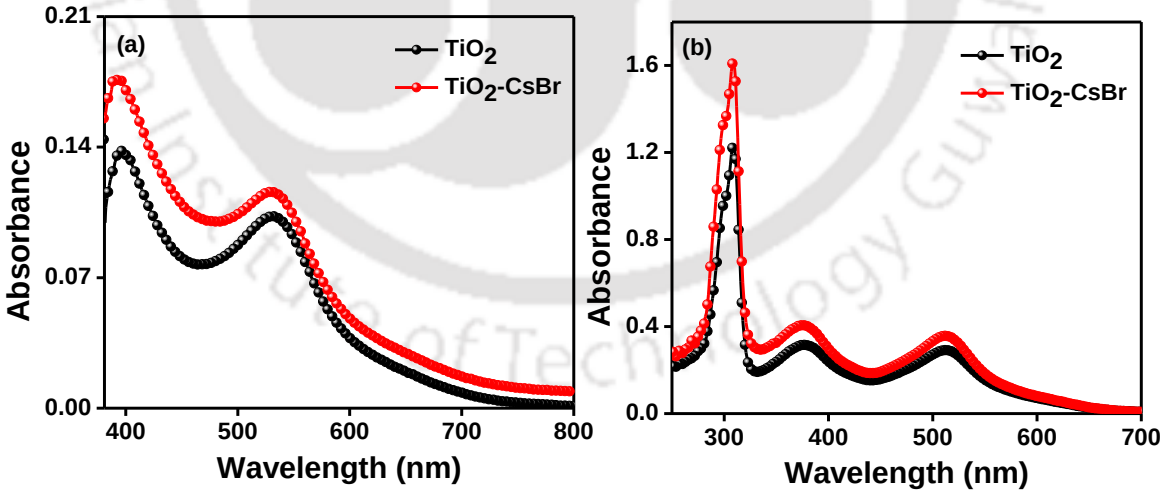

Figure 4. 8: Dye loaded absorption spectra of TiO_2 and CsBr-TiO_2 photoanodes, (a) Absorption spectra of N719 dye solutions desorbed from TiO_2 and CsBr-TiO_2 ETL film in 0.1 M NaOH solution in ethanol and DI water (V:V=1:1).

photoanodes. Corresponding spectra are recorded in Fig. 4.8(b) and found that the absorption intensity for TiO_2-CsBr doped photoanode is higher than the pristine TiO_2. The improvement

of absorption intensity for TiO_2-CsBr film is due to its relatively higher effective surface area. The quantitative valuation of the dye molecules on TiO_2 and TiO_2-CsBr surfaces are found to be $1.74 \times 10^{-7}\ M/cm^2$ and $2.69 \times 10^{-7}\ M/cm^2$, respectively. The enhancement in dye adsorption improves charge carrier injection and generates a higher current density for DSSCs [16][38][41]. Comparing the absorption peaks for photoanodes loaded with N719 dye and absorption spectra of N719 desorbed from photoanode showed blue shift. The blue shift absorption spectrum of photoanode is caused by less aggregation of dye molecules on electrode surface and better deprotonation [59].

Chemical composition and XRD patterns of TiO_2 and TiO_2-CsBr ETLs

In order to identify the chemical composition, EDX spectra of TiO_2 and TiO_2-CsBr doped mesoporous films are recorded and shown in Fig. 4.9. The elements present in the films are identified by EDX, and the corresponding atomic percentages are inset in Fig. 4.9(a and b). The amount of Br is small compared to Cs in TiO_2 matrix. The presence of carbon is not detected in the EDX spectra, proving that the carbon component is completely burned out during the annealing process.

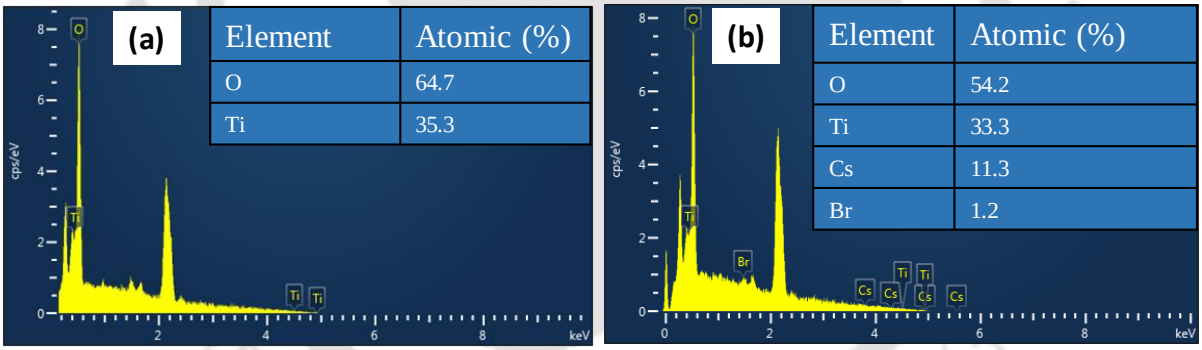

Figure 4. 9: EDX spectra with inset atomic percentage of (a) TiO_2 and (b) TiO_2-CsBr coated film on FTO surface.

Further, XRD analysis is also studied to understand the crystal structure of TiO_2 and TiO_2-CsBr films and their respective patterns are presented in Fig. 4.10. The patterns are recorded in the 2θ values ranging from 20° to 70° (5 degrees/min) using a high-resolution diffractometer with CuKα radiation (λ=1.54 Å). All samples exhibited a similar phase structure and it shows diffraction peaks of (101), (200), and (211) planes at Bragg angles of 25.35°, 48.06°, and 55°, respectively and are anatase phase [60]. The CsBr-TiO_2 film exhibited new peaks at 20.6°, 29.3°, 38°, and 47.02° compared to pristine TiO_2 film, and it confirmed the incorporation of

CsBr in titania matrix. These peaks are related to face center cubic (FCC) structure of CsBr to [hkl] Miller index [111], [110], [111], and [210] respectively [61].

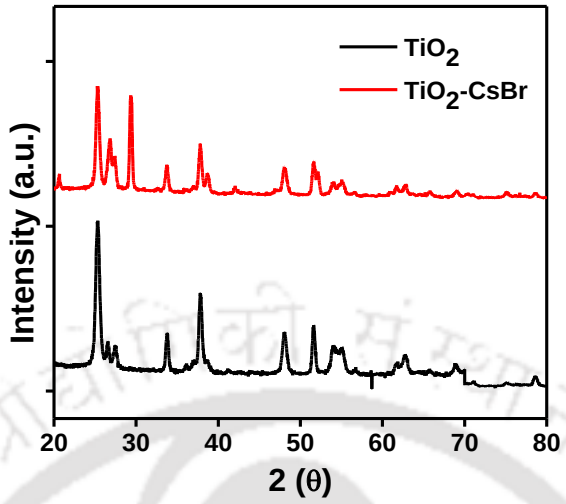

Figure 4. 10: XRD pattern of TiO_2 and TiO_2-CsBr films.

4.4 Conclusion

TiO_2-CsBr based ETL has been successfully developed and utilized as a photoanode material in DSSCs. TiO_2-CsBr photoanode enhanced the device performance up to 9.28% form 7.61% efficiency of pristine TiO_2. The significant enhancement in performance is attributed to a negative shift in flat band potential (V_{fb}) from -0.46 to -0.50 V, improved charge carrier density and increasing electron life in the modified devices. It was observed that CsBr doping triggered a fine tuning of work function from -4.51 to -4.21 eV and increased in CBM from -3.7 to -3. 55 eV. Thus, TiO_2-CsBr photoanode promoted favorable band alignment for TiO_2/N719 heterojunction, which enhanced electron injection and transport by suppressing the back transfer of photogenerated electrons. The surface morphology also indicated an enhanced in effective surface area for maximum dye loading that correspondingly increased the absorption coefficient. Increasing the doping concentration further reverses the device efficiency due to recombination process within the devices. The CsBr incorporation in TiO_2 presents a generic method to tailor the features of transport layers which is simple, effective and can be widely applied for next generation DSSCs and other optoelectronic devices.

4.5 References

[1] B. O'Regan, M. Grätzel, A low-cost, high-efficiency solar cell based on dye-sensitized colloidal TiO_2 films, Nature. 353 (1991) 737–740. doi:10.1038/353737a0.

[2] M. Grätzel, Highly Efficient Nanocrystalline Photovoltaic Devices, Platin. Met. Rev. 38 (1994) 151–159.

[3] M. Grätzel, Dye-sensitized solar cells, J. Photochem. Photobiol. C Photochem. Rev. 4 (2003) 145–153. doi:10.1016/s1389-5567(03)00026-1.

[4] M. Grätzel, Recent Advances ins sensitized Mesoscopic Solar Cells, Acc. Chem. Res. 42 (2009) 1788–1798. doi:10.1021/ar900141y.

[5] K. Kakiage, Y. Aoyama, T. Yano, K. Oya, J.I. Fujisawa, M. Hanaya, Highly-efficient dye-sensitized solar cells with collaborative sensitization by silyl-anchor and carboxy-anchor dyes, Chem. Commun. 51 (2015) 15894–15897. doi:10.1039/c5cc06759f.

[6] M. Ye, X. Wen, M. Wang, J. Iocozzia, N. Zhang, C. Lin, Z. Lin, Recent advances in dye-sensitized solar cells: From photoanodes, sensitizers and electrolytes to counter electrodes, Mater. Today. 18 (2015) 155–162. doi:10.1016/j.mattod.2014.09.001.

[7] X. Chen, S.S. Mao, Titanium dioxide nanomaterials: Synthesis, properties, modifications and applications, Chem. Rev. 107 (2007) 2891–2959. doi:10.1021/cr0500535.

[8] X. Yin, B. Wang, M. He, T. He, Facile synthesis of ZnO nanocrystals via a solid state reaction for high performance plastic dye-sensitized solar cells, Nano Res. 5 (2012) 1–10. doi:10.1007/s12274-011-0178-X.

[9] S.-Y.L. and J.-J.W. Geng-Jia Chang, Room-temperature chemical integration of ZnO nanoarchitectures on plastic substrates for flexible, Nanoscale. 6 (2014) 1329–1334. doi:10.1039/c3nr05267b.

[10] W. Chen, Y. Qiu, S. Yang, A new ZnO nanotetrapods/SnO_2 nanoparticles composite photoanode for high efficiency flexible dye-sensitized solar cells, Phys. Chem. Chem. Phys. 12 (2010) 9494–9501. doi:10.1039/c000584c.

[11] H. Tang, K. Prasad, R. Sanjinès, P.E. Schmid, F. Lévy, Electrical and optical properties of TiO 2 anatase thin films, J. Appl. Phys. 75 (1994) 2042–2047. doi:10.1063/1.356306.

[12] S. Thogiti, J.Y. Park, C.T. Thanh Thuy, D.K. Lee, B.K. Min, H.J. Yun, J.H. Kim, High-Performance Dye-Sensitized Solar Cells through Graded Electron Transport in Band-

Engineered W-TiO_2 Cascade Layer, ACS Sustain. Chem. Eng. 6 (2018) 13025–13034. doi:10.1021/acssuschemeng.8b02543.

[13] J. Liu, L. Zhu, S. Xiang, H. Wang, H. Liu, W. Li, H. Chen, Cs-Doped TiO_2 Nanorod Array Enhances Electron Injection and Transport in Carbon-Based CsPbI3 Perovskite Solar Cells, ACS Sustain. Chem. Eng. 7 (2019) 16927–16932. doi:10.1021/acssuschemeng.9b04772.

[14] W. Li, J. Yang, J. Zhang, S. Gao, Y. Luo, M. Liu, Improve photovoltaic performance of titanium dioxide nanorods based dye-sensitized solar cells by Ca-doping, Mater. Res. Bull. 57 (2014) 177–183. doi:10.1016/j.materresbull.2014.05.034.

[15] M. Nada, T. Gonda, Q. Shen, H. Shimada, T. Toyoda, N. Kobayashi, Electric characteristics of Li_2O-doped TiO_2 nanocrystalline film and its application to dye-sensitized solar cells, Jpn. J. Appl. Phys. 48 (2009) 2–6. doi:10.1143/JJAP.48.025505.

[16] M.A.K.L. Dissanayake, J.M.K.W. Kumari, G.K.R. Senadeera, C.A. Thotawatthage, B.E. Mellander, I. Albinsson, A novel multilayered photoelectrode with nitrogen doped TiO_2 for efficiency enhancement in dye sensitized solar cells, J. Photochem. Photobiol. A Chem. 349 (2017) 63–72. doi:10.1016/j.jphotochem.2017.08.067.

[17] J.C. Zhang, Z.Y. Han, Q.Y. Li, X.Y. Yang, Y. Yu, W.L. Cao, N, S-doped TiO_2 anode effect on performance of dye-sensitized solar cells, J. Phys. Chem. Solids. 72 (2011) 1239–1244. doi:10.1016/j.jpcs.2011.07.014.

[18] A. Subramanian, H.W. Wang, Effects of boron doping in TiO_2 nanotubes and the performance of dye-sensitized solar cells, Appl. Surf. Sci. 258 (2012) 6479–6484. doi:10.1016/j.apsusc.2012.03.064.

[19] H. Imahori, S. Hayashi, T. Umeyama, S. Eu, A. Oguro, S. Kang, Y. Matano, T. Shishido, S. Ngamsinlapasathian, S. Yoshikawa, Comparison of electrode structures and photovoltaic properties of porphyrin-sensitized solar cells with TiO_2 and Nb, Ge, Zr-added TiO_2 composite electrodes, Langmuir. 22 (2006) 11405–11411. doi:10.1021/la061527d.

[20] S.K. Pathak, A. Abate, P. Ruckdeschel, B. Roose, K.C. Gödel, Y. Vaynzof, A. Santhala, S.I. Watanabe, D.J. Hollman, N. Noel, A. Sepe, U. Wiesner, R. Friend, H.J. Snaith, U. Steiner, Performance and Stability Enhancement of Dye-Sensitized and Perovskite Solar Cells by Al Doping of TiO2, Adv. Funct. Mater. 24 (2014) 6046–6055. doi:10.1002/adfm.201401658.

[21] S.P. Berglund, S. Hoang, R.L. Minter, R.R. Fullon, C.B. Mullins, Investigation of 35 elements as single metal oxides, mixed metal oxides, or dopants for titanium dioxide for dye-sensitized solar cells, J. Phys. Chem. C. 117 (2013) 25248–25258. doi:10.1021/jp4073747.

[22] A. Latini, C. Cavallo, F.K. Aldibaja, D. Gozzi, D. Carta, A. Corrias, L. Lazzarini, G. Salviati, Efficiency improvement of DSSC photoanode by scandium doping of mesoporous titania beads, J. Phys. Chem. C. 117 (2013) 25276–25289. doi:10.1021/jp409813c.

[23] Z. Liu, Y. Li, C. Liu, J. Ya, E. Lei, W. Zhao, D. Zhao, L. An, TiO_2 photoanode structure with gradations in V concentration for dye-sensitized solar cells, ACS Appl. Mater. Interfaces. 3 (2011) 1721–1725. doi:10.1021/am200232g.

[24] R.T. Ako, P. Ekanayake, D.J. Young, J. Hobley, V. Chellappan, A.L. Tan, S. Gorelik, G.S. Subramanian, C.M. Lim, Evaluation of surface energy state distribution and bulk defect concentration in DSSC photoanodes based on Sn, Fe, and Cu doped TiO_2, Appl. Surf. Sci. 351 (2015) 950–961. doi:10.1016/j.apsusc.2015.06.015.

[25] D. Cahen, G. Hodes, M. Grätzel, J.F. Guillemoles, I. Riess, Nature of Photovoltaic Action in Dye-Sensitized Solar Cells, J. Phys. Chem. B. 104 (2000) 2053–2059. doi:10.1021/jp993187t.

[26] J. Zhang, W. Peng, Z. Chen, H. Chen, L. Han, Effect of cerium doping in the TiO_2 photoanode on the electron transport of dye-sensitized solar cells, J. Phys. Chem. C. 116 (2012) 19182–19190. doi:10.1021/jp3060735.

[27] Y. Duan, N. Fu, Q. Liu, Y. Fang, X. Zhou, J. Zhang, Y. Lin, Sn-doped TiO_2 photoanode for dye-sensitized solar cells, J. Phys. Chem. C. 116 (2012) 8888–8893. doi:10.1021/jp212517k.

[28] C. Zhang, S. Chen, L.E. Mo, Y. Huang, H. Tian, L. Hu, Z. Huo, S. Dai, F. Kong, X. Pan, Charge recombination and band-edge shift in the dye-sensitized Mg 2+-doped TiO_2 solar cells, J. Phys. Chem. C. 115 (2011) 16418–16424. doi:10.1021/jp2024318.

[29] A. Klasen, P. Baumli, Q. Sheng, E. Johannes, S.A. Bretschneider, I.M. Hermes, V.W. Bergmann, C. Gort, A. Axt, S.A.L. Weber, H. Kim, H.J. Butt, W. Tremel, R. Berger, Removal of Surface Oxygen Vacancies Increases Conductance Through TiO_2 Thin Films for Perovskite Solar Cells, J. Phys. Chem. C. 123 (2019) 13458–13466. doi:10.1021/acs.jpcc.9b02371.

[30] J. Tak Kim, S. Ho Kim, Surface modification of TiO_2 electrode by various over-layer coatings and O2 plasma treatment for dye sensitized solar cells, in: Sol. Energy Mater. Sol. Cells, Elsevier, 2011: pp. 336–339. doi:10.1016/j.solmat.2010.04.045.

[31] Y.-B.H. Won-Yeop Rho, Ho-Sub Kim, Woo-Jae Chung, Jung Sang Suh, Bong-Hyun Jun, Enhancement of power conversion efficiency with TiO_2 nanoparticles/nanotubes-siver nanopartices composites in dye-sensitized solar cels, Applied Surf. Sci. 429 (2018) 23–28.

[32] S. Iwamoto, Y. Sazanami, M. Inoue, T. Inoue, T. Hoshi, K. Shigaki, M. Kaneko, A. Maenosono, Fabrication of dye-sensitized solar cells with an open-circuit photovoltage of 1 V., ChemSusChem. 1 (2008) 401–403. doi:10.1002/cssc.200700163.

[33] K. Gelderman, L. Lee, S.W. Donne, Flat-band potential of a semiconductor: Using the Mott-Schottky equation, J. Chem. Educ. 84 (2007) 685–688. doi:10.1021/ed084p685.

[34] F. Fabregat-Santiago, G. Garcia-Belmonte, J. Bisquert, P. Bogdanoff, A. Zaban, Mott-Schottky Analysis of Nanoporous Semiconductor Electrodes in Dielectric State Deposited on SnO_2 (F) Conducting Substrates, J. Electrochem. Soc. 150 (2003) E293. doi:10.1149/1.1568741.

[35] M. Hossain, R.N. Arunagirinathan, R. Garai, R.K. Gupta, P.K. Iyer, Enhancing the efficiency and ambient stability of perovskite solar cells via multifunctional trap passivation molecule, J. Mater. Chem. C. 9 (2021) 14309–14317. doi:10.1039/d1tc03852d.

[36] T.R.C.K. Wijayarathna, G.M.L.P. Aponsu, Y.P.Y.P. Ariyasinghe, E.V.A. Premalal, G.K.R. Kumara, K. Tennakone, A high efficiency indoline-sensitized solar cell based on a nanocrystalline TiO_2 surface doped with copper, Nanotechnology. 19 (2008). doi:10.1088/0957-4484/19/48/485703.

[37] Y. Xie, N. Huang, S. You, Y. Liu, B. Sebo, L. Liang, X. Fang, W. Liu, S. Guo, X.Z. Zhao, Improved performance of dye-sensitized solar cells by trace amount Cr-doped TiO_2 photoelectrodes, J. Power Sources. 224 (2013) 168–173. doi:10.1016/j.jpowsour.2012.09.078.

[38] L. Wei, P. Wang, Y. Yang, Z. Zhan, Y. Dong, W. Song, R. Fan, Enhanced performance of the dye-sensitized solar cells by the introduction of graphene oxide into the TiO_2 photoanode, Inorg. Chem. Front. 5 (2018) 54–62. doi:10.1039/c7qi00503b.

[39] S. Suresh, T.G. Deepak, C. Ni, C.N.O. Sreekala, M. Satyanarayana, A.S. Nair, V.P.P.M. Pillai, The role of crystallinity of the Nb_2O_5 blocking layer on the performance of dye-sensitized solar cells, New J. Chem. 40 (2016) 6228–6237. doi:10.1039/c6nj01133k.

[40] A. Merazga, F. Al-Subia, A. M. Albaradi, A. Badawi, A. Y. Jaber, A. A. B. Alghamdi, Effect of sol–gel MgO spin-coating on the performance of TiO_2-based dye-sensitized solar cells, Mater. Sci. Semicond. Process. 41 (2016) 114–120.

[41] J. Xu, G. Wang, J. Fan, B. Liu, S. Cao, J. Yu, g-C3N4 modified TiO_2 nanosheets with enhanced photoelectric conversion efficiency in dye-sensitized solar cells, J. Power Sources. 274 (2015) 77–84.

[42] Q. Wang, J-E. Moser, M. Grätzel, Electrochemical Impedance Spectroscopic Analysis of Sensitization-Based Solar Cells, J. Phys. Chem. B. 109 (2005) 14945–14953. doi:10.1002/ijch.201500007.

[43] J. Bisquert, Theory of the impedance of electron diffusion and recombination in a thin layer, J. Phys. Chem. B. 106 (2002) 325–333. doi:10.1021/jp011941g.

[44] T. Hoshikawa, M. Yamada, R. Kikuchi, K. Eguchi, Impedance Analysis of Internal Resistance Affecting the Photoelectrochemical Performance of Dye-Sensitized Solar Cells, J. Electrochem. Soc. 152 (2005) E68–E73. doi:10.1149/1.1849776.

[45] C. Rama Krishna, S. Raj, Y.T. Yu, Synthesis and electrophoretic deposition of hollow-TiO_2 nanoparticles for dye sensitized solar cell applications, J. Alloys Compd. 672 (2016) 212–222. doi:10.1016/j.jallcom.2016.02.164.

[46] P. Zhong, X. Ma, X. Chen, R. Zhong, X. Liu, D. Ma, M. Zhang, Z. Li, Morphology-controllable polycrystalline TiO_2 nanorod arrays for efficient charge collection in dye-sensitized solar cells, Nano Energy. 16 (2015) 99–111. doi:10.1016/j.nanoen.2015.06.007.

[47] J.Y. Seo, R. Uchida, H.S. Kim, Y. Saygili, J. Luo, C. Moore, J. Kerrod, A. Wagstaff, M. Eklund, R. McIntyre, N. Pellet, S.M. Zakeeruddin, A. Hagfeldt, M. Grätzel, Boosting the Efficiency of Perovskite Solar Cells with CsBr-Modified Mesoporous TiO_2 Beads as Electron-Selective Contact, Adv. Funct. Mater. 28 (2018) 1–7. doi:10.1002/adfm.201705763.

[48] C. Maheu, L. Cardenas, E. Puzenat, P. Afanasiev, C. Geantet, UPS and UV spectroscopies combined to position the energy levels of TiO_2 anatase and rutile nanopowders, Phys. Chem. Chem. Phys. 20 (2018) 25629–25637. doi:10.1039/c8cp04614j.

[49] A. Klein, C. Körber, A. Wachau, F. Säuberlich, Y. Gassenbauer, R. Schafranek, S.P. Harvey, T.O. Mason, Surface potentials of magnetron sputtered transparent conducting oxides, Thin Solid Films. 518 (2009) 1197–1203. doi:10.1016/j.tsf.2009.05.057.

[50] W. Zhu,* Z. Zhang, W. Chai, Q. Zhang, D. Chen, Z. Lin, J. Chang, J. Zhang, C. Zhang,Y. Hao Band alignment engineering towards 10.71%-efficiency carbon-based, all-inorganic planar $CsPbIBr_2$ perovskite solar cells, ChemSusChem. 12 (2019) 2318.

[51] A. Tricoli, A.S. Wallerand, M. Righettoni, Highly porous TiO_2 films for dye sensitized solar cells, J. Mater. Chem. 22 (2012) 14254–14261. doi:10.1039/c2jm15953h.

[52] X. Li, J. Yu, M. Jaroniec, Hierarchical photocatalysts, Chem. Soc. Rev. 45 (2016) 2603–2636. doi:10.1039/c5cs00838g.

[53] D. Chen, F. Huang, Y.B. Cheng, R.A. Caruso, Mesoporous anatase TiO_2 beads with high surface areas and controllable pore sizes: A superior candidate for high-performance dye-sensitized solar cells, Adv. Mater. 21 (2009) 2206–2210. doi:10.1002/adma.200802603.

[54] T. Rajaramana, G.R.A.Kumara, D. Velauthapillai, P. Ravirajan, M. Senthilnanthanan, Ni/N co-doped P25 TiO_2 photoelectrodes for efficient Dye-Sensitized Solar Cells, Mater. Sci. Semicond. Process. 135 (2021) 106062.

[55] R. Liu, W. Yang, L. Qiang, Enhanced efficiency for dye-sensitized solar cells using a surface-treated, J. Power Sources. 199 (2012) 418–425. doi:10.1016/j.jpowsour.2011.10.072.

[56] H. Xu, X. Tao, D.T. Wang, Y.Z. Zheng, J.F. Chen, Enhanced efficiency in dye-sensitized solar cells based on TiO_2 nanocrystal/nanotube double-layered films, Electrochim. Acta. 55 (2010) 2280–2285. doi:10.1016/j.electacta.2009.11.067.

[57] P. Wen, Y. Han, W. Zhao, Influence of TiO_2 nanocrystals fabricating dye-sensitized solar cell on the absorption spectra of N719 sensitizer, Int. J. Photoenergy. 2012 (2012) 1–8. doi:10.1155/2012/906198.

[58] E. Dell'Orto, L. Raimondo, A. Sassella, A. Abbotto, Dye-sensitized solar cells: Spectroscopic evaluation of dye loading on TiO_2, J. Mater. Chem. 22 (2012) 11364–11369. doi:10.1039/c2jm30481c.

[59] M. Adil Afroz, K.K. Sonigara, T. Bhim Raju, S.S. Soni, P. Krishnan Iyer, Effect of fluorine substitution and position on phenylene spacer in carbazole based organic sensitizers for dye sensitized solar cells, Phys. Chem. Chem. Phys. 19 (2017) 28579–28587. doi:10.1039/C7CP05226J.

[60] S. Saekow, W. Maiakgree, W. Jarernboon, S. Pimanpang, V. Amornkitbamrung, High intensity UV radiation ozone treatment of nanocrystalline TiO_2 layers for high efficiency of

dye-sensitized solar cells, J. Non. Cryst. Solids. 358 (2012) 2496–2500. doi:10.1016/j.jnoncrysol.2012.01.050.

[61] M.O. Farea, A.M. Abdelghany, M.S. Meikhail, A.H. Oraby, Effect of cesium bromide on the structural, optical, thermal and electrical properties of polyvinyl alcohol and polyethylene oxide, J. Mater. Res. Technol. 9 (2020) 1530–1538. doi:10.1016/j.jmrt.2019.11.078.

High performance PANI-PSSNa doped counter electrode for dye-sensitized solar cells

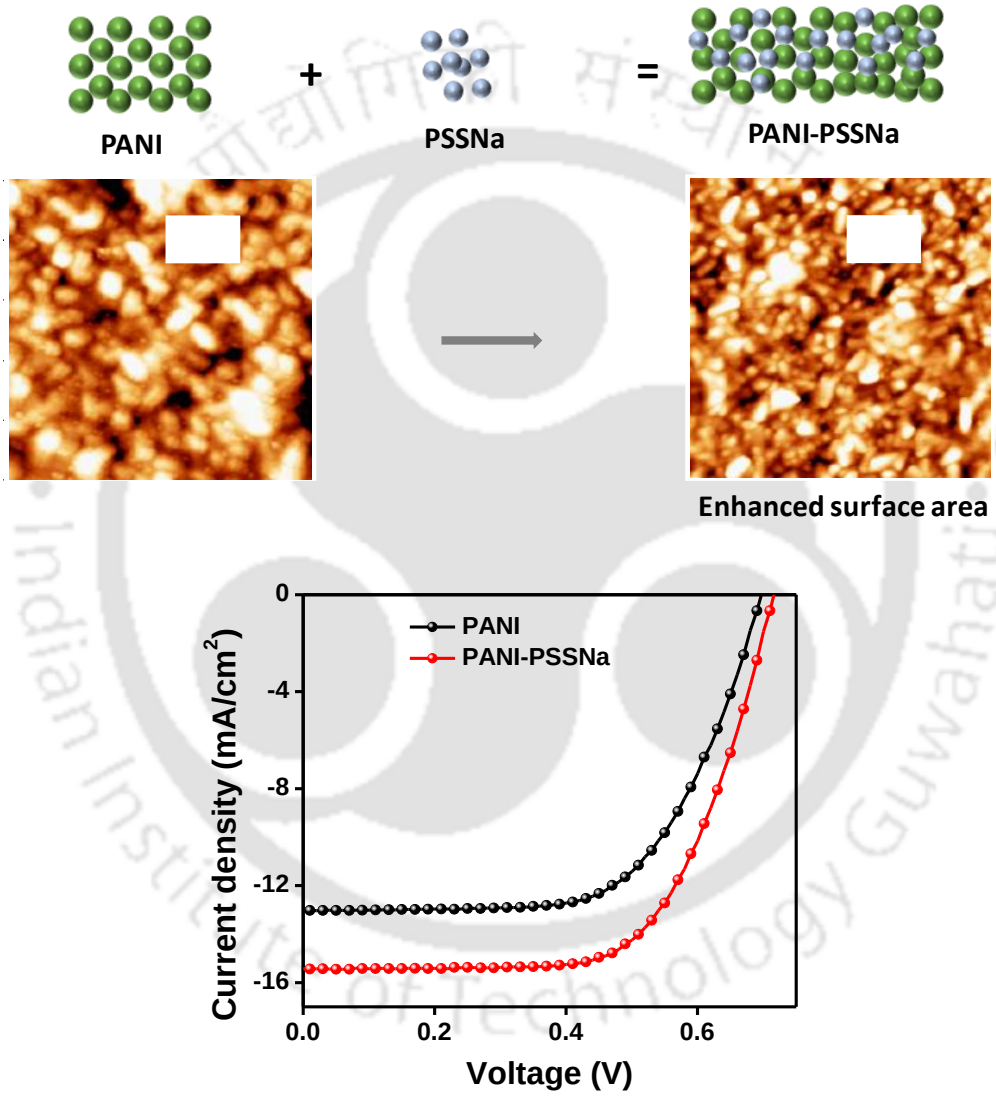

Chandan Dawo and Harsh Chaturvedi, Appl. Phys. A, Volume 128, 640, 2022. https://doi.org/10.1007/s00339-022-05739-*y*

5.1 Introduction

The essential requirement for high-performance DSSCs is that CEs with high electrocatalytic properties i.e. transfer electrons to reduce I_3^- species from the liquid electrolyte rapidly. Platinum (Pt).is the best choice for CE as a catalyst to accelerates the rate of I_3^- reduction. Although Pt has these characteristics, as a rare noble metal, it is expensive and costs over 40% of the solar cell regardless of its preparation process [1-2]. Therefore, an alternative approach has been focused on developing low-cost and high-performance materials for CEs. Fortunately, conducting polymer can produce high catalytic activity with low-cost CEs. Many inexpensive conducting polymer such as polypyrrole (PPy) [3-4], poly (3,4-ethylenedioxythiophene) (PEDOT) [5-7], and polyaniline (PANI) [8] etc. has been explored as an alternative to Pt CE. PANI is one of the most intensively studied polymers among the conducting polymer due to its easy preparation at low cost, high conductivity, excellent environment stability, and I_3^- reduction properties [9]. The unique properties of PANI is that, from insulating emeraldine base (EB) to conducting emeraldine salt (ES), its conductivity states can be controlled by charge transfer doping and protonation. There were various reports based on PANI doped with an acid such as H_2SO_4 [10], benzene sulphonic acid and HCl [11], camphor sulfonic acid [12-13], silver [14] and carbon-based materials [15-16]. In m-cresol, the solubility of PANI is good, which permits more electron transport by execution as a secondary dopant and inspires a change in the molecular structure of PANI. PANI doped with camphor sulfonic enhance electrical properties and surface roughness [17].

Herein, inspired by the unique properties of PANI, an attempt has been made to utilize PANI and PANI-PSSNa doped as efficient CEs for DSSCs. Prepared PANI and PANI-PSSNa in m-cresol by spin-coating on FTO glass with different percent, and their effect are investigated systematically for DSSCs performance. The fabricated device based on PANI-PSSNa doped CEs demonstrates high electrocatalytic activity, low electron transfers resistance, and better performance. The PANI based CEs are not only inexpensive it also does not involve any high-temperature annealing process. These CEs can be fabricated easily using simple coating and printing techniques for large-scale production. The electrochemical properties of CEs are investigated with the help of CV, Tafel plot, and impedance spectroscopy. The surface morphology and composition of PANI and PANI-PSSNa composite, spin-coated on FTO glass are studied by Field emission scanning electron microscope (FESEM), atomic force microscope (AFM) and Fourier transforms infrared (FTIR).

5.2 Experimental section

Chemicals and Materials. All chemicals and materials were purchased from different commercial sources for the experiments and used as received. Transparent fluorine-doped tin oxide (FTO) glass-7 Ω/square (Sigma- Aldrich) was used as a substrate for both electrodes. TiO_2 powder (Sigma-Aldrich, 22 nm) was used as working electrode, N719 dye (Sigma-Aldrich), tert-butanol (Sigma- Aldrich), lithium iodide (Sigma-Aldrich), acetonitrile (Sigma-Aldrich), absolute ethanol, iodine (Himedia), lithium perchlorate ($LiClO_4$, Sigma-Aldrich), 1-butyl-3-methylimidazolium iodide (Sigma-Aldrich), 4-tert butylpyridine (Sigma-Aldrich), guanidium thiocyanate (Sigma-Aldrich), valeronitrile (Sigma-Aldrich), Poly (sodium 4-styrenesulphonate) (MW=70000, Sigma-Aldrich), Anhydrous isopropanol (Sigma-Aldrich), PANI powder (MW =15000, Sigma-Aldrich) and Chloroplatinic acid hexahydrate ($H_2PtCl_6.6H_2O$, Sigma-Aldrich).

Preparation of PANI-PSSNa CEs

PANI was dispersed in m-cresol at different weight percent (1, 2, and 3 Wt.%), and the prepared solutions were ultrasonicated for 6 hours to mix thoroughly. Then spin-coated on FTO substrate as a catalyst for CE and fabricated DSSCs. After the optimized Wt.% of PANI in m-cresol, the solution is mixed with desired percent (5, 10, and 15%) of PSSNa to form PANI-PSSNa composite. Again, the varied solutions are ultrasonicated for 4 hours to dissolve PANI-PSSNa completely in m-cresol. The undoped and doped CEs are fabricated by depositing directly on clean FTO glass substrates for 55 secs at 1500 rpm. Then the CEs are kept on a hot plate for drying at 150 °C for 30 min to remove the m-cresol solvent. Fig. 5.1 shown the schematic diagram of preparing PANI-PSSNa counter electrode.

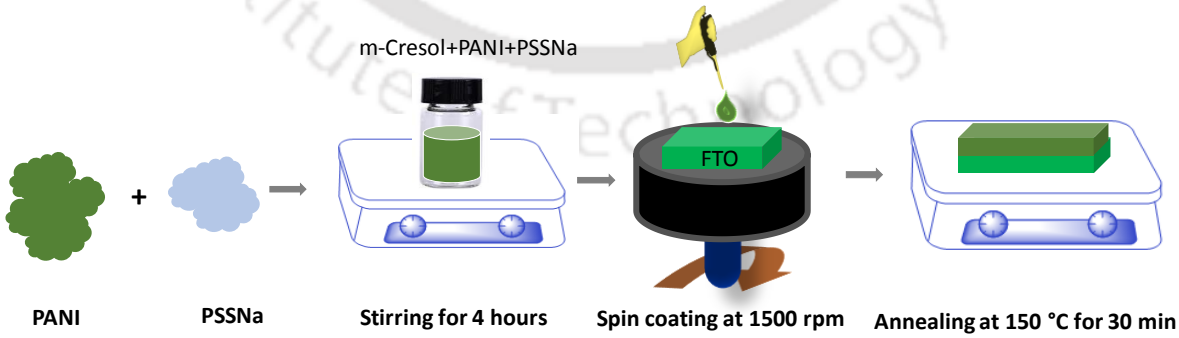

Figure 5. 1 Schematic illustration of the preparation of PANI-PSSNa counter electrodes.

Preparation of TiO_2 Working Electrode

At first FTO glass was cleaned with detergent solution in an ultra-sonicate bath for 15 min followed by sonication in Mili-Q water, acetone, and 2-propanol, respectively. Then the substrates were dried by using a hot air dryer. After that, UV-O_3 treatment was performed for 15 min to clean organic contaminants. The TiO_2 paste consists of 600 mg P25 powder, 5 mL ethanol, 100 µL acetic acid 500 µL milli-Q water, 3 gm trpineol and 3 gm ethyl cellulose (15 Wt.% in ethanol). The mixture was stirred overnight and spin coated at 5000 rpm for 45 second on the clean substrate. After drying the first layer at 100 $^{\circ}$C for 10 min, the second layer was applied by doctor blade technique using Sigma paste and baked at 100 $^{\circ}$C for 20 min. Then, it was calcined at 450 $^{\circ}$C for 30 min after which the surface of TiO_2 ETLs was treated in a UV-O_3 system for 10 min time.

Device fabrication and testing

Working electrodes are submerged for 1 day into 0.3 mM N719 in acetonitrile and tert-butyl alcohol solution at a volumetric ratio of 1:1 to sensitize it in dark conditions. The I^-/I_3^- electrolyte solution of is made of 0.05 M I_2, 0.5 M LiI, 0.1 M guanidium thiocyanate, 0.5 M 4-tert-butylpyridine and 0.5 M 1-butyl- 3-methylimidazolium iodide are dissolved in the mixture of acetonitrile/valeronitrile (V:V = 17:3) solvents. Sensitized TiO_2 working electrode and CEs (PANI and PANI-PSSNa) are sealed by Surlyn film (60 µm, Ossila), a hot melt spacer pressed at 80 °C to fabricate sandwich-type solar cells. Liquid electrolyte is injected into the hole between working and CE to complete the fabrication process. The photovoltaic performance of DSSCs are performed with a Keithley 2400 source meter from -1 to 1 V in a step of 10 mV. The current density-photovoltage (J-V) characteristics curves of DSSCs are measured at irradiation of 100 mW/cm^2 (AM 1.5 G), a solar light simulator with 450 Watt xenon arc lamp (Newport, Oriel Sol 3A). The active area of DSSCs are 0.25 cm^2. A set of 10 devices were prepared to confirm the reproducibility of the experiment.

5.3 Results and discussion

Cyclic voltammetry

To utilize PANI and PANI-PSSNa as a catalyst in CEs for DSSCs, it is necessary to compare and verify their catalytic activity with the standard platinum (Pt) counter electrode. Regarding this, cyclic voltammetry (CV) was performed for the respective catalytic film in 50 ml of acetonitrile solution containing 66.92 mg of LiI, 531.95 mg of $LiClO_4$, and 12.69 mg of I_2. Fig 5.2(a) shows the CV curves of PANI, PANI-PSSNa and Pt CEs in the range from –0.6 V to 1V

at the scan rate of 100 mV/sec. The oxidation reaction in equation (Eq.) (5.1) and the reduction reaction in equation (5.2) give the positive and negative potential in the CV curve, respectively.

$$I_3^- + 2e^- \leftrightarrow 3I^- \qquad 5.1$$

$$3I_2 + 2e^- \leftrightarrow 2I_3^- \qquad 5.2$$

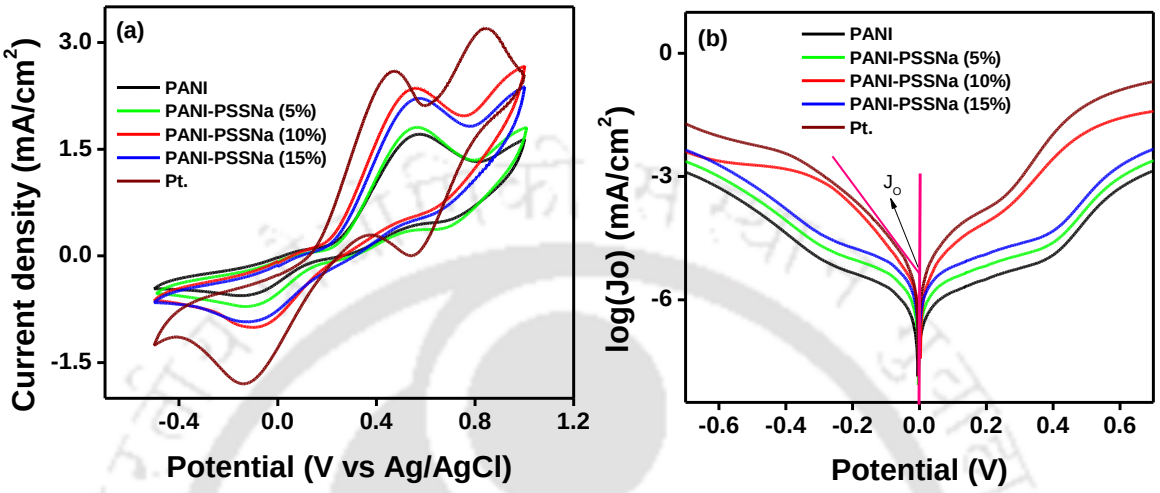

Figure 5. 2: Cyclic voltemetry measurement in three electrodes system with 50 ml of acetonitrile solution containing 66.92 mg of LiI, 531.95 mg of $LiClO_4$, and 12.69 mg of I_2 and (b) Corresponding Tafel plot of DSSCs based on PANI, PANI-PSSNa and Pt counter electrodes.

Table 5. 1: Electrochemical properties of PANI, PANI-PSSNa and Pt.

Counter electrodes	**I_{CP} (mA/cm2)**	**I_{AP} (mA/cm2)**	**E_{CP} (V)**	**E_{AP} (V)**	**ΔE_{pp} (V)**
PANI	-0.55	1.69	-0.12	0.57	0.69
PANI-PSSNa (5%)	-0.70	1.81	-0.10	0.54	0.64
PANI-PSSNa (10%)	-0.97	2.33	-0.05	0.53	0.58
PANI-PSSNa (15%)	-0.90	2.24	-0.07	0.54	0.61
Pt	-1.80	2.56	-0.11	0.45	0.56

The parameters of CV such as cathodic peak current density (I_{CP}), anodic peak current density (I_{AP}), cathodic peak voltage (E_{CP}), anodic peak voltage (E_{AP}) and ΔE_{pp} of each sample are summarized in Table 5.1. CEs catalytic ability is illustrated by two important parameters: peak current density (I_P) and peak-to-peak separation (ΔE_{pp}). The ΔE_{pp} is calculated from Eq. (5.3).

$$\Delta E_{pp} = \left|E_p(anodic) - E_p(cathodic)\right| \qquad 5.3$$

In DSSCs, to regenerate the dye molecules and complete the circuit conductivity, the reduction of I_3^- will take place in CE. So, studying the reduction of I_3^- at the negative potential side is crucial which represent I_{CP} in the CV above. PANI shows a I_{CP} of -0.55 mA/cm^2, whereas PANI-PSSNa (10%) has -0.97 mA/cm^2. At the same time, peak-to-peak voltage separation for the PANI film is 0.69 V compared to 0.58 V for the PANI-PSSNa (10%). Fast reaction rate in CV generate higher I_{CP} and smaller absolute value of ΔE_{pp}, that reflects a better catalytic activity of CE [18-19]. Therefore, the PANI-PSSNa film exhibited better capability for the reduction of I_3^- than PANI. Moreover, the $\Delta E_{pp}$of PANI-PSSNa (10%) and Pt electrode is 0.58 V and 0.56 V, which is almost equivalent to Pt electrode and it can be an alternative materials of expensive Pt CE in DSSCs.

Tafel plot

In order to reconfirm the catalytic activities and the charge transfer characteristic of the catalytic films, Tafel polarization measurement is performed with DSSCs based on PANI, PANI-PSSNa and Pt CEs. Fig. 5.2(b) demonstrate the plots of logarithmic current density (J_o) versus applied potential (V) at ambient temperature. Tafel characteristic curve can be separated into three parts; the curve in the middle region at very low voltage (|V| > 0.01 V) with a steeper slope signifies the Tafel zone which exactly determines the electro catalytic activity of the electrode, at low voltage (|V| ≤ 0.12 V) describes the polarization zone, and at very high voltage (|V| > 0.4 V) indicates the diffusion zone which represent the diffusion coefficient of I_3^-/I_- in DSSCs. The exchange current density (J_o) is calculated from the intercept of the linear fitting lines from the cathodic or anodic branches and their respective slope are in the order of Pt= -7.99 > PANI-PSSNa (10%)= -7.05 > PANI-PSSNa (15%)= -5.12 > PANI-PSSNa (5%)= -4.58 > and PANI = -4.50. In Tafel zone, the cathodic branch shows a sharper slope for PANI-PSSNa than PANI electrodes. Correspondingly PANI-PSSNa produced higher J_O that suggests greater conductivity which is a key factor for high catalytic activity. This indicates that PANI-PSSNa electrode has greater electrocatalytic activity than PANI for reducing $I_3^-/I^-$and has a great potential to act as CE for DSSCs. Theoretically, J_o can also be evaluated using the following Eq. (5.4).

$$J_o = \frac{RT}{nFR_{CT}} \qquad 5.4$$

where R is the gas constant, R_{CT} is the charge transfer resistance, n (= 2) is the number of electrons in the electrolytes for reduction of I_3^-/I^-, T is the absolute temperature, and F is the Faraday's constant [14, 20-21].

Electrochemical impedance spectroscopy (EIS) analysis

The kinetics and energetics of electron transport and recombination in DSSCs have been explored using powerful electrochemical impedance spectroscopy (EIS). EIS measurement is performed with DSSCs based on PANI, PANI-PSSNa and Pt CEs, similar to the one used in

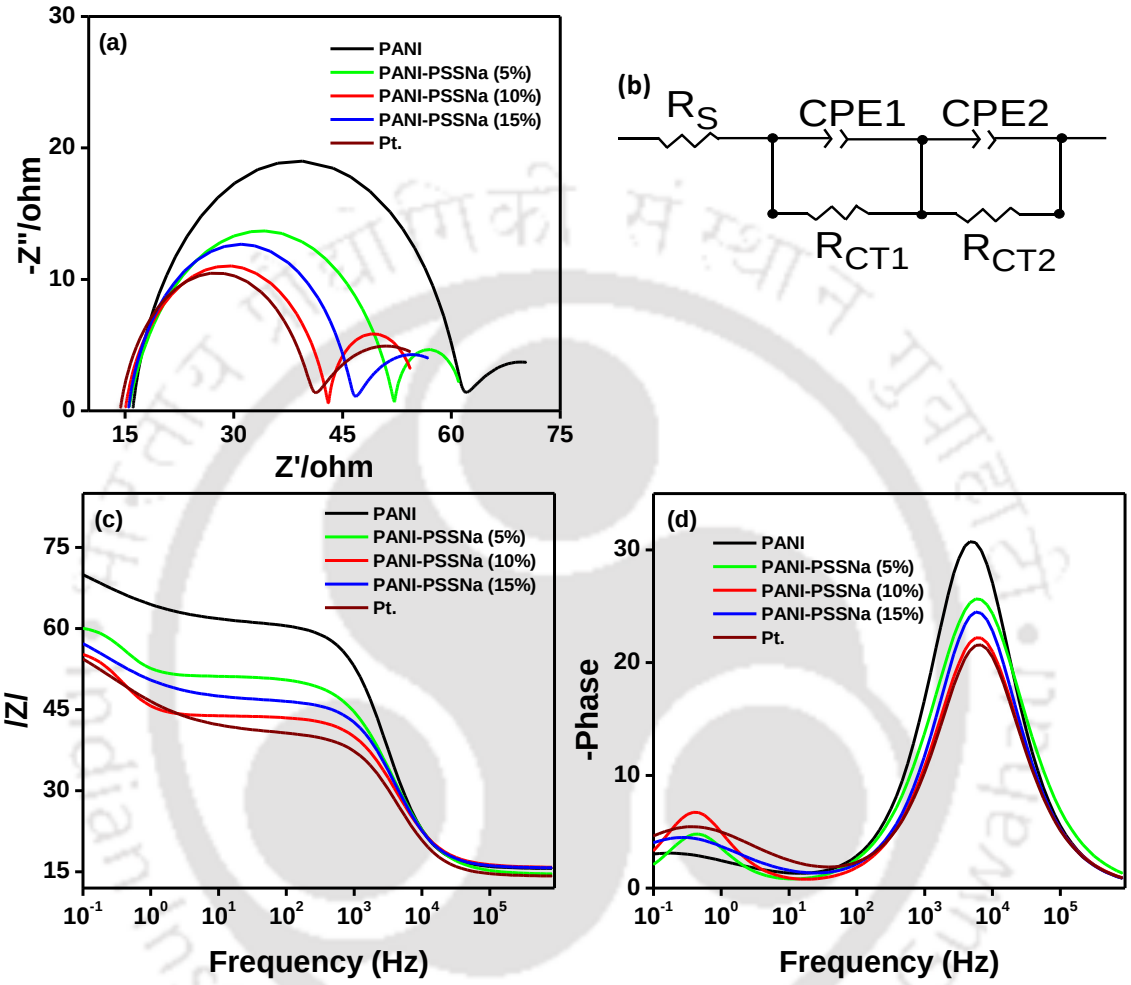

Figure 5. 3: (a) Typical Nyquist plot, corresponding (b) Equivalent circuit of Nyquist plot (c) Bode magnitude, and (d) Phase plot of DSSCs based on PANI, PANI-PSSNa with different conc. and Pt CEs.

Tafel polarization. EIS results are illustrated in the form of Nyquist plots to elucidate the role of CEs on photovoltaic performance. The complex Nyquist plot Fig. 5.3(a) has a semicircle, which presents the properties and quality of DSSCs. Then the Nyquist spectra are fitted in EC Lab software to obtained equivalent circuit and their values are summarized in Table 5.2. The corresponding fitted equivalent circuit of the plot is shown in Fig. 5.3(b), containing series resistance (R_S), representing the total sheet resistance of conducting substrates, charge-transfer resistance (R_{CT}), and constant phase element (CPE). The R_{CT} related to the heterogeneous electron exchange during I_3^-/I^- redox couple at the electrolyte/CE interface [22-26]. The

PANI-PSSNa CEs shows a lower R_S of 14 $\pm$1.2 Ω than PANI CE of 16.50 Ω. According to the above photovoltaic performance, decreasing Rs is beneficial in accelerating high electron transfer, leading to improved J_{SC} and FF. In the high frequency region, the 'R_{CT1} and CPE1′ gives first EIS semicircle, which represented the impedance at photoanode/electrolyte interface. The EIS pattern of PANI, PANI-PSSNa and Pt CEs are almost same except semicircle size, indicating similar electrocatalytic activity toward I_3^-/I^- redox electrolytes but at different reaction rate. The second semicircle due to R_{CT2} and CPE2 represent charge transfer resistance at electrolyte/CE interface. The R_{CT} values obtained in the Table 5.2 are in the order of Pt < PANI-PSSNa < PANI. Thus, a counter electrode with reduced R_{CT} experience small overpotential for an electron moving from CE to the electrolyte. The EIS results can also be interpreted with the Tafel results (Eq. 5. 4), where Jo is inversely proportional to R_{CT}. A decreased in R_{CT} indicates fast electron transfer, while larger R_{CT} hinder sluggish electron movement. The total impedance $z(\omega)$ of the equivalent circuit can be expressed as

$$z(\omega) = R_S + \frac{R_{CT1}}{1+(\omega R_{CT1} CPE1)^2} - j\frac{\omega R_{CT1}^2 CPE1}{1+(\omega R_{CT1} CPE1)^2} + \frac{R_{CT2}}{1+(\omega R_{CT2} CPE2)^2} - j\frac{\omega R_{CT2}^2 CPE2}{1+(\omega R_{CT2} CPE2)^2} \qquad 5.5$$

The real and imaginary parts of the impedance are $R_S + \frac{R_{CT1}}{1+(\omega R_{CT1} CPE1)^2} + \frac{R_{CT2}}{1+(\omega R_{CT2} CPE2)^2}$ and $-\frac{\omega R_{CT1}^2 CPE1}{1+(\omega R_{CT1} CPE1)^2} - \frac{\omega R_{CT2}^2 CPE2}{1+(\omega R_{CT2} CPE2)^2}$ respectively. When $\omega \to \infty$, the capacitive impedance is very low, it eventually shunts the R_{CT}. Therefore, only ohmic resistance R_S is present at high-frequency intercept. As frequency starts decreasing, the capacitive impedance increases. The Bode magnitude and phage complex plots are depicted in Fig. 5.3(c and d). The Bode magnitude /Z/ is inversely proportional to frequency whereas in phage plot, phage increases with increasing characteristic frequency (f_{max}) and can be used to determine the interface electron lifetime (τ). The τ can be obtained using the following relation [27-28].

$$\tau = \frac{1}{2f_{max}} \qquad 5.6$$

Where f_{max} is the maximum frequency obtained from bode plot. The f_{max} for PANI and PANI-PSSNa (10%) counter electrodes were 5000 Hz and 6273 HZ, respectively. From equation (5.6) we can relate that f_{max} is inversely proportional to τ. It is also observed from phase angle plot that at maximum frequency (f_{max}), phase decreases with decreasing value of R_{CT}. The calculated τ for PANI and PANI-PSSNa (10%) are 0.318 µsec and 0.253 µsec respectively. A lower τ indicates a faster reduction of I_3^-, that might increases the photoelectric conversion kinetics. The overall EIS analysis specifies a substantial reduction in charge transfer

resistance, recombination rate, higher electrocatalytic activity, and decreased interface electrons lifetime (τ) for PANI-PSSNa CEs. After performing a comprehensive analysis of the CV, Tafel and EIS results, we can conclude that the catalytic activity is in the order of Pt > PANI-PSSNa > PANI.

Table 5. 2: Parameter of EIS equivalent circuit.

Counter electrodes	R_S (Ω)	R_{ct1}(Ω)	CPE1(F)	R_{ct2}(Ω)	CPE2(μF)
PANI	16.01	18.17	0.069	45.13	4.43
PANI-PSSNA (5%)	15.57	16.28	0.057	34.12	5.29
PANI-PSSNa (10%)	15.20	15.38	0.048	30.94	5.71
PANI-PSSNa (15%)	15.10	13.34	0.036	27.94	7.36
Pt	14.43	12.34	0.032	26.55	7.55

J-V characteristics of DSSCs

The device's performance with various concentration (conc.) of m-cresol in PANI is shown in Fig. 5.4 and their parameters are summarized in Table 5.3. The device with optimized Wt.% of m-cresol in PANI is then doped with various concentrations (5, 10, and 15%) of PSSNa. Then in order to measure the electrical conductivity of PANI and PANI-PSSNa (10%), the FTO coated glass is cut into 2x 1.5 cm dimension, and a thickness of 1 mm is etched in the middle of the FTO glass to isolate its conductivity. The disperse PANI and PANI-PSSNa is

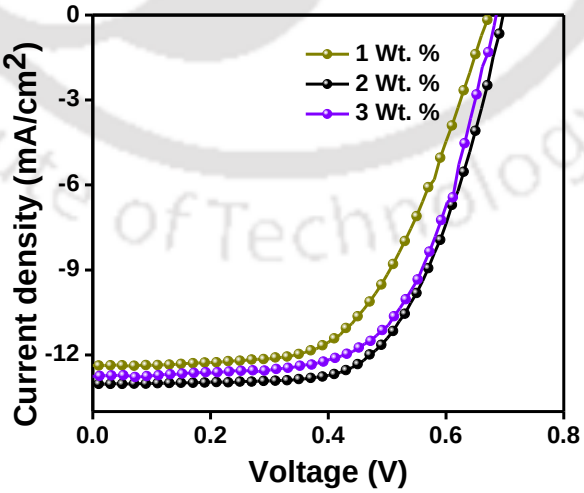

Figure 5. 4: J-V characteristics of DSSCs with various concentration of m-cresol in PANI.

spin-coated on the etching area to perform a conductivity test and are measured by a conventional two probe method under laboratory conditions. Linear scan of dark current (I) as a function of voltage(V) curves for undoped and doped PANI samples are shown in Fig. 5.5(a).

Table 5. 3: Electrical parameters of DSSCs with different Wt.% of m-cresol PANI.

Wt.% of PANI in m-Cresol.	J_{SC} (mA/cm2)	V_{OC} (mV)	FF (%)	PCE (Average)[a] (%)
1	12.34	673.30	57.05	4.90±0.28
2	13.01	697.10	62.90	5.71±0.21
3	12.62	681.40	62.20	5.12±0.25

A sharp slope of J-V curve is observed for doped PANI-PSSNa, which indicated that the electrical conductivity of PANI-PSSNa enhanced. The electrical properties of PANI considerably influence the photovoltaic performance of DSSCs. J−V characteristics curves for

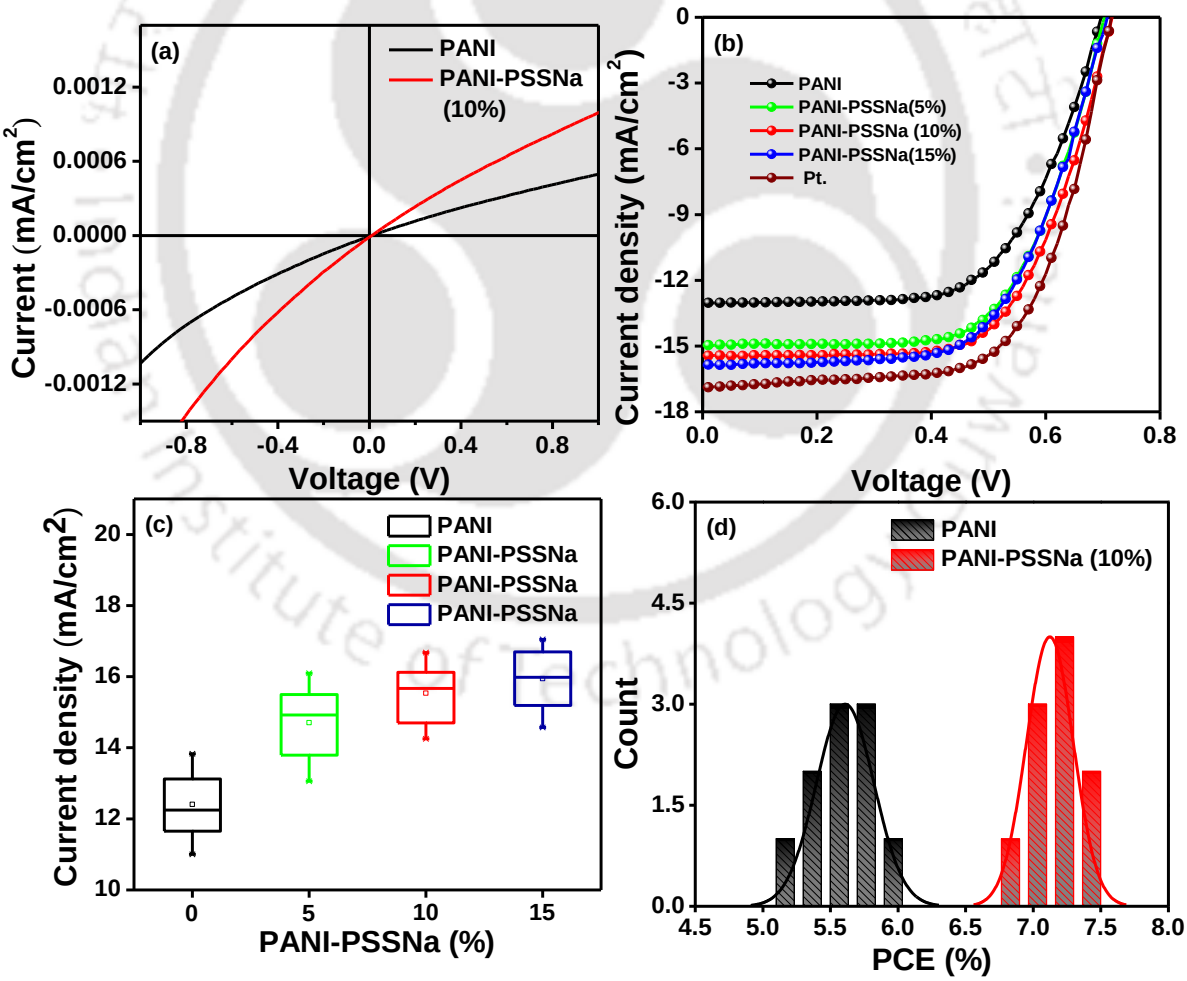

Figure 5. 5: (a) Conductivity test of PANI and PANI-PSSNa (b) J-V curves (c) $J_{SC\ box}$ chart and (d) PCE histogram of DSSCs with different conc. of PANI-PSSNa CEs.

DSSCs based on PANI, PANI-PSSNa and Pt CEs are shown in Fig. 5.5(b). The device parameter J_{SC}, V_{OC}, FF, and PCE performance are extracted from Fig. 5.5(b) and summarized in Table (5.4). The fabricated device based on undoped PANI yielded J_{SC} =13.01 mA/cm^2, V_{OC} =697.10 mV, FF = 62.90%, and Ƞ = 5.71%. For undoped PANI CE, poor device performance is witnessed due to the low conductivity, which cannot readily transfer electrons [17]. As observed from the J-V curves, the doped PANI-PSSNa CEs enhanced overall photovoltaic performance since the electron can be more easily transferred with low resistance than PANI. The PANI-PSSNa (10%) based device show a PCE of 7.15% with J_{SC} =15.43 mA/cm^2, V_{OC} =716.20 mV, FF = 64.70%. The performance of PANI-PSSNa electrode is almost comparable to Pt electrode, with a decreased of only 9.14% PCE, which is reasonably good considering the cost of Pt. However, if the PSSNa conc. goes above 10%, then the overall PCE decreases with an increasing PSSNa. The box chart of J_{SC} and histogram of PCE with and without PSSNa based DSSCs result are illustrated in Fig. 5.5(c and d), respectively. These J-V curve results are in agree with CV, Tafel, and EIS data, suggesting that PANI-PSSNa film generates a better electrocatalytic activity than that of the PANI film. Therefore, PANI-PSSNa based CEs can be considered as an alternative material to replace expensive Pt for the development of cost-effective and efficient DSSCs in the near future.

Table 5. 4: Parameters of DSSCs with different Conc. of PSSNa in PANI.[5]

CEs with different % of PSSNA in PANI	**J_{SC} (mA/cm^2)**	**V_{OC} (mV)**	**FF (%)**	**PCE (Average)[a] (%)**
0	13.01	697.10	62.90	5.71 ±0.21
5	14.96	702.50	64.60	6.76 ±0.31
10	15.43	716.20	64.70	7.15 ±0.17
15	15.87	707.40	62.00	6.96 ±0.26
Pt	16.91	714.77	65.20	7.87 ±0.12

[a]Average of 10 devices.

[5]Performances of DSSCs were measured with 0.25 cm^2 active area under AM 1.5, 100 mW/cm^2 irradiation. Liquid electrolytes (0.05M I_2, 0.5M LiI, 0.1M guanidium thiocyanate, 0.5M 4-tert-butylpyridine and 0.5M 1-Butyl-3-methylimidazolium iodide dissolved in acetonitrile/valeronitrile (V: V= 85:15) solvent. Dye solution (0.3 mM N719), PANI and PANI-PSSNa CEs.

Surface morphology of PANI and PANI-PSSNa.

The spin coated image of PANI doped with different conc. of PSSNa are shown in Fig. 5.6 and the corresponding 0% and 10% FESEM and AFM images are shown in Fig. 5.7(a and b) and

Fig. 5.7(c, d, e and f) respectively. The FESEM and AFM microstructure images determine the surface morphology of PANI and PANI-PSSNa coated on FTO glass. From the FESEM images, we observed that the surface of the electrodes exhibits a porous structure with pinhole-free uniform grain-sized. It must be underlined that a thick film with loosely bound structure and lower surface area grain sizes are observed in the PANI coated film. But it is seen that the incorporation of PSSNa influences the surface morphology of PANI. It is observed that PSSNa particles are uniformly dispersed in PANI matrix. The FESEM images exhibited by PANI-PSSNa complex have clear and quite regular interfacial grain sizes condition with more porous

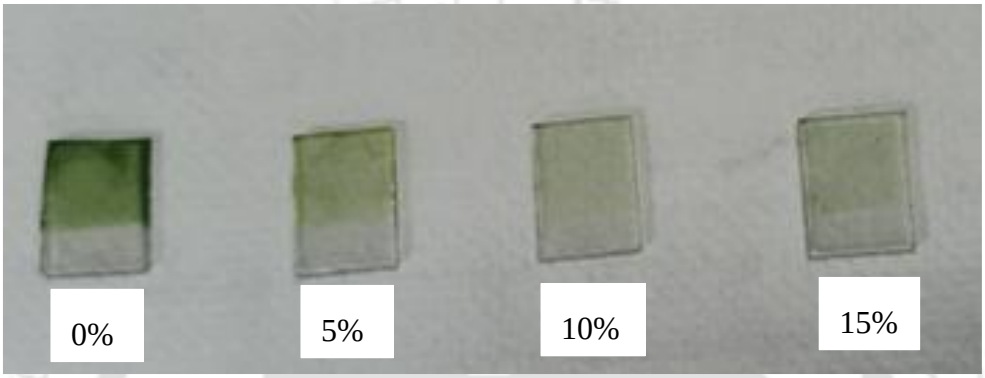

Figure 5. 6: Image of PANI doped with different con. of PSSNa

structure, which is essential for high catalytic activity [9, 29-30]. The change in morphology of PANI-PSSNa arises from the effect of interaction on the orientation of polymer. The 2D and 3D AFM images are also compared before and after doping. The RMS roughness for the PANI and PANI-PSSNa are 16 and 22 µm, respectively. So, it indicated that the surface roughness and solvent evaporation of PANI–PSSNa CEs enhanced [12][31]. The PANI-PSSNa film mainly consists of a uniformly oriented porous grain network with a high surface area, essential for a high catalytic activity to reduce I_3^- ions. Probably due to enhance surface roughness area, there are extra catalytic active sites of PANI-PSSNa CE, that contribute much better photovoltaic performance than that of the PANI based DSSCs.

FTIR analysis

FTIR technique was utilized to detect different functional groups present in the counter electrode. Fig. 5.8 depicts the FTIR spectra of PANI, PSSNa, and PANI-PSSNa coated on FTO glass in the range of 500-4000 cm^{-1}. The major characteristics peaks 2926, 1736, 1547, 1457, 1363, 1218, 829, 714, 585 cm^{-1} are observed in the PANI film. From the PANI spectrum, the

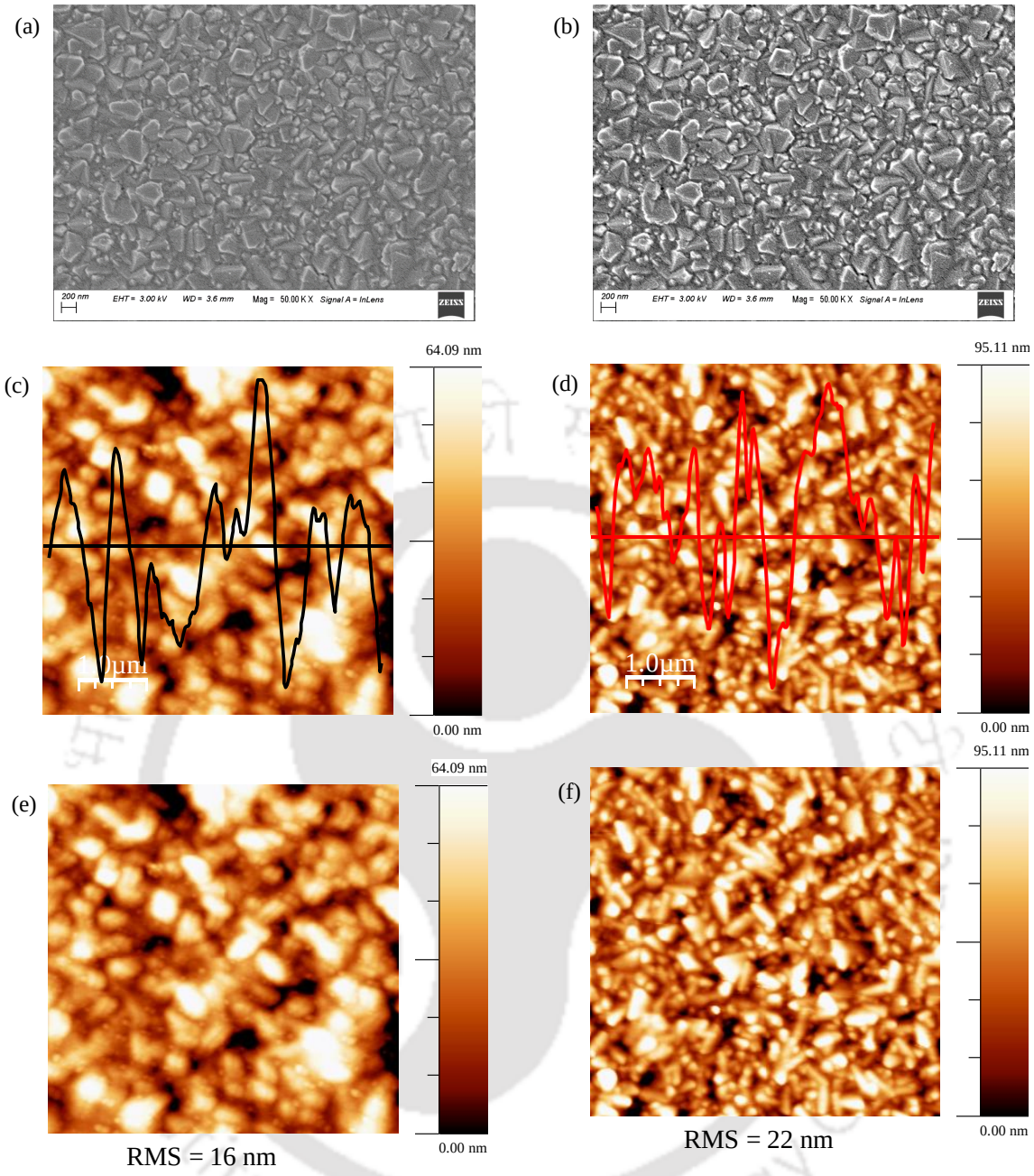

Figure 5. 7: FESEM image of (a) PANI and (b) PANI-PSSNa (10%) coated on FTO glass surface. Corresponding 2D and 3D AFM image (c), (d), (e) and (f).

peak at 2926 is characterized to the C-H asymmetric stretching vibration. The most significant peak at about 1736 cm^{-1} corresponds to the C=O stretching vibration of the carbonyl group [32]. The characteristic peaks at 1547 cm^{-1} and 1457 cm^{-1} in all samples are due to the C=C stretching in the quinoid and benzene ring [31]. The absorption appears at 1363 and 1218 cm^{-1} are attributed to C-N stretching band of an aromatic amine [33]. The wide absorption at 3319 cm^{-1} is assigned to water molecules absorbed in the PSSNa due to the hydrophilic nature of

sulfonic acid group. Peaks obtained at 1027 and 580 cm^{-1} are due to the stretching of sulfonate (S=O) group and C-S of PSSNa [34-35]. In the spectra of PANI-PSSNa composites, almost all the characteristic peaks of PSSNa and PANI are visible.

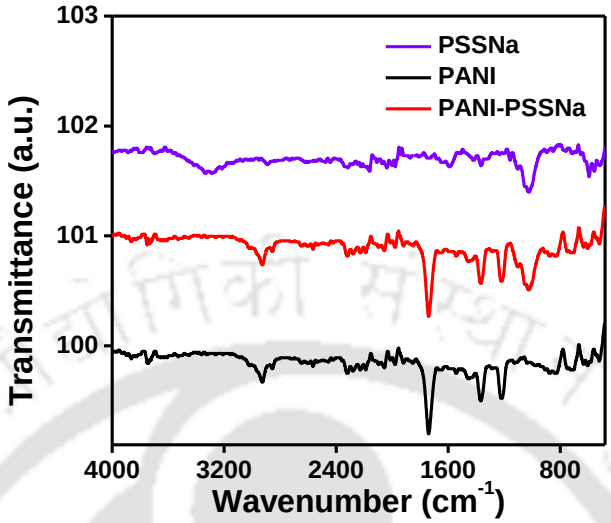

Figure 5. 8: FTIR spectra of PSSNa, PANI and PANI-PSSNa coated on FTO glass.

5.4 Conclusion

In summary, PANI and PANI-PSSNa doped CEs have been prepared by spin-coating technique, and their photovoltaic performance of the DSSCs are compared with Pt electrode. The PANI-PSSNa doped CEs enhance the efficiency of DSSCs compared to PANI CE. A broad investigation has been performed by electrochemical analyses such as CV, Tafel, and Nyquist plots to determine the substantial increases in electrocatalytic activity toward reduction of I_3^- ions in the electrolytes. The overall DSSCs performance increased from 5.71(±0.21) to 7.15% (±0.17) was attained by adding optimal amounts of PSSNa to the PANI. The improved photovoltaic parameters such as J_{SC}, V_{OC}, FF, and η of the cells are attributed to the increase in surface roughness that creates a greater number of active reaction sites on CEs for high electrocatalytic activity, decreased recombination, and enhanced electrical conductivity. Although the PCE of DSSC with PANI-PSSNa CE is little lower than that of Pt CE (7.87%), the excellent photoelectric properties, low temperature processed, inexpensive cost and easy fabrication methods available such as spin coating, spray coating, and printing etc. for large-scale production allow the PANI-PSSNa CE to be a credible substitute used in DSSCs.

5.5 References

[1] G.R. Li, F. Wang, Q.W. Jiang, X.P. Gao, P.W. Shen, Carbon nanotubes with titanium nitride as a low-cost counterelectrode material for dye-sensitized solar cells, Angew. Chemie - Int. Ed. 49 (2010) 3653–3656. doi:10.1002/anie.201000659.

[2] K.H. Park, S.J. Kim, R. Gomes, A. Bhaumik, High performance dye-sensitized solar cell by using porous polyaniline nanotubes as counter electrode, Chem. Eng. J. 260 (2015) 393–398. doi:10.1016/j.cej.2014.08.105.

[3] L.C. and S.Y. Jiangbin Xia, Application of polypyrrole as a counter electrode for a dye-sensitized solar cell, J. Mater. Chem. 21 (2011) 4644–4649. doi:10.1039/c0jm04116e.

[4] J.K. and S.S.I. Sang Soo Jeon, Chulwoo Kim, Spherical polypyrrole nanoparticles as a highly efficient counter electrode for dye-sensitized solar cells, Jounal Matrials Chem. 21 (2011) 8146–8151. doi:10.1039/c1jm10112a.

[5] O.I. Teketel Yohannes, Photoelectrochemical studies of the junction between poly [3-(4-octylphenyl)thiophene] and a redox polymer electrolyte, Sol. Energy Mater. Sol. Cells. 51 (1998) 193–202.

[6] Y. Saito, T. Kitamura, Y. Wada, S.Y. Ã, Application of Poly (3 , 4-ethylenedioxythiophene) to Counter Electrode in Dye-Sensitized Solar Cells, Chem. Lett. 31(10) (2002) 1060–1061.

[7] T. Xu, D. Kong, H. Tang, X. Qin, X. Li, A. Gurung, K. Kou, L. Chen, Q. Qiao, W. Huang, Transparent MoS 2 / PEDOT Composite Counter Electrodes for Bifacial Dye-Sensitized Solar Cells, ACS Omega. 5 (2020) 8867–8696.

[8] Z.Y. Jun Zhang, Tubshin Hreid, Xiaoxue Li, Wei Guo, Linping Wang, Xiaoting Shi, Haiquan Su, Nanostructured polyaniline counter electrode for dye-sensitised solar cells: Fabrication and investigation of its electrochemical formation mechanism, Electrochim. Acta. 55 (2010) 3664–3668.

[9] L.F. Qinghua Li, Jihuai Wu *, Qunwei Tang, Zhang Lan, Pinjiang Li, Jianming Lin, Application of microporous polyaniline counter electrode for dye-sensitized solar cells, Electrochem. Commun. 10 (2008) 1299–1302.

[10] T.H. Sheha Wang, Shan Lu, Xuemin Li, Xuehua Zhang, Shengtai He, Study of H2SO4

concentration on properties of H2SO4 doped polyaniline counter electrodes for dye-sensitized solar cells, J. Power Sources. 242 (2013) 438–446.

[11] C.B. N. Karaog˘lan, Synthesis and optical characterization of benzene sulfonic acid doped polyaniline, Eng. Sci. Technol. , an Int. J. 21 (2018) 1152–1158.

[12] S. Cho, S.H. Hwang, C. Kim, J. Jang, Polyaniline porous counter-electrodes for high performance dye-sensitized solar cells, J. Mater. Chem. 22 (2012) 12164–12171. doi:10.1039/c2jm30594a.

[13] S. Ameen, M.S. Akhtar, Y.S. Kim, O. Yang, H. Shin, Sulfamic Acid-Doped Polyaniline Nanofibers Thin Film-Based Counter Electrode : Application in Dye-Sensitized Solar Cells, (2010) 4760–4764.

[14] S. Ghani, R. Sharif, S. Shahzadi, N. Zafar, A.W. Anwar, A. Ashraf, A.A. Zaidi, A.H. Kamboh, S. Bashir, Simple and inexpensive electrodeposited silver/polyaniline composite counter electrodes for dye-sensitized solar cells, J. Mater. Sci. 50 (2015) 1469–1477. doi:10.1007/s10853-014-8708-z.

[15] H. Sun, Y. Luo, Y. Zhang, D. Li, Z. Yu, K. Li, Q. Meng, In situ preparation of a flexible polyaniline/carbon composite counter electrode and its application in dye-sensitized solar cells, J. Phys. Chem. C. 114 (2010) 11673–11679. doi:10.1021/jp1030015.

[16] W.X. Guiqiang Wang, Shuping Zhou, Graphene/polyaniline nanocomposite as counter electrode of dye-sensitized solar cells, Mater. Lett. 69 (2012) 27–29.

[17] and S.S.I. Sang Soo Jeon, Chulwoo Kim, Tae Hyun Lee, Young Woo Lee, Kwangseok Do, Jaejung Ko, Camphorsulfonic Acid-Doped Polyaniline Transparent Counter Electrode for Dye-Sensitized Solar Cells, J. Phys. Chem. C. 116 (2012) 22743–22748.

[18] S.H.J. Iftikhar Ali Sahito, Kyung Chul Sun, Alvira Ayoub Arbab Muhammad Bilal Qadir, Yun Seon Choi, Flexible and conductive cotton fabric counter electrode coated with graphene nanosheets for high efficiency dye sensitized solar cell, J. Power Sources. 319 (2016) 90–98.

[19] S. Gnanasekar, P. Kollu, S.K. Jeong, A.N. Grace, Pt-free , low-cost and efficient counter electrode with carbon wrapped VO 2 (M) nanofiber for dye- sensitized solar cells, (2019) 1–12.

[20] G. Yue, J. Wu, Y. Xiao, J. Lin, M. Huang, Low cost poly(3,4-ethylenedioxythiophene): Polystyrenesulfonate/carbon black counter electrode for dye-sensitized solar cells, Electrochim. Acta. 67 (2012) 113–118. doi:10.1016/j.electacta.2012.02.009.

[21] M. Wu, X. Lin, Y. Wang, L. Wang, W. Guo, D. Qi, X. Peng, A. Hagfeldt, M. Grätzel, T. Ma, Economical Pt-free catalysts for counter electrodes of dye-sensitized solar cells, J. Am. Chem. Soc. 134 (2012) 3419–3428. doi:10.1021/ja209657v.

[22] W. Maiaugree, S. Pimanpang, W. Jarernboon, V. Amornkitbamrung, Influence of Acid Modification Multiwall Carbon Nanotube Counter Electrodes on the Glass and Flexible Dye-Sensitized Solar Cell Performance, Int. J. Photoenergy. 2016 (2016). doi:10.1155/2016/2853046.

[23] W.W. PeihuiLuo, Haijun Niu, Gang Zheng, Xuduo Bai, Milin Zhang, Enhancement of photoelectric conversion by high-voltage electric field assisted crystallization of a novel ternary-encapsulated spherical TiO_2 aggregate for solar cells, Electrochim. Acta. 55 (2010) 2697–2705.

[24] K.E. T. Hoshikawa, M. Yamada, R. Kikuchi, Impedance analysis for dye-sensitized solar cells with a three-electrode system, J. Electroanal. Chem. 577 (2005) 339–348.

[25] M. Adachi, M. Sakamoto, J. Jiu, Y. Ogata, S. Isoda, Determination of parameters of electron transport in dye-sensitized solar cells using electrochemical impedance spectroscopy, J. Phys. Chem. B. 110 (2006) 13872–13880. doi:10.1021/jp061693u.

[26] and M.G. Qing Wang, Jacques-E. Moser, Electrochemical Impedance Spectroscopic Analysis of Dye- Sensitized Solar Cells, J. Phys. Chem. B. 109 (2005) 14945–14953. doi:10.1002/ijch.201500007.

[27] W.W. Liu, W. Jiang, Y.C. Liu, W.J. Niu, M.C. Liu, K. Zhao, L.Y. Zhang, L. Lee, L. Bin Kong, Y.L. Chueh, Platinum-Free Ternary Metallic Selenides as Nanostructured Counter Electrode for High-Efficiency Dye-Sensitized Solar Cell by Interface Engineering, ACS Appl. Energy Mater. 3 (2020) 3704–3713. doi:10.1021/acsaem.0c00172.

[28] W. Liu, H.G. Wang, X. Wang, M. Zhang, M. Guo, Titanium mesh supported TiO_2 nanowire arrays/Nb-doped TiO_2 nanoparticles for fully flexible dye-sensitized solar cells with improved photovoltaic properties, J. Mater. Chem. C. 4 (2016) 11118–11128.

doi:10.1039/c6tc03680e.

[29] A.M. Mocioiu, I.A. Tudor, O.C. Mocioiu, Application of polyaniline for flexible semiconductors, Coatings. 11 (2021) 1–10. doi:10.3390/coatings11010049.

[30] Y. Qiu, S. Lu, S. Wang, X. Zhang, S. He, T. He, High-performance polyaniline counter electrode electropolymerized in presence of sodium dodecyl sulfate for dye-sensitized solar cells, J. Power Sources. 253 (2014) 300–304. doi:10.1016/j.jpowsour.2013.12.061.

[31] H.K. Swarup Biswas, Jaebum Jeong, Jae Won Shim, Improved charge transport in PANI: PSS by the uniform dispersion of silver nanoparticles, Appl. Surf. Sci. 483 (2019) 819–826.

[32] M.K. Mohanapriya, K. Deshmukh, K. Chidambaram, M.B. Ahamed, K.K. Sadasivuni, D. Ponnamma, M.A.A. AlMaadeed, R.R. Deshmukh, S.K.K. Pasha, Polyvinyl alcohol (PVA)/polystyrene sulfonic acid (PSSA)/carbon black nanocomposite for flexible energy storage device applications, J. Mater. Sci. Mater. Electron. 28 (2017) 6099–6111. doi:10.1007/s10854-016-6287-2.

[33] A. John, S.K. Mahadeva, J. Kim, The preparation, characterization and actuation behavior of polyaniline and cellulose blended electro-active paper, Smart Mater. Struct. 19 (2010). doi:10.1088/0964-1726/19/4/045011.

[34] B. Sydulu Singu, P. Srinivasan, S. Pabba, Benzoyl Peroxide Oxidation Route to Nano Form Polyaniline Salt Containing Dual Dopants for Pseudocapacitor, J. Electrochem. Soc. 159 (2011) A6–A13. doi:10.1149/2.036201jes.

[35] C.S. Stan, M. Popa, M. Olariu, M.S. Secula, Synthesis and characterization of PSSA-Polyaniline composite with an enhanced processability in thin films, Open Chem. 13 (2015) 467–476. doi:10.1515/chem-2015-0057.

Carbon nanotubes/PANI composite as an efficient counter electrode material for Dye-sensitized solar cell

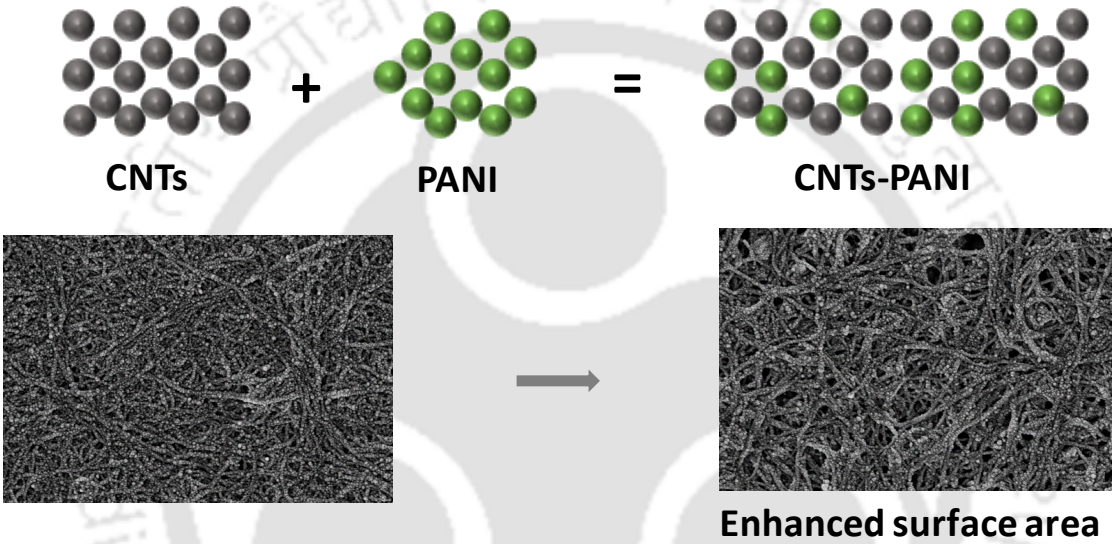

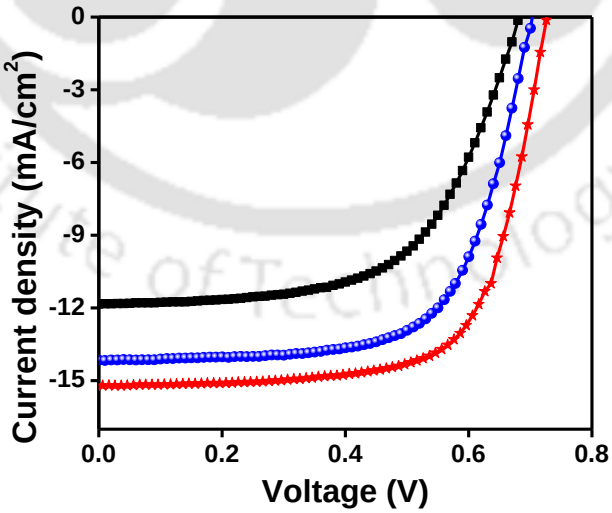

Chandan Dawo, Parameswar Krishnan Iyer, and Harsh Chaturvedi, Materials Science & Engineering B, Volume 297, 2023, 116722, https://doi.org/10.1016/j.mseb.2023.116722

6.1 Introduction

The role of counter electrode in DSSCs is to reduce the redox species, which are the mediators for regenerating the dye after electron injection. Generally, iodide/triiodide electrolytes act as a redox mediator between the photoanode and counter electrode (CE). CE is an essential component and its main role is to reduce the redox species tri-iodide (I_3^-) to iodide (I^-). The characteristics of high-performance CEs are as follows: (i) low resistance to minimize loss of open-circuit voltage (ii) high conductivity and catalytic activity for the reduction of tri-iodide ion (I_3^-).The most frequently used catalyst material in the counter electrode (CE) is Pt due to its excellent chemical and physical properties such as high catalytic activity, thermal and electrical conductivity, etc. CE without Pt layer has high resistant for reducing a standard triiodide/iodide in electrolyte [1-3]. The main problem associated with Pt is very expensive, which costs more than 40% of the total device, scarcity and limited corrosion resistance toward iodine are the main drawbacks [4-6]. Therefore, developing low-cost alternative materials as a catalyst for cathode has become an important trend for commercial applications [7]. A various number of materials have been explored as catalyst for CEs:, transition metal cobalt sulphides (CoS) [8], phosphides[9], nitrides [10], carbides [11] ,oxides [12-13] and conductive polymers [14-17]. Among the various other counter electrodes catalysts, carbon-based has been recognized as a competitive candidate as far as availability of materials and low cost are concerned, carbon-based materials like carbon black [18-20], carbon bead [21], graphite [22-23], activated carbon [24], mesoporous carbon [25-26], carbon nanofibers [27-28], graphene [29], and carbon nanotubes [30-31] have been fruitfully utilised as a CEs. They have outstanding properties like high surface area, electrocatalytic activity, thermal stability, electrical conductivity, and corrosion resistance toward iodide/tri-iodide electrolytes [32-36]. CNTs have been regarded as an innovative material due to their outstanding mechanical, electrical, flexibility, and optical properties that open the way to future applications in photovoltaic devices. They also have good corrosion resistance for liquid electrolytes, making the devices excellent stability for prolonged use. For the first time, Suzuki et al. successfully fabricated single-walled carbon nanotubes (SWCNTs) as a counter electrode in DSSCs and obtained an energy conversion of 4.5% [30]. Mirzaei et al. prepared CE based on nanocomposite of amorphous ruthenium sulfide nanoparticles, reduced graphene oxide, and functionalized multi-walled carbon nanotubes (MWCNTs), leading to an efficiency upto 13% [37]. Zambrzycki et al. developed CEs from hierarchical

carbon nanofibers/carbon nanotubes/NiCo (eCNF/CNT/NiCoNP) ternary nanocomposites and obtained a PCE of 7% [5]. Zhang et al. developed CE from double-walled carbon nanotubes (DWCNTs) materials by mixing ethyl cellulose and terpineol via screen printing technique and attained an efficiency of 6.05% [38]. Lee et al. used multi-walled carbon nanotubes (MWCNTs) CE by casting method and achieved a PCE of 7.67% [39]. Veerappan et al. prepared CE made of Carbon nanofibers (CNFs) by doctor blade technique, followed by sintering at 100°C under a vacuum oven for 5 hrs achieving an efficiency of 6.4% [40]. Nam et al. fabricated vertically aligned MWCNTs CE through chemical vapor deposition by screen printing technique that facilitates ion and electron transport and improves the PCE up to 10.04% [41]. To enhance the electrocatalytic properties of CEs, conducting polymers like polypyrrole (PPy) [31], Polyaniline (PANI) [42-44], P3HT [45-46] and Poly (3,4-ethylenedioxythiophene) (PEDOT) [47-50] has been incorporated with CNTs as a catalyst. Herein, with an aim to improve the performance of DSSCs, carbon nanotubes (CNTs) and conducting polymer PANI composite are used as an efficient catalyst for triiodide reduction. The main issue with CNTs is their low loading on the surface of glass substrate. Therefore, PANI is used as an additive to modify the CNTs electrodes due to its low cost, good catalytic activity for triiodide reduction, high thermal and chemical stability [51-53].

6.2 Experiment section

Chemicals and Materials

Fluorine doped tin oxide (FTO) coated glass-7 Ω/square, Titanium dioxide powder (Degussa P25, 21 nm), Terpineol, Diisopropoxidebis (acetylacetonate), Tert-butanol, Valeronitrile, Lithium iodide,4-tert butylpyridine, DMF, m-cresol, Anhydrous isopropanol, 1-butyl-3-methylimidazolium iodide, Ruthenium dye (N719), Acetonitrile, Sodium hydroxide (NaOH), and Chloroplatinic acid hexahydrate ($H_2PtCl_6.6H_2O$) and Polyaniline (MW= 15,000) were purchased from Sigma-Aldrich. Other chemicals for the experiments were obtained from different sources such as Absolute ethanol from Fisher scientific, Ethylcellulose and Iodine from Himedia, Acetic acid from Merck and CNTs powder from Nopo.

Preparation of counter electrodes

Counter electrodes were prepared using CNTs and PANI in different weight percent (Wt.%) (3, 6, and 9) and dispersed in m-cresol at 100 mg/mL concentration. Then the

CNTs-PANI composites was kept in magnetic stirrer for 3 hrs to mix thoroughly. During stirring, 2 to 3 drops of terpineol and ethyl cellulose (15 Wt.% in ethanol) were also added to the composite and subsequently stirred for some time. As the paste mixed thoroughly, a thin layer was formed by doctor blade coating over the FTO coated glass substrate as a CEs. The coated layer was kept at room temperature to dry naturally and sintered at 400 °C for 30 min. Fig. 6.1 shown the schematic diagram of preparing composite CNTs-PANI counter electrode. The idea of CNTs dispersion in m-cresol came to our mind with our previous work, where we dispersed Polyaniline in m-cresol at different weight percent and improved the device performance [43]. M-cresol in Polyaniline interacts with the polymer chain and works as secondary doping. This inspired us to investigate the dispersion of CNTs in m-cresol. Typically, most common solvents such as ionic liquids, super acids, dimethylformamide (DMF), N-methyl-2-pyrrolidone (NMP), and 1,2-dichrolobenzene etc. can be directly used to disperse some types of nanotubes at very low concentrations [54]. However, the limitation with these solvents were the low loading of CNTs on glass substrate. CNTs readily dispersed in m-cresol at a much higher concentration than common solvents. In addition to dispersion, highly processable CNTs gel and paste can be obtained as the concentration increases. We observed that CNTs were well dispersed in m-cresol after stirrer, making the past much thicker with higher viscosity. One week later, we checked the dispersion of CNTs in m-cresol and found no sign of aggregation, making m-cresol unique as a CNTs solvent. The Platinized (Pt) counter electrode (CE) was prepared from $H_2PtCl_6.6H_2O$ solution in anhydrous 2-propanol for comparison.

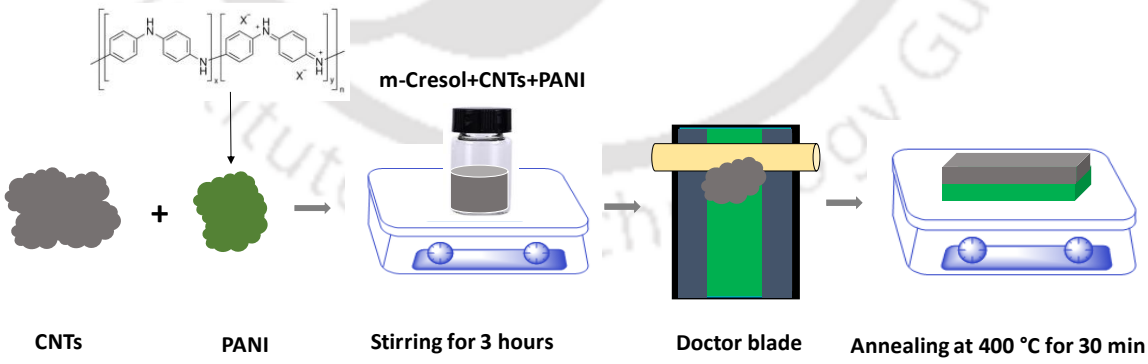

Figure 6. 1: The schematic diagram of preparing composite CNTs-PANI counter electrodes

Device fabrication and testing

FTO-coated transparent glass substrates (1.5 ×2 cm^2) were ultra-sonicate baths in a detergent solution for 15 minutes and washed in a running tape, then sonication in deionised

water, acetone, and propanol. After drying the substrates, UV-Ozone treatment for 10 min to eradicate the organic contaminants. An ethanol solution of 0.15 M containing diisopropoxidebis (acetylacetonate) was spin-coated at 4500 rpm for 55 secs and sintered at 400 °C for 30 min as a blocking layer. The mesoporous TiO_2 films were formed above the blocking layer by the doctor blade technique and subsequently heated at 400 °C for 30 min. After bringing down to ambient temperature, immersed into 3×10^{-4} M N719 dye solution for 24 hours so that adsorption takes place successfully on mesoporous films. Liquid I^-/I_3^- electrolyte composed of 0.05M I2, 0.5M LiI, 0.1M guanidium thiocyanate, 0.5M 4-tert-butylpyridine and 0.5M 1-Butyl-3-methylimidazolium iodide in acetonitrile/valeronitrile (Volume ratio of 85:15) solvent. The CEs and photoanodes were sealed by 60 µm thick surlyn film (Ossila), and the space between them was filled with liquid electrolyte. The current density and voltage (J-V) characteristic curves were measured from -1 to 1V by 2400 source meter (Keithley, USA), under one-sun (AM-1.5G 100 mW/cm2 intensity). The IPCE spectrum of DSSCs were obtained by applying monochromatic light with continuously varying the wavelength of the excitation light and were carried out by Newport monochromator (Model 74125) and the Xenon lamp (Newport, Model 67005). The measurements were carried out with an active area of 0.25 cm^2.

6.3 Results and discussion

Electrical parameters of DSSCs

We examined the photovoltaic characteristic of the DSSCs employing CNTs, CNTs-PANI and Pt counter electrodes. Fig. 6.2(a) described the current density-voltage (J-V) curves of the best DSSC with the corresponding electrodes for comparison. The box charts of current density and PCE of different CEs were shown in Fig. 6.2(c and d). The champion DSSC with CNTs, CNTs-PANI, and Pt electrodes shown an impressive PCE of 4.83%, 6.67% and 7.70%, respectively and their parameters were tabulated in Table 6.1. As expected, DSSC using Pt electrode presented the best performance compared to the CNTs base CEs. This could be due to the semi-transparent nature with good light reflection that leads to lower internal resistance and yield higher PCE. However, the performance of CNTs based photovoltaic devices were comparable to that of Pt. The parameters of the DSSC with CNTs based CE exhibit a short-circuit current density (J_{SC}) of 11.84 mA/cm^2, open-circuit voltage (V_{OC}) of 681.70 mV, and fill factor (FF) of 59.90%, respectively. After incorporating CNTs

with conducting polymer PANI (6 Wt.%), the photovoltaic performance enhanced up to 38% with J_{SC} of 14.19 mA/cm^2, V_{OC} of 699.10 mV, and FF of 67.35%. Further increasing of PANI concentration up to 9 Wt.% does not improve the PCE, it remains almost constant with 6 Wt.% results. The lower PCE of the CNTs based CEs might be due to the thick catalytic layer, which offers higher total internal resistance and the opaque nature that cannot induce the effect of light reflection [40]. The incident photon to current conversion efficiency (IPCE) spectra, shown a broad band in the region of 250-800 nanometre (nm)

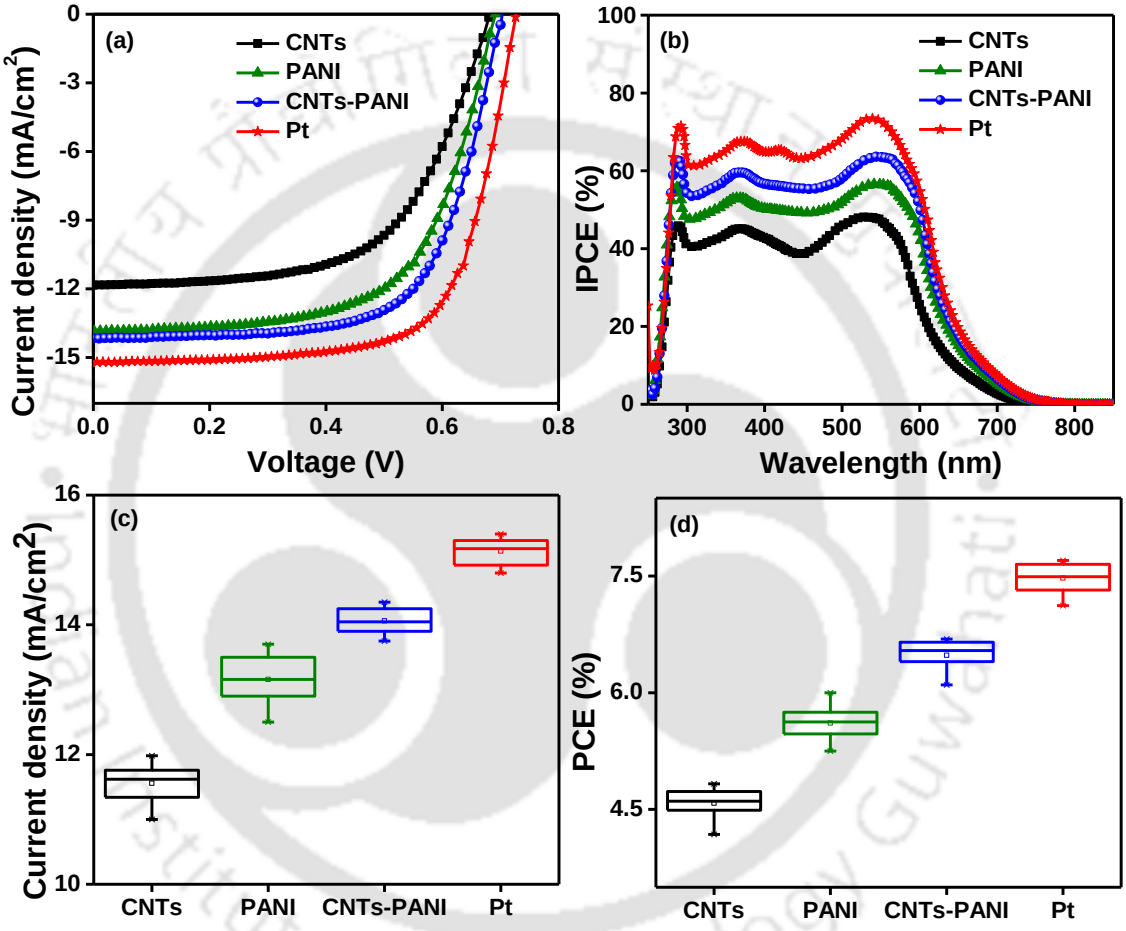

Figure 6. 2: (a) JV characteristics curves, corresponding (b) IPCE spectra, (c) J_{SC} and (d) PCE box charts of DSSCs based on CNTs, CNTs-PANI and Pt CEs.

with a maximum value at 535 nm. From Fig. 6.2(b) we observed that the IPCE curves of the DSSCs with its CEs were in the order of CNTs <CNTs-PANI< Pt. The lowest IPCE value was found for DSSC prepared from CNTs CE. The value of IPCE% increased from 49% to 61% at 535 nm wavelength after CNTs-PANI composite. Pt has the highest IPCE% value of 76% at 535 nm wavelength. The results obtained in the IPCE curves were in agreement with the JV curves. Although the PCE of CNTs-PANI CEs were slightly lower

than those of DSSC with Pt electrode, from economic feasibility point of view CNTs-based CEs can be an alternative to expensive Pt electrode for future practical applications.

Table 6. 1: Electrical parameters of best DSSCs with different CEs.[6]

CEs	J_{SC} (mA/cm^2)	V_{OC} (mV)	FF (%)	PCE (Average)[a] (%)
CNTs	11.84	681.7	59.9	4.83±0.19
PANI	13.83	687.0	62.1	5.90±0.22
CNTs-PANI	14.19	699.1	67.3	6.67±0.21
Pt	15.20	727.9	69.6	7.70±0.20

[a]Average of 10 devices

[6]Performances of DSSCs were measured with 0.25 cm^2 working area under AM 1.5, 100 mW/cm^2 irradiation. Liquid electrolytes (0.05M I_2, 0.5M LiI, 0.1M guanidium thiocyanate, 0.5M 4-tert-butylpyridine and 0.5M 1-Butyl-3-methylimidazolium iodide dissolved in acetonitrile/valeronitrile (V: V= 85:15) solvent, 0.3 mM N719 dye solution, CNTs and CNTs/PANI CEs.

Impedance analysis

In order to evaluate the charges transfer processes in DSSCs, electrochemical impedance spectra (EIS) measurement was conducted at a bias potential of 0.7V in the frequency ranging from 10^5 to 10^{-1} Hz at ambient conditions. EIS technique is regarded as a diagnostic tool for analysing the charge transport process in DSSCs. The impedance spectra of three devices (CNTs, CNTs-PANI and Pt) were fitted with Nyquist plots and its equivalent circuit inset was shown in Fig. 6.3(a). The Nyquist spectra with fitted equivalent circuit have series resistance (R_S), constant phase element (CPE), charge transfer resistance (Rct), charge recombination resistance (Rcr) and Nernst diffusion impedance (W) [16, 55-57]. The Rs represents the total ohmic resistance of the devices. It has only a resistive component, so present before the onset of the spectra at high-frequency region, and their values are 28.37, 26.15 and 20.11 Ω for CNTs, CNTs-PANI and Pt CEs based devices. The Nyquist plot features two semicircles in the impedance spectra; in the high-frequency range (small semicircle) and in the mid-frequency range (large semicircle). The parallel combination of Rct and CPE1 (constant phase element at counter electrode side) represents the small semicircle which indicates charge transfer impedance spectra at electrolytes/CEs interface, while Rcr and CPE2 (constant phase element at photoanode side) at the FTO/TiO_2/ N719/electrolytes interface signifies recombination resistance, respectively. The R_{ct} values decreased in the order of CNTs> CNTs-PANI > Pt and their corresponding values from the equivalent circuit are 72.77 > 36.17 > 14.12 (Ω). The Nernst diffusion

impedance (W) of the device was also in the same order CNTs> CNTs-PANI> Pt, with the values 27.14> 17.79> 2.25, respectively. CNTs incorporating with PANI might interconnect to form networks that are required for fast ion transport, thus leading to lower Rs, Rct, Rcr and W values. Thus, a DSSC with reduced Rs, Rct and W experience lower recombination process, small over potential for an electron moving from CE to the electrolyte and faster diffusion of electrolytes, respectively.

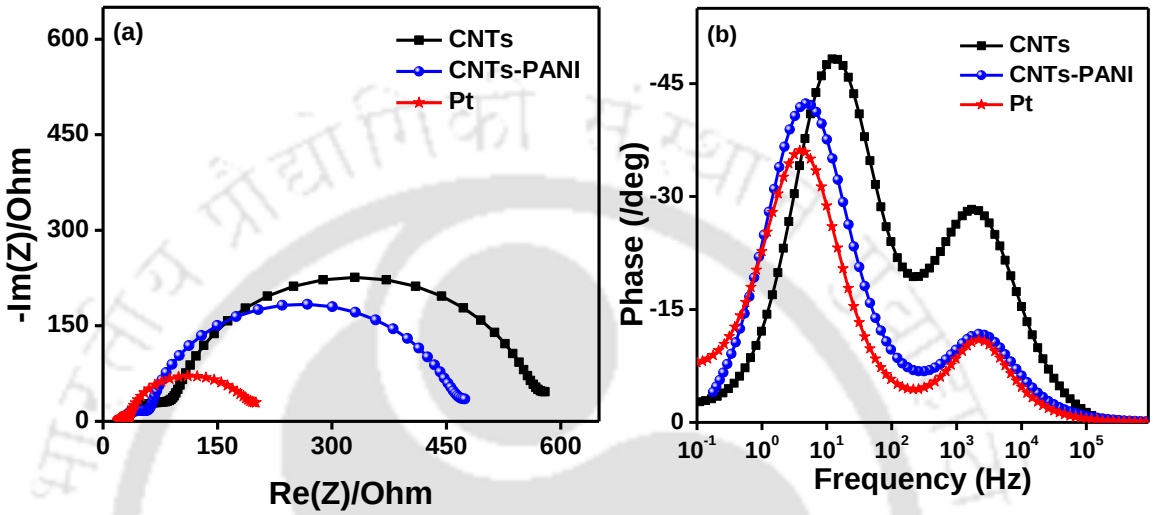

Figure 6. 3: Impedance spectra of DSSCs (a) Nyquist plot and (b) Bode plot based on CNTs, CNTs-PANI and Pt CEs.

Table 6. 2: Parameters of Nyquist spectra fitted to equivalent circuit.

Counter Electrodes	Rs (Ω)	CPE1 ($10^{-6}F$)	Rct (Ω)	CPE2 ($10^{-3}F$)	Rcr (Ω)	Electron life (ms)
CNTs	28.3	36.6	72.7	0.11	446.3	49.09
CNTs-PANI	26.1	19.2	36.1	0.25	392.2	98.05
Pt	20.1	14.6	14.1	0.67	163.9	109.81

The Bode phase plots of the corresponding EIS result were illustrated in Fig.6.3(b). Similarly, like the Nyquist plot in the bode plot, we observed two peak frequencies in the intermediate and high-frequency range. The intermediate frequencies described the charge transfer at photoanode/electrolytes interface, while the high frequencies region is attributed to the charge transfer at CEs/electrolyte interface. The effective electron lifetime (τ_e) at the CE/electrolytes interface was estimated using the following equation [58].

$$\tau_e = 1/2\pi f_{max} \qquad 6.1$$

Where f_{max} (1858, 2167, and 2302 Hz) is the peak frequency. The τ_e of the CNTs, CNTs-PANI and Pt based device were 8.57, 7.34 and 6.91 ms, respectively. τ_e is reciprocal to the maximum peak frequency; the lower values of τ_e specify faster reduction of triiodide ion that enhanced electron transfer rate with low resistance and correspondingly improved the PCE.

Cyclic voltammetry (CV) and Tafel analysis

With a purpose to test the catalytic activity of CNTs, CNTs-PANI and Pt CEs, CV measurement was performed in a three-electrode system, with Ag/AgCl as the reference electrode and Pt wire as the counter electrode. The electrolytes for the test consist of 0.5 mM I_2, 0.1 M $LiClO_4$, and 5 mM LiI, in an acetonitrile solution. The CV curves of CNT, CNTs-PANI and Pt cathodes were measured at a scan rate of 50 mV/s, and were presented in Fig. 6.4(a). It is a well-known fact that the electron migration rate constant is directly related to the catalytic reaction and number of active site of CEs [59][60]. To ensure good catalytic property toward I_-/I_3^- reduction, the CV characteristic curves shows oxidation/reduction peaks. The peaks at a positive voltage, denoted by peak Pt_{OX} and C_{OX} represent the oxidation reaction of iodide to triiodide (I_- to I_3^-) and at a negative branch,

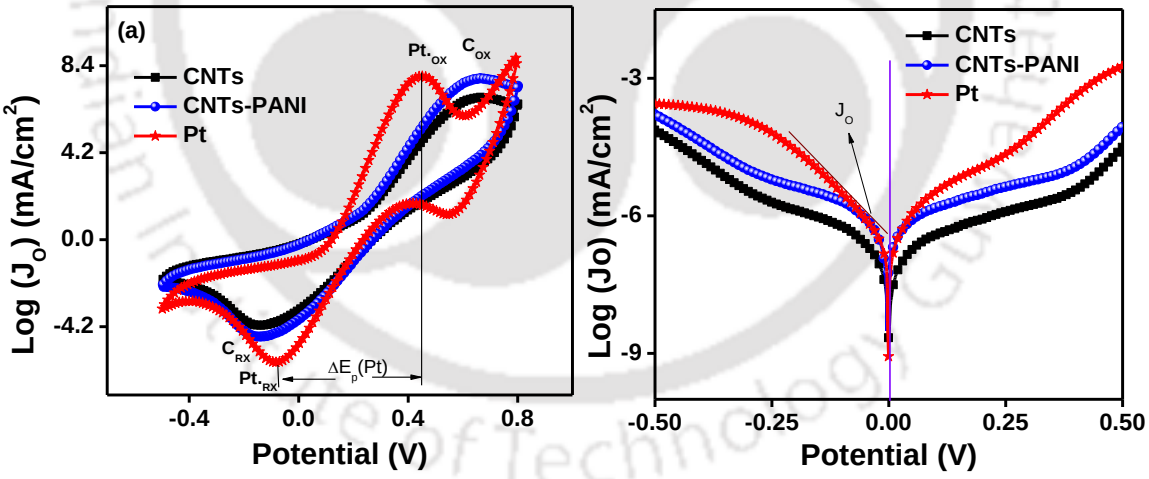

Figure 6. 4: (a) Cyclic voltammetry measurement of CNTs, CNTs-PANI and Pt CEs in an acetonitrile solution consist of 0.5 mM I_2, 0.1 M $LiClO_4$, and 5 mM LiI and (b) Tafel plot of DSSCs based on corresponding CEs.

indicated by peak Pt_{RX} and C_{RX}, defined the reduction reaction of triiodide to iodide (I_3^- to I_-). The peak current (I_P) and peak-to-peak separation (ΔE_P) are used to determine the electrocatalytic performances of CEs. A lower ΔE_P and a higher I_P specify a better catalytic activity for the triiodide (I_3^-) reduction process. In other words, the redox reaction occurred

at a lower potential on Pt surface than that of CNTs, demonstrating a lower over-potential of Pt electrode. The value of I_P and ΔE_P are listed in Table 6.3. According to the value of ΔE_P and I_P, Pt electrode exhibits better electrocatalytic properties than CNTs-PANI in DSSCs.

Table 6. 3: Electrochemical properties of CNTs, CNTs-PANI and Pt CEs.

Counter electrodes	**I_P (mA/cm^2), positive**	**I_P (mA/cm^2), negative**	**ΔE_P (V)**
CNTs	6.85	-4.08	0.63-0.14=0.49
CNTs-PANI	7.77	-4.62	0.63-0.12= 0.47
Pt	8.00	-5.97	0.45-0.09=0.36

To further reconfirm the catalytic and interfacial charge transfer characteristics of DSSCs based on CNTs, CNTs-PANI, and Pt CEs, Tafel measurements was performed. Theoretically, Tafel plot can be separated into three zones: Tafel (middle zone with sharp slope, $|V|<$ 0.01V); polarization (low potential, $|V|<$ 0.12V) and diffusion (horizontal, $|V|<$ 0.40V) [21][61]. Tafel plots measured the logarithmic current density versus voltage (V) and was illustrated in Fig. 6.4(b). Pt coated CE possesses higher exchange current density (J_O) than carbon, which indicates that Pt catalyst has faster electron migration ability at CE/electrolyte interface. The higher J_O value is attributed to excellent electrocatalytic activity. The relation between J_o and R_{ct} can be described according to following equation.

$$J_o = RT/nFR_{\mathrm{ct}} \qquad 6.2$$

where, n (=4) is the number of electron in the electrochemical reaction, F is Faraday's constant, R_{ct} is the charge transfer resistance, R is the gas constant, and T is the absolute temperature. J_o is reciprocal to Rct, this result is consistent with the obtained result of Rct from EIS data. The limiting diffusion current density (J_{Lim}) obtained at high potential from Tafel plot and its value is directly related to the diffusion coefficient of $I_3^-/I_$redox couples in the electrolyte. The J_{Lim} values from the Tafel plot are in the order of CNTs< CNTs-PANI< Pt and their corresponding values are -4.15, -3.83 and -3.53 mA/cm^2, respectively. The results of CV and Tafel polarization is well-assorted with the J-V characteristics and EIS data.

Raman Analysis

RAMAN spectroscopy (LabRam, HORIBA JOBIN YVON) characterised the chemical structures of CEs materials. It is a powerful tool and is highly sensitive to carbon-carbon bonds. It reveals deep information about their structures and capable of discerning even slight changes in structure [62]. Based on the results of RAMAN spectra in Fig. 6.5(a), the sample consists of single-walled carbon nanotube (SWNT) and multi-walled carbon nanotube (MWNT). The presence of SWNTs was confirmed from the radial breathing modes (RBM) in lower frequency at 219.40 cm^{-1} and 257.20 cm^{-1}, respectively. The peaks at 1338 cm^{-1} 1570 cm^{-1}, 2664 cm^{-1} corresponding to D, G and 2D band of carbon structures were separately shown in Fig. 6.5(b) [63-67]. Usually the D band defines the structural defects and G band indicates the tangential C=C stretching and the vibrations of sp^2 hybridization [68]. Defects generate more surface area that is useful for constructing an effective catalytic activity. After doping, we observed a strong peak intensity of D band compared to that of the pristine CNTs, which reveals that sp^3 hybridized carbons were generated as the functional groups and were attached to the surfaces of the CNTs. The peak intensity ratio between the D and the G bands (I_D/I_G) were 0.125 and 0.168, respectively. The intensity ratio (I_D/I_G) was increased for CNTs-PANI due to the increase in number of defect sites in the edge plane which modified surface structures of CNTs

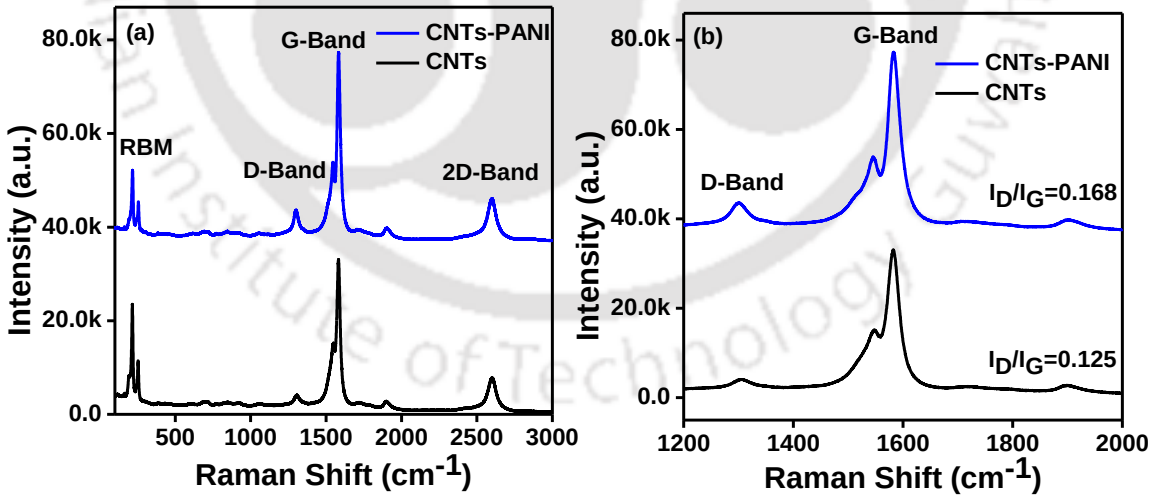

Figure 6. 5: Raman spectra of (a) CNTs and (b) CNTs-PANI films coated on FTO glass.

Surface morphology

The surface morphology of CNTs, CNTs-PANI, and Pt coated on FTO glass substrates were studied using FESEM and AFM. Fig. 6.6(a, b, and c) shows the FESEM image of the corresponding electrode and we observed a different structure of morphologies, specially CNTs based and Pt CE. As shown in the FESEM images, the surface of CNTs has a fibrous, tangled porous structure and initially it has slightly agglomerated, but they became well separated after being composited with PANI. In addition, we observed the surface of CNTs-PANI became rougher, which enhanced the electronic transport efficiency of CE [69-71]. These results suggest that the interaction between CNTs-PANI became sufficiently strong to allow the agglomerated CNTs to disperse. On the other hand, the Pt has an island or irregular stone masonry wall like compact structure [40]. The unique structure of CEs made the catalytic film highly active and transfer electrons faster in the devices to show better

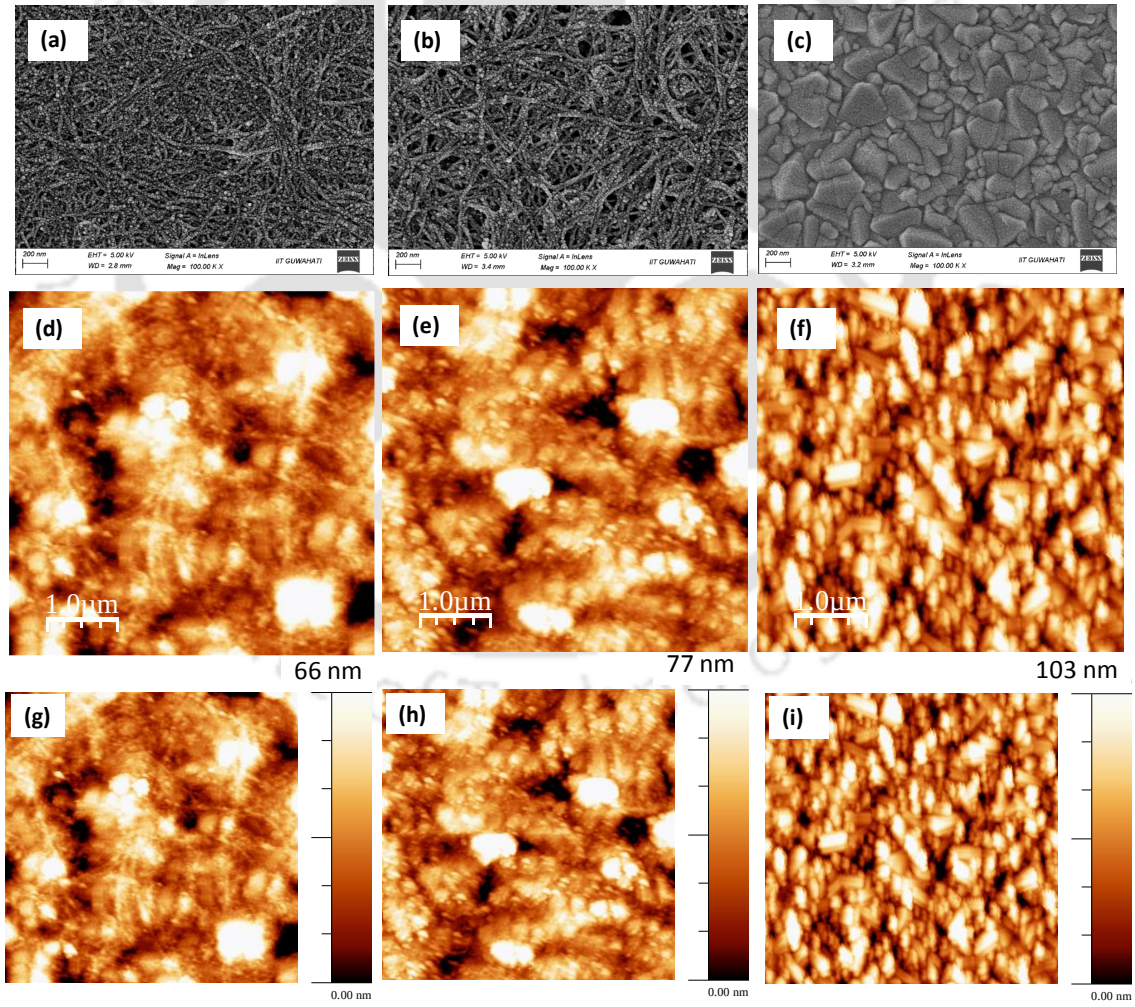

Figure 6. 6: FESEM images of (a) CNTs (b) CNTs-PANI and (c) Pt coated on FTO glass substrate. Corresponding 2D and 3D AFM images (d-i).

performance. The 2D (Fig. 6.6(d, e and f)) and 3D (Fig. 6.6(g, h and i)) AFM images of CNTs, CNTs-PANI and Pt were analyzed using WSxM software. Based on the AFM results, the counter electrodes have different root mean square (RMS) roughness factor and were in the order of CNTs < CNTs-PANI< Pt with corresponding value 12, 15 and 23 nm, respectively. The degree of surface roughness quantifies the effective surface area of the film and it has a significant impact on electrochemical properties. There is a direct correlation between the surface area and electrocatalytic activity, higher the effective surface area better the electrocatalytic activity [72-73]. CNTs-PANI catalyst layer possesses a larger surface area than CNTs, which offer better electrocatalytic active sites for reducing the triiodide ions. These trends were clearly seen in the J–V curves, EIS and CV analysis.

6.4 Conclusion

In summary, cost-effective CNTs and CNTs-PANI composite materials were introduced as a catalyst layer to replace the expensive Pt in the DSSCs. The DSSCs performance increased from 4.83 to 6.67% after CNTs was incorporated with conducting polymer PANI. The enhancement in conversion efficiency is ascribed to a more efficient charge transfer by suppressing the charge recombination process. The deposited CNTs-PANI layer exhibited a more fibrous porous nanostructure with higher surface roughness than CNTs. The enhanced surface area leads to intimate contact with the electrolytes and effectively increases the rate of reaction from triiodide to iodide ions conversion. This device result offers a promising reality of commercial application for DSSCs with cost-effective and mass manufacturing solar technology. Although the PCE of DSSC with CNTs-PANI was lower than that of Pt CE, the inexpensive cost, excellent photoelectric properties, and easily available materials for large-scale production allow the CNTs based CEs to be an alternative material for DSSCs.

6.5 References

[1] E. Akman, H.S. Karapinar, Electrochemically stable, cost-effective and facile produced selenium@activated carbon composite counter electrodes for dye-sensitized solar cells, Sol. Energy. 234 (2022) 368–376. doi:10.1016/j.solener.2022.02.011.

[2] M. Gulen, Lithium perchlorate-assisted electrodeposition of CoS catalyst surpassing the performance of platinum in dye sensitized solar cell, J. Mater. Sci. 57 (2022) 3513–3524. doi:10.1007/s10853-021-06752-x.

[3] C. Dawo, H. Chaturvedi, Recent advances in the development of flexible dye-sensitized solar cells: fabrication, challenges and applications-a review, Flex. Print. Electron. 8 (2023). doi:10.1088/2058-8585/acb660.

[4] G. Veerappan, K. Bojan, S.W. Rhee, Sub-micrometer-sized graphite as a conducting and catalytic counter electrode for dye-sensitized solar cells, ACS Appl. Mater. Interfaces. 3 (2011) 857–862. doi:10.1021/am101204f.

[5] A.F.-S. Marcel Zambrzycki , Robert Piech, Sonia Ruiz Raga, Monica Lira-Cantu, Hierarchical carbon nanofibers/carbon nanotubes/NiCo nanocomposites as novel highly effective counter electrode for dye-sensitized solar cells: A structure-electrocatalytic activity relationship study, Car. 203 (2023) 97–110. doi:https://doi.org/10.1016/j.carbon.2022.11.047.

[6] M. Mirzaei, M.B. Gholivand, Design of hierarchical MoSe2-NiSe2 nanotubes anchored on carbon nanotubes as a counter electrode for dye-sensitized solar cells, J. Taiwan Inst. Chem. Eng. 135 (2022) 104378. doi:10.1016/j.jtice.2022.104378.

[7] H. Kim, H. Choi, S. Hwang, Y. Kim, M. Jeon, Fabrication and characterization of carbon-based counter electrodes prepared by electrophoretic deposition for dye-sensitized solar cells, Nanoscale Res. Lett. 7 (2012) 2–5. doi:10.1186/1556-276X-7-53.

[8] M. Wang, A.M. Anghel, N.C. Ha, N. Pootrakulchote, CoS Supersedes Pt as Efficient Electrocatalyst for Triiodide Reduction in Dye-Sensitized Solar Cells, J. AM. CHEM. SOC. 131 (2009) 15976–15977.

[9] and S.E. Abdullah Yildiz, Takwa Chouki, Aycan Atli, Moussab Harb, Sammy W. Verbruggen, Rajeshreddy Ninakanti, Efficient Iron Phosphide Catalyst as a Counter Electrode in Dye- Sensitized Solar Cells, ACS Appl. Energy Mater. 4 (2021) 10618−10626. doi:https://doi.org/10.1021/acsaem.1c01628.

[10] M. Wu, Q. Zhang, J. Xiao, C. Ma, X. Lin, C. Miao, Y. He, Y. Gao, A. Hagfeldt, T. Ma, Two flexible counter electrodes based on molybdenum and tungsten nitrides for dye-sensitized solar cells, J. Mater. Chem. 21 (2011) 10761–10766. doi:10.1039/c1jm11422k.

[11] H. Zhou, Y. Shi, D. Qin, J. An, L. Chu, C. Wang, Y. Wang, W. Guo, L. Wang, T. Ma, Printable fabrication of Pt-and-ITO free counter electrodes for completely flexible quasi-solid dye-sensitized solar cells, J. Mater. Chem. A. 1 (2013) 3932–3937.

doi:10.1039/c3ta00960b.

[12] M.S. Wu, J.F. Wu, Pulse-reverse electrodeposition of transparent nickel phosphide film with porous nanospheres as a cost-effective counter electrode for dye-sensitized solar cells, Chem. Commun. 49 (2013) 10971–10973. doi:10.1039/c3cc45670f.

[13] Y. Wang, M. Wu, X. Lin, Z. Shi, A. Hagfeldt, T. Ma, Several highly efficient catalysts for Pt-free and FTO-free counter electrodes of dye-sensitized solar cells, J. Mater. Chem. 22 (2012) 4009–4014. doi:10.1039/c2jm15182k.

[14] K.M. Lee, C.Y. Hsu, P.Y. Chen, M. Ikegami, T. Miyasaka, K.C. Ho, Highly porous PProDOT-Et2 film as counter electrode for plastic dye-sensitized solar cells, Phys. Chem. Chem. Phys. 11 (2009) 3375–3379. doi:10.1039/b823011k.

[15] Q. Qin, J. Tao, Y. Yang, Preparation and characterization of polyaniline film on stainless steel by electrochemical polymerization as a counter electrode of DSSC, Synth. Met. 160 (2010) 1167–1172. doi:10.1016/j.synthmet.2010.03.003.

[16] X. Yin, F. Wu, N. Fu, J. Han, D. Chen, P. Xu, M. He, Y. Lin, Facile synthesis of poly(3,4-ethylenedioxythiophene) film via solid-state polymerization as high-performance Pt-free counter electrodes for plastic dye-sensitized solar cells, ACS Appl. Mater. Interfaces. 5 (2013) 8423–8429. doi:10.1021/am401719e.

[17] J.M. Pringle, V. Armel, D.R. MacFarlane, Electrodeposited PEDOT-on-plastic cathodes for dye-sensitized solar cells, Chem. Commun. 46 (2010) 5367–5369. doi:10.1039/c0cc01400a.

[18] M.G. Andreas Kay, Low cost photovoltaic modules based on dye sensitized nanocrystalline titanium dioxide and carbon powder, Sol. Energy Mater. Sol. Cells. 44 (1996) 99–117.

[19] M.G. Takurou N. Murakami, Counter electrodes for DSC: Application of functional materilas as catalysts, Inorganica Chim. Acta. 361 (2008) 572–580.

[20] K.D.M.S.P.K. Kumarasinghe, G.R.A. Kumara, R.M.G. Rajapakse, D.N. Liyanage, K. Tennakone, Activated coconut shell charcoal based counter electrode for dye-sensitized solar cells, Org. Electron. 71 (2019) 93–97. doi:10.1016/j.orgel.2019.05.009.

[21] C. Gao, H. Wang, Z. Hu, M. Wu, A novel carbon bead string cathode for dye-sensitized solar cells, Electrochim. Acta. 255 (2017) 9–14. doi:10.1016/j.electacta.2017.09.132.

[22] Y.Y. Li, C.T. Li, M.H. Yeh, K.C. Huang, P.W. Chen, R. Vittal, K.C. Ho, Graphite with Different Structures as Catalysts for Counter Electrodes in Dye-sensitized Solar Cells, Electrochim. Acta. 179 (2015) 211–219. doi:10.1016/j.electacta.2015.06.007.

[23] H.A. M.A.K.L. Dissanayake, J.M.K.W. Kumari, G.K.R. Senadeera, T. Jaseetharan, Janith Weerasinghe, A low-cost, vein graphite_tin oxide nanoparticles based composite counter electrode for efficient dye-sensitized solar cells, Mater. Sci. Eng. B. 273 (2021) 115440. doi:https://doi.org/10.1016/j.mseb.2021.115440.

[24] K.M. Kiyoaki Imoto, Kohshin Takahashi, Takahiro Yamaguchi, Teruhisa Komura, Jun-ichi Nakamura, High-performance carbon counter for dye-sensitized solar cells, Sol. Energy

Mater. Sol. Cells. 79 (2003) 459–469.

[25] S.Z. Guiqiang Wang, Wei Xing, Application of mesoporous carbon to counter electrode for dye-sensitized solar cells, J. Power Sources. 194 (2009) 568–573.

[26] L.K.B. and J.S.Y. Sung Min Cha, Goli Nagaraju, S. chandra Sekhar, Fallen leaves derived honeycomb-like porous carbon as a metal-free and low cost counter electrode for dye sensitized solar cell with excellent tri-iodide reduction, J. Colloid Interface Sci. 513 (2018) 843–851.

[27] M.W. Hongyue Guo, Yajing Zhu, Wenyan Li, Haikuo Zheng, Kezhong Wu, Keqiang Ding, Bei Ruan, Anders Hagfeldt, Tingli Ma, Synthesis of highly effective Pt/carbon fiber composite counter electrode catalyst for dye-sensitized solar cells, Electrochim. Acta. 176 (2015) 997–1000.

[28] C.W. Ju Qiu, Dayong He, Hao Wang, Wenyan Li, Bolun Sun, Yuying Ma, Xiaofeng Lu, Morphology-controlled fabrication of NiCo2S4 nanostructures decorating carbon nanofibers as low-cost counter electro.pdf, Electrochim. Acta. 367 (2021) 137451. doi:https://doi.org/10.1016/j.electacta.2020.137451.

[29] K. Lukaszkowicz, M. Szindler, A. Drygała, L.A. Dobrzański, M. Prokopiuk vel Prokopowicz, I. Pasternak, A. Przewloka, M.M. Szindler, M. Domański, Graphene-based layers deposited onto flexible substrates: Used in dye-sensitized solar cells as counter electrodes, Appl. Surf. Sci. 424 (2017) 157–163. doi:10.1016/j.apsusc.2017.02.040.

[30] K. Suzuki, M. Yamaguchi, M. Kumagai, S. Yanagida, Application of carbon nanotubes to counter electrodes of dye-sensitized solar cells, Chem. Lett. 32 (2003) 28–29. doi:10.1246/cl.2003.28.

[31] S.R. Shengjie Peng, Yongzhi wu, Peining Zhu, Velmurugan Thavasi, Subodh G. Mhaisalkar, Facile fabrication of polypyrrole/functionalized multiwalled carbon nanotubes composite as counter electrodes in low-cost dye-sensitized solar cells, J. Photochem. Photobiol. A Chem. 223 (2011) 97–102.

[32] J. Wu, Z. Lan, J. Lin, M. Huang, Y. Huang, L. Fan, G. Luo, Y. Lin, Y. Xie, Y. Wei, Counter electrodes in dye-sensitized solar cells, Chem. Soc. Rev. 46 (2017) 5975–6023. doi:10.1039/c6cs00752j.

[33] and H.P. Anders Hagfeldt, Gerrit Boschloo, Licheng Sun, Lars Kloo, Dye-Sensitized Solar Cells, Chem. Rev. 110 (2010) 6595–6663.

[34] K. Miettunen, M. Toivola, G. Hashmi, J. Salpakari, I. Asghar, P. Lund, A carbon gel catalyst layer for the roll-to-roll production of dye solar cells, Carbon N. Y. 49 (2011) 528–532. doi:10.1016/j.carbon.2010.09.052.

[35] N. Shahzad, Lutfullah, T. Perveen, D. Pugliese, S. Haq, N. Fatima, S.M. Salman, A. Tagliaferro, M.I. Shahzad, Counter electrode materials based on carbon nanotubes for dye-sensitized solar cells, Renew. Sustain. Energy Rev. 159 (2022) 112196.

doi:10.1016/j.rser.2022.112196.

[36] M. Aftabuzzaman, C. Lu, H.K. Kim, Recent progress on nanostructured carbon-based counter/back electrodes for high-performance dye-sensitized and perovskite solar cells, Nanoscale. 12 (2020) 17590–17648. doi:10.1039/d0nr04112b.

[37] M.M.B. Gholivand, Synthesis of ruthenium sulfide nanoparticles decorated on reduced graphene oxide/multi-walled carbon nanotubes as a catalytic counter electrode for dye-sensitized solar cells exceeding 13 % efficiency, Sol. Energy. 242 (2022) 212–224. doi:https://doi.org/10.1016/j.solener.2022.07.010.

[38] D.W. Zhang, X.D. Li, S. Chen, F. Tao, Z. Sun, X.J. Yin, S.M. Huang, Fabrication of double-walled carbon nanotube counter electrodes for dye-sensitized solar sells, J. Solid State Electrochem. 14 (2010) 1541–1546. doi:10.1007/s10008-009-0982-3.

[39] W.J. Lee, E. Ramasamy, D.Y. Lee, J.S. Song, Efficient dye-sensitized solar cells with catalytic multiwall carbon nanotube counter electrodes, ACS Appl. Mater. Interfaces. 1 (2009) 1145–1149. doi:10.1021/am800249k.

[40] G. Veerappan, W. Kwon, S.W. Rhee, Carbon-nanofiber counter electrodes for quasi-solid state dye-sensitized solar cells, J. Power Sources. 196 (2011) 10798–10805. doi:10.1016/j.jpowsour.2011.09.004.

[41] J.G. Nam, Y.J. Park, B.S. Kim, J.S. Lee, Enhancement of the efficiency of dye-sensitized solar cell by utilizing carbon nanotube counter electrode, Scr. Mater. 62 (2010) 148–150. doi:10.1016/j.scriptamat.2009.10.008.

[42] K.H. Park, S.J. Kim, R. Gomes, A. Bhaumik, High performance dye-sensitized solar cell by using porous polyaniline nanotubes as counter electrode, Chem. Eng. J. 260 (2015) 393–398. doi:10.1016/j.cej.2014.08.105.

[43] C. Dawo, H. Chaturvedi, High performance PANI-PSSNa doped counter electrode for dye-sensitized solar cells, Appl. Phys. A Mater. Sci. Process. 128 (2022) 1–9. doi:10.1007/s00339-022-05739-y.

[44] M.M. Mohsen Khodadadi Yazdi, Hoda Saeidi, Payam Zarrintaj, Mohammad Reza Saeb, PANI-CNT nanocomposites, in: Fundamntal Emerg. Appl. Polyaniline, Elsevier, 2019: pp. 143–163.

[45] H. Wang, G. Liu, X. Li, P. Xiang, Z. Ku, Y. Rong, M. Xu, L. Liu, M. Hu, Y. Yang, H. Han, Highly efficient poly(3-hexylthiophene) based monolithic dye-sensitized solar cells with carbon counter electrode, Energy Environ. Sci. 4 (2011) 2025–2029. doi:10.1039/c0ee00821d.

[46] H. Lee, Y. Cho, Y. Yeo, S. Park, W.S. Shin, S. Jin, J. Lee, M. Kim, DYE-SENSITIZED SOLAR CELLS WITH P3HT / FULLERENE DERIVATIVES, (2006) 259–262.

[47] C.P. Lee, K.Y. Lai, C.A. Lin, C.T. Li, K.C. Ho, C.I. Wu, S.P. Lau, J.H. He, A paper-based electrode using a graphene dot/PEDOT:PSS composite for flexible solar cells, Nano Energy.

36 (2017) 260–267. doi:10.1016/j.nanoen.2017.04.044.

[48] G.T. Yue, J.H. Wu, Y.M. Xiao, J.M. Lin, M.L. Huang, L.Q. Fan, Y. Yao, A dye-sensitized solar cell based on PEDOT: PSS counter electrode, Chinese Sci. Bull. 58 (2013) 559–566. doi:10.1007/s11434-012-5352-3.

[49] Z.Y. Jun Zhang, Xiaoxue Li, Wei Guo, Tubshin Hreida, Jinfeng Houc, Haiquan Su, Electropolymerization of a poly(3,4-ethylenedioxythiophene) and functionalized, multi-walled, carbon nanotubes counter electrode for dye-sensitized solar cells and characterization of its performance, Electrochim. Acta. 56 (2011) 3147–3152.

[50] B. Fan, X. Mei, K. Sun, J. Ouyang, Conducting polymer/carbon nanotube composite as counter electrode of dye-sensitized solar cells, Appl. Phys. Lett. 93 (2008) 1–4. doi:10.1063/1.2996270.

[51] Y. Qiu, S. Lu, S. Wang, X. Zhang, S. He, T. He, High-performance polyaniline counter electrode electropolymerized in presence of sodium dodecyl sulfate for dye-sensitized solar cells, J. Power Sources. 253 (2014) 300–304. doi:10.1016/j.jpowsour.2013.12.061.

[52] K. Saranya, M. Rameez, A. Subramania, Developments in conducting polymer based counter electrodes for dye-sensitized solar cells - An overview, Eur. Polym. J. 66 (2015) 207–227. doi:10.1016/j.eurpolymj.2015.01.049.

[53] H.K. Swarup Biswas, Jaebum Jeong, Jae Won Shim, Improved charge transport in PANI: PSS by the uniform dispersion of silver nanoparticles, Appl. Surf. Sci. 483 (2019) 819–826.

[54] K. Chiou, S. Byun, J. Kim, J. Huang, Additive-free carbon nanotube dispersions, pastes, gels, and doughs in cresols, Proc. Natl. Acad. Sci. U. S. A. 115 (2018) 5703–5708. doi:10.1073/pnas.1800298115.

[55] M.G. Qing Wang, Jacques-E. Moser, Electrochemical Impedance Spectroscopic Analysis of Dye- Sensitized Solar Cells, J. Phys. Chem. B. 109 (2005) 14945–14953. doi:10.1002/ijch.201500007.

[56] P.B. Rahul Kumar, Siva Sankar Nemala, Sudhanshu Mallick, Synthesis and characterization of carbon based counter electrode for dye sensitized solar cells (DSSCs) using sugar free as a carbon metrials, Sol. Energy. 144 (2017) 215–220. doi:10.1016/j.jallcom.2018.03.181.

[57] S.N.F. Zainudin, H. Abdullah, M. Markom, Electrochemical studies of tin oxide based-dye-sensitized solar cells (DSSC): a review, J. Mater. Sci. Mater. Electron. 30 (2019) 5342–5356. doi:10.1007/s10854-019-00929-6.

[58] X. Tao, P. Ruan, X. Zhang, H. Sun, X. Zhou, Microsphere assembly of TiO_2 mesoporous nanosheets with highly exposed (101) facets and application in a light-trapping quasi-solid-state dye-sensitized solar cell, Nanoscale. 7 (2015) 3539–3547. doi:10.1039/c4nr06865c.

[59] Y. Zhang, P. Wang, T. Zhang, B. Gou, High-Efficiency Dye-Sensitized Solar Cells Based on Kesterite Cu2ZnSnSe4Inlaid on a Flexible Carbon Fabric Composite Counter Electrode, ACS Omega. 5 (2020) 24898–24905. doi:10.1021/acsomega.0c03686.

[60] K.B. Bhojanaa, S.K.N. Santhosh, P.V.M. Senthil, P.P. Ramasamy, Enhanced electrochemical and photovoltaic performance for - MoO 3 nanorods at different calcination temperature based counter electrode in Pt ‑ free dye ‑ sensitized solar cells applications, SN Appl. Sci. 2 (2020) 1750.

[61] W. Shao, W. Wu, High-Efficiency (Over 10%) Parallel Tandem Dye-Sensitized Solar Cells Based on Tri-Carbon Electrodes, Trans. Tianjin Univ. (2022) 414–422. doi:10.1007/s12209-022-00318-x.

[62] K. Susmitha, M.M. Kumari, A.J. Berkmans, M.N. Kumar, L. Giribabu, S. V. Manorama, M. Raghavender, Carbon nanohorns based counter electrodes developed by spray method for dye sensitized solar cells, Sol. Energy. 133 (2016) 524–532. doi:10.1016/j.solener.2016.03.059.

[63] S. Kim, O. Dovjuu, S.-H. Choi, H. Jeong, J.-T. Park, Photovoltaic Characteristics of Multiwalled Carbon Nanotube Counter-Electrode Materials for Dye-Sensitized Solar Cells Produced by Chemical Treatment and Addition of Dispersant, Coatings. 9 (2019) 250. doi:10.3390/coatings9040250.

[64] A. Mukhtar, X.M. Cao, T. Mehmood, D. shuang Wang, K. ming Wu, Structural characterization of self-assembled chain like Fe-FeOx Core shell nanostructure, Nanoscale Res. Lett. 14 (2019). doi:10.1186/s11671-019-3128-2.

[65] A.E. Lewandowska, M.A. Banares, F. Tielens, M. Che, S. Dzwigaj, Different kinds of tetrahedral v species in vanadium-containing zeolites evidenced by diffuse reflectance UV-vis, raman, and periodic density functional theory, J. Phys. Chem. C. 114 (2010) 19771–19776. doi:10.1021/jp107589d.

[66] J. Etchepare, M. Merian, L. Smetankine, Vibrational normal modes of SiO2. I. α and βquartz, J. Chem. Phys. 60 (1974) 1873–1876. doi:10.1063/1.1681287.

[67] V. Ranieri, D. Bourgogne, S. Darracq, M. Cambon, J. Haines, O. Cambon, R. Le Parc, C. Levelut, V. Ranieri, D. Bourgogne, S. Darracq, M. Cambon, J. Haines, Raman scattering study of alpha-quartz and Si (1-x) GexO2 solid solutions To cite this version : HAL Id : hal-00434422, Phys. Rev. B. 79 (2009) 224304–8. doi:10.1103/PhysRevB.79.224304.

[68] L. Bokobza, J.-L. Bruneel, M. Couzi, Raman Spectra of Carbon-Based Materials (from Graphite to Carbon Black) and of Some Silicone Composites, C. 1 (2015) 77–94. doi:10.3390/c1010077.

[69] L. Saad, M.Y. Feteha, S. Ebrahim, M. Soliman, T.M. Abdel-Fattah, Dye Sensitized Solar Cell Based on Polyaniline-Carbon Nanotubes/Graphite Composite, ECS J. Solid State Sci. Technol. 3 (2014) M55–M60. doi:10.1149/2.0051410jss.

[70] S.M. Haihong Niu, Shengxian Qin, Xiaoli Mao, Shouwei Zhang, Renbao Wang, Lei Wan, Jinzhang Xu, Axle-sleeve Structured MWCNTs_Polyaniline Composite Film as Cost-

effective Counter-Electrodes for High Efficient Dye-Sensitized Solar Cells _ Elsevier Enhanced Reader.pdf, Electrochim. Acta. 121 (2014) 285–293. doi:https://doi.org/10.1016/j.electacta.2013.12.059.

[71] T.-Y. Jeng-YuLin, Jen-HungLiao, A composite counter electrode of CoS_MWCNT with high electrocatalytic activity for dye-sensitized solar cells, Electrochem. Commun. 13 (2011) 977–980.

[72] W. Li, G. Long, Q. Chen, Q. Zhong, High-efficiency layered sulfur-doped reduced graphene oxide and carbon nanotube composite counter electrode for quantum dot sensitized solar cells, J. Power Sources. 430 (2019) 95–103. doi:10.1016/j.jpowsour.2019.05.020.

[73] S. Cho, S.H. Hwang, C. Kim, J. Jang, Polyaniline porous counter-electrodes for high performance dye-sensitized solar cells, J. Mater. Chem. 22 (2012) 12164–12171. doi:10.1039/c2jm30594a.

CHAPTER 7 Low temperature flexible DSSC

UV Ozone based rapid low temperature fabrication of flexible dye sensitized solar cells

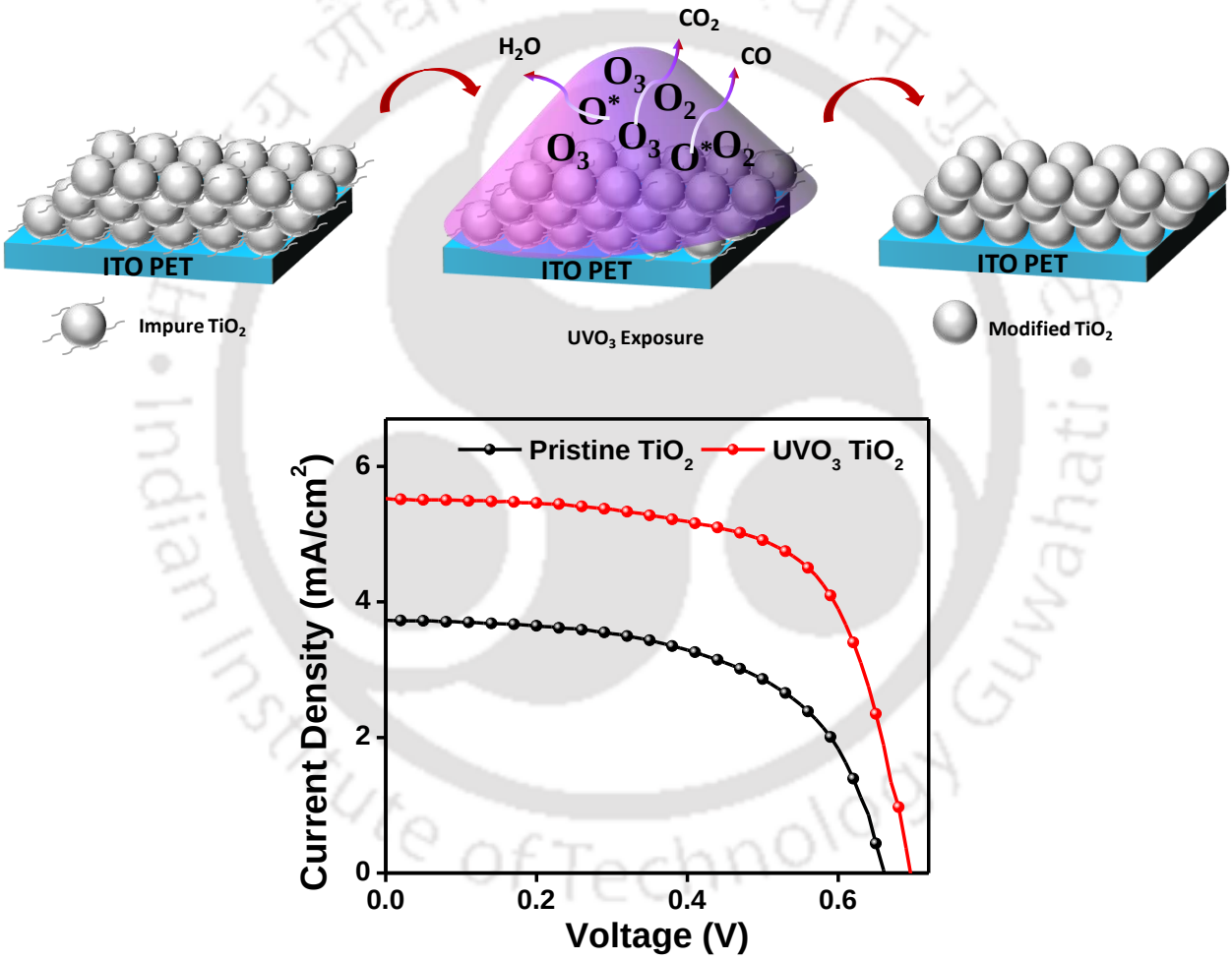

Chandan Dawo, Maimur Hossain, Parameswar Krishnan Iyer, Harsh Chaturvedi, Synthetic Metals, Volume 291, 2022, https://doi.org/10.1016/j.synthmet.2022.117172.

7.1 Introduction

Flexible dye sensitized solar cells (FDSSCs) have attracted incredible attention globally for the last two decades because of its unique characteristics like lightweight, flexibility, cost-effective and easy processing [1-5]. It has enormous potential to be utilized in wearable electronic, large scale industrial roofing and portable powering devices [6-8]. Flexible substrates such as stainless steel (StS) [9-10], Tatanium (Ti) [11-12], and plastic usually ITO coated polyethylene naphthalate (PEN) and polyethylene terephthalate (PET)[13-14] etc., were used to prepare electrodes for FDSSCs. The traditional DSSCs required glass substrates which have a very high temperature resistance above 450 °C to remove organic binder used in highly viscous TiO_2 paste and reported the highest PCE up to 14.30% [15] The electrodes with flexible metal substrates can also be annealed at high temperatures to improve the interconnection of ETL (TiO_2 particles), electronic connection leading to better charge transfer and collection [16]. Among the flexible metallic materials, StS and Ti foil is found to be chemically stable whereas, copper and aluminium are dissolved in electrolytes [17-18]. Park et al. prepared photoanode by introduced a thin TiOx layer by spin coating on the ITO and SiOx-sputtered StS substrate to controlling the dark current, the efficiency of cell fairly achieved 8.6% with Pt coated ITO PET counter electrode (CE) [10]. Ito et al. developed FDSSCs, which achieved relatively high efficiencies up to 7.2% with metallic Ti substrates [19]. Liu et al. fabricated FDSSC on Ti substrate by Er^{3+} and Yb^{3+} codoped with TiO_2 photoanode and obtained efficiency of 8.1% [20]. Yun et al. fabricated photoanode on Ti substrate and Pt coated FTO glass as CE and obtained an efficiency of 9.20%, [21]. To best of our knowledge, the highest efficiency of FDSSCs is 10.28% on Ti wire substrate [22] These method of FDSSCs fabrication is not energy efficient due to the involvement of high processing temperature [23-24]. Therefore, the replacement of high temperature resistance substrates by low processing temperature i.e., plastic is highly encouraging to reduce its manufacturing cost. Also, the use of plastic substrate enables solution-based printing and coating techniques that are cost-effective, improve productivity, and are compatible with R2R manufacturing process [25]. The preparation of electrodes on plastic substrates limits their maximum processing temperature up to 150 °C due to thermal instability. Therefore, the electron transport layer (ETL) were usually prepared without binder [26]. Preparing TiO_2 paste without an organic binder is the biggest challenge in fabricating photoanode. The most commonly used solvent alcohol or water-based binder-free titanium paste usually exhibits poor viscosity. Paste with high viscosity is preferred for

smooth printing of TiO_2 film without crack. Investigation on various factors associated with paste for making highly viscous has been carried out with the addition of hydrochloric acid, water, and ammonia that changed the viscosity vigorously. Viscosity enhanced the inter-particle connectivity that improved device performance compared to ethanol-based pastes. With modified paste, the power conversion efficiencies of 4.9% were achieved for FDSSC [27]. Park et al. [28] also reported a similar kind of work, prepared binder-free highly viscous paste by adding ammonia through chemical sintering and obtained a power conversion efficiency of 2.55%. The low temperature processed TiO_2 based ETL need additional processing step to improve the mechanical stability and electron transport property. Several low temperature post processing techniques such as microwave irradiation [29-30], mechanical compression [25, 31-32], cold isostatic pressing (CIP) [33], lift-off techniques [7], and building block [34-35] etc., have been successfully applied for enhancing the performance of FDSSCs. Compared to conventional heating, microwaves heating is much more efficient in energy transfer as it directly interacts with the contents. Uchida et al.[29] sintered TiO_2 layer on ITO PET in a microwave oven at 2.45 GHz and 28 GHz frequency, and fairly obtained a conversion efficiency of 0.74% and 2.2% respectively for FDSSCs. The high frequency heating improved the efficiency of the device is mainly due to a noticeable enhancement in the current density. An external force was applied to the low-temperature processed TiO_2 film coated on a flexible substrate to enhance 3D connectivity of TiO_2 particles. Weerasinghe et al. processed TiO_2 photoanode for flexible ITO coated PET with P25 powder by this method, and achieved a PCEs of 6.30% [33]. In Japan Arakawa et al. reported the highest efficiency for plastic DSSCs by applying compression techniques to TiO_2 particles (20 and 100 nm). Optimizing the TiO_2 film thickness around 10 μm and obtained maximum power conversion efficiency of 8.10% [25]. However, mechanically compressed low temperature TiO_2 film is not chemically bonded but only a physical contact. This method still affected the electron transport properties in devices, therefore FDSSCs showed lower efficiency compared to rigid DSSCs. In CIP, the TiO_2 film is sealed in an elastic medium in a vacuum, and high pressure is applied in all directions through a liquid medium. Weerasinghe et al. processed TiO_2 photoanode for flexible ITO coated PET with P25 powder by CIP method, have fairly achieved high PCEs of 6.30% and 7.40% for simulated sun lights power of 100 and 15 mW/cm^2, respectively [33] Dürr group presented another new approach, allowing the use of paste containing organic binders and annealing at high temperatures. In this technique, a thin layer of gold on glass substrate approximately 10-20 nm is prepared and

above that a TiO_2 layer is formed. The deposited film is sintered at 450 °C to obtain a high-quality mesoporous layer. By dissolving the gold layer in iodine/iodide, the TiO_2 layer can be removed from the glass substrate and then transferred on a flexible substrate; this technique is known as lift-off or building block. A thin layer of TiO_2 nanoparticle average 10 nm is applied on a flexible substrate for better bonding of TiO_2 transfer layer. The final contact is established using the compression method between adhesion and the porous layer. By this technique an efficiency of 5.8% has been reported on flexible PET substrate [7]. Huang et al. fabricated FDSSCs on ITO PEN using the building blocks technique that showed much higher conversion efficiency (6.59%) compared to the conventional method (4.94%) made from the same TiO_2 nanoparticles (18 nm) [36]. However, this technique is quite complex, and the TiO_2 films can be easily broken during the transfer process.

Herein, we have developed a generic approach to fabricate low temperature processed TiO_2 film based efficient FDSSCs. TiO_2 precursor suspension using P25 and small amount of titanium isopropoxide (TTIP) as a binder in a mixture of ethanol and de-ionized (DI) water were utilized for coating TiO_2 film. An optimal quantity of TTIP with TiO_2 nanoparticles assisted the formation of uniform and mechanically stable film after processing at a comparably lower temperature (120 °C). To further enhance the quality and transport property of the TiO_2 film, it was undergone through UVO_3 treatment which removed the organic contaminants. Consequently, to understand the impact of UVO_3 treatment on the photo-physical properties of low temperature processed TiO_2 film was analysed by Fourier transform infrared spectroscopy (FTIR), X-ray photoelectron spectroscopy (XPS), X-ray diffraction (XRD), Ultraviolet (UV)-visible and Photoluminescence (PL) spectroscopy before and after UVO_3 treatment. The current density-voltage (J-V) characteristics and interfacial electrical properties of FDSSCs devices were also studied. The results demonstrated significant enhancement in the PCE after UVO_3 treatment due to the improved transport property. Thus, this work illustrates the fabrication of low-temperature processed FDSSCs and can be utilised as an expedient tool in development of future low-cost FDSSCs.

7.2 Experimental section

Materials. Transparent Indium tin oxide (ITO) coated polyethylene terephthalate (PET), sheet resistance 60 Ω/square (Sigma- Aldrich) were utilized for all the devices. P25 (22 nm), *tert*-

Butanol, 4-tert Butylpyridine, 1-butyl-3-methylimidazolium iodide, Anhydrous isopropanol, Chloroplatinic acid hexahydrate Acetonitrile, Titanium (IV) isopropoxide, Lithium iodide, Valeronitrile, Guanidium thiocyanate were procured from Sigma Aldrich. Iodine and Sodium hydroxide were procured form Merk and Himedia respectively.

Low temperature TiO_2 Paste preparation

Our first and foremost objective was to obtain efficient TiO_2 precursor suspension, which contained a mixture of TiO_2 and molecular titania precursor. P25 powder was chosen as the nanocrystalline TiO_2 precursor because of its high photocatalytic activity. Further, TTIP was used as an interconnecting agent of TiO_2 nanoparticles and it has stable nature under ambient condition. However, the film became unstable and peeled off when the concentration of TTIP increased further. The low temperature TiO_2 paste consists of 1 gm P25 TiO_2 nanoparticles, 148µL TIIP, 10 ml ethanol, and 140µL of DI water. The solution was sonicated for 10 min and stirred for 30 min. Then the solution was poured into mortar pestle and grinded for several hours to obtain high viscosity TiO_2 colloid.

Fabrication of photoanode on flexible ITO PET

ITO PET substrate was dipped into 50% aqueous ethanol solution for 60 min and then cleaned with absolute solution for several times. The PET substrates were dried by using a hot air dryer and then treated in UV-O_3 system for 1 min. Multilayer working electrode was deposited by spin coating and doctor blade technique. TiO_2 colloid solution was dropped onto the cleaned PET substrates, then spin-coated at 4000 rpm for 45 sec followed by subsequent thermal annealing at 80 °C for 5 min to remove the solvent. This step was repeated for two times, then the coated films were treated by UVO_3 for 5 min. Further, another mesoporous layer of TiO_2 was deposited above the spin coated film by doctor blade technique and baked at 120 ºC for half an hour. This method has some drawbacks like incomplete necking of nanoparticle and presence of remaining organic contaminants. Therefore, the surface of TiO_2 based ETLs was treated in UVO_3 system to remove organic contaminants. Fig. 7.1 show the schematic representation of TiO_2 film fabrication process for FDSSCs.

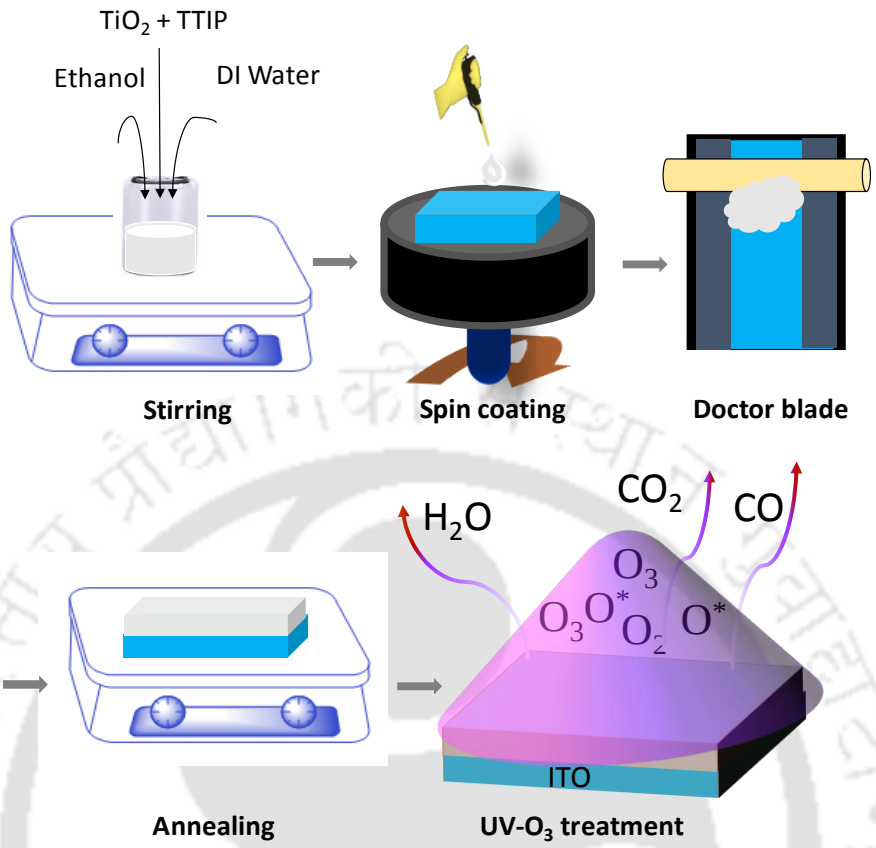

Figure 7. 1: Schematic illustration of high performance electron transport layer for FDSSCs.

Device fabrication and testing

TiO_2 working electrodes were submerged into 0.3 mM of N719 solution in Acetonitrile and tert-Butanol solution (volume ratio 1:1) and remained overnight to sensitize it in dark condition. Platinum (Pt) counter electrode were prepared by spin coating Chloroplatinic acid hexahydrate solution (5 mg in 1ml of anhydrous 2-propanol) on pre-cleaned ITO PET at 4000 rpm for 50 secs followed by sintering at 80 ºC for 5 min and UVO_3 treatment for 60 min. The I^-/I_3^- electrolyte solution of was made with 0.05 M Iodine, 0.5 M Lithium Iodide, 0.1 M Guanidium thiocyanate, 0.5 M 1-Butyl-3-methylimidazolium iodide, and 0.5 M 4-tert-Butylpyridine dissolved in the mixture of acetonitrile/valeronitrile (V/V= 85:15) solvents. Sensitized TiO_2 working electrode and Pt counter electrodes were assembled and sealed by a Surlyn film (60 µm, Ossila) which acts as a hot melt spacer to prepare sandwich type photovoltaic cells. Liquid electrolytes were injected between working and counter electrode for the completion of the fabrication process. The J-V

characteristics of FDSSCs device, which have been measured under AM 1.5 G with 100 mW/cm^2 The active area of all FDSSCs were 0.16 cm^2.

7.3 Results and discussion

UVO_3 treatment on low temperature electron transport layer

The TiO_2 solution was prepared with small amount of TTIP as a binder, which is crucial for fabricating uniform and stable film. However, the cross linking of residual organic species in TiO_2 paste may hinders charge transport and affects device performance. To overcome this shortcoming, a simple UVO_3 system was utilized to decompose the organic species and coalescence of TiO_2 nanoparticles to yield high quality ETL. The UVO_3 system produced two ultraviolent light of wavelength 185 and 254 nm simultaneously. The corresponding wavelengths produces the photonic energy much greater than the bond energies of residual organic species. The atmospheric oxygen (O_2), when irradiated at 185 nm; it converts into ozone (O_3) and atomic oxygen (O*). Again, at 254 nm UV light, O_3 decomposes into O_2 and O*. Very strong oxidizing atom O* is produced during the course of formation and breakdown of ozone (O_3). Highly reactive O* and O_3 react strongly with residual organic substances present in the paste and burn out these residual substances and generate volatile molecules such as CO, H_2O, CO_2 and N_2 etc. [25, 37-38]. The schematic representation of the UV ozone exposure was illustrating in Fig. 7.2(a). Zhang et al. prepared pre-sintered TiO_2 photoanode for FDSSC and achieved an efficiency of 3.27% using post-treatment of UVO_3 [39]. The binder-free TiO_2 paste coated film on the substrate turns yellowish while drying at 200°C. The yellowish photoanode shows poor performance with lower power conversion efficiency. While exposing the photoanode to UV Ozone treatment bleaches out the yellow colour and remarkably enhances the photovoltaics performance up to 5.40% [40]. Zardetto et al. demonstrated fully UV treated FDSSC and fairly obtained a PCE of 4.30% under one sun [2]. A similar kind of study has been done by exposing the photoanode with UV light and improving the power conversion efficiency of the flexible DSSCs [41-42].

FTIR analysis

To gain better insight into the impact of UVO_3 treatment on low temperature processed TiO_2 film, FTIR measurement was conducted. FTIR spectra shown in Fig. 7.2(b) were compared before and

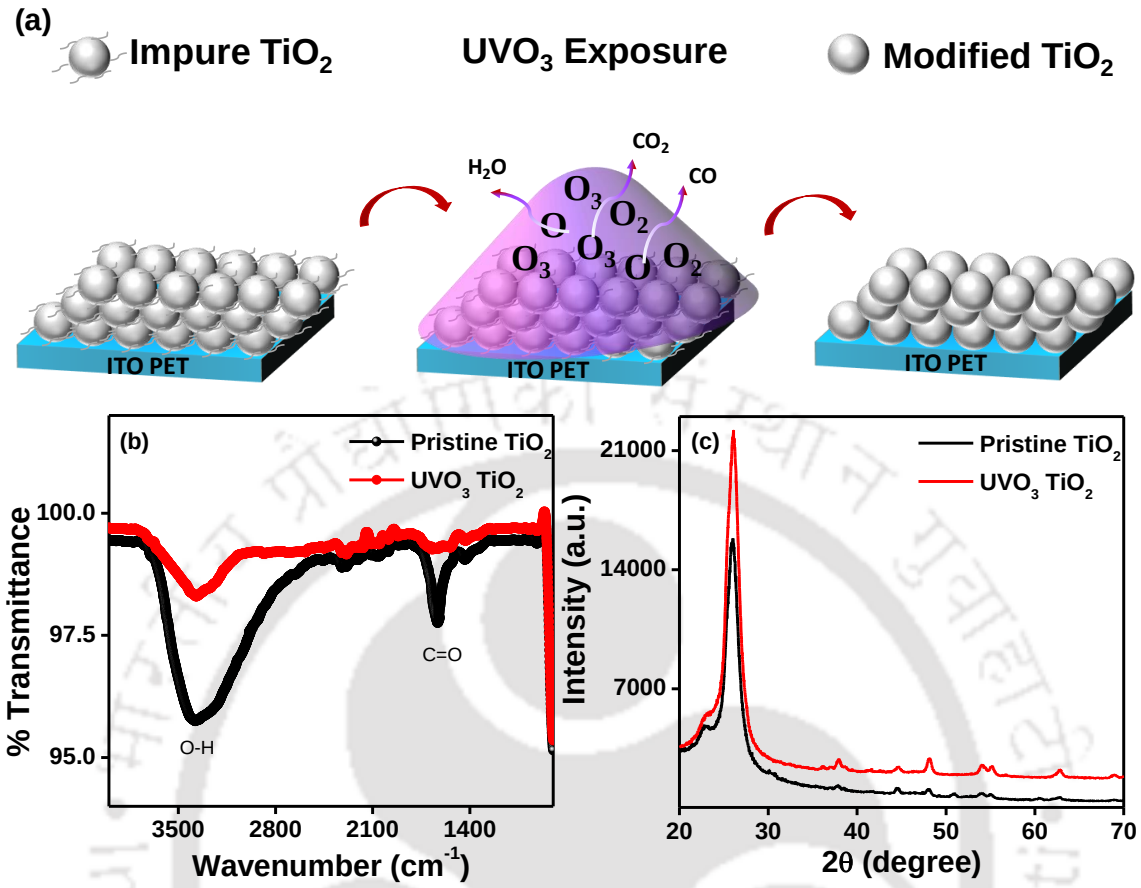

Figure 7. 2: (a) Schematic representation of UVO_3 treatment for the preparation of high quality TiO_2 film. (b) FTIR spectra, and (c) XRD spectra of TiO_2 film without and with the treatment of UVO_3.

after UVO_3 exposure for 4 hours. The absorption band around 3300 to 3500 cm^{-1} is related to the stretching mode of hydroxyl (O-H) group and 1600 to 1700 cm^{-1} are bending mode of carbonyl group (C=O), respectively, indicating the residual hydroxyl groups and water molecules of the TiO_2 film. There is an additional board peak located around 1435 to 1335 cm^{-1}, which are corresponding to the symmetric stretching vibration of COO^- [40-41, 43]. As the TiO_2 film was UVO_3 treated, a significant decline was observed in the peak intensity of the O-H stretching and C=O bending, which was an indication of organic residue removal from the TiO_2 film, which substantially improved the quality of ETL.

XRD analysis

To further understand the impact of UVO_3 treatment on the crystalline nature of TiO_2 film, XRD patterns were analysed before and after UVO_3 treatment. From Fig. 7.2(c), it was evident that peak

intensity for (1 0 1) plane at 25.99° corresponding to anatase phase was enhanced after UVO_3 treatment which can be correlated with improved crystallinity of TiO_2 film [44]. The enhanced crystalline nature of ETL can contribute in improving transport properties of photovoltaic device.

XPS analysis

To investigate the chemical and structural changes in TiO_2 films, the XPS measurement was used to analyse the impact of UVO_3 treatment. Fig. 7.3(a, b, c, d, e and f) demonstrates the high-resolution C 1s, O 1s and Ti 2p XP spectra of TiO_2 films before and after UVO_3 treatment. In Fig. 7.3(a), two peaks were observed at 284.2 eV and 285.7 eV [39]. The TiO_2 film without UVO_3 exposure presented larger C-O bonding peak, which illustrated that the organic species was not properly removed from TiO_2 surface even after annealing at 120 °C for 30 min. Carbon contamination can acts as an interfacial trap sites and diminish photovoltaic efficiency due to the insufficient necking of TiO_2 nanoparticles. It also adversely affects the dye loading on TiO_2 film producing relatively lower current density. Interestingly, after UVO_3 exposure on TiO_2 film in Fig. 7.3(b), the C-O bonding peak available at 284.2 eV disappeared from the C 1s spectrum. The peak intensity was also significantly decreased compared to the untreated TiO_2 film, which indicated that organic species from untreated TiO_2 film were substantially reduced after UVO_3 exposure [38-39]. The O 1s peak of the TiO_2 film before and after UVO_3 processing were fitted with two Gaussian peaks. The central O 1s peak recorded at 531±0.1 eV should be corresponding to the lattice oxygen of TiO_2 [45]. Another peak on the shoulder at 532.2±0.2 eV is ascribed to the development of Ti^{3+} state by the formation of oxygen vacancy. Based on the high-resolution O 1s spectrum after UVO_3 treatment, the relative peak area of Ti_2O_3 was increased significantly which can create more oxygen vacancies and change the oxidation state from Ti^{4+} to Ti^{3+}. This can introduce excess electrons on the surface of TiO_2, thus enhanced the functionality of the surface. The high resolution XP spectra of Ti 2p were displayed in Fig. 7.3(e and f). For untreated TiO_2 film, two peaks of Ti 2p located at 458.0 eV and 463.7 eV were assigned to Ti^{4+} $2p_{3/2}$ and Ti^{4+} $2p_{1/2}$, respectively. For UVO_3 treated TiO_2 sample, two peaks presented at 458.3 and 464.1 eV should be attributed to the energy levels of Ti^{4+} $2p_{3/2}$ and Ti^{4+} $2p_{1/2}$, respectively[46]. UVO_3 treatment effectively promoted the creation of Ti-O-Ti bonds which can enhance the conductive properties and significantly reduce charge carrier recombination rate. The relative change in peak area revealed that the surface charge states of TiO_2 layer were tuned with UVO_3 exposure.

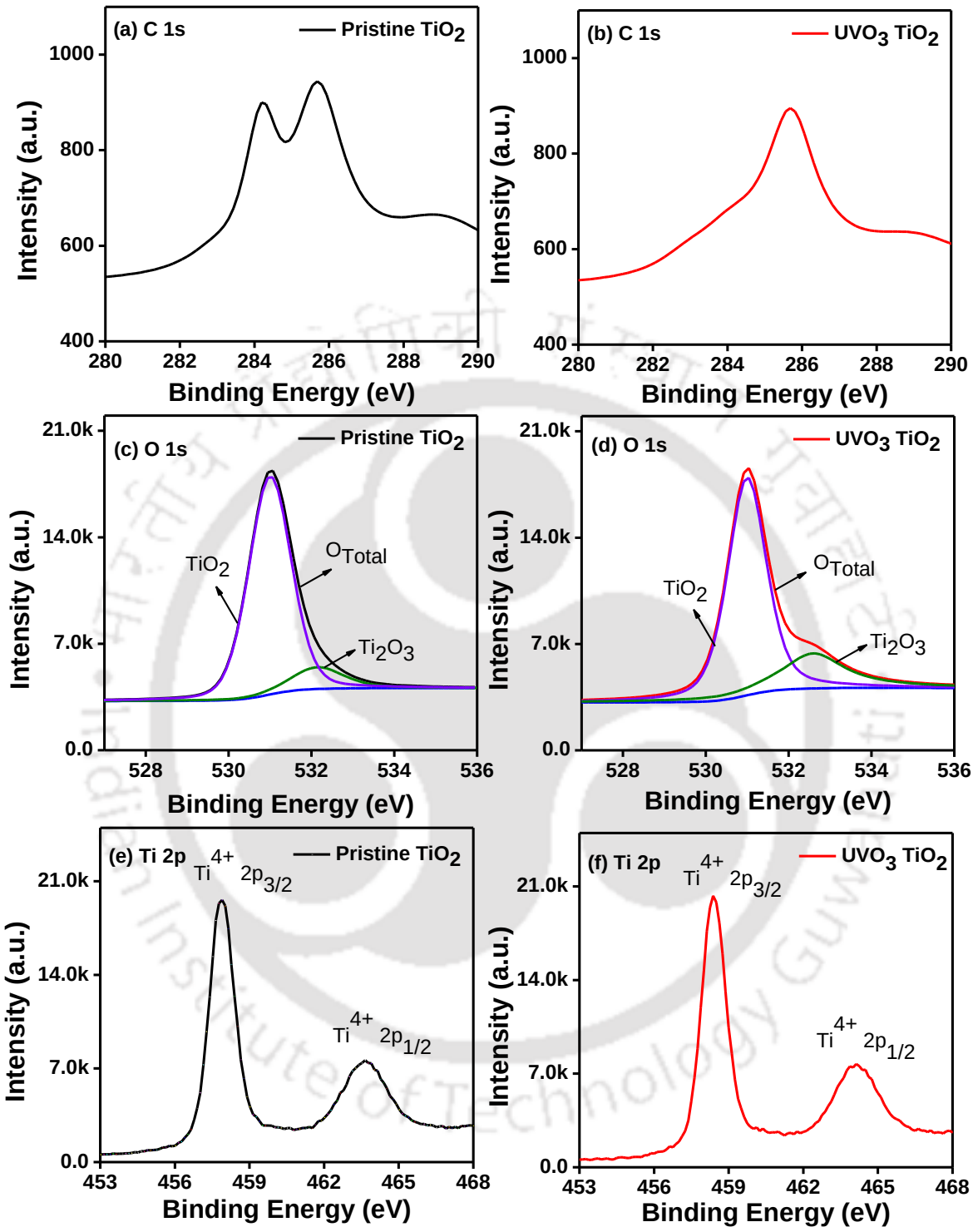

Figure 7. 3: XP spectra of TiO_2 film on ITO PET with 0 and 4 hrs: C 1s (a and b); O 1s (c and d), and Ti 2p (e and f).

Photoluminescence (PL) analysis

Further PL spectra were utlized to analyse the extent of charge carrier trapping, transfer, and to gain the insight the fate of electrons and holes in a semiconductor. PL spectra of the TiO_2 films were measured by exciting at 320 nm. The excitation of 320 nm wavelength is corresponding to a photon energy of 3.88 eV, which is higher than the bandgap of TiO_2 [41, 47-49]. Comparing the spectra of the film before and after UVO_3 treatment, it was observed that photoluminescence emission peak intensity was lower for the untreated film compared to UVO_3 treated film. The lower intensity of the untreated TiO_2 film can be corelated to non-radiative recombination caused by the organic species. Contrarily, the improvement of PL emission of TiO_2 film after UVO_3 treatment is indicating the improved film quality and lower non-radiative recombination.

UV-Visible analysis

Fig. 7.4(a) demonstrates the absorption spectra of N719 dye desorbing from the TiO_2 working electrodes. To desorbed the dye from the TiO_2 layers with a dimensions of 0.5 cm × 2.5 cm and a thickness of around 3.5 μm were immersed in 4 mL of 0.1 M sodium hydroxide solution in a mixture of DI water and ethanol (V: V= 1:1) [50]. This process was carried out to quantify the amount of dye adsorbed on the surface of TiO_2 working electrodes. After complete desorption of the dye, the solutions turn out to be dark pink colour, then UV-vis absorption spectra of same solutions were analysed. The concentration of the desorbed dye per cm^2 area were estimated by using Beer's law. It was also noticed that the absorption intensity increased in the electrodes after UVO_3 treatment. The amount of dye loading concentration was ~1.936×10^{-7} mol cm^{-2} for untreated film while 2.865×10^{-7} mol cm^{-2} for UVO_3 treated film. The increased in dye absorption can significantly increase the current density of the device. This enhancement in dye absorption attribute to decrease in contact angle due to high hydrophilic nature of the TiO_2 film caused by UVO_3 exposure [51-52].

Transmittance analysis

Transmittance study was conducted to investigate the transparency of deposited TiO_2 films on the ITO PET substrates The UV-vis transmittance spectra of the ITO PET, TiO_2/ITO PET and UVO_3 TiO_2/ITO PET were compared and displayed in Fig. 7.4(b). The bare ITO PET substrate displays highest transmittance in the absorbance range of the visible region. After the deposition of TiO_2 films by spin coating and doctor blade technique the transmittance decreased compared to bare

ITO PET. The decrease of transmittance was caused by the absorption of the nanocrystal TiO_2 film. The transmittance of the TiO_2/ITO PET film improved after UVO_3 treatment. The increasing order of the transmittance can be written as TiO_2/ITO PET<UVO_3 TiO_2/ITO PET< ITO PET.

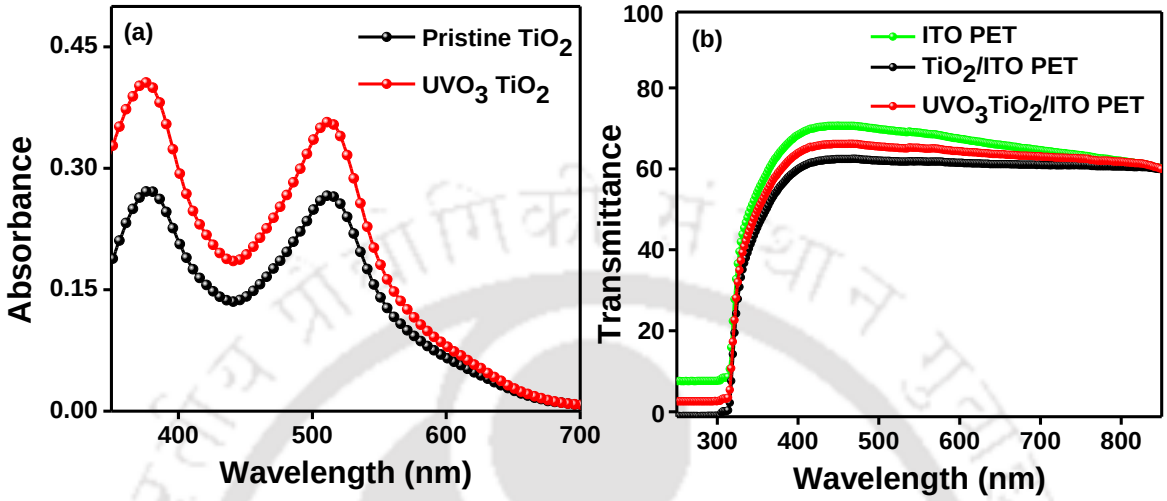

Figure 7. 4: UV-vis absorption spectra of N719 dye's desorbed from TiO_2 film before and after UVO_3 exposure in 4 mL of 0.1 M sodium hydroxide solution in a mixture of DI water and ethanol (V: V= 1:1) and (b) Transmittance spectra of bare ITO PET, TiO_2/ITO PET, and UVO_3 TiO_2/ ITO PET.

Electrical parameters of FDSSCs

To evaluate the effectiveness of UVO_3 treated electrodes, we compared the performance of FDSSCs without and with UVO_3 treatment TiO_2 film. The J-V characteristics of FDSSCs device, which have been measured under AM 1.5 G with 100 mW/cm^2 were shown in Fig. 7.5(a). FDSSCs with TiO_2 film processed at 120 °C without UVO_3 treatment exhibited poor PCE of 1.43% with J_{SC} of 3.73 mA/cm^2, V_{OC} of 661 mV and FF of 58.10%. The poor performance of the FDSSCs without UVO_3 was due to the presence of undesired organic species and poor inter-particles necking which resulted in high charge carrier recombination [53-54]. After UVO_3 exposure, the FDSSCs exhibited enhanced photovoltaic performance achieving the highest PCE of 2.54% with J_{SC} of 5.52 mA/cm^2, V_{OC} of 695 mV, and FF of 65.80%. The photovoltaic parameters were significantly improved for UVO_3 treated devices up to 4 hours of exposure and produced a higher degree of reproducibility for all device parameters (Fig. 7.5(b)). The box charts of J_{SC}, FF as a function of time were presented in Fig. 7.5(c, and d). Although oxygen vacancies created by UVO_3 system initially enhanced the transport property of TiO_2 films, excess of oxygen vacancies resulted in serious carrier recombination at the interface between dye photo absorption layer and TiO_2 ETL.

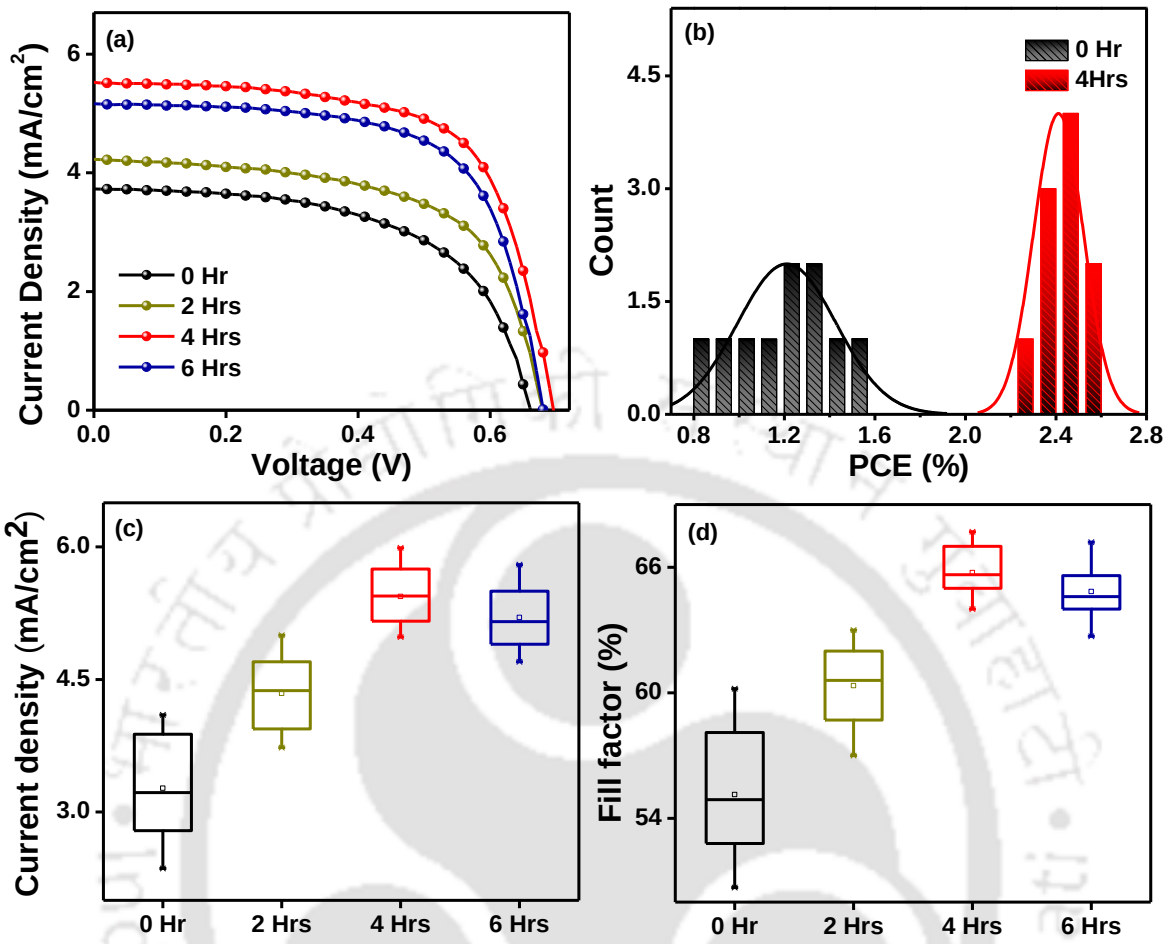

Figure 7. 5: (a) J-V curves of flexible DSSCs on ITO/PET substrates with different duration of UVO_3 treatment performed on TiO_2 films, (b) PCE histogram of FDSSCs with 0 and 4 hrs UVO_3 exposure of TiO_2 film. Box charts of (c) J_{SC}, and (d) FF of the FDSSCs as a function of UVO_3 treatment time.

Table 7. 1: Parameters of FDSSCs under a different duration of UVO_3 exposure.[7]

UVO_3 treatment time (Hours)	**J_{SC} (mA/cm^2)**	**V_{OC} (mV)**	**FF (%)**	**PCE (Average)[b](%)**
0	3.73	661.10	58.10	1.43(1.21± 0.21)
2	4.23	679.60	61.12	1.76(1.94± 0.19)
4	5.52	695.90	65.80	2.53(2.41± 0.10)
6	5.16	680.40	65.20	2.31(2.20± 0.18)

[b]Average of 10 devices.

[7]Performances of DSSCs were measured with 0.25 cm^2 working area under AM 1.5, 100 mW/cm^2 irradiation. Liquid electrolytes consist of 0.05M I_2, 0.5M LiI, 0.1M guanidium thiocyanate, 0.5M 4-tert-butylpyridine and 0.5M 1-Butyl-3-methylimidazolium iodide dissolved in acetonitrile/valeronitrile (V: V= 85:15) solvent. 0.3 mM N719 dye solution and Platinized counter electrodes.

This resulted in decline of the shunt resistance (R_{SH}) and V_{OC} which collectively reduced the device performance [46]. Therefore, an inferior photovoltaic performance was observed for longer (6 hours) UVO_3 treated devices.

Impedance analysis

To further comprehend the charge carrier dynamics of FDSSCs upon UVO_3 treatment, electrochemical impedance spectroscopy (EIS) measurements were conducted. Impedance spectroscopy is an effective technique for analysing the kinetics of electrons transfer and recombination in FDSSCs, which also can provide information about diffusion of I^-/I_3^- in the electrolytes, electron transfer at the TiO_2/dye/electrolytes interface and the redox reaction at Pt counter electrode [27-28, 55-62]. Impedance spectra were measured in dark condition at an applied potential equal to open circuit voltage. The Nyquist plot of the FDSSCs based on low temperature processed TiO_2 film was displayed in Fig. 7.6(a). EIS data were fitted according to the equivalent circuit model to interpret the results. Based on that, the intercept with the real axis at high frequency region represent the total ohmic resistance of the device i.e. contact resistance between

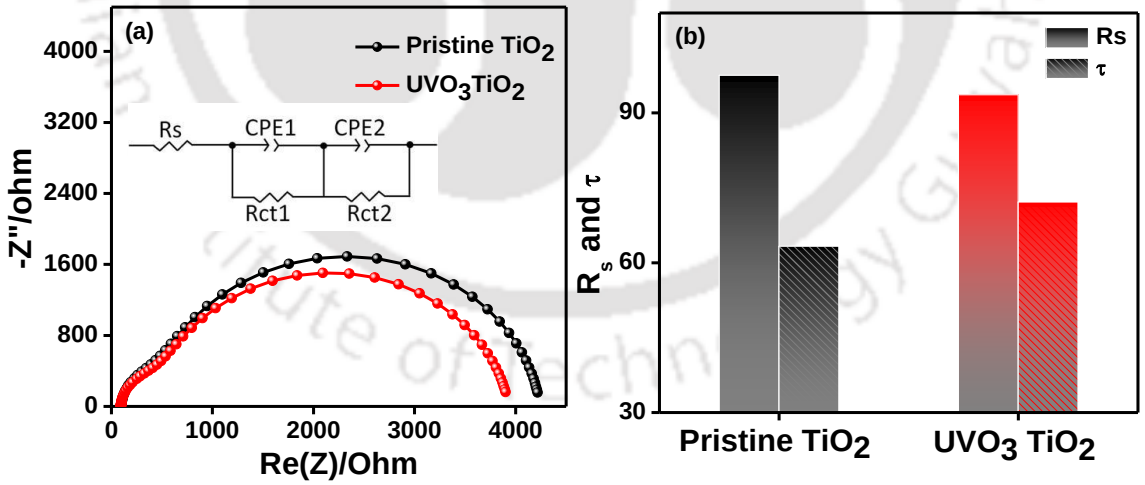

Figure 7. 6: (a) Nyquist plots (Inset equivalent circuit) and (b) Corresponding Ohmic resistance (R_S) and Electron life (τ) for FDSSCs before and after UVO_3 exposure of TiO_2 ETL layer.

the TiO_2 film and transparent conducting oxide (R_S). The fitting parameter of the equivalent circuit were obtained using EC-Lab software and shown in Table 7.2. The calculated values of Rs were 97.50Ω and 93.64Ω, and effective electron life (τ) were 63.28ms and 72.12ms for photoelectrode without and with UVO_3 treatment, respectively. The histogram diagram of R_S and τ as a function of UVO_3 were shown in fig. 7.6(b). Suggesting the organic substances present before the UVO_3 exposure acts as a trap site on the TiO_2 surface allowing photogenerated electrons trapped and recombine with I_3^- in the electrolytes and produced bigger semi-circle of impedance spectrum [39]. The low FF of the device without UVO_3 exposure is also due to higher R_S value. The removal of the organic species using UVO_3 treatment decreased Rs which facilitated charge transport and collection, thereby increased electron lifetime in the devices.

Table 7. 2: Parameters of EIS equivalent circuit.

Substrate	**Rs(Ω)**	**Rct1(Ω)**	**CPE1(μF)**	**Rct2(Ω)**	**CPE2(μF)**	**τ_e(ms)**
ITO PET	97.50	350	7.24	3729	16.97	63.28
	93.64	341	6.18	3501	20.61	72.12

Stability analysis

The stability of FDSSC over 500 bending cycles was analysed and shown in Fig. 7.7. The photovoltaic device retained 83% of its initial efficiency after this mechanical stress. A major decline was observed in J_{SC} of the device which adversely impacted the overall device performance.

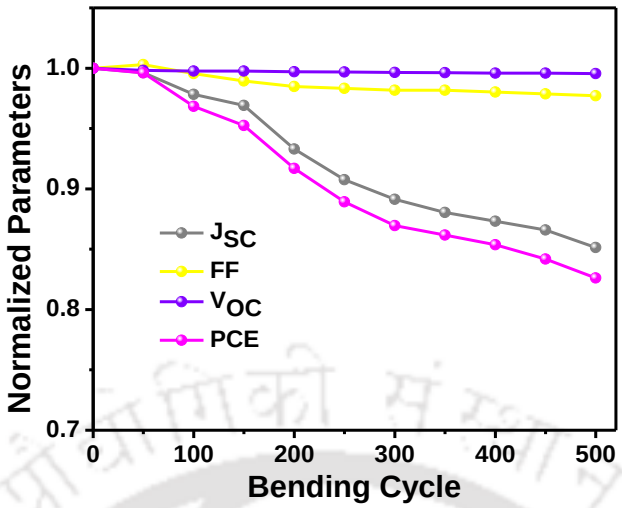

Figure 7. 7: Stability analysed of FDSSCs over 500 bending cycles.

FESEM and AFM analysis

Fig. 7.8(a and b) displayed the surface morphology of TiO_2 films before and after UVO_3 exposure. Few cracks were observed in untreated TiO_2 film. These micro cracks are formed due to shrinkage during the drying process of TiO_2 film. This result indicated that the necking of TiO_2 particles was poor without UVO_3 treatment which may result into higher degree of traps states [41][63]. For the UVO_3 treated devices, a significant improvement was observed in uniformity and TiO_2 particle necking which suppressed the non-radiative recombination and enhanced the photovoltaic performance significantly. The structural characteristic of the TiO_2 films before and after UVO_3 treated were subsequently explored using conducting AFM. The microscope was operated under

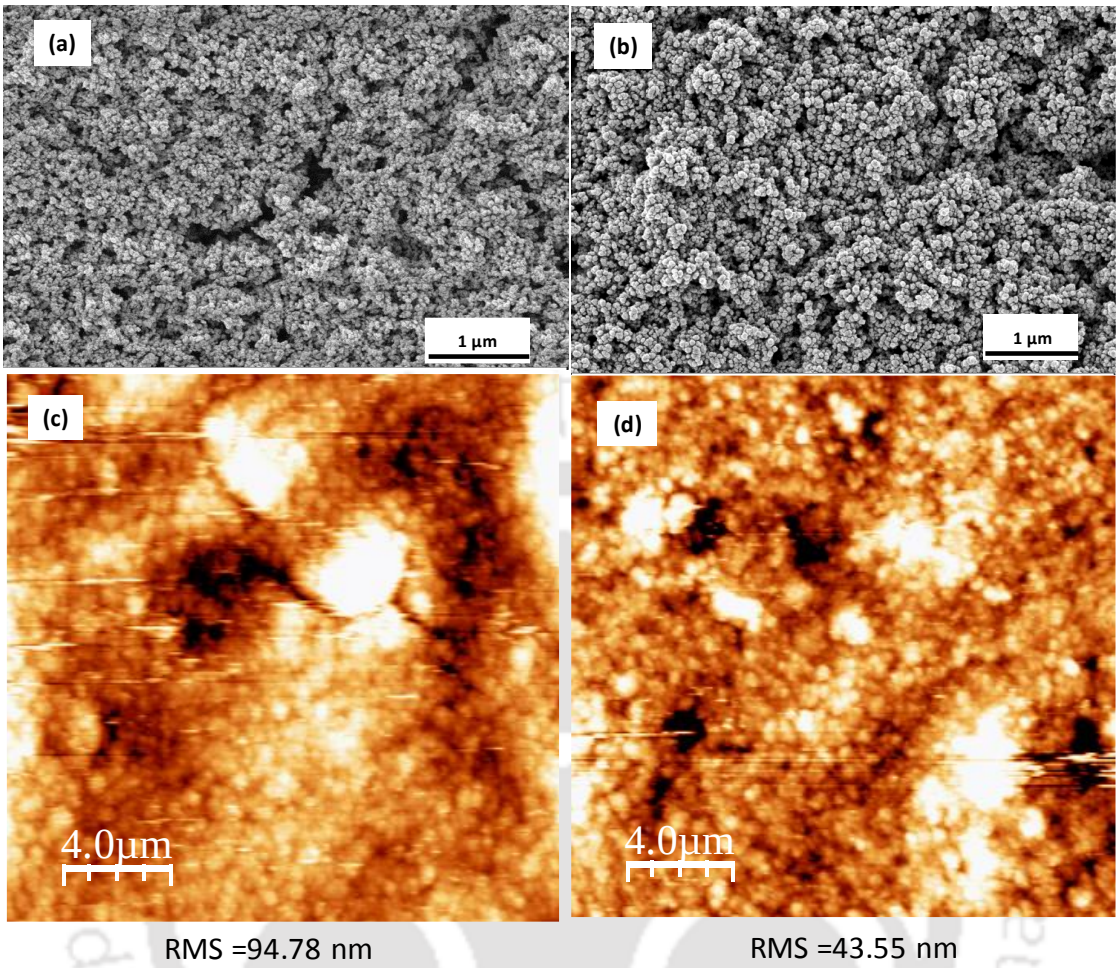

Figure 7. 8: FESEM and AFM images of TiO_2 films on ITO PET substrates (a and c) after only processing at 120 °C and (b and d) after processing at 120 °C followed by UVO_3 exposure.

tapping mode also known as intermittent contact mode. The scan size was 4 µm. image and analysed using WSxM software. Fig. 7.8(c, d) displays the 2D AFM images of pristine and UVO_3 treated TiO_2 films and the corresponding average root mean square (RMS) roughness parameter were 94.78 and 43.55 nm respectively. The difference in the roughness factors arises due to the surface UVO_3 treatment. The lower roughness was observed after the 4 hrs UVO_3 treatment, which indicates that the surface treatment enable uniform films by reducing the surface contamination [46][64]. UVO_3 treatment significantly improved the TiO_2 film quality which validates the higher efficiency of FDSSCs after optimal UVO_3 treatment.

7.4 Conclusion

In summary, it has been demonstrated that utilization of a simple technique such as UVO_3 treatment can substantially improve the quality of relatively low temperature processed TiO_2 film by increasing uniformity and mechanical stability. UVO_3 treatment was found to be effective in removing organic species arising from precursor materials. The crystallinity of TiO_2 film was enhanced significantly after UVO_3 treatment in comparison to the pristine TiO_2 film. Further, J-V plots of FDSSCs demonstrated that devices with UVO_3 treatment for 4 hours achieved the highest efficiency of 2.53% compared to 1.43% of pristine device. From the observations of EIS, it was evident that organic species formed trap states and promoted recombination reactions in pristine devices without UVO_3 treatment. However, UVO_3 treatment significantly increased the photo-generated electrons lifetime and enhanced device performance. This unique and cost-effective method can assist in fabricating highly efficient low temperature processed FDSSCs which can be further scaled up and implemented in roll-to-roll manufacturing.

7.5 References

[1] B. O'Regan, M. Grätzel, A low-cost, high-efficiency solar cell based on dye-sensitized colloidal TiO_2 films, Nature. 353 (1991) 737–740. doi:10.1038/353737a0.

[2] V. Zardetto, F. Di Giacomo, D. Garcia-alonso, W. Keuning, M. Creatore, C. Mazzuca, A. Reale, A. Di Carlo, T. M. Brown, Fully Plastic Dye Solar Cell Devices by Low-Temperature UV-Irradiation of both the Mesoporous TiO_2 Photo- and Platinized Counter-Electrodes, Adv. Energy Mater. 3 (2013) 1292–1298. doi:10.1002/aenm.201300101.

[3] D. Kuang, J. Brillet, P. Chen, M. Takata, S. Uchida, H. Miura, K. Sumioka, S. M. Zakeeruddin, M. Grätzel, Application of Highly Ordered TiO_2 Nanotubes Arrays in Flexible Dye-Sensitized Solar Cells, ACSNaNo. 2 (2008) 1113–1116.

[4] M. Grätzel, The Advent of Mesoscopic Injection Solar Cells, Prog. Photovoltaics Res. Appl. 14 (2006) 429–442. doi:10.1002/pip.

[5] M. Grätzel, Dye-sensitized solar cells, J. Photochem. Photobiol. C Photochem. Rev. 4 (2003) 145–153. doi:10.1016/s1389-5567(03)00026-1.

[6] Y. Galagan, Flexible Solar Cells, in: Roll. Manuf. Process Elem. Recent Adv., 2018: pp. 325–362. doi:10.1002/9781119163824.ch11.

[7] M. Dürr, A. Schmid, M. Obermaier, S. Rosselli, A. Yasuda, G. Nelles, Low-temperature fabrication of dye-sensitized solar cells by transfer of composite porous layers, Nat. Mater. 4 (2005) 607–611. doi:10.1038/nmat1433.

[8] H. Santa- Nokki, J. Kallioinen, T. Kololuoma, V. Tuboltsev, J. Korppi-Tommola, Dynamic preparation of TiO_2 film for fabrication of dye-sensitized solar cells, J. Photochem. Photobiol. A Chem. 182 (2006) 187–191.

[9] Y. Jun, J. Kim, M.G. Kang, A study of stainless steel-based dye-sensitized solar cells and modules, Sol. Energy Mater. Sol. Cells. 91 (2007) 779–784. doi:10.1016/j.solmat.2007.01.007.

[10] J.H. Park, Y. Jun, H.-G. Yun, S.-Y. Lee, M.G. Kang, Fabrication of an Efficient Dye-Sensitized Solar Cell with Stainless Steel Substrate, J. Electrochem. Soc. 155 (2008) F145. doi:10.1149/1.2909548.

[11] L. Lin, C. Lee, R. Vittal, K. Ho, Selective conditions for the fabrication of a flexible dye-sensitized solar cell with Ti / TiO_2 photoanode, J. Power Sources. 195 (2010) 4344–4349. doi:10.1016/j.jpowsour.2010.01.031.

[12] H.W. Chen, K.C. Huang, C.Y. Hsu, C.Y. Lin, J.G. Chen, C.P. Lee, L.Y. Lin, R. Vittal, K.C. Ho, Electrophoretic deposition of TiO_2 film on titanium foil for a flexible dye-sensitized solar cell, Electrochim. Acta. 56 (2011) 7991–7998. doi:10.1016/j.electacta.2010.10.099.

[13] J. Halme, J. Saarinen, P. Lund, Spray deposition and compression of TiO_2 nanoparticle films for dye-sensitized solar cells on plastic substrates, Sol. Energy Mater. Sol. Cells. 90 (2006) 887–899. doi:10.1016/j.solmat.2005.05.013.

[14] B. Zhao, Z. He, X. Cheng, D. Qin, M. Yun, M. Wang, X. Huang, J. Wu, H. Wu, Y. Cao, Flexible polymer solar cells with power conversion efficiency of 8.7%, J. Mater. Chem. C. 2 (2014) 5077–5082. doi:10.1039/c3tc32520b.

[15] K. Kakiage, Y. Aoyama, T. Yano, K. Oya, J.I. Fujisawa, M. Hanaya, Highly-efficient dye-sensitized solar cells with collaborative sensitization by silyl-anchor and carboxy-anchor dyes, Chem. Commun. 51 (2015) 15894–15897. doi:10.1039/c5cc06759f.

[16] S.K. Balasingam, M.G. Kang, Y. Jun, Metal substrate based electrodes for flexible dye-sensitized solar cells: Fabrication methods, progress and challenges, Chem. Commun. 49 (2013) 11457–11475. doi:10.1039/c3cc46224b.

[17] T. Ma, X. Fang, M. Akiyama, K. Inoue, H. Noma, E. Abe, Properties of several types of novel counter electrode for dye-sensitized solr cells, J. Electroanal. Chem. 574 (2004) 77–83.

[18] X. Fang, T. Ma, M. Akiyama, G. Guan, S. Tsunematsu, E. Abe, Flexible counter electrodes based on metal sheet and polymer film for dye sensitized solar cells, Thin Solid Films. 472 (2004) 242–245.

[19] S. Ito, N.L.C. Ha, G. Rothenberger, P. Liska, P. Comte, S.M. Zakeeruddin, P. Péchy, M.K. Nazeeruddin, M. Grätzel, High-efficiency (7.2%) flexible dye-sensitized solar cells with Ti-metal substrate for nanocrystalline-TiO_2 photoanode, Chem. Commun. (2006) 4004–4006. doi:10.1039/b608279c.

[20] W. Liu, H. Zhang, H.-G. Wang, M. Zhang, M. Guo, Titanium mesh supported TiO_2

nanowire arrays_upconversion luminescence Er3+-Yb3+ codoped TiO_2 nanoparticles novel composites for flexible dye-sensitized solar cells, Appl. Surf. Sci. 422 (2017) 304–315.

[21] H.G. Yun, B.S. Bae, M.G. Kang, A simple and highly efficient method for surface treatment of Ti substrates for use in dye-sensitized solar cells, Adv. Energy Mater. 1 (2011) 337–342. doi:10.1002/aenm.201000044.

[22] J. Zhang, Z. Wang, X. Li, J. Yang, C. Song, Y. Li, J. Cheng, Q. Guan, B. Wang, Flexible Platinum-Free Fiber-Shaped Dye Sensitized Solar Cell with 10.28% Efficiency, ACS Appl. Energy Mater. 2 (2019) 2870–2877. doi:10.1021/acsaem.9b00207.

[23] M. Grätzel, Conversion of sunlight to electric power by nanocrystalline dye-sensitized solar cells, J. Photochem. Photobiol. A Chem. 164 (2004) 3–14. doi:10.1016/j.jphotochem.2004.02.023.

[24] T.B. Raju, J. V. Vaghasiya, M.A. Afroz, S.S. Soni, P.K. Iyer, Effect of mono- and di-anchoring dyes based on o,m-difluoro substituted phenylene spacer in liquid and solid state dye sensitized solar cells, Dye. Pigment. 174 (2020). doi:10.1016/j.dyepig.2019.108021.

[25] T. Yamaguchi, N. Tobe, D. Matsumoto, T. Nagai, H. Arakawa, Highly efficient plastic-substrate dye-sensitized solar cells with validated conversion efficiency of 7.6%, Sol. Energy Mater. Sol. Cells. 94 (2010) 812–816. doi:10.1016/j.solmat.2009.12.029.

[26] J. Lin, Y. Peng, A.R. Pascoe, F. Huang, Y.B. Cheng, Y.U. Heo, A. Nattestad, W. Seung, S.K. Kim, H.J. Yoon, S.W. Kim, Y. Yamauchi, S.X. Dou, J.H. Kim, A Bi-layer TiO_2 photoanode for highly durable, flexible dye-sensitized solar cells, J. Mater. Chem. A. 3 (2015) 4679–4686. doi:10.1039/c4ta06656a.

[27] H.C. Weerasinghe, G. V. Franks, J.D. Plessis, G.P. Simon, Y.B. Cheng, Anomalous rheological behavior in chemically modified TiO_2 colloidal pastes prepared for flexible dye-sensitized solar cells, J. Mater. Chem. 20 (2010) 9954–9961. doi:10.1039/c0jm02063j.

[28] N.G. Park, K.M. Kim, M.G. Kang, K.S. Ryu, S.H. Chang, Y.J. Shin, Chemical sintering of nanoparticles: A methodology for low-temperature fabrication of dye-sensitized TiO_2 films, Adv. Mater. 17 (2005) 2349–2353. doi:10.1002/adma.200500288.

[29] S. Uchida, M. Tomiha, H. Takizawa, M. Kawaraya, Flexible dye-sensitized solar cells by 28 GHz microwave irradiation, Chem. J. Photochem. Photobiol. A Chem. 164 (2004) 93–

96.

[30] C.W. Hsu, C.R. Ke, L.C. Chen, P. Chen, J.M. Ting, Effects of microwave condition on the formation and characteristics of TiO_2 submicron-sized beads and its use in all-plastic flexible dye-sensitized solar cells, Sol. Energy Mater. Sol. Cells. 144 (2016) 7–13. doi:10.1016/j.solmat.2015.08.013.

[31] H. Lindström, A. Holmberg, E. Magnusson, L. Malmqvist, A. Hagfeldt, A new method to make dye-sensitized nanocrystalline solar cells at room temperature, J. Photochem. Photobiol. A Chem. 145 (2001) 107–112. doi:10.1016/S1010-6030(01)00564-0.

[32] H.W. Chen, Y. Te Liao, J.G. Chen, K.C.W. Wu, K.C. Ho, Fabrication and characterization of plastic-based flexible dye-sensitized solar cells consisting of crystalline mesoporous titania nanoparticles as photoanodes, J. Mater. Chem. 21 (2011) 17511–17518. doi:10.1039/c1jm12980e.

[33] H. C. Weerasinghe, P. M. Sirimanne, G. P. Simon, Y.-B. Cheng, Cold isostatic pressing technique for producing highly efficient flexible dye-sensitised solar cells on plastic substrates, Prog. PHOTOVOLTAICS Res. Appl. 20 (2011) 231–332. doi:10.1002/pip.

[34] F. Huang, D. Chen, X. L. Zhang, R.A. Caruso, Y.B. Cheng, Dual-function scattering layer of submicrometer-sized mesoporous TiO_2 beads for high-efficiency dyesensitized solar cells, Adv. Funct. Mater. 20 (2010) 1301–1305. doi:10.1002/adfm.200902218.

[35] D. Chen, L. Cao, F. Huang, P. Imperial, Y.B. Cheng, R.A. Caruso, Synthesis of monodisperse mesoporous titania beads with controllable diameter, high surface areas, and variable pore diameters (14-23 nm), J. Am. Chem. Soc. 132 (2010) 4438–4444. doi:10.1021/ja100040p.

[36] F. Huang, D. Chen, Q. Li, R.A. Caruso, Y.B. Cheng, Construction of nanostructured electrodes on flexible substrates using pre-treated building blocks, Appl. Phys. Lett. 100 (2012). doi:10.1063/1.3695080.

[37] J. R. Vig, UV / Ozone cleaning of Surfaces, J. Vac. Sci. Technol. A. 3 (1985) 1027– 1034. doi:10.1116/1.573115.

[38] B.-K. Lee, J.-J. Kim, .Enhanced efficiency of dye-sensitized solar cells by UV–O_3 treatment of TiO_2 layer, Curr. Appl. Phys. 9 (2009) 404–408. doi:10.1016/j.cap.2008.03.017.

[39] D. Zhang, T. Yoshida, T. Oekermann, K. Furuta, H. Minoura, Room-temperature synthesis of porous nanoparticulate TiO_2 films for flexible dye-sensitized solar cells, Adv. Funct. Mater. 16 (2006) 1228–1234. doi:10.1002/adfm.200500700.

[40] T.-Y. Lee, H.-S. Kim, N.-G. Park, Evaluation of Limiting Factors Affecting Photovoltaic Performance of Low-Temperature-Processed TiO_2 Films in Dye-Sensitized Solar Cells, Chemphyschem. 15 (2014) 1098–1105. doi:DOI: 10.1002/cphc.201301043.

[41] D. Gutiérrez -Tauste, I. Zumeta, E. Vigil, M. A. Hernández-Fenollosa, X. Domènech, J. A. Ayllón, New low temperature preparation method of the TiO_2 porous photoelectrode for dye-sensitized solar cell using UV irradiation, J. Photochem. Photobiol. A Chem. 175 (2005) 165–171.

[42] J. Nemoto, M. Sakata, T. Hoshi, H. Ueno, M. Kaneko, All-plastic dye-sensitized solar cell using a polysaccharide film containing excess redox electrolyte solution, Jour Electroanal. Chem. 599 (2007) 23–30.

[43] J.H. Yune, I. Karatchevtseva, G. Triani, K. Wagner, D. Officer, A study of TiO_2 binder-free paste prepared for low temperature dye-sensitized solar cells, J. Mater. Res. 28 (2013) 488–496. doi:10.1557/jmr.2012.354.

[44] X. Zhang, J. Yao, M. Ali, J. Wei, H. Wang, L.Y. Yeo, J.R. Friend, D.R. MacFarlane, UV/ozone-assisted low temperature preparation of mesoporous TiO_2 with tunable phase composition and enhanced solar light photocatalytic activity, J. Mater. Chem. A. 2 (2014) 18791–18795. doi:10.1039/c4ta04020a.

[45] G. Liu, W. Jaegermann, J. He, V. Sundstro, L. Sun, XPS and UPS characterisation of the TiO_2/ZnPcGly Heterointerface: Alignment of Energy Levels, J. Phys. Chem. B. 106 (2002) 5814–5819.

[46] Y. Chu, H. Cai, L. Huang, Z. Xing, Y. Du, J. Ni, J. Li, J. Zhang, High-Efficient Flexible Perovskite Solar Cells with Low Temperature TiO_2 Layer via UV / Ozone Photo-Annealing Treatment, Phys. Status Solidi A. 216 (2019) 1800669–9. doi:10.1002/pssa.201800669.

[47] B. Liu, X. Zhao, Q. Zhao, X. He, J. Feng, Effect of heat treatment on the UV-vis-NIR and PL spectra of TiO_2 films, J. Electron Spectrosc. 148 (2005) 158–163.

[48] D.K. Pallotti, L. Passoni, P. Maddalena, F. Di Fonzo, S. Lettieri, Photoluminescence

Mechanisms in Anatase and Rutile TiO_2, J. Phys. Chem. C. 121 (2017) 9011–9021. doi:10.1021/acs.jpcc.7b00321.

[49] J.G. Yu, H.G. Yu, B. Cheng, X.J. Zhao, J.C. Yu, W.K. Ho, The Effect of Calcination Temperature on the Surface Microstructure and Photocatalytic Activity of TiO_2 Thin Films Prepared by Liquid Phase Deposition, J. Phys. Chem. B. 107 (2003) 13871–13879. doi:10.1021/jp036158y.

[50] E. Dell'Orto, L. Raimondo, A. Sassella, A. Abbotto, Dye-sensitized solar cells: Spectroscopic evaluation of dye loading on TiO_2, J. Mater. Chem. 22 (2012) 11364–11369. doi:10.1039/c2jm30481c.

[51] C. Dawo, M. Adil, P. Krishnan, H. Chaturvedi, Effect of UV-ozone exposure on the dye-sensitized solar cells performance, 208 (2020) 212–219.

[52] S. Saekow, W. Maiakgree, W. Jarernboon, S. Pimanpang, V. Amornkitbamrung, High intensity UV radiation ozone treatment of nanocrystalline TiO_2 layers for high efficiency of dye-sensitized solar cells, in: J. Non. Cryst. Solids, 2012: pp. 2496–2500. doi:10.1016/j.jnoncrysol.2012.01.050.

[53] K.M. Lee, S.J. Wu, C.Y. Chen, C.G. Wu, M. Ikegami, K. Miyoshi, T. Miyasaka, K.C. Ho, Efficient and stable plastic dye-sensitized solar cells based on a high light-harvesting ruthenium sensitizer, J. Mater. Chem. 19 (2009) 5009–5015. doi:10.1039/b903852c.

[54] H. Lee, D. Hwang, S.M. Jo, D. Kim, Y. Seo, D.Y. Kim, Low-temperature fabrication of TiO_2 electrodes for flexible dye-sensitized solar cells using an electrospray process, ACS Appl. Mater. Interfaces. 4 (2012) 3308–3315. doi:10.1021/am3007164.

[55] N. Fu, X. Li, Y. Liu, Y. Liu, M. Guo, W. Li, H. Huang, Low temperature transfer of well-tailored TiO_2 nanotube array membrane for efficient plastic dye-sensitized solar cells, J. Power Sources. 343 (2017) 47–53. doi:10.1016/j.jpowsour.2017.01.028.

[56] Q. Wang, J.-E. Moser, M. Grätzel, Electrochemical Impedance Spectroscopic Analysis of Dye-Sensitized Solar Cells, J. Phys. Chem. B. 109 (2005) 14945–14953. doi:10.1002/ijch.201500007.

[57] M. Adachi, M. Sakamoto, J. Jiu, Y. Ogata, S. Isoda, Determination of parameters of electron transport in dye-sensitized solar cells using electrochemical impedance spectroscopy, J.

Phys. Chem. B. 110 (2006) 13872–13880. doi:10.1021/jp061693u.

[58] J. Bisquert, Theory of the impedance of electron diffusion and recombination in a thin layer, J. Phys. Chem. B. 106 (2002) 325–333. doi:10.1021/jp011941g.

[59] R. Kern, R. Sastrawan, J. Ferber, R. Stangl, J. Luther, Modeling and interpretation of electrical impedance spectra of dye solar cells operated under open-circuit conditions, Electrochim. Acta. 47 (2002) 4213–4225. doi:10.1016/S0013-4686(02)00444-9.

[60] T. Hoshikawa, M. Yamada, R. Kikuchi, K. Eguchi, Impedance Analysis of Internal Resistance Affecting the Photoelectrochemical Performance of Dye-Sensitized Solar Cells, J. Electrochem. Soc. 152 (2005) E68–E73. doi:10.1149/1.1849776.

[61] T. Hoshikawa, M. Yamada, R. Kikuchi, K. Eguchi, Impedance analysis for dye-sensitized solar cells with a three-electrode system, J. Electroanal. Chem. 577 (2005) 339–348.

[62] P. Zhang, C. Wu, Y. Han, T. Jin, B. Chi, J. Pu, L. Jian, Low-temperature preparation of hierarchical structure TiO_2 for flexible dye-sensitized solar cell, J. Am. Ceram. Soc. 95 (2012) 1372–1377. doi:10.1111/j.1551-2916.2011.04984.x.

[63] Q. Zeng, Y. Yu, L. Wu, B. Qi, J. Zhi, Low-temperature fabrication of flexible TiO_2 electrode for dye-sensitized solar cells, Phys. Status Solidi. 207 (2010) 2201–2206. doi:10.1002/pssa.200925629.

[64] R. Liu, W. Yang, L. Qiang, Enhanced efficiency for dye-sensitized solar cells using a surface-treated, J. Power Sources. 199 (2012) 418–425. doi:10.1016/j.jpowsour.2011.10.072.

CHAPTER 8 Conclusions and future prospects

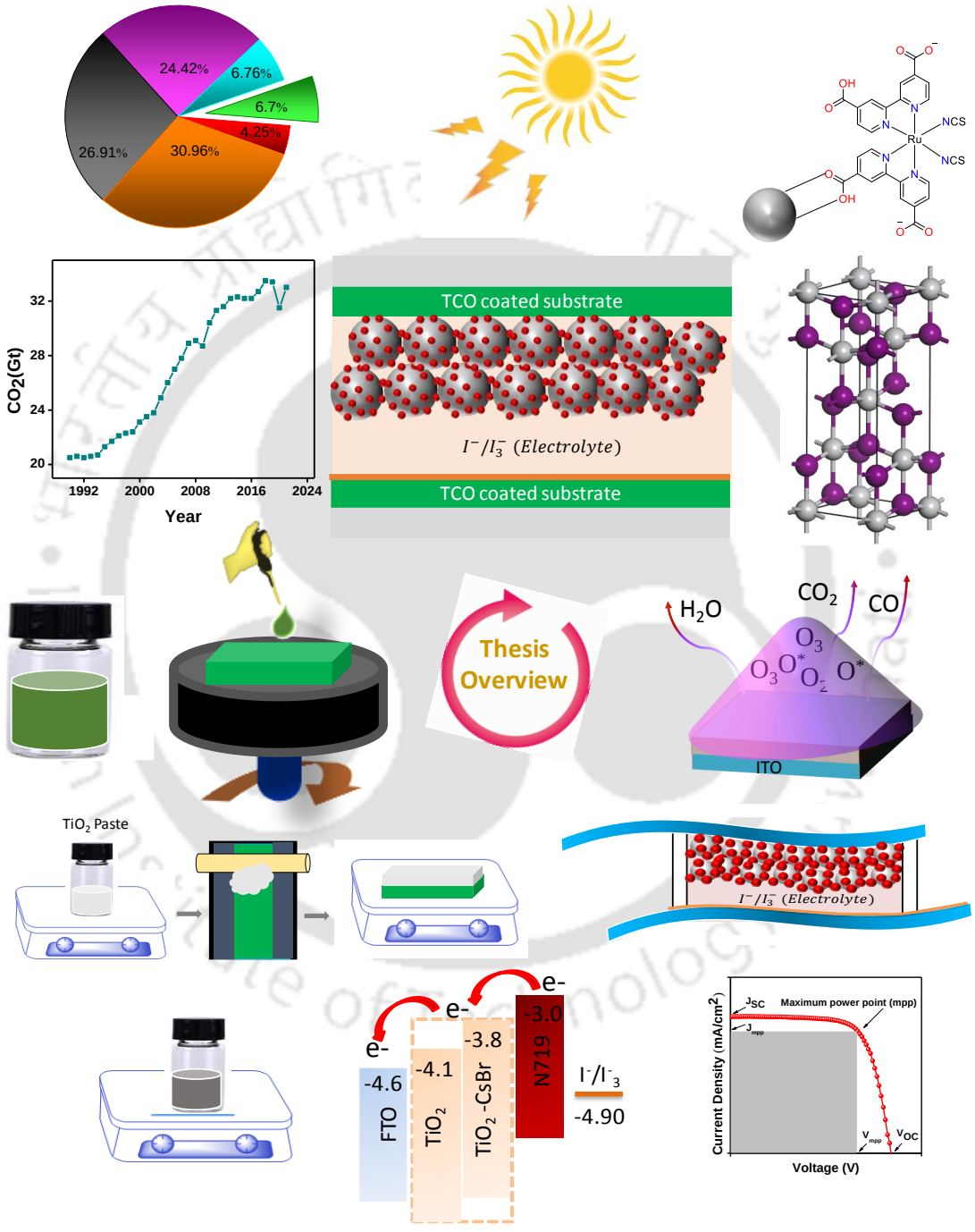

8.1 Conclusions

For the last two decades, significant attention has been attracted toward DSSCs due to their simple fabrication process and raw materials availability. The objective of this thesis was to develop an efficient and economically competitive electrode to further enhance the power conversion efficiency of DSSCs.

Chapter 1 of this thesis highlight the photovoltaic technology, a brief introduction of DSSCs development, their device structure including different components and working principle. Then different parameters used to define performance of solar cell.

Chapter 2 illustrated electrode preparation method and different characterization techniques used for analyzing the performance of DSSCs.

Chapter 3 deal with the investigation and optimization of UVO_3 exposured on TiO_2 electron transport layer. UVO_3 treatment removed the organic contaminants from the TiO_2 ETL, increase wettability and increase the oxygen vacancies by changing the surface state from Ti^{4+} to Ti^{3}. The effect of UV-O_3 exposure on the efficiency of DSSCs has been carefully analysed and optimized. The fabricated device with optimized time for 10 min UV-O_3 exposure shows the best PCE of 8.34% with good reproducibility. Thus, UVO_3 could be used as a tool to optimize the optical, electrochemical and electron injection properties in DSSC to obtain high efficiency.

Chapter 4 described the bandgap engineering of conventional TiO_2 electron transport layer with cesium bromide (CsBr) doping. The properties of doping were comprehensively analysis and related with the photovoltaic performance of DSSCs. It was observed that CsBr doping trigger a decreased in work function from -4.51 to -4.21 eV, increased in CBM from -3.7 to -3.55 eV, and a negative shift in flat band potential (V_{fb}) from -0.46 to -0.50V. TiO_2-CsBr photoanode promoted favourable band alignment for TiO_2/N719 heterojunction, which enhanced electron injection and transport by suppressing the back transfer of photogenerated electrons. Moreover, the doping of CsBr enhanced effective surface area of the electrode and increased maximum dye loading that correspondingly improve absorption coefficient. Finally, our TiO_2-CsBr doped photoanode enhanced device performance from 7.61 to 9.28% efficiency. Hence, bandgap engineering of TiO_2-CsBr doped ETL could be used to solve the inferior performance of DSSC based on conventional TiO_2.

Chapter 5 elucidated a simple approach to prepare an efficient and cost effective counter electrodes (CEs) for DSSCs based on Polyaniline (PANI) doped with Poly (sodium 4-styrenesulphonate) (PSSNa). The precise control of PSSNa in PANI provide higher effective surface area, improved electrocatalytic activity, facilitated higher electron transfer, and suppressed charge recombination which were the desired properties of CE for solar cell fabrication. The PANI-PSSNa doped CEs significantly improved the electrocatalytic activity and fairly obtained a conversion efficiency of 7.15%.

Chapter 6 focussed on the comparative study of Pt, CNTs, and CNTs-PANI CEs on DSSCs performance. The deposited CNTs-PANI layer exhibited a more porous nanostructure with higher surface roughness than CNTs and efficiency increased from 4.98 to 5.98% after CNTs was doped with conducting polymer PANI. Although the PCE of DSSC with CNTs-PANI was lower than that of Pt CE (7.87%), the inexpensive cost, excellent photoelectric properties, and easily available materials for large-scale production allow the CNTs based CEs to be an alternative material for DSSCs.

Chapter 7 demonstrated the preparation of binder free TiO_2 based electron transport layer (ETL) for flexible dye sensitized solar cells (FDSSCs). An additional post treatment Ultravoilet-Ozone (UVO_3) is performed to improve the performance of FDSSCs. UVO_3 treatment not only removed the organic contaminants but also significantly improved the crystallinity of film. TiO_2 ETL treated with UVO_3 decreased series resistance, electron recombination, substantially increased electron life and correspondingly show an efficiency of 2.53% compared to 1.43% for untreated device. The simple cost effective preparation procedure and improved device performance enable this fabrication method to be an alternative to conventional techniques.

Future prospect

Extensive studies on DSSCs have been conducted on various factors, such as interfacial contacts, tuning dye for maximum absorption, band gap engineering, and surface morphology etc. Explored different methods and materials were developed to enhance the performance of DSSCs. These advancements have stimulated rapid growth of DSSCs in last two decades. Nevertheless, quite a few challenges persist to further enhance the efficiency and to match the standard of commercialization.

According to the results in this present work, we suggest some works for the future that could be carried out:

The photovoltaic technology can be divided into two part according to the power required by the devices i.e., large terrestrial power production panel facilities and small portable electronics module. DSSCs can be implemented in both the cases. Comparing to other photovoltaic technologies, DSSCs performed better under indoor environment with artificial light sources. For example, Internet of Things (IoT) is attracting scientific and technological attention globally in these days. For IoT devices used batteries as a power sources and need charging often for the secondary batteries or replacement as their lifespan is restricted within months to years. These problem do not occur with DSSCs, since the cells turn the room light directly into electricity without external power supply. IoT devices equipped with DSSCs operate autonomously and therefore do not need long term maintenance, such as battery replacements. In addition, the power required for IoT devices is basically low and can be supplied under room light conditions. This performance of DSSCs has inspired us to carried out an extensive research in indoor applications. But most DSSCs are test under a standard AM 1.5G condition. No measuring system has yet been developed and validated for evaluating the characteristics of the indoor DSSCs.

With the raising demand of emerging applications such as portable power supply, internet of things (IoT) devices, wearable and high integrated microelectronic devices FDSSCs have drawn significant attention. But the poor stability of the device caused by deterioration, evaporation and leakage of liquid electrolytes due to the weak adhesion force of sealing materials on bendable surface are the biggest issues. Therefore, the stability of DSSCs have to be taken care off with the development of technology. To improve the stability and lifetime of FDSSCs robust sealing and encapsulation through transparent films is required.

For the successful realisation of DSSCs at practical applications, the issues on unfavourable bending, stability, and low performance on large area device should be address carefully.

List of Publications

1. **Chandan Dawo**, Mohammad Adil Afroz, Parameswar Krishnan Iyer, Harsh Chaturvedi, Effect of UV-ozone exposure on the dye-sensitized solar cells performance. Solar Energy, Volume 208, 2020, Pages 212-219, https://doi.org/10.1016/j.solener.2020.07.064.
2. **Chandan Dawo**, Harsh Chaturvedi, High performance PANI-PSSNa doped counter electrode for dye-sensitized solar cells. Appl. Phys. A, Volume 128, 640, 2022. https://doi.org/10.1007/s00339-022-05739-y.
3. **Chandan Dawo**, Maimur Hossain, Parameswar Krishnan Iyer, Harsh Chaturvedi, UV Ozone based rapid low temperature fabrication of flexible dye sensitized solar cells, Synthetic Metals, Volume 291, 2022, https://doi.org/10.1016/j.synthmet.2022.117172.
4. **Chandan Dawo** and Harsh chaturvedi, Recent advances in the development of flexible dye-sensitized solar cells: Fabrication, challenges and applications- a review, Flexible and Printed Electronics, Volume 8, 2023, 013001, doi 10.1088/2058-8585/acb660.
5. **Chandan Dawo**, Parameswar Krishnan Iyer, Harsh Chaturvedi, Carbon nanotubes/PANI composite as an efficient counter electrode material for dye sensitized solar cell, Materials Science & Engineering B, Volume 297, 2023, 116722, https://doi.org/10.1016/j.mseb.2023.116722.
6. Govind Sharma, **Chandan Dawo** and Chhagan Lal, Revealing the Photophysics of N719 Dye based Dye-Sensitized Solar Cell, Optical Materials. Volume 142, 2023, 114113, https://doi.org/10.1016/j.optmat.2023.114113.
7. Govind Sharma, **Chandan Dawo**, Uttam K. Kumawat, Saurabh K. Saini, R.K. Singhal, Chhagan Lal, Revealing the relaxation kinetics of curcumin based dye-sensitized solar cell, Materials Science and Engineering B, Volume 298, 2023, 116905,https://doi.org/10.1016/j.mseb.2023.116905.

Conferences/workshop/seminar

1. Presented *poster* **in 6th International Conference on Advanced Nanomaterials and Nanotechnology 2020,** IIT Guwahati.
2. Seminar on **Basics of Small Angle X-ray Scattering,** IIT Guwahati.
3. Oral presentation on **High performance PANI-PSSNa doped counter electrode for dye-sensitized solar cells, North East Research conclave (**NERC) 2022, IIT Guwahati.

-----End-----